

University of California
Santa Barbara

Modeling Electronic Properties of Complex Oxides

A dissertation submitted in partial satisfaction
of the requirements for the degree

Doctor of Philosophy
in
Electrical and Computer Engineering

by

Karthik Krishnaswamy

Committee in charge:

Professor Chris G. Van de Walle, Co-chair

Professor Chris Palmstrøm, Co-chair

Professor Umesh K. Mishra

Professor Robert A. York

December 2016

The Dissertation of Karthik Krishnaswamy is approved.

Professor Umesh K. Mishra

Professor Robert A. York

Professor Chris Palmstrøm, Committee Co-chair

Professor Chris G. Van de Walle, Committee Co-chair

November 2016

Modeling Electronic Properties of Complex Oxides

Copyright © 2016

by

Karthik Krishnaswamy

Acknowledgements

I am extremely grateful to have interacted with a phenomenal set of talented individuals during my time as a graduate student. My advisor, Prof. Chris G. Van de Walle, has been immensely supportive throughout my Ph.D. career, taught me to be a good researcher, and inspired me to perform better every time. Chris has taught me many valuable skills over the years that are essential in a good scientist. One of the most important skills that I learned from him is to be very critical of everyone's thoughts, ideas and opinions, especially of one's own. He also has an exceptional ability to clearly and effectively communicate complex ideas to any audience. I believe, that a constant exposure to these qualities has enhanced my thought process and my approach to any problem. I am greatly indebted to him for all his contributions towards my research, and for providing a conducive environment for carrying out my research.

I would like to especially thank Prof. Chris Palmstrøm for his advice and constant feedback on my research work, and also for serving as a Committee Co-chair. I owe my gratitude to my other excellent committee members, Profs. Umesh K. Mishra and Robert A. York, for their help, cooperation, friendly advice, and valuable feedback during the dissertation process.

I have greatly benefitted from being in the company of exceptional people within Chris' group, and have rejoiced many conversations I have had with them. Prof. Anderson Janotti and Dr. Cyrus E. Dreyer, with whom I have collaborated during my first year in the group and continue to collaborate, have always been very supportive and mentored

me on density functional theory, surface calculations, and complex oxides. I could not have begun my research career without their support and guidance. Since then, I have had many great and fruitful collaborations with some of the other members of Chris' group: Drs. Hartwin Peelaers, Daniel Steiauf, Burak Himmetoglu, Youngho Kang, John L. Lyons, Lars Bjaalie, and Luke Gordon. I am also grateful to the other postdocs in the group: Prof. Audrius Alkauskas, Dr. Minseok Choi, Dr. Anindya Roy, Dr. Leigh Weston, Dr. Qimin Yan, Dr. Justin Weber, Dr. Joel Varley, Dr. Darshana Wickramaratne and Dr. Zhen Zhu, who were always there to help out, answer my questions on physics and computation, and provide valuable career advice. Special thanks to all of Chris' current and past students: Patrick McBride, Jimmy Shen, Wennie Wang, Michael Swift, Hiral Tailor, Nicholas Adamski, and Andrew Rowberg, for all the interesting, amusing, and useful conversations on a wide variety of topics. I owe my sincere gratitude to all of them for having a strong and positive influence on me and my research; it certainly enriched my days as a graduate student.

Working on projects related to the EXtreme Electron concentration Oxide DEvices (EXEDE) MURI, and the Center for Low Energy Systems Technology (LEAST) has given me the pleasure of interacting and exchanging ideas with brilliant people at UCSB as well as at other universities in the country. I'm fortunate for the very interesting, insightful and fruitful conversations on a variety of topics with Profs. Susanne Stemmer, S. James Allen, Debdeep Jena, and Siddharth Rajan that have influenced my research. I have drawn inspiration from the experimental work done in the group of Prof. Su-

sanne Stemmer, which is at forefront of growth and characterization of complex-oxide heterostructures. I would also like to thank Dr. Amit Verma for the useful discussions and feedback.

I am thankful to the funding agencies, Department of Energy and the LEAST Center that have provided financial support. I also thank the supercomputing facilities and agencies: XSEDE, CNSI, and NERSC for providing access to supercomputers, which has been indispensable for carrying out my research.

Finally, I am forever grateful to my parents, Sankari Krishnaswamy and Krishnaswamy Mahalingam, as well as my sister Shvitra for providing love, support, and encouragement, and for instilling the confidence in me to pursue a career in research.

Curriculum Vitæ

Karthik Krishnaswamy

Education

- 2016 Ph.D. in Electrical and Computer Engineering, University of California, Santa Barbara, USA
- 2013 M.S. in Electrical and Computer Engineering, University of California, Santa Barbara, USA
- 2011 B.E. in Telecommunication Engineering, M.S.Ramaiah Institute of Technology, Bangalore, India

Publications

- [1] **K. Krishnaswamy**, C. E. Dreyer, A. Janotti, and C. G. Van de Walle, “Structure and energetics of LaAlO_3 (001) surfaces,” *Phys. Rev. B* **90**, 235436 (2014).
- [2] **K. Krishnaswamy**, C. E. Dreyer, A. Janotti, and C. G. Van de Walle, “First-principles study of surface charging in $\text{LaAlO}_3/\text{SrTiO}_3$ heterostructures,” *Phys. Rev. B* **92**, 085420 (2015).
- [3] H. Peelaers, **K. Krishnaswamy**, L. Gordon, D. Steiauf, A. Sarwe, A. Janotti, and C. G. Van de Walle, “Impact of electric-field dependent dielectric constants on two-dimensional electron gases in complex oxides,” *Appl. Phys. Lett.* **107**, 183505 (2015).
- [4] J. L. Lyons, **K. Krishnaswamy**, L. Gordon, A. Janotti, and C. G. Van de Walle, “Identification of Microscopic Hole-Trapping Mechanisms in Nitride Semiconductors,” *IEEE Electron Device Lett.* **37**, 154 (2016).
- [5] **K. Krishnaswamy**, L. Bjaalie, B. Himmetoglu, A. Janotti, L. Gordon, and C. G. Van de Walle, “ BaSnO_3 as a channel material in perovskite oxide heterostructures,” *Appl. Phys. Lett.* **108**, 083501 (2016).
- [6] L. Bjaalie, A. Janotti, **K. Krishnaswamy**, and C. G. Van de Walle, “Point defects, impurities, and small hole polarons in GdTiO_3 ,” *Phys. Rev. B* **93**, 115316 (2016).
- [7] **K. Krishnaswamy**, B. Himmetoglu, Y. Kang, A. Janotti, and C. G. Van de Walle, “First-principles analysis of electron transport in BaSnO_3 ,” *submitted* (2016).
- [8] **K. Krishnaswamy**, A. Janotti, L. Bjaalie, and C. G. Van de Walle, “Surprising stability of the polar (001) surface of the Mott insulator GdTiO_3 ,” *in preparation* (2016).
- [9] Y. Kang, **K. Krishnaswamy**, H. Peelaers, and C. G. Van de Walle, “First-principles calculation of electron mobility in $\beta\text{-Ga}_2\text{O}_3$,” *in preparation* (2016).

Contributed Talks

- 2014 “Electronic Structure and Stability of LaAlO_3 using first-principles calculations,” *American Physical Society March meeting*, Denver, Colorado, USA
- 2015 “Surface charging in $\text{LaAlO}_3/\text{SrTiO}_3$ heterostructures,” *American Physical Society March meeting*, San Antonio, Texas, USA
- 2016 “First-principles calculations of LO phonon scattering in BaSnO_3 ,” *American Physical Society March meeting*, Baltimore, Maryland, USA

Awards

- 2014 - 2015 DOW/MRL-UCSB travel grant to attend the *American Physical Society March meetings*

Abstract

Modeling Electronic Properties of Complex Oxides

by

Karthik Krishnaswamy

Complex oxides are a class of materials that have recently emerged as potential candidates for electronic applications owing to their interesting electronic properties. The goal of this dissertation is to develop a fundamental understanding of these electronic properties using a combination of first-principles approaches based on density functional theory (DFT), and Schrödinger-Poisson (SP) simulations.

The formation of a high-density ($3.3 \times 10^{14} \text{ cm}^{-2}$) two-dimensional electron gas (2DEG) at polar/nonpolar complex oxide interfaces, such as the $\text{LaAlO}_3/\text{SrTiO}_3$ (LAO/STO) and $\text{GdTiO}_3/\text{SrTiO}_3$ (GTO/STO) interfaces, has raised tremendous interest in complex oxides. However, the mechanism responsible for the 2DEG formation has not yet been agreed upon due to various aspects of experimental observations conflicting with the proposed models. We resolve these conflicts with a consistent model based on polar discontinuities, and explain the role played by surface terminations and surface charging. The study of surface charging using DFT calculations is difficult due to the condition of maintaining charge neutrality. We overcome this complication by developing a rigorous and general methodology for computing the energetics of charged surfaces for semicon-

ductors and insulators. The developed methodology addresses a common problem in surface science: the exchange of charges between a reservoir and a surface.

Another challenge in the modeling of the high-density 2DEG at interfaces is the correct incorporation of the electric-field dependence of the static dielectric permittivity in materials such as STO, which is due to its incipient ferroelectric nature. So far, a field-dependent dielectric response has not been implemented in any of the commercially available SP solvers. We develop a methodology, in conjunction with the SP solver *nextnano*³, to account for this field dependence selfconsistently with the resulting band bending in the 2DEG.

Confinement of the high-density 2DEG requires a sufficiently large conduction-band offset at the interface. Confinement is particularly challenging in complex oxides such as BaSnO₃ (BSO) that have a low density of states (DOS). Using SP simulations of BSO heterostructures with possible barrier materials (including STO, LaInO₃, and KTaO₃) we quantitatively study 2DEG confinement in BSO. The results of the simulations serve as a guide to engineer barriers for BSO-based heterostructures.

Finally, carrier mobility is another important component determining the performance of electronic devices. The mobility of electrons in many complex oxides, including STO, tends to be low ($\sim 10 \text{ cm}^2\text{V}^{-1}\text{s}^{-1}$) at room temperature. Recent experimental demonstrations of high electron mobility ($300 \text{ cm}^2\text{V}^{-1}\text{s}^{-1}$) in BSO have, therefore, come as a surprise to the complex oxide community. Using accurate first-principles calculations, we study longitudinal-optical-phonon (LO-phonon) and ionized impurity scattering mech-

anisms in BSO. Our analysis reveals that the low DOS in BSO is the reason behind BSO's high mobility in comparison to STO and other complex oxides, which have a high DOS. The insights gained from the study provide a recipe for identifying or designing high-mobility complex oxides.

Overall, four different aspects of complex oxides were addressed by the accomplishments in this dissertation: (1) developing a rigorous and general methodology for surface charging in thin films, which is a common scenario in surface science; (2) correct implementation of a field-dependent dielectric permittivity in an SP solver; (3) assessing the carrier confinement in the high-density 2DEG within BSO, which has a low DOS; and (4) understanding the impact of LO-phonon and ionized impurity scattering mechanisms on carrier mobility in complex oxides.

Contents

Acknowledgements	iv
Curriculum Vitae	vii
Publications	vii
Abstract	ix
List of Figures	xv
List of Tables	xxii
1 Introduction to complex oxides	1
1.1 Complexity in complex oxides: One chemical formula ABO_3 , many properties	3
1.2 Polar <i>vs.</i> nonpolar orientations	5
1.3 Mechanism of 2DEG formation	7
1.3.1 Key experimental observations	7
1.3.2 Models proposed in literature	8
1.3.3 Our model	12
1.4 Field-dependent dielectric constant	13
1.5 Search for high electron mobility	14
1.6 Summary	15
2 Theoretical methods and tools	17
2.1 First-principles theory	17
2.1.1 Many-body Schrödinger equation	18
2.1.2 Density functional theory	22
2.1.3 Practical aspects	34
2.2 Schrödinger-Poisson solver	38
2.2.1 Schrödinger-Poisson equation	38

2.2.2	Field-dependent dielectric permittivity	40
2.3	Boltzmann transport theory	41
2.3.1	Boltzmann transport equation	41
2.3.2	Relaxation-time approximation	43
2.3.3	Electron-phonon scattering	46
2.3.4	Ionized impurity scattering	49
2.3.5	Hall mobility and Hall factor	50
3	Implementing field dependence of dielectric constant into Schrödinger-Poisson solver	52
3.1	Introduction	53
3.2	Implementation details	55
3.3	Results and discussion	58
3.4	Conclusion	61
4	First-principles theory of surface charging	63
4.1	Introduction	63
4.2	First-principles methodology for charged surfaces	69
4.2.1	First-principles method	69
4.2.2	Surface energy of neutral reconstructed LaAlO_3 surfaces	71
4.2.3	Methodology to treat charged surfaces	72
4.3	Electronic structure of the bulk and surface LaAlO_3	83
4.3.1	Bulk	83
4.3.2	Surface	85
4.4	Surface energetics of LAO in STO/LAO heterostructures	89
4.4.1	Reference structure	91
4.4.2	Neutral surfaces of LAO	91
4.4.3	Charged surfaces of LAO	94
4.4.4	Energetics of LAO/STO with surface charging	98
4.5	Surface stability and its effect on 2DEG density	102
4.5.1	Unreconstructed AlO_2 -termination	102
4.5.2	Energetics due to surface defects and reconstructions	102
4.5.3	Effect of surface defects and reconstructions on the 2DEG density	106
4.6	Conclusions	111
5	Surface study of a Mott insulator: GdTiO_3	113
5.1	Introduction	113
5.2	Computational methodology	116
5.3	Bulk properties	119
5.4	Surface band structure	120
5.5	Results and discussion of surface energies	124
5.5.1	Native surface terminations	124
5.5.2	H-adatom reconstruction on TiO_2 termination	126

5.5.3	Implications for polar surfaces of Mott insulators	128
5.6	Impact on 2DEG at STO/GTO interface	129
5.7	Conclusion	131
6	First-principles analysis of electron transport in complex oxides	133
6.1	Introduction	133
6.2	Atomic and Electronic structure	136
6.3	Computational implementation of transport calculation	138
6.4	Results	143
6.4.1	LO-phonon scattering	143
6.4.2	Ionized impurity scattering	150
6.4.3	Total drift mobility	151
6.4.4	Mobility <i>vs.</i> electron density	152
6.5	Discussion	155
6.5.1	Comparison with experimental measurements	155
6.5.2	Comparison to other perovskite oxides	160
6.5.3	Enhancing mobility in BaSnO ₃	162
6.6	Conclusion	164
7	Evaluating BaSnO₃ as a channel material	165
7.1	Introduction	166
7.2	First-principles method	169
7.3	Band structure and band offsets for BaSnO ₃	170
7.4	Schrödinger-Poisson	173
7.5	Results and Discussion of SP simulations	174
7.6	Conclusions	176
8	Summary and future prospects	178
8.1	Overall summary	178
8.2	Prospects for future research in complex oxides	181
8.2.1	Extensions of the present work	181
8.2.2	General challenges for use of complex oxides in electronic applications	185
A	Reading list	189
A.1	Books and review articles	189
A.2	Original articles	192
B	Extended Fröhlich model	194
C	Hyperbolic dispersion	196
	Bibliography	199

List of Figures

1.1	Some common perovskite crystal structures	5
1.2	Alternating (a) neutral planes with 0 net charge in nonpolar ABO_3 , and (b) charged planes with +1 or -1 net charge per areal unit cell in polar CDO_3 perovskites oxides, when viewed along the [001] direction.	7
1.3	Polar catastrophe model: (a) 2DEG at the STO/LAO heterointerface with alternating charged planes of LAO and neutral planes of STO is pictured as forming due to charge transfer <i>from</i> the LAO surface. (b) Band diagram of the heterointerface showing the diverging potential in LAO, and the consequent transfer of electrons from the LAO surface to the interface.	10
3.1	Dielectric constant as a function of the electric field. The dashed line is determined by fitting Eq. 3.1 to the experimental measurements of Ref. [24]. These experimental data points are not continuous as they were obtained from 3 different samples. The solid line is determined by integrating over the field, as expressed in Eq. 3.2. The curve fitting, integration and plotting were done by my colleague, Dr. Hartwin Peelaers. The inset shows a schematic band diagram of the confinement of a 2DEG at an interface between STO and a barrier material. The band bending reflects the presence of an electric field.	54
3.2	Algorithm implemented to account for the field-dependent dielectric permittivity in a Schrödinger-Poisson solver.	58
3.3	(a) Calculated electric field near the STO/GTO heterojunction. The junction is located at 0 nm. (b) Corresponding dielectric constant, as determined from Eq. 3.2 using the calculated average electric field in each region.	59
3.4	Electron distribution at the STO/GTO interface (left axis, dashed lines) assuming either a constant dielectric constant ($\epsilon=300$) or a field-dependent ϵ . The corresponding conduction-band profile is shown in solid lines (right axis).	62

4.1	Schematic illustration of (a) the supercell used to calculate a symmetric neutral slab with dielectric constant ε with vacuum on either side, (b) the process of adding charge (shown in yellow) to the surface of the slab with a uniform compensating background charge (shown in blue) spread throughout the supercell, and (c) an auxiliary system with reference electrodes at the cell edges.	70
4.2	Averaged electrostatic potential energy in a supercell containing a slab of LAO with unreconstructed neutral (relaxed) AlO_2 -terminated surfaces. The dotted (red) line corresponds to the planar average of the potential energy in the xy plane; the solid (blue) line is the one-dimensional macroscopic average. The dashed (black) line indicates the average of the electrostatic potential energy taken over the entire supercell, which is arbitrarily set to zero here (a common convention in first-principles calculations). The top panel shows the geometry of the supercell, aligned to the plot of the potential energy.	76
4.3	Electrostatic potential energies in a supercell containing a slab of LAO with unreconstructed AlO_2 -terminated surfaces, to which a charge of $0.25e^-$ per areal unit cell is added. The calculated uncorrected electrostatic potential energy (labelled $-e\tilde{V}$) shifted to set the value at $\pm L_z/2$ (supercell boundaries) to 0 eV, is shown by the dotted (blue) curve. The electrostatic potential energy corrected by removing contributions due to CBC (labelled $-eV$) is shown by the solid light (orange) curve, and the potential energy due to the CBC is shown as solid black curve. The average value of the uncorrected potential energy, labeled $-e\langle\tilde{V}\rangle$, is shown by the dotted horizontal line. The positions of the reference electrodes are indicated by arrows and labeled “ref. el.”	80
4.4	(a) Schematic of the structure of cubic LAO, showing two unit cells with the AlO_6 octahedra. (b) Alternating layers of AlO_2 and LaO in a slab, with the surface terminating in an AlO_2 plane. (c) Schematic depicting alternating charged planes and $0.5e^-$ transferred from LaO planes to the neighboring AlO_2 -planes in the bulk. The surface is shown terminated by an AlO_2 plane and lacks $0.5 e^-$	84
4.5	Electronic structure of bulk cubic phase LAO. The direct (5.04 eV) and indirect (4.88 eV) band gaps are indicated. The zero of energy was set to the valence-band maximum at the R -point.	85
4.6	Projected band structures for unreconstructed (but relaxed) (1×1) surfaces of LAO: (a) LaO-terminated and (b) AlO_2 -terminated. Solid (gray) curves represent projected bulk states. Dashed (blue) curves indicate spin-up (majority spin) surface states and dotted (red) curves represent spin-down surface states. For the AlO_2 -terminated surface in (b), spin-up and spin-down states are degenerate. The Fermi level E_F is indicated by horizontal solid (black) lines.	86

4.7	Band diagram for the interface between semi-infinite SrTiO ₃ and (a) semi-infinite LaAlO ₃ showing band offsets and the formation of an intrinsic two-dimensional electron gas (2DEG), and (b) LaAlO ₃ with a finite thickness less than the critical thickness, terminated by an AlO ₂ plane containing surface states to which electrons from the 2DEG can transfer, leading to an insulating interface. The values for the band offsets are taken from Ref. [82].	90
4.8	Surface energy (in eV/Å ²) for (2×2) O-vacancy (V _O) (black), (3×2) Al-atom (Al _{ad}) (blue), and the (3×2) La-vacancy (V _{La}) (orange) reconstructions on the LaAlO ₃ surface as a function of μ _O . The unreconstructed AlO ₂ (green) and LaO (red) terminations are also shown. The regions shaded by diagonal crosshatching indicate the range of surface-energy values for LaO-terminated surfaces, and those shaded by solid colors are for AlO ₂ -terminated surfaces, under the conditions within which LAO is stable; the boundaries indicated by dashed lines correspond to Al-rich conditions and those indicated by solid lines correspond to La-rich conditions. Details of stability regions and limiting conditions are discussed in the text.	93
4.9	Surface energy change (in eV/Å ²) with respect to the neutral surface as a function of surface charge (in units of the magnitude of electronic charge) per (1×1) unit. Negative charge indicates added electrons and positive charge corresponds to electrons removed (or holes added). Solid squares (blue) are results without correction and open circles (green) represent corrected values. The solid (red) line shows the results of Eq. 4.9, based on Koopmans' theorem generalized for charged surfaces.	96
4.10	Surface energy (in eV/Å ²) for AlO ₂ -terminated thin films of LAO as a function of μ _O under Al-rich conditions (see Eq. 4.3a). Results for an LaO-terminated surface with a (3×2) La-vacancy reconstruction are included for comparison. The dotted (gray) line labeled “2uc AlO ₂ ” is the corrected surface energy after electron transfer to the unreconstructed AlO ₂ -terminated surface for a 2-unit-cell LAO film. Solid lines refer to the minimized surface energy under a combination of electron transfer and an Al-atom surface density of C _{Al_{ad}} at each μ _O corresponding to a 2-unit-cell LAO film [light (orange) line] and a 4-unit-cell film [dark (blue) line]. The dashed lines refer to surface energies of (3×2) La-vacancy [V _{La} (3×2)] (red), (2×2) O-vacancy [V _O (2×2)] (black), and (3×2) Al-atom [Al _{ad} (3×2)] (blue) reconstructions, and the unreconstructed (but relaxed) AlO ₂ -terminated surface (green).	103

4.11	2DEG density (in units of 10^{14} cm^{-2}) under Al-rich conditions as a function of LAO thickness for different surface defects, namely, Al-adsorbate (Al_{ad}) (green), O-vacancy (V_{O}) (red), and H-adsorbate (H_{ad}) for $\mu_{\text{H}} = -1 \text{ eV}$ (solid orange) and for $\mu_{\text{H}} = -2 \text{ eV}$ (dotted blue) at (a) $\mu_{\text{O}} = 0 \text{ eV}$, and (b) $\mu_{\text{O}} = -2 \text{ eV}$. For comparison, the 2DEG density in the absence of surface defects is plotted in gray (labeled “no defects”). The maximum 2DEG density corresponding to $3.3 \times 10^{14} \text{ cm}^{-2}$ is indicated by the black horizontal bar.	109
5.1	(a) Top view of the (001) plane of the 20-atom distorted perovskite structure of GdTiO_3 indicating the lattice parameters and O-Ti-O bond angles, and (b) side view depicting its polar nature with alternating TiO_2 and GdO planes along the [001] direction.	114
5.2	Stability region of GdTiO_3 (yellow region enclosed by solid lines) along with its competing phases, namely $\text{Gd}_2\text{Ti}_2\text{O}_7$, Gd_2O_3 , and TiO_2 as a function of μ_{Ti} and μ_{O} . The phase boundary with Gd_2O_3 is indicated as Gd-rich, while the boundary with TiO_2 is indicated as Ti-rich.	119
5.3	Surface atomic structure indicating the in-plane O-Ti-O bond angles of the (a) bare (but relaxed) TiO_2 termination, and (b) H-adsorbate reconstruction of the TiO_2 termination. The charge densities of the highest occupied (in green) and lowest unoccupied (in red) surface states of the bare termination are also shown in (a). Charge on the Ti atoms are also indicated.	121
5.4	Surface band structure of (a) TiO_2 -terminated, and (b) GdO-terminated GTO projected onto the 2D (001) Brillouin zone. The gray regions are bulk states projected onto the 2D surface BZ. The solid (red) lines are the spin-up (majority spin) channel of the surface supercell, while dashed (blue) lines represent the spin-down (minority spin) channel. The Fermi levels (E_{F}), determined based on the occupation of states in the slab supercell calculations, are also indicated. The vacuum level for each of the terminations is set to 0 eV.	123
5.5	Surface energy ($\text{meV}/\text{\AA}^2$) of TiO_2 -termination (solid red), GdO-termination (dashed blue) and (1×1) H-adsorbate reconstruction on TiO_2 -termination (open circles) calculated under (a) Gd-rich and (b) Ti-rich conditions is plotted as a function of μ_{O} . Under Gd-rich conditions, the formation of competing phases of GTO restricts μ_{O} to the range $-5.24 \text{ eV} < \mu_{\text{O}} < -3.62 \text{ eV}$, while under Ti-rich conditions the restricted range, $-4.58 \text{ eV} < \mu_{\text{O}} < -3.62 \text{ eV}$, is smaller. The gray box in panel (b) indicates the μ_{O} values for which GTO is unstable under the constraint imposed by Ti-rich conditions. See text in Sec. 5.2 and Fig. 5.2 for a more detailed explanation.	125

5.6	Band lineup between GTO, LAO and STO from Ref. [82] is shown referenced to the vacuum level calculated for the TiO ₂ -terminated GTO surface. Dotted red lines show unoccupied surface state levels for the TiO ₂ -terminated GTO and AlO ₂ -terminated LAO surfaces [see Figs. 5.4(a) and 4.6(b)]. The Fermi level E_F in STO (dashed black line) was calculated using SP simulations assuming a 2DEG density of $3.3 \times 10^{14} \text{ cm}^{-2}$ (see Table 3.1). Electron transfer occurs from the 2DEG to low-lying LAO surface states, but the transfer to high-lying GTO surface states is far less favorable.	129
6.1	Band structure of BSO calculated from first principles using the HSE06 hybrid functional. The inset indicates the high symmetry points in the Brillouin zone. The indirect gap $R \rightarrow \Gamma$ is 2.40 eV, and the direct gap at Γ is 2.88 eV.	137
6.2	Dispersion of the lowest CB around Γ , showing the slight anisotropy evident from the difference in dispersion along the high-symmetry directions (Γ -X, Γ -M, and Γ -R) (shaded in blue). The fitted hyperbolic dispersion (solid orange line) and parabolic dispersion (dashed black line) are shown. Fermi levels for different electron densities are also indicated.	141
6.3	(Color online) Calculated scattering rates [10^{14} s^{-1}] <i>versus</i> electron wavevector k (\AA^{-1}) for LO-phonon scattering (orange dotted lines), ionized impurity scattering (blue dashed lines) and the total rate obtained via Matthiessen's rule (black solid lines) at RT (300 K) for electron densities (a) 10^{19} cm^{-3} and (b) 10^{20} cm^{-3} . Values are plotted along $\Gamma \rightarrow X$ but are representative of all directions in the BZ due to the almost isotropic band structure. Note the different vertical scales in panels (a) and (b). The Fermi level ε_F is indicated by vertical dashed lines.	145
6.4	(Color online) Calculated mobility <i>versus</i> temperature for LO-phonon scattering (μ_{LO}) (solid red circles) for $n=10^{20} \text{ cm}^{-3}$. The calculated mobility due to scattering from the individual phonon modes is shown: μ_{LO1} (purple open squares), μ_{LO2} (green open circles), and μ_{LO3} (orange triangles) with energies 18, 51 and 88 meV, respectively. The lines are analytic fits for the mobilities based on the BE distribution (see text): μ_{LO} (black solid line), μ_{LO1} (purple dotted lines), μ_{LO2} (green dashed line), and μ_{LO3} (orange dash-dot line).	149
6.5	Calculated drift mobility <i>versus</i> temperature in the case of ionized impurity scattering (μ_{imp}) for five different electron densities: 10^{17} (blue squares), 10^{18} (orange open circles), 10^{19} (green solid circles), 10^{20} (red open triangles), and 10^{21} (black closed triangles) cm^{-3}	151
6.6	Calculated drift mobility <i>versus</i> temperature due to a combination of LO-phonon and ionized impurity scattering (μ_{tot}) for five different electron densities: 10^{17} (blue squares), 10^{18} (orange open circles), 10^{19} (green solid circles), 10^{20} (red open triangles), and 10^{21} (black closed triangles) cm^{-3}	152

6.7	(a) Calculated drift mobility <i>versus</i> electron density (cm^{-3}) at 300 K (RT) for LO-phonon scattering, μ_{LO} (orange dotted line), and ionized impurity scattering, μ_{imp} (blue dashed line), as well as the total drift mobility, μ_{tot} (black solid line). (b) Comparison of the screened (orange dotted line) and unscreened (green open circles on dotted line) values for μ_{LO} <i>versus</i> electron density.	154
6.8	(Color online) Calculated Hall factor r_{H} <i>versus</i> carrier concentration for ionized impurity (blue dashed line) and LO-phonon scattering (orange dotted line).	157
6.9	(Color online) Solid lines: calculated Hall mobility <i>versus</i> temperature due to ionized impurity and LO-phonon scattering, with addition of a temperature-independent scattering contribution: $(1/\mu_{\text{imp}}+1/\mu_{\text{LO}}+1/\mu_{\text{add}})^{-1}$, for different experimental doping densities. Symbols indicate the corresponding experimental Hall measurements (a) on bulk crystals from Ref. [37], for $8 \times 10^{19} \text{ cm}^{-3}$ (solid red circles) and $1.2 \times 10^{20} \text{ cm}^{-3}$ (solid green triangles) doping, and (b) on thin films from Ref. [148], for $6 \times 10^{19} \text{ cm}^{-3}$ (open orange circles) and $7 \times 10^{19} \text{ cm}^{-3}$ (open blue triangles) doping. For bulk crystals (a), μ_{add} is $4500 \text{ cm}^2\text{V}^{-1}\text{s}^{-1}$ for $8 \times 10^{19} \text{ cm}^{-3}$, and $1000 \text{ cm}^2\text{V}^{-1}\text{s}^{-1}$ for $1.2 \times 10^{20} \text{ cm}^{-3}$, and for thin films (b), μ_{add} is $210 \text{ cm}^2\text{V}^{-1}\text{s}^{-1}$ for $6 \times 10^{19} \text{ cm}^{-3}$, and $475 \text{ cm}^2\text{V}^{-1}\text{s}^{-1}$ for $7 \times 10^{19} \text{ cm}^{-3}$	158
7.1	Schematic band diagrams depicting (a) delta doping at a nonpolar interface, and (b) polar discontinuity doping at a polar interface.	167
7.2	Fermi level relative to the CBM ($E_{\text{F}} - E_{\text{c}}$) as a function of electron density in BSO at 300 K based on the first-principles HSE06 band structure (solid blue line) and compared to values obtained from SP simulations (solid red circles) using a parabolic effective mass $m_{\text{fit}} = 0.26 m_e$ that produces the best fit for electron densities upto 10^{21} cm^{-3} . The inset shows the atomic structure of BSO, with alternating planes of BaO and SnO_2 along [001].	169
7.3	Natural band alignment between BSO, STO, LIO, and KTO calculated from first principles. The band alignment calculations were performed by my colleague, Dr. Lars Bjaalie. The BSO band structure was referenced to the vacuum level based on a calculation for an SnO_2 -terminated surface.	172
7.4	Computed 2DEG density confined in BSO as a function of dopant sheet concentration based on SP simulations for delta-doped BSO/STO interfaces with $d=2 \text{ nm}$ (blue solid squares) or 10 nm (purple solid circles). Values for polar-discontinuity-doped BSO/LIO (orange triangle) and BSO/KTO (red cross) interfaces are also shown. The ideal situation, where all the electrons introduced are confined in BSO, is shown as a dashed green line.	175

7.5 2DEG density confined in BSO as a function of CBO for various sheet dopant concentrations placed at $d=2$ nm in the barrier. The results for the polar BSO/KTO (solid triangle) and BSO/LIO (solid diamond) interfaces are also shown. CBO values for STO, SHO and SZO are indicated by arrows.176

List of Tables

3.1	Field-dependent properties of the 2DEG, namely peak position, peak height, Fermi level relative to conduction-band minimum, minimum value of ϵ and maximum value of the electric field, for different 2DEG densities.	61
5.1	Enthalpy of formation (ΔH_f), in units of eV/(formula unit), for GdTiO ₃ and its competing phases.	118
6.1	The effective mass near Γ , m_Γ^* and the nonparabolicity parameter α for the hyperbolic fit (Eq. 6.1) along three high-symmetry directions.	141
6.2	Calculated drift mobility values (in $\text{cm}^2\text{V}^{-1}\text{s}^{-1}$) at RT (300 K) taking into account scattering due to LO phonons (μ_{LO}), ionized dopants (μ_{imp}), and their total (μ_{tot}) for different electron densities n (cm^{-3}). The corresponding Fermi level ϵ_F (eV) (referenced to the conduction-band minimum, CBM), Fermi wavevector k_F (\AA^{-1}), and the screening wavevectors $q_{\infty, \text{scr}}$ (\AA^{-1}) (Eq. 2.41) and q_{scr} (\AA^{-1}) are also given.	147
7.1	Structural and electronic properties of perovskites calculated from first principles (unless otherwise noted). The band offsets reported were calculated by my colleague, Dr. Lars Bjaalie.	171

Chapter 1

Introduction to complex oxides

The goal of any civilization is advancement, both societal and technological. The past few centuries have seen a tremendous number of scientific discoveries and breakthroughs that have accelerated technological advancements, the most recent of them being the semiconductor technology that has made computers ubiquitous in our lives. The *field-effect transistor*, which is the basic building block of modern electronic devices, was conceptualized by Julius Lilienfeld Edgar [1] in 1930. However, the beginning of the semiconductor industry can be attributed to the momentous achievement of three physicists from Bell Labs: John Bardeen, Walter Brattain and William Shockley, who practically demonstrated the first transistor [2], a point-contact transistor, in 1947. Later, the advent of semiconductor integrated circuits, invented by Jack Kilby [3] in 1958, started off the incredible advances that drove semiconductor devices towards their current form of a semiconductor chip packed with 5.7 billion transistors. The semiconductor industry de-

voted the rest of the 20th century to making modern cost-effective and high-performance electronic devices manufacturable at a grand scale.

At the heart of the semiconductor technology lies silicon, a semiconducting material that can be switched between conducting and insulating states by inducing carriers through current injection or applying a field: the basic working principle of a transistor. Over the years, most of the efforts have gone towards perfecting the material growth of silicon, and overcoming obstacles in fabricating denser integrated circuits by packing smaller and more energy-efficient transistors. Silicon is the second-most abundant element in the earth's crust after oxygen. It possesses many properties, such as a high quality semiconductor-oxide interface and good carrier mobility, that are suitable for producing high-performance and cost-effective devices. This is a major reason for the continued dominance of silicon as the primary semiconductor, even after half a century.

Along the way, advances in the semiconductor device technology have continually impacted advances in computing technologies that have found their place in a diverse range of applications covering medical, entertainment, finance, and science, including modeling the behavior of semiconductors itself. We are at a point in time where the demands of computing technologies have risen above the functionalities that silicon has to offer. In order to continue advances in computing, an alternative materials technology that can lead to better computing performance will soon be necessary. The alternative materials technology could also lead to a much wider and rich range of functionalities that includes ferroelectricity, superconductivity, magnetism, and metal-insulator transition.

The integration of multiple functionalities into a single device could lead to the creation of new avenues in computing. Despite historical cues, this alternative technology need not necessarily be based on a single material, and indeed no single material could be capable of offering the wide range of functionalities. Instead, it could consist of a collection of multiple materials that are inter-compatible and complementary, and their combination can lead to rich, diverse and perhaps previously unrealizable computing functionalities.

Based on this reasoning, a class of materials called “complex oxides” has recently emerged as the basis of one such promising alternative materials technology. The first step towards realizing any new technology is to obtain a fundamental understanding of the underlying physics associated with the candidate materials. This is no simple task, especially when the number and variety of materials involved are plenty and novel. This doctoral dissertation is an attempt from the perspective of electronic applications to develop such an understanding, and uncover the fundamental physics behind some of the phenomena observed in complex oxides.

1.1 Complexity in complex oxides: One chemical formula ABO_3 , many properties

Complex oxides or “mixed oxides” form a class of chemical compounds that consist of oxygen as the anion and two or more cations (or less frequently, one element existing in multiple oxidation states within the same compound) [4]. The number of different

possible combinations of cations and oxygen not only leads to a variety of stable compounds, but also gives rise to many unique material properties. Although complex oxides have been known to exist for a long time now, it was only after the discovery of high- T_c superconductivity [5] in 1986, by Bednorz and Muller at IBM, that intense focus on the growth and study of these compounds began. Since then, a variety of phenomena such as ferroelectricity, ferromagnetism, colossal magnetoresistance, multiferroics, metal-insulator transitions, field-dependent dielectric constant, and formation of a high-density two-dimensional electron gas (2DEG) at interfaces [4]. From a theoretical standpoint, all of this diversity and complexity emerges from *just* the switching and introduction of the A - and B -site cations. The rich complexity in phenomena observed in these oxides earns them their name, “complex” oxides.

In this work, we restrict ourselves to the study of the subset of complex oxides that have a perovskite structure. An ideal perovskite oxide has the chemical formula ABO_3 , and has a cubic crystal structure with the B -site cation six-fold coordinated to oxygen atoms in the form of an octahedra as shown in Fig. 1.1(a). Some examples of this type are $KTaO_3$, the room-temperature phase of $SrTiO_3$ and $BaSnO_3$, and cubic $LaAlO_3$ stabilized by pseudomorphic growth. Most other perovskite oxides show deviations from this ideal cubic structure to accommodate rotation and tilting of the B -site octahedra, and commonly occur in the tetragonal [Fig. 1.1(b)], rhombohedral [Fig. 1.1(c)], or orthorhombic [Fig. 1.1(d)] crystal structures.

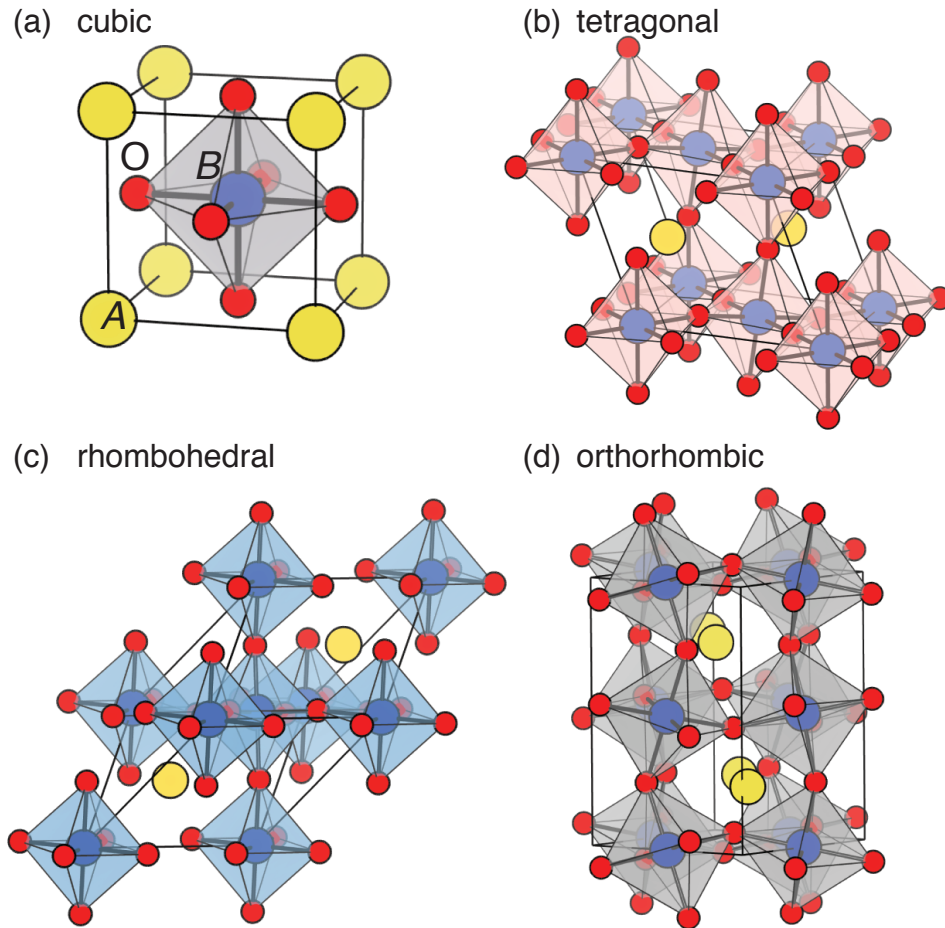


Figure 1.1: Some common perovskite crystal structures

The following sections briefly introduce some key concepts that are common across perovskite oxides, and form the basis for formulating the theory developed in this dissertation.

1.2 Polar *vs.* nonpolar orientations

The perovskite oxides can be viewed as composed of alternating planes of AO and BO_2 along the $[001]$ direction as shown in Fig. 1.2 for the cubic crystal structure, which is

also true for most other lower-symmetry crystal structures. In the ionic limit, depending on the number of valence electrons contributed, the A and B ions may each assume a charge, adding to +6 charge (typically, +3 each or, +2 and +4, or +1 and +5) to maintain charge neutrality while O assumes a -2 charge. Thus, each plane assumes a net charge per areal unit cell or becomes neutral depending on the charge on each ion.

For example, in materials with +2 charge on A and +4 charge on B , both the $B^{+4}O_2^{-2}$ and the $A^{+2}O^{-2}$ assume a net charge of 0 (alternating neutral planes). Due to the absence of separation of charges across planes that would cause the [001] direction to be polar, these materials are termed “nonpolar” along [001]. We emphasize that without specifying the crystal direction, the material itself cannot be termed “nonpolar”. Therefore, throughout this dissertation, we will explicitly mention the direction, and refer to a material that is nonpolar along the [001] direction as “[001] nonpolar”. $SrTiO_3$ is a typical example, where Sr has +2 charge while Ti has +4 charge. Other [001]-nonpolar perovskite oxides studied in this work are $BaSnO_3$, $SrZrO_3$ and $HfZrO_3$. On the other hand, materials with a +3 charge on each of the A and B ions have alternating planes of -1 ($B^{+3}O_2^{-2}$) and $+1$ ($A^{+3}O^{-2}$) charge per areal unit cell. Since the separation of charges leads to the [001] direction being polar, these compounds are termed “polar” along the [001] direction, which we will refer to as “[001] polar”. Within this ionic picture, the symmetry of such stacking leads to each *donor-like* AO plane donating $0.5e^-$ per areal unit cell to the *acceptor-like* BO_2 plane above and $0.5e^-$ to the BO_2 plane below, as shown in Fig. 1.2(b). $LaAlO_3$ is a typical example of this kind, in which both La and Al

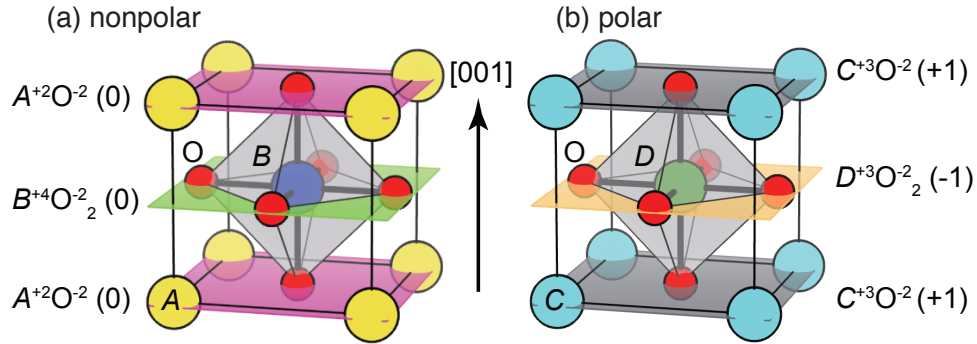


Figure 1.2: Alternating (a) neutral planes with 0 net charge in nonpolar ABO_3 , and (b) charged planes with +1 or -1 net charge per areal unit cell in polar CDO_3 perovskites oxides, when viewed along the [001] direction.

have +3 charge each. Other [001]-polar perovskites studied in this work include $GdTiO_3$, $KTaO_3$ and $LaInO_3$.

1.3 Mechanism of 2DEG formation

Observations of a 2DEG with high carrier density [6, 7, 8, 9] at the (001) interface between a [001]-nonpolar material, $SrTiO_3$ (STO) and a [001]-polar material $LaAlO_3$ (LAO) have generated great interest in the study of complex-oxide heterostructures. In spite of decade-long investigations, the fundamental mechanisms governing the 2DEG formation and its density are not yet fully established.

1.3.1 Key experimental observations

The key experimental observations presented in the literature [6, 7, 8, 9, 10, 11, 12, 13] can be summarized as follows:

1. A thin film of LAO deposited or grown on STO is observed to contain a 2DEG of density ranging between 1×10^{13} – 6×10^{13} cm^{-2} from transport measurements [6, 7, 10, 11].
2. There is a critical thickness of 4 unit cells (uc) for LAO thin films required to observe the 2DEG, and below this critical value the interface remains insulating [7].
3. The 2DEG is observed only if STO terminates on a TiO_2 layer such that a TiO_2 -LaO interface forms. The SrO- AlO_2 interface is found to be insulating.
4. In a similar polar/nonpolar system, namely the $\text{GdTiO}_3/\text{SrTiO}_3$ (GTO/STO) interface, the 2DEG density has been observed to be 3.3×10^{14} cm^{-2} from transport measurements [12].
5. In the GTO/STO system, experiments have not shown any dependence of the 2DEG density on the GTO thickness [12].

1.3.2 Models proposed in literature

Several theoretical models have been proposed to explain the experimental observations of the 2DEG. Here, we will mention some of the most prominent and widely-discussed models in the literature, and briefly discuss their key features.

1.3.2.1 Polar catastrophe model

The polar catastrophe model [6,14] is based on the view that LAO is polar, consisting of alternating charged planes as discussed in Section 1.2. This picture is perfectly valid in the case of bulk LAO, where periodic boundary conditions maintain infinite stacking sequence of +1 and -1 charged planes along the [001] direction. The polar catastrophe model uses this ionic picture to explain the formation of a 2DEG at the heterointerface between a semi-infinite STO and a thin film of LAO terminated by a surface layer of LAO [see Fig. 1.3(a)]. The model argues from electrostatic considerations that such a stacking of charged planes leads to a finite electric field within LAO, which in turn leads to a diverging potential in LAO as its thickness is increased. The effect of this growing potential is to raise the valence-band maximum (VBM) of LAO at its surface higher with increasing thickness. Beyond a certain critical thickness, the potential drop ΔV across LAO would cause the VBM to align with the energetic position of the STO conduction-band minimum (CBM) as depicted in Fig. 1.3(b). At this point, electrons would flow from the VBM at the LAO surface into the CBM of STO at the interface to screen the field, and form a 2DEG. Since the polar nature of LAO causes the diverging potential, which creates a “catastrophic” situation that leads to electron flow beyond a critical thickness, this model is referred to as the “polar catastrophe” model.

Within this model, a field and hence a potential drop must *always* occur across LAO to cause the 2DEG formation. In other words, the 2DEG formation *cannot* occur in the *absence* of a potential drop, since the CBM of STO and the VBM at the LAO surface

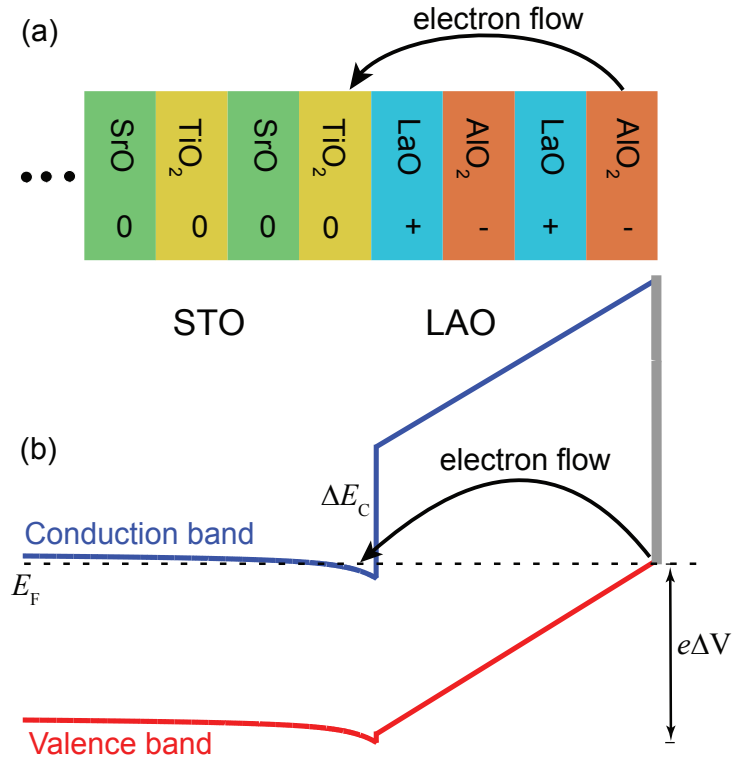


Figure 1.3: Polar catastrophe model: (a) 2DEG at the STO/LAO heterointerface with alternating charged planes of LAO and neutral planes of STO is pictured as forming due to charge transfer *from* the LAO surface. (b) Band diagram of the heterointerface showing the diverging potential in LAO, and the consequent transfer of electrons from the LAO surface to the interface.

would no longer align in such a situation. From Gauss' law, a transfer of $0.5e^-$ per areal unit cell from the surface to the interface, corresponding to a 2DEG density of $3.3 \times 10^{14} \text{ cm}^{-2}$ in STO, would *completely* screen the field across LAO. This situation leads to a contradiction within the polar catastrophe model, i.e., the 2DEG forms in the *absence* of a field across LAO. Therefore, the observation of a 2DEG of density $3.3 \times 10^{14} \text{ cm}^{-2}$ at the GTO/STO heterointerface cannot be explained by the polar catastrophe model.

1.3.2.2 Oxygen vacancy formation

After the discovery [6] of the 2DEG at the interface, there were multiple reports [6, 15, 16] on the 2DEG density being much higher than $6 \times 10^{13} \text{ cm}^{-2}$ at the LAO/STO interface when grown under oxygen-poor conditions. This led to the proposal that formation of oxygen vacancies, which are donors in STO, is the cause for the 2DEG [6, 14]. Later, with improved growth methods and annealing in oxygen that reduced the oxygen vacancy concentrations, it became clear that even though oxygen vacancies influence the 2DEG, the formation of the 2DEG itself cannot be explained by oxygen vacancies alone [7, 8, 9]. Spatial mapping of the 2DEG before and after annealing in O-rich conditions reaffirmed this conclusion [17]. This shows the importance of minimizing oxygen vacancies and other donor defects to observe the true 2DEG density at the LAO/STO interface.

1.3.2.3 Cation intermixing

At the LAO/STO interface, Sr/La cation intermixing is often observed [18]. La in STO is a shallow donor [19]. Therefore, based on these observations, cation intermixing was proposed to play a major role in the 2DEG formation [18, 20]. However, it is highly unlikely that intermixing could *cause* 2DEG densities on the order of 1×10^{13} – $6 \times 10^{13} \text{ cm}^{-2}$, which would require a huge density of La dopants being present in STO.

1.3.3 Our model

From the brief discussion of the models in literature, it is clear that a complete and consistent model capable of explaining all the experimental findings in the LAO/STO as well the GTO/STO heterostructures is lacking. The model we use was proposed by Janotti *et al.* [21], and is the most consistent model so far, in our opinion. In this model, the 2DEG formation can be understood within the ionic picture presented in Sec. 1.2, but keeping in mind in principle one always starts with neutral atoms and that the ionic charges result from adding or removing electrons. Along the [001] orientation, LAO is polar with alternating $+1$ and -1 charged planes [Fig. 1.2(a)], while STO is nonpolar with neutral planes [Fig. 1.2(b)]. Due to the symmetry of the stacking along [001], the LaO plane (charged $+1$) donates $0.5e^-$ per areal unit cell to each of the neighboring AlO_2 planes (charged -1). On the other hand, there is no transfer of charges between the planes in STO along its [001] orientation.

At the interface between LAO and STO, the symmetry gets broken. If the interface is of the type LaO-TiO_2 , the LaO plane donates $0.5e^-$ per areal unit cell to the TiO_2 plane of STO, which does not require the donated electrons for bonding. These electrons end up occupying the conduction-band minimum of STO, and are confined near the interface due to its band offset with LAO. This is the basic mechanism behind the formation of a high-density 2DEG, corresponding to $0.5e^-$ per areal unit cell ($\sim 3.3 \times 10^{14} \text{ cm}^{-2}$).

It is important to note the difference between our model and the polar catastrophe model. The key aspect of our model is that the source of electrons for the 2DEG arises

from the interface itself. This is in contrast to the polar catastrophe model, which argues that the source of electrons is at the surface.

In Chapters 4 and 5, we build on this model to explain some of the other key experimental observations, such as the critical thickness of LAO thin films, and the difference between the LAO/STO and GTO/STO heterostructures.

1.4 Field-dependent dielectric constant

In many of the perovskite oxides, including STO, the dielectric properties depend strongly on the applied electric field [22, 23, 24] as well as the temperature. As first theorized by Cochran [25], this property arises due to the presence of a soft transverse optical phonon mode [26, 27]. Ensuing experimental work by Cowley [26], who measured the temperature dependence of the lowest transverse optical mode frequency, verified this concept. This observation also showed that it is the response of the soft mode to the electric field and temperature that gives STO its static dielectric properties, and makes it an “incipient” ferroelectric [26, 28].

At perovskite oxide heterostructures with a high-density 2DEG, the confinement of the carriers in the interfacial potential well is associated with the presence of a large electric field. The potential profile that confines the carriers is dependent on the dielectric properties of the material (STO, in the case of LAO/STO). Given that the electric field affects the dielectric properties, and that the dielectric properties in turn affect the electric field, modeling of the interface should take the field dependence of the dielectric constant

into account selfconsistently. To date, only a few analyses and simulations [27, 29, 30, 31] have accounted for this field dependence at the interface that confines a 2DEG. These analyses are based on tight-binding models, and have focused on limited-size systems with only a few STO layers. Their description of the field-dependent dielectric properties relies on low-temperature experimental data, which do not apply at room temperature. Although these analyses provide qualitative insights when the field-dependent dielectric permittivity is included, they do not provide a quantitatively accurate description of the 2DEG, specifically at room temperature. Taking the field dependence of the dielectric constant into account is not only important for gaining theoretical insights, but is also crucial for the correct interpretation of experimental $C-V$ measurements at large electric fields [32].

The topic of Chapter 3 will be to incorporate the field dependence of the dielectric constant in STO into a Schrödinger-Poisson solver for simulating complex oxide heterostructures with the high-density 2DEG. Implementing the field dependence into an SP solver will have the benefit of describing systems at larger length scales, and can be generalized for other systems with field-dependent dielectric properties.

1.5 Search for high electron mobility

High electron mobility is typically required for applications in electronics. Unfortunately, the room-temperature (RT) mobility in many of the perovskite oxides is low [33]. While STO low-temperature mobility can be as high as $53,000 \text{ cm}^2\text{V}^{-1}\text{s}^{-1}$, its RT mo-

bility is at best $10 \text{ cm}^2\text{V}^{-1}\text{s}^{-1}$ [12, 34, 35], which is more than an order of magnitude lower than in most traditional semiconductors. Due to this limitation, there has been a search for higher-mobility perovskite oxides. Recently, a high RT electron mobility of $320 \text{ cm}^2\text{V}^{-1}\text{s}^{-1}$ was demonstrated in the transparent cubic perovskite oxide BaSnO_3 (BSO) [36, 37, 38]. This has renewed the interest in perovskite oxides for transparent conducting applications. However, the fundamental reason as to why BSO has a high RT mobility, while the RT mobility in STO is an order of magnitude lower, remains to be understood. Analyzing electron transport in BSO using first-principles techniques, uncovering the fundamental mechanism of limited-mobility in STO, and laying out guidelines for the design of high-mobility perovskite oxides will be the goals of Chapter 6.

1.6 Summary

We briefly reviewed the historical developments that led to the semiconductor industry, and how silicon has played a dominant role in it. Complex oxides have recently emerged as an alternative materials technology to the silicon technology, and seem promising for incorporating multiple different functionalities. One of the recently-discovered phenomena relating to complex oxides is the high-density 2DEG at a polar/nonpolar heterointerface, such as LAO/STO and GTO/STO. Contrary to other models that attempt to explain the 2DEG formation, we understand the formation mechanism as being the consequence of a polar discontinuity, which provides a source of electrons right at the interface. The work that will be reported in Chapters 4 & 5 builds on this

model; the material covered in Chapter 4 was published as a journal article in *Physical Review B*, Ref. [39]. Some of the complex oxides have electric-field-dependent dielectric permittivity, which is important to taken into account for modeling the properties of the high-density 2DEG. This modeling will be carried out in Chapter 3; the material covered in that chapter was published as a journal article in *Applied Physics Letters*, Ref. [40]. Another important aspect to consider for electronic devices is the carrier mobility, and most complex oxides tend to have a low RT mobility. Studying scattering mechanisms that limit RT mobility in complex oxides will help in the search for high-mobility complex oxides. Such a study will be undertaken in the context of BSO in Chapter 6. In addition, confinement of 2DEG in BSO heterostructures will be studied in Chapter 7; the material covered in that chapter was published as a journal article in *Applied Physics Letters*, Ref. [41].

Chapter 2

Theoretical methods and tools

2.1 First-principles theory

This section gives a brief introduction on first-principles methods, specifically density functional theory (DFT), which is the foundational theory upon which most of the work in this dissertation rests. It is utilized to obtain the fundamental properties of materials, including their atomic structure, enthalpy of formation, lattice parameters, electronic band structure, and band alignments. It is not the purpose of this section to be exhaustive, or rigorous in describing all of the theoretical methods available. Interested readers are referred to the many textbooks, and seminal and review articles that are available; a few of them are listed in Appendix [A](#). We begin with the most basic equation governing all quantum-mechanical systems, the many-body Schrödinger equation, and discuss the challenges involved in practical application.

2.1.1 Many-body Schrödinger equation

Any non-relativistic quantum-mechanical system (in the absence of any external perturbation) obeys the well-known Schrödinger equation,

$$\hat{\mathcal{H}}\Psi = E\Psi, \quad (2.1)$$

whose exact many-particle interacting Hamiltonian (total energy operator) is given by

$$\hat{\mathcal{H}} = -\frac{\hbar^2}{2m_e} \sum_i \frac{1}{2} \nabla_i^2 + \frac{1}{2} \sum_{i \neq j} \frac{e^2}{|\mathbf{r}_i - \mathbf{r}_j|} - \sum_{i,I} \frac{Z_I}{|\mathbf{r}_i - \mathbf{R}_I|} - \sum_I \frac{\hbar^2}{2M_I} \nabla_I^2 + \frac{1}{2} \sum_{I \neq J} \frac{Z_I Z_J e^2}{|\mathbf{R}_I - \mathbf{R}_J|}. \quad (2.2)$$

The first term on the right-hand side in Eq. 2.2 represents the kinetic energy of electrons, the second term represents the Coulomb energy due to electron-electron and the third represents electron-ion interactions, while the fourth term represents the ionic contributions due to the kinetic energy of ions and last term represents the Coulomb repulsion due to ion-ion interaction. The lower-case indices i and j denote electrons, and the upper-case indices I and J denote nuclei (or ions in a valence-only model). The positional coordinates for the electrons are denoted by \mathbf{r} , while \mathbf{R} denotes nuclear positions.

Even though the Hamiltonian $\hat{\mathcal{H}}$ in the Schrödinger equation is exact in principle, its solution is intractable except for very small systems with one or at most two electrons. However, with a few approximations, the equation can be simplified. The first of the ap-

proximations that we make is the Born-Oppenheimer (BO) approximation, which ignores the kinetic energy of the nuclei and assumes them to be classical rigid objects without a wavefunction. Mathematically, it takes the nuclear mass M_I to be infinite, which is an excellent approximation for most purposes, considering their mass relative to electrons. Within this approximation, for a given many-particle wavefunction Ψ , one can obtain the system's total energy, i.e., the expectation value of the Hamiltonian $\hat{\mathcal{H}}$, as:

$$E = \frac{\langle \Psi | \hat{\mathcal{H}} | \Psi \rangle}{\langle \Psi | \Psi \rangle} = \langle \hat{T} \rangle + \langle \hat{V}_{ee} \rangle + \int d\vec{r} n(\vec{r}) \hat{V}_{\text{ext}} + E_{II}, \quad (2.3)$$

where $\langle \hat{T} \rangle$ is the electronic kinetic energy, and $\langle \hat{V}_{ee} \rangle$ is the energy due to electron-electron interactions. The third term represents the attractive Coulomb energy due to the interaction between ions and electrons with the potential external to the electrons indicated by \hat{V}_{ext} ; and the final term E_{II} is the classical Coulomb repulsion energy between the ions, which is also external to the electron system. All of the electronic properties, for the ground as well as excited states, can be obtained by finding the many-particle eigen wavefunction Ψ that minimize the total energy of the system given by Eq. 2.3. The Rayleigh-Ritz variational principle is a well-known method to obtain the stationary eigensolutions for a given Hamiltonian. From this ground-state wavefunction, any ground-state electronic property defined by the operator \hat{O} can be obtained from the relation:

$$\langle \hat{O} \rangle = \frac{\langle \Psi | \hat{O} | \Psi \rangle}{\langle \Psi | \Psi \rangle}. \quad (2.4)$$

In principle, once the *true* ground-state wavefunction of the system has been identified, excited-state properties can also be obtained by employing perturbative techniques on the ground-state wavefunction. However, in practice, identifying the *true* ground state can be complicated by the possible existence of multiple ground states with *similar* (but not *identical*) energies, and the excited-state properties critically depend on the accuracy of the ground-state wavefunctions.

2.1.1.1 Hartree-Fock method

In order to simplify the Schrödinger equation further, a second approximation called the Hartree-Fock approximation is often used. In this method, the many-body wavefunction Ψ is approximated by a single Slater determinant made up of single-particle wavefunctions (referred to as “Hartree-Fock orbitals”), and the determinant is constructed to obey the antisymmetric property that is characteristic of fermions:

$$\Psi(\mathbf{r}_1, \mathbf{r}_2, \dots, \mathbf{r}_N) = \begin{vmatrix} \phi_1(\mathbf{r}_1) & \phi_1(\mathbf{r}_2) & \cdots & \phi_1(\mathbf{r}_N) \\ \phi_2(\mathbf{r}_1) & \phi_2(\mathbf{r}_2) & \cdots & \phi_2(\mathbf{r}_N) \\ \vdots & \vdots & \vdots & \vdots \\ \phi_2(\mathbf{r}_1) & \phi_2(\mathbf{r}_2) & \cdots & \phi_2(\mathbf{r}_N) \end{vmatrix}. \quad (2.5)$$

Substituting the expression for the many-body wavefunction (Eq. 2.5) into the Schrödinger equation Eq. 2.3 and using Eq. 2.2 (with the Born-Oppenheimer approximation) leads to the expression for the electronic part of the ground-state energy within the Hartree-Fock

method:

$$E = \sum_i \int d\mathbf{r} \phi_i^*(\mathbf{r}) \left[-\frac{\hbar^2}{2m_e} \nabla_i^2 + V_{\text{ext}} \right] \phi_i(\mathbf{r}) \quad (2.6)$$

$$+ \frac{1}{2} \sum_{i,j,\sigma_i,\sigma_j} \int d\mathbf{r} d\mathbf{r}' \phi_i^{\sigma_i*}(\mathbf{r}) \phi_j^{\sigma_j*}(\mathbf{r}') \frac{1}{|\mathbf{r} - \mathbf{r}'|} \phi_i^{\sigma_i}(\mathbf{r}) \phi_j^{\sigma_j}(\mathbf{r}') \quad (2.7)$$

$$- \frac{1}{2} \sum_{i,j,\sigma} \int d\mathbf{r} d\mathbf{r}' \phi_i^{\sigma*}(\mathbf{r}) \phi_j^{\sigma*}(\mathbf{r}') \frac{1}{|\mathbf{r} - \mathbf{r}'|} \phi_i^{\sigma}(\mathbf{r}') \phi_j^{\sigma}(\mathbf{r}). \quad (2.8)$$

Here, the first term represents the sum of the kinetic energies of the single-particle wavefunctions and their potential energies due to the attractive external potential attributed to ions. The second term indicates the direct electron-electron Coulomb interaction, i.e., the repulsion between electrons regardless of their spin, which is evident from the summation being performed over all the spin indices σ_i and σ_j . The third term represents the exchange interaction energy that arises due to the antisymmetric property of fermions and is calculated between electrons of the same spin. It is important to note that the direct term includes the specific case of $i = j$ in the sum, which is a spurious energy contribution representing an electron interacting with itself (usually referred to as the “self-interaction” energy). However, in Hartree-Fock theory, this energy is *exactly* cancelled by the corresponding term $i = j$ in the exchange energy contribution.

Even after making the Hartree-Fock approximation, solving the many-body Schrödinger equation remains intractable, except for very small systems. This is related to the fundamental aspect that for an N -electron system, the many-body wavefunction depends on N spatial coordinates $\mathbf{r}_1, \mathbf{r}_2, \dots, \mathbf{r}_N$, each being a vector with 3 components; for example,

x , y and z . This dependence means that solving for the eigenfunction of the Schrödinger equation involves $3N$ independent coordinates. Therefore, however many approximations one may use to attempt to solve the many-body Schrödinger equation explicitly, the computational complexity of calculating total energy and other properties of the system, all of which depend on the many-body wavefunction, will remain intractably high for large systems. This raises the question of whether there exists a completely different method that is specifically *not* based on the many-body wavefunction, but is rather based on a quantity defined by fewer variables for calculating the properties of the system. The answer to this question lies with density functional theory (DFT), the foundation of which rests on the rigorously proven theorem that the full Hamiltonian of a many-body interacting system can be written *entirely and exactly* in terms of the electronic density $n(\mathbf{r})$ alone.

2.1.2 Density functional theory

Here, we look briefly at the history that led to the development of DFT, introduce the key concepts involved in the theory, and mention a few practical aspects associated with its implementation.

2.1.2.1 Initial attempts and approximations

The notion that the electronic density was sufficient to describe the properties of an electronic system was not a newly-introduced concept in DFT. In fact, shortly after

the formulation of the Schrödinger equation in 1926, Llewellyn Thomas [42] and Enrico Fermi [43, 44] (independently) developed a semiclassical description of the kinetic energy of a system of electrons in terms of its total electronic density alone. By including the classical electron-ion and electron-electron Coulomb energy, they were able to compute the energy of atoms, and the method came to be known as the Thomas-Fermi model. Its energy expression is given as:

$$E_{\text{tot}} = \frac{3}{10}(3\pi^3)^{2/3} \int d^3r n^{5/3}(\mathbf{r}) + \frac{1}{2} \int d^3r \int d^3r' \frac{n(\mathbf{r})n(\mathbf{r}')}{|\mathbf{r} - \mathbf{r}'|} + \int d^3r n(\mathbf{r})V_{\text{ext}}, \quad (2.9)$$

with the first term being the Thomas-Fermi kinetic energy, the second term representing the Hartree energy E_{Hartree} or the classical electrostatic energy due to Coulomb repulsion between electrons, and the third term expressing the electron-ion potential energy. Although inaccurate mainly due to its neglect of the consequence of Pauli's exclusion principle—namely, the *exchange energy*, which was later included by Dirac in 1928—it is considered as the first attempt at describing an electronic system based on its density alone, and it serves as a precursor to density functional theory, which was to be developed 40 years later.

2.1.2.2 Hohenberg-Kohn theorem

Until 1964, refinements to the Thomas-Fermi model were being utilized to describe, albeit only crudely, inhomogeneous electron systems. The seminal ground-breaking paper [45] by Pierre Hohenberg and Walter Kohn in 1964 generalized the key concept in

the Thomas-Fermi model, i.e., the ground-state electronic density being a fundamental quantity in electronic structure theory, and established a formal proof that the Hamiltonian of any interacting electron system can be expressed as a *unique* functional (upto an additive constant) of the variable density function. This constitutes the foundation of DFT. The proof is surprisingly simple, and involves an argument by *reductio ad absurdum*, with the variational principle being the central concept. The reader is referred to the seminal paper [45] for the proof, and is encouraged to read the biography of Walter Kohn [46] written by Andrew Zangwill for a deep appreciation of the role played by the variational principle in Walter Kohn's career.

Given the Hamiltonian that is *uniquely* determined by a functional of the electronic density $n(\mathbf{r})$, it is trivial to obtain the ground-state many-body wavefunction that gives the lowest energy for the system through the method of variational principle. This fact leads to the central concept of DFT that the many-body wavefunction, and hence *all* the ground-state properties of an interacting electronic system is a functional of the electronic density alone. Building on this understanding further, Hohenberg and Kohn showed [45] that there exists a unique functional $F[n(\mathbf{r})]$ describing the kinetic energy of the electrons $T[n]$ and the electron-electron interactions $E_{\text{int}}[n]$ that is universal for *any* number of electrons and for *any* external potential. Therefore, the total energy of a

many-body interacting system can be written as a functional of the density:

$$E_{\text{HK}}[n] = F[n] + \int d^3r n(\vec{r}) V_{\text{ext}} + E_{\text{II}} \quad (2.10)$$

$$= T[n] + E_{\text{int}}[n] + \int d^3r n(\vec{r}) V_{\text{ext}} + E_{\text{II}} \quad (2.11)$$

If the *exact* functional form of $F[n(\mathbf{r})]$ is known, all that is necessary to describe a quantum system is known. One can readily identify one of the terms of the functional as the Hartree term given by the second term in Eq. 2.9. Unfortunately, this is also the only term that has been identified, while the exact functional form of the remaining terms, although universal, still remains unknown.

Nonetheless, progress was made in the following year, when Walter Kohn and Lu Jeu Sham [47] carried the Hohenberg-Kohn approach further to obtain a set of selfconsistent equations that explicitly included exchange and correlation effects, in an approximate manner, based on the homogeneous electron gas. The result became the Kohn-Sham approach to solving the many-body interacting Hamiltonian that has made practical application of DFT possible.

2.1.2.3 The auxiliary Kohn-Sham system

The Kohn-Sham approach begins with the *ansatz* that the ground-state density of the many-body *interacting* Hamiltonian is *exactly* equal to the ground-state density of an auxiliary fictional system consisting of *non-interacting* particles. The Hamiltonian of the *non-interacting* system consists of the usual kinetic energy operator (now a single-particle

operator) and an *effective* (spin-dependent) potential $v_{\text{KS}}(\mathbf{r})$ (known as the Kohn-Sham potential), each of which acts on the single-particle wavefunctions $\phi_i(\mathbf{r})$ (also known as Kohn-Sham orbitals). This simplification, which is still *exact* in principle within the Kohn-Sham *ansatz*, leads to a set of single-particle equations that can be selfconsistently solved to yield the exact density, which includes all the many-body interactions:

$$\hat{H}_{\text{KS}} = -\frac{1}{2}\nabla^2 + v_{\text{KS}}(\mathbf{r}). \quad (2.12)$$

It follows from the Hohenberg-Kohn theorem that the Kohn-Sham potential, and also the Kohn-Sham Hamiltonian, are *unique* functionals of the ground-state density. In essence, the Kohn-Sham approach is to rewrite the total energy functional, defined in the Hohenberg-Kohn approach in Eq. 2.11, as:

$$E_{\text{KS}}[n] = T_s[n] + E_{\text{xc}}[n] + E_{\text{Hartree}}[n] + \int d\mathbf{r} V_{\text{ext}}(\mathbf{r})n(\mathbf{r}) + E_{II}, \quad (2.13)$$

where the kinetic energy is defined in terms of the Kohn-Sham orbitals ϕ_i as:

$$T_s[n] = -\frac{1}{2} \sum_{i=1}^N \langle \phi_i | \nabla^2 | \phi_i \rangle = \frac{1}{2} \sum_{i=1}^N \int d\mathbf{r} |\nabla \phi_i(\mathbf{r})|^2, \quad (2.14)$$

and the Hartree or direct term is the same as in Thomas-Fermi theory:

$$E_{\text{Hartree}}[n] = \frac{1}{2} \int d^3r \int d^3r' \frac{n(\mathbf{r})n(\mathbf{r}')}{|\mathbf{r} - \mathbf{r}'|}. \quad (2.15)$$

It is very important to note that the Kohn-Sham equation for the total energy, Eq. 2.13 is *exact* within the Kohn-Sham *ansatz*.

Now, all that is required is to determine the functional form of the exchange and correlation (XC) energy $E_{xc}[n]$ in Eq. 2.13 that captures *all* the electron-electron interactions *excluding* the Hartree energy $E_{\text{Hartree}}[n]$. The exact functional form of $E_{xc}[n]$ is not obvious, and has not been obtained to date. However, in an effort to obtain an approximate expression for the functional form, Kohn and Sham drew inspiration from the description of properties of an interacting homogeneous electron gas. This approach led to the formulation of the local density approximation (LDA) to the XC functional $E_{xc}[n]$, the first approximation of its kind that is still being used for practical electronic structure applications even 50 years after its inception. Almost all of the theoretical developments in DFT have centered around improving approximations to the XC functional, while still keeping the method of obtaining the solution computationally tractable and inexpensive. Below, we briefly discuss some of the most commonly used XC functionals and discuss their benefits and drawbacks.

2.1.2.4 Exchange and correlation (XC) functionals

Local density approximation (LDA)

The spin-independent LDA was proposed by Kohn and Sham. This approximation for the XC functional utilizes the exchange and correlation properties of the homogeneous electron gas to describe inhomogeneous systems. The exchange energy is approximated

in the LDA by taking the well-known analytical form for the exchange energy of a homogeneous electron gas of density $n(\mathbf{r})$ and applying it at every local point \mathbf{r} :

$$E_x[n(\mathbf{r})] = -\frac{3}{4} \left(\frac{3}{\pi} \right)^{1/3} \int d\mathbf{r} n^{4/3}(\mathbf{r}). \quad (2.16)$$

The correlation energy can be written in the form:

$$E_c[n(\mathbf{r})] = \int d\mathbf{r} n(\mathbf{r}) \varepsilon_c(n(\mathbf{r})), \quad (2.17)$$

where $\varepsilon_c(n(\mathbf{r}))$ is the correlation energy per particle of the homogeneous electron gas. The form of the analytic expression for $\varepsilon_c(n(\mathbf{r}))$ at a local point \mathbf{r}_0 is based on the correlation energy per particle in a homogeneous electron gas of uniform density $n(\mathbf{r}_0)$. Analytical forms are available only in the low-density and high-density limits. With the help of quantum Monte Carlo simulations of the homogeneous electron gas, Ceperley and Adler [48] obtained the correlation energies at arbitrary densities. Later, Perdew and Zunger [49] utilized these data and obtained a parameterized expression for the correlation energy functional, which is widely adopted now. Minor improvements to the parameterization based on QMC simulations have been carried out by Perdew and Wang [50].

Generalized Gradient Approximation (GGA)

The GGA goes slightly further by including the dependence on the gradient of the elec-

tronic density $\nabla n(\mathbf{r})$ in addition to the local-density dependence:

$$E_{\text{xc}}[n(\mathbf{r})] = \int d\mathbf{r} f[n(\mathbf{r}), \nabla n(\mathbf{r})], \quad (2.18)$$

For practical calculations, $f[n(\mathbf{r}), \nabla n(\mathbf{r})]$ needs to be in the form of parametrized analytic expressions. However, many choices for the analytic form of f exist, and various GGA functionals have been proposed [50]. The most commonly used GGA functional for solid state problems is, at present, the functional developed by Perdew, Burke, and Ernzerhof [51], referred to as the PBE functional, in which the XC functional is defined as

$$E_{\text{xc}}^{\text{GGA}}[n(\mathbf{r})] = \int d\mathbf{r} n(\mathbf{r}) \varepsilon_{\text{xc}}^{\text{unif}}(n(\mathbf{r})) F_{\text{xc}}[n(\mathbf{r}), \nabla n(\mathbf{r})], \quad (2.19)$$

with $F_{\text{xc}}[n(\mathbf{r}), \nabla n(\mathbf{r})]$ being the enhancement factor that accounts for the nonlocality over the local exchange $\varepsilon_{\text{xc}}^{\text{unif}}$. Due to the inclusion of information about the density gradient, GGA functionals are often referred to as “semi-local approximations” to the XC functional.

Self-interaction error

As in the Hartree-Fock method, the Hartree or direct term $E_{\text{Hartree}}[n]$ in the Kohn-Sham energy functional (third term in Eq. 2.13) contains the spurious self-interaction contribution representative of an electron repelling itself. In the Hartree-Fock method, however, this spurious contribution is *exactly* cancelled by an equally spurious term in the exchange term. But, in DFT, due to the unknown form of the exchange and correlation

functional, this spurious contribution from the Hartree term is only partially cancelled by $E_{xc}[n]$. This absence of exact error cancellation leads to over-delocalization of the Kohn-Sham eigenfunctions and can lead to qualitatively incorrect predictions of the electronic properties.

The infamous “band gap problem”

Another drawback of traditional DFT methods is the so-called “band gap problem.” The Kohn-Sham eigenvalues themselves do not have a rigorous physical meaning in the context of a many-body interacting system, except for the highest occupied eigenvalue, which represents the change in total energy when an electron is removed from the system, i.e., its ionization energy. No other eigenvalues represent the true energies for removal/addition of electrons from/to the many-body interaction system. However, with each of the eigenvalues, we can associate a mathematical meaning as the change in the total energy of the system with change in the occupation of the state, described by the Slater-Janak theorem, which gives the eigenvalues as:

$$\varepsilon_i = \frac{dE[n]}{dn_i} = \int d\mathbf{r} \frac{dE[n]}{dn(\mathbf{r})} \frac{dn(\mathbf{r})}{dn_i}, \quad (2.20)$$

In other words, each eigenvalue is the derivative of the total energy with respect to the occupation of its state. The band gap in semiconductors and insulators is reflected in this definition as a discontinuity in this derivative for fully occupied orbitals. Increasing the occupation of a fully occupied orbital requires the filling of the next higher lying band (conduction band) that is separated from the valence band by a finite gap and results

in a discontinuous change in the total energy. In the context of DFT, this discontinuity occurs in the derivative of the kinetic energy term $T_s[n]$, as well as in the derivative of the *exact* XC functional $E_{xc}[n]$. The discontinuity due to varying occupation of completely filled bands in the kinetic energy term $T_s[n]$ (Eq. 2.14) is understood as occupying a conduction band orbital $\phi_{CB}(\mathbf{r})$ that has a different character and kinetic energy than the valence band orbital $\phi_{VB}(\mathbf{r})$. Therefore, occupying a conduction band orbital for an insulator or semiconductor leads to a discontinuous change in the kinetic energy. A similar argument applies to the derivative discontinuity in the *exact* XC functional with respect to occupancy for insulating systems, in which the change in the density causes a discontinuous change in the XC energy functional. The derivative discontinuity in the XC functional is the change in the Kohn-Sham potential that acts on *all* the electron orbitals in the system by a constant amount. Therefore, even for the *exact* XC functional within the Kohn-Sham approach, the derivative discontinuity of the total energy functional will *not* necessarily be equal to the band gap. None of the traditional functionals, such as LDA or GGA, contain this derivative discontinuity in the XC functional, and incorporation of the discontinuity into an XC functional is very difficult.

As we have seen above, the gap between the highest-occupied molecular orbital (HOMO) and the lowest-unoccupied molecular orbital (LUMO) is not an actual physical quantity within the Kohn-Sham formalism. One practical approach to determine the “true” fundamental excitation gap of a finite system is to calculate the selfconsistent change in the total energy upon addition of an electron, which is known as the

“ Δ SCF” method (Δ indicates the energy change and SCF stands for selfconsistent field calculation). However, for periodic systems, the energy-*versus*-momentum-wavevector relation describing the conduction (lowest empty band) and valence (highest occupied band) bands of semiconductors and insulators are convenient and extremely useful to obtain essential insights into their electronic properties. Therefore, somehow “fixing” the band-gap problem in DFT would be useful for studying the properties of solid-state materials. For this reason, there have been many XC functionals proposed to overcome this band gap problem. Hybrid functionals, which are discussed below, fall under this category, and they are known to yield accurate enough results with acceptable computational cost [52, 53].

2.1.2.5 Hybrid functionals and HSE06 functional

Hybrid functionals form a class of functionals that combine the orbital-dependent Hartree-Fock approach and an explicit density functional. The spirit behind hybrid functionals is to utilize the idea of coupling constant integration. The change in total energy due to variation of a parameter λ can be written as:

$$\frac{\partial E}{\partial \lambda} = \langle \Psi_\lambda \left| \frac{\hat{\mathcal{H}}}{\partial \lambda} \right| \Psi_\lambda \rangle. \quad (2.21)$$

For example, the quantity e^2 , which is a factor in any Coulomb interaction can be varied as λe^2 . The coupling constant integration method is to integrate this energy change $\partial E / \partial \lambda$ between $\lambda = 0$, which represents the non-interacting limit, and the fully interacting limit

defined by $\lambda = 1$. Hybrid functionals specifically utilize this method by approximating the exchange-correlation functional $E_{xc}[n]$ with the information at the end points, namely $\lambda = 0$ representing the non-interacting Hartree-Fock limit, and $\lambda = 1$ representing full interacting DFT limit. The XC hybrid functional is generally approximated as:

$$E_{xc}[n] = E_{xc}^{\text{DFA}}[n] + \alpha (E_x^{\text{HF}} - E_x^{\text{DFA}}[n]), \quad (2.22)$$

where $E_{xc}^{\text{DFA}}[n]$ is a traditional density functional approximation (DFA) to the XC functional (LDA or GGA), E_x^{HF} is the exact exchange from Hartree-Fock theory (given by the third term in Eq. 2.8) calculated based on the Kohn-Sham single-particle orbitals, $E_x^{\text{DFA}}[n]$ is the exchange part of the DFA functional, and α is the fraction of the exact exchange “mixed in” with the DFA. This method of combining is often referred to as “mixing in” some fraction α (known as the “mixing parameter”) of Hartree-Fock exchange into a traditional density functional. Several hybrid functionals have been proposed; see Sec. 2 in Ref. [54].

For our study, we use a range-separated hybrid functional developed by Heyd, Scuseria and Ernzerhof [55] in 2003 and slightly modified [55] in 2006 (HSE06). The advantage of using HSE06 lies in its ability to yield accurate results, but at a lower computational cost compared to other hybrid functionals, which is accomplished by its range-separated treatment of the Hartree-Fock exchange. In HSE06, the DFA XC functional $E_{xc}^{\text{DFA}}[n]$ is a GGA functional developed by Perdew, Burke and Ernzerhof (PBE) $E_{xc}^{\text{PBE}}[n]$. However, the speciality of HSE06 lies in its separation of the $1/r$ Coulomb term in the exact

exchange E_x^{HF} from Hartree-Fock theory into a long-range part $E_x^{\text{HF,LR}}$ and a short-range contribution $E_x^{\text{HF,SR}}$ via error functions $\text{erfc}(\omega r)$ and $\text{erf}(\omega r)$ that depend on the screening parameter ω as:

$$\frac{1}{r} = \frac{\text{erfc}(\omega r)}{r} + \frac{\text{erf}(\omega r)}{r}. \quad (2.23)$$

The HSE06 hybrid functional is given by:

$$E_{\text{xc}}^{\text{HSE}} = E_x^{\text{PBE,LR}}(\omega) + E_x^{\text{PBE,SR}}(\omega) + E_c^{\text{PBE}} + \alpha [E_x^{\text{HF,SR}}(\omega) - E_x^{\text{PBE,SR}}(\omega)], \quad (2.24)$$

where α is 25% and the screening parameter $\omega = 0.20 \text{ \AA}^{-1}$. The HSE06 functional has been tested on many isolated systems such as atoms and molecules as well as periodic solid-state systems such as semiconductors and insulators [52, 55]. It has yielded accurate quantities, such as formation enthalpy and fundamental band gap consistent with experimental observations. However, the specific value of 25% for the mixing parameter α has no special significance, but has rather been chosen based on a rationale from perturbation theory [51]. It is common practice to adjust the value of α to yield accurate band-gap values.

2.1.3 Practical aspects

2.1.3.1 Periodic boundary conditions, plane waves and pseudopotentials

Although many different implementations for DFT calculations exist, for calculating solid state properties it is logical to take advantage of the lattice periodicity. Therefore,

expressing the lattice periodic part of the Bloch wavefunctions using a plane-wave basis set is effective. The size of the basis set is often expressed in terms of the largest kinetic energy called the cutoff energy, usually on the order of 200–500 eV. The more localized wavefunctions require a higher cutoff energy. Regardless, the cutoff energy of the basis should be chosen based on tests for convergence of the physical property of interest. The use of plane waves makes the practical implementation using Fast Fourier transform (FFT) efficient. Since rapidly varying and localized wavefunctions require a higher cutoff energy and hence a larger basis set, expanding the core electrons that are localized close to the nucleus in terms of plane waves is extremely expensive. This huge computational cost is avoided by the use of pseudopotentials that are meant to reproduce the potential due to the nucleus as well as the core electrons outside a specified radius. This is a reasonable approximation since the valence electrons are the ones that determine most of the interactions between atoms including the formation of bonds in solids. For all our studies, we will use the projector augmented wave (PAW) method for pseudopotentials [56].

2.1.3.2 Supercells

In DFT calculations, the unit cell that is being periodically repeated is often referred to as a “supercell”. This concept is trivial in the context of calculating bulk properties, where indeed the unit represents the volume repeated to obtain the crystal. However, the concept of supercells can be extended to study properties that are not exactly periodic,

such as defects, surfaces, interfaces and isolated molecules. This is accomplished by constructing a supercell with the necessary geometry, and ensuring that the supercell is large enough to avoid any interactions between the periodic images of the supercell. For example, a surface supercell is constructed as a thick slab of the material, whose surfaces and their periodic images are separated by a vacuum region of sufficient thickness. The thickness of the slab as well as the vacuum region is tested for convergence of the quantity of interest, for example the surface energy. Similarly, defects can be studied by embedding the defect into a large enough supercell such that the periodic images of the defects are separated enough to avoid interactions.

2.1.3.3 Maintaining charge neutrality

The long-range Coulomb interactions in extended systems must be treated with care. In order to ensure the total energy of the periodic system does not diverge, charge neutrality of the supercell must always be maintained. However, often it is extremely valuable to obtain the properties of charged systems, where an electron is added or removed to the supercell; for example to obtain the properties of charged defects [57]. This breaks the charge neutrality condition. The computational approach to still maintain charge neutrality is to add a uniformly distributed background of opposite charge. In plane-wave codes, it is accomplished by setting the $\mathbf{G} = 0$ Fourier component of the electrostatic potential to zero. This has yielded excellent results for computing the properties of charged defects, provided that the spurious interactions between defects in neighboring

supercells are corrected by applying an appropriate correction scheme [57]. However, for charged surface supercells, this approach leads to complications due to part of the background countercharges occurring in the vacuum region of the cell. This leads to spurious electrostatic interactions between the background charges and the slab within the same supercell. Identifying these difficulties and overcoming them by a clear methodology will be addressed in Chapter 4.

2.1.3.4 Available codes

There are a number of popular DFT codes available that differ in the variety of features implemented, basis sets, pseudopotentials, their accuracy of results as well as their computational efficiency. Some of the codes are:

1. Vienna *ab-initio* Simulation Package (VASP) (Ref. [58], URL: <https://www.vasp.at>)
2. Quantum ESPRESSO (Ref. [59], URL: <http://www.quantum-espresso.org>)
3. ABINIT (Ref. [60], URL: <http://www.abinit.org>)
4. SIESTA (Ref. [61], URL: <http://departments.icmab.es/leem/siesta>)
5. CPMD (Ref. [62], URL: <http://www.cpmd.org>)

A larger list can be found at http://dft.sandia.gov/codes_list.html. For all of our DFT studies we will use the VASP code.

2.2 Schrödinger-Poisson solver

Although DFT has been proven to be an extremely accurate first-principles tool, the practical size of systems that can be calculated is limited to about 1000 atoms. For hybrid functionals and other wavefunction-based functionals, the limit is much lower; fewer than 200–300 atoms. These limitations are not fundamental to the theory, but are limitations due to computational constraints, such as memory required and long computation time. Frequently, for example at the level of a transistor device, the systems of interest are on the order of 10 nm or larger. Performing DFT calculations for these systems would be intractable with the current level of computational resources. Overcoming the computational limitations for such large systems can be accomplished by continuum models that express the material properties on a higher level of abstraction. These models rely on input parameters that are measured, fitted to experiment, or calculated from first-principles, but can be incredibly useful as well as accurate for large systems. For electronic structure, one such commonly used method is the Schrödinger-Poisson (SP) method that will be used in this dissertation, specifically in Chapters 3 & 7.

2.2.1 Schrödinger-Poisson equation

The idea behind SP simulations is to solve the single-particle Schrödinger equation (within the effective mass approximation),

$$-\frac{\hbar^2}{2} \nabla \left[\frac{1}{m^*(\mathbf{r})} \nabla \right] \psi_n(\mathbf{r}) + V(\mathbf{r})\psi_n(\mathbf{r}) = E_n \psi_n(\mathbf{r}) \quad (2.25)$$

that is coupled to the Poisson equation,

$$\nabla \cdot [\epsilon(\mathbf{r})\nabla V(\mathbf{r})] = -\rho(\mathbf{r}). \quad (2.26)$$

Here $\psi_n(\mathbf{r})$ is the single-particle wavefunction of state n , E_n is its eigenvalue, $m^*(\mathbf{r})$ is the effective mass describing the E -vs.- k dispersion of the band structure, $\rho(\mathbf{r})$ is the *total* charge density including the electronic and hole wavefunctions as well as any fixed or ionized charges that may be present, $\epsilon(\mathbf{r})$ is the static dielectric permittivity of the medium, and $V(\mathbf{r})$ is the electrostatic potential due to $\rho(\mathbf{r})$. Eqs. 2.26 and 2.25 are coupled through the charge density $\rho(\mathbf{r})$ that depends on the wavefunctions $\psi_n(\mathbf{r})$ obtained by solving Eq. 2.25, and the electrostatic potential $V(\mathbf{r})$ that enters the Schrödinger equation. The solution to these two coupled equations is obtained by solving for the electrostatic potential and the charge density selfconsistently, i.e., until the electrostatic potential does not cause a change (within a given tolerance value) in the charge density.

Under steady state, the divergence of current in the system should vanish ($\nabla \cdot \mathbf{J} = 0$), where the current is given by

$$\mathbf{J} = \mu(\mathbf{r})\rho(\mathbf{r})\nabla E_F. \quad (2.27)$$

Here the carrier mobility $\mu(\mathbf{r})$ is, in general, dependent on the spatial coordinate. Specifically, under thermal equilibrium (i.e., without any applied voltage bias), $\nabla E_F = 0$, i.e., the Fermi level E_F is a constant, which consequently leads to $\mathbf{J} = 0$. The eigenstates of the Schrödinger equation are occupied according to their energetic position with respect

to this constant Fermi level. Our notation E_F for the Fermi level in this section and in Chapter 7 is to be consistent within the field of semiconductor device physics. In the next section and in Chapter 6, we will use the notation ε_F for the Fermi energy, which is more common within the condensed matter physics community.

2.2.2 Field-dependent dielectric permittivity

The dielectric constant $\epsilon(\mathbf{E}, \mathbf{r})$ appearing in the Poisson equation (Eq. 2.26) can have a dependence on the electric field present in the medium, in addition to its spatial dependence. As mentioned in the introduction in Sec. 1.4, this is especially important in complex oxides. The dielectric properties of these materials strongly depend on the electric field due to their incipient ferroelectric behavior. In heterostructures, the presence of a two-dimensional electron gas leads to large band bending in the region of the confined electron gas [63]. This in turn gives rise to large electric fields in the region, which can alter the dielectric response of the medium and modify the confining potential. Therefore, the simulation of complex oxide heterostructures must be able to capture the effect of a field-dependent dielectric response. An implementation of this dependence into an existing SP solver is not yet available, and is an area of active research. The field dependence of the dielectric response is currently not implemented in commercial SP solvers. In Chapter 3, we undertake such an implementation via a wrapper script, and simulate SrTiO₃/LaAlO₃ and SrTiO₃/GdTiO₃ heterostructures.

2.3 Boltzmann transport theory

The purpose of this section is to give a brief introduction to the Boltzmann transport equation (BTE) that governs carrier transport in a material. The relaxation-time approximation, which simplifies the solution to this equation, will also be discussed. These equations will be employed in Chapter 6 for computing the electron mobility in the high-mobility perovskite oxide, BaSnO₃.

2.3.1 Boltzmann transport equation

The BTE describes the statistical distribution of a thermodynamical system of carriers in different momentum states under *non-equilibrium* conditions. The solution to the BTE gives the non-equilibrium distribution function, taking into account the loss mechanisms and the driving forces that affect the distribution. From the resulting distribution function, one can obtain the *mobility* for the particles of interest, and consequently the transport properties of the medium of transport, such as the thermal conductivity (transport of phonons and electrons) and electronic conductivity (transport of electrons). Although the BTE is more generally applicable for systems under non-equilibrium, most systems of interest can be considered close to equilibrium. This assumption allows us to make certain simplifications to the BTE. The general form of the BTE for the *near-equilibrium* distribution $f(\mathbf{r}, \mathbf{k}, t)$ that depends on the spatial coordinates \mathbf{r} , momentum

wavevector \mathbf{k} and time t is given by

$$\frac{\partial f}{\partial t} + \dot{\mathbf{r}} \cdot \nabla_{\mathbf{r}} f + \dot{\mathbf{k}} \cdot \nabla_{\mathbf{k}} f = \left(\frac{df}{dt} \right)_{\text{coll}} = \mathcal{I}_{\mathbf{k}}(f). \quad (2.28)$$

The equation essentially states that the time evolution of the distribution function df/dt is determined by the spatial gradient of the distribution $\nabla_{\mathbf{r}} f$, which causes diffusion of particles; the acceleration $\dot{\mathbf{k}}$ due to an applied force; and any collision mechanisms that are represented by the right-hand term $(\partial f/\partial t)_{\text{coll}}$, which is given by the *collision integral* $\mathcal{I}_{\mathbf{k}}(f)$.

Since we are interested in calculating the electronic conductivity due to a uniform applied electric field, we can ignore spatial gradients (i.e., $\nabla_{\mathbf{r}} f = 0$ in Eq. 2.28). Neglecting the $\nabla_{\mathbf{r}} f$ term, and using a semi-classical model that relates the electron momentum and the force due to the electric field as $\hbar \dot{\mathbf{k}} = -e\mathbf{E}$ in Eq. 2.28, we obtain the following simplified BTE:

$$\frac{\partial f_{\mathbf{k}}}{\partial t} - \frac{e}{\hbar} \mathbf{E} \cdot \nabla_{\mathbf{k}} f_{\mathbf{k}} = \left(\frac{df_{\mathbf{k}}}{dt} \right)_{\text{coll}} = \mathcal{I}_{\mathbf{k}}\{f_{\mathbf{k}}\}. \quad (2.29)$$

The solution to this integro-differential equation is complicated by the presence of the *collision integral*, which is an integral over the distribution function f . In order to make the solution tractable, certain simplifying assumptions about the *collision integral* can be made. The most common approximation is the relaxation-time approximation, which we briefly discuss below.

2.3.2 Relaxation-time approximation

In the relaxation-time approximation, the *collision* integral is approximated and defined to be:

$$\left(\frac{df}{dt}\right)_{\text{coll}} = -\frac{f_{\mathbf{k}} - f_{\mathbf{k}}^0}{\tau(\mathbf{k})} \quad (2.30)$$

$$\left(\frac{d\delta f_{\mathbf{k}}}{dt}\right)_{\text{coll}} = -\frac{\delta f_{\mathbf{k}}}{\tau(\mathbf{k})} \quad (2.31)$$

where $f_{\mathbf{k}}^0$ is the unperturbed equilibrium distribution function, i.e., the distribution function present in the absence of any external applied force (and hence time independent), and $\delta f_{\mathbf{k}}$ is the deviation of the distribution from $f_{\mathbf{k}}^0$. The quantity $\tau(\mathbf{k})$, which is in general dependent on \mathbf{k} , is the transport relaxation time that, in essence, characterizes the time decay of a perturbed system to return to its equilibrium state when the perturbation is removed. This can be seen by solving Eq. 2.31 for $\delta f_{\mathbf{k}}$, whose solution is of the form $\exp[-t/\tau(\mathbf{k})]$.

Substituting Eq. 2.31 into Eq. 2.29, and integrating over time t with the initial condition that at $t = -\infty$ the system is in equilibrium, i.e., $\delta f_{\mathbf{k}} = 0$ leads to the expression for the change in the distribution function due to the electric field $\mathbf{E} = \mathbf{E}_0 e^{-i\omega t}$:

$$\delta f_{\mathbf{k}} = e\mathbf{E}_0 \cdot \mathbf{v}_{\mathbf{k}} \frac{\partial f_{\mathbf{k}}^0}{\partial \varepsilon_{\mathbf{k}}} \frac{\tau(\mathbf{k})e^{-i\omega t}}{1 - i\omega\tau(\mathbf{k})}, \quad (2.32)$$

where $\varepsilon_{\mathbf{k}}$ is the energy eigenvalue, and the band velocity is given by

$$\mathbf{v}_{\mathbf{k}} = \hbar^{-1} \nabla_{\mathbf{k}} \varepsilon_{\mathbf{k}}. \quad (2.33)$$

Under direct-current conditions ($\omega \rightarrow 0$),

$$\delta f_{\mathbf{k}} = e \mathbf{E}_0 \cdot \mathbf{v}_{\mathbf{k}} \frac{\partial f_{\mathbf{k}}^0}{\partial \varepsilon_{\mathbf{k}}} \tau(\mathbf{k}). \quad (2.34)$$

From the deviation in the distribution function $\delta f_{\mathbf{k}}$ for different momentum states, we can obtain the electric current:

$$\mathbf{J} = -e \int_{\Omega_{\text{BZ}}} \frac{d^3 \mathbf{k}}{8\pi^3} \delta f_{\mathbf{k}} \mathbf{v}_{\mathbf{k}}, \quad (2.35)$$

where the integration is over the Brillouin zone (BZ). The electric current is related to the electric field \mathbf{E}_0 through the conductivity σ as $\mathbf{J} = \sigma \mathbf{E}_0$, and by substituting the expression for $\delta f_{\mathbf{k}}$ from Eq. 2.34 into Eq. 2.35, we get:

$$\mathbf{J} = \sigma \mathbf{E}_0 = -e^2 \int_{\Omega} \frac{d^3 \mathbf{k}}{8\pi^3} (\mathbf{E}_0 \cdot \mathbf{v}_{\mathbf{k}}) \mathbf{v}_{\mathbf{k}} \frac{\partial f_{\mathbf{k}}^0}{\partial \varepsilon_{\mathbf{k}}} \tau(\mathbf{k}). \quad (2.36)$$

For a general crystal structure, the conductivity is a second-rank tensor with six independent (and three dependent) components. From Eq. 2.36, we can obtain the expression

for the direct-current conductivity tensor, whose components $\alpha\beta$ are given by:

$$\sigma_{\alpha\beta} = e^2 \int_{\Omega} \sum_n \frac{d^3\mathbf{k}}{8\pi^3} \sum_{\mathbf{k}} \left(-\frac{\partial f_{\mathbf{k}}^0}{\partial \varepsilon_{\mathbf{k}}} \right) \tau_n(\mathbf{k}) v_{\mathbf{k}}^{\alpha} v_{\mathbf{k}}^{\beta}, \quad (2.37)$$

where $v_{\mathbf{k}}^{\alpha}$ and $v_{\mathbf{k}}^{\beta}$ are the Cartesian components of the velocity vector $\mathbf{v}_{\mathbf{k}}$. The subscript in $\tau_n(\mathbf{k})$ indicates the band index n , which is summed over to obtain the total conductivity due to all the bands. For a cubic crystal structure, the conductivity tensor becomes isotropic, i.e., there is only one independent component, and the second-rank tensor reduces to a scalar given by

$$\sigma = \sigma_{\alpha\alpha} = e^2 \int_{\Omega} \sum_n \frac{d^3\mathbf{k}}{8\pi^3} \left(-\frac{\partial f_{\mathbf{k}}^0}{\partial \varepsilon_{\mathbf{k}}} \right) \tau_n(\mathbf{k}) (v_{\mathbf{k}}^{\alpha})^2. \quad (2.38)$$

Since we will deal with materials having a cubic crystal structure in this work, we use Eq. 2.38 to calculate the conductivity. From the electric conductivity, the *drift* mobility for a given carrier concentration n can be obtained from the relation $\mu = \sigma/(ne)$. The factor $\partial f_{\mathbf{k}}^0/\partial \varepsilon_{\mathbf{k}}$ in the conductivity integral in Eq. 2.37 is peaked at the Fermi level and decays to negligible values within a range of $\pm 10 k_{\text{B}}T$, where T is the temperature and k_{B} is the Boltzmann constant. This restricts $\tau_n(\mathbf{k})$ and $v_{\mathbf{k}}$ entering in the calculation of mobilities to values around the Fermi level $\varepsilon_{\text{F}} \pm 10 k_{\text{B}}T$. The \mathbf{k} -dependent scattering rate is specific to the scattering mechanism. In our study, we take into account the two dominant scattering mechanisms at room temperature that are unavoidable for impurity-

doped systems: electron-phonon scattering and ionized impurity scattering. Below, we discuss and give the expression for the scattering time $\tau_n(\mathbf{k})$ for these two mechanisms.

2.3.3 Electron-phonon scattering

The \mathbf{k} -dependent rate describing an electron-phonon scattering mechanism is obtained from Fermi's golden rule as [64, 65, 66, 67]

$$\begin{aligned} \tau_n^{-1}(\mathbf{k}) &= \frac{2\pi}{\hbar} \sum_{\nu, m} \int_{\Omega} \frac{d^3\mathbf{q}}{(2\pi)^3} |g_{\mathbf{q}\nu}(\mathbf{k}, n, m)|^2 (1 - \hat{v}_{n\mathbf{k}} \cdot \hat{v}_{m\mathbf{k}+\mathbf{q}}) \\ &\times [(n_{\mathbf{q}\nu} + f_{m, \mathbf{k}+\mathbf{q}}) \delta(\varepsilon_{m, \mathbf{k}+\mathbf{q}} - \varepsilon_{n, \mathbf{k}} - \hbar\omega_{\mathbf{q}\nu}) \\ &+ (1 + n_{\mathbf{q}\nu} - f_{m, \mathbf{k}+\mathbf{q}}) \delta(\varepsilon_{m, \mathbf{k}+\mathbf{q}} - \varepsilon_{n, \mathbf{k}} + \hbar\omega_{\mathbf{q}\nu})], \end{aligned} \quad (2.39)$$

where $g_{\mathbf{q}\nu}(\mathbf{k}, n, m)$ is the electron-phonon coupling matrix element between states in bands n and m , $n_{\mathbf{q}\nu}$ is the phonon occupation given by the Bose-Einstein (BE) distribution, and $\hbar\omega_{\mathbf{q}\nu}$ is the energy of phonon mode ν . The first energy-conserving δ function (containing the $-\hbar\omega$ term) represents the phonon absorption process, while the second δ function (containing the $+\hbar\omega$ term) represents the phonon emission process. The velocity factor, $(1 - \hat{v}_{n\mathbf{k}} \cdot \hat{v}_{m\mathbf{k}+\mathbf{q}})$ accounts for the directionality of the current due to the scattered carriers.

Although Eq. 2.39 is generally applicable to scattering due to both optical and acoustic phonons, we will focus on scattering by longitudinal optical (LO) phonons, which is the dominant mechanism limiting room-temperature conductivity [64], and neglect scattering by the transverse optical (TO) and acoustic phonons. To compute the electron-phonon

(el-ph) coupling matrix element $g_{\mathbf{q}\nu}(\mathbf{k})$ for LO-phonon scattering, we use the generalized Fröhlich model, which is applicable to materials with more than one LO mode. Contributions to the polarizability due to different optical branches are explicitly included by using the expression for the coupling matrix elements derived by Toyozawa [68, 69] based on the generalized Lyddane-Sachs-Teller relation. The phonon energy is approximated to be independent of \mathbf{q} as in the Fröhlich model. A short derivation of the expression is presented in Appendix B. Here we present the final expression for the matrix element (in SI units):

$$|g_{\mathbf{q}\nu}|^2 = \frac{q^2}{\left(q^2 + q_{\infty, \text{scr}}^2 F\left(\frac{q}{2k_{\text{F}}}\right)\right)^2} \left(\frac{e^2 \hbar \omega_{\text{L}, \nu}}{2\epsilon_{\infty} \epsilon_0 V_{\text{cell}}} \right) \times \left[\frac{\prod_j \left(1 - \frac{\omega_{\text{T}, j}^2}{\omega_{\text{L}, \nu}^2}\right)}{\prod_{j \neq \nu} \left(1 - \frac{\omega_{\text{L}, j}^2}{\omega_{\text{L}, \nu}^2}\right)} \right], \quad (2.40)$$

where ϵ_0 is the vacuum permittivity, ϵ_{∞} is the electronic part of the dielectric constant, and q is the phonon wavevector. For a material with a single LO mode Eq. 2.40 reduces to the familiar form derived by Fröhlich [70].

In the Fröhlich model [70] and in first-principles methods [67], a divergence occurs near $q = 0$ due to the long-range nature of the polarization field in a dielectric. However, the presence of conduction band (CB) electrons causes this long-range field to be screened, and by including this screening via the screening wavevector $q_{\infty, \text{scr}}$ in the expression for the el-ph matrix element (Eq. 2.40), the divergence is avoided [67, 71, 72]. In principle, screening due to CB electrons is q dependent, and is given by Lindhard theory. However, in practice, evaluating the full expression from Lindhard theory becomes computationally

expensive, except at 0 K where an analytic expression can be obtained [67, 73]. Therefore, to circumvent the large computational cost, we will compute the screening wavevector $q_{\infty, \text{scr}}$ using Thomas-Fermi theory [73], which is the $q \rightarrow 0$ limit of Lindhard theory, in a medium described by the high-frequency (clamped-ion) dielectric constant ϵ_{∞} :

$$q_{\infty, \text{scr}}^2 = \frac{e^2}{\epsilon_{\infty} \epsilon_0} \frac{\partial n}{\partial \epsilon_{\text{F}}} = \frac{e^2}{\epsilon_{\infty} \epsilon_0} \int_{\epsilon_{\text{CBM}}}^{\infty} d\epsilon \left(-\frac{\partial f}{\partial \epsilon} \right) D(\epsilon), \quad (2.41)$$

where the density of states $D(\epsilon)$ depends on the E -vs.- k dispersion relation (see Appendix C for an expression for the hyperbolic dispersion). The q dependence, which becomes important for phonon wavevectors q comparable to the Fermi wavevector k_{F} , is included via the Lindhard function $F(q/2k_{\text{F}})$ [64, 67, 73] in Eq. 2.39, which has an analytic form only at 0 K:

$$F(x) = \frac{1}{2} + \frac{1-x^2}{4x} \ln \left| \frac{1+x}{1-x} \right|, \quad x = \frac{q}{2k_{\text{F}}}. \quad (2.42)$$

The Fermi wavevector k_{F} can be obtained by solving for k using the E -vs.- k dispersion relation at the Fermi energy ϵ_{F} . For nondegenerate doping densities, where ϵ_{F} lies below the CBM, we use the average energy of a classical gas $3k_{\text{B}}T/2$ to solve for k_{F} .

In principle, the screening also affects the LO-phonon frequencies [72, 74, 75, 76] near Γ as:

$$\omega_{\text{L}, \nu}^2(q) = \frac{q^2 \omega_{\text{L}, \nu}^2 + q_{\infty, \text{scr}}^2 \omega_{\text{T}, \nu}^2}{q^2 + q_{\infty, \text{scr}}^2}, \quad (2.43)$$

which goes to $\omega_{\text{T},\nu}^2$ at $q = 0$, and approaches $\omega_{\text{L},\nu}^2$ for $q^2 \gg q_{\infty,\text{scr}}^2$. However, for our system, we estimated the impact of including this q dependence on the scattering rate by calculating the average of the matrix element $|g_{\mathbf{q},\nu}|^2$ over q , and find it to make less than 5% difference. Therefore, we neglect the q dependence of the frequencies, and use the unscreened q -independent LO frequency values in our study.

2.3.4 Ionized impurity scattering

To treat ionized/charged impurity scattering, two approaches are commonly used: the Brooks-Herring (BH) and Conwell-Weisskopf (CW) approaches [77]. Both approaches are based on the Born approximation (elastic scattering), and differ only in the manner in which screening is treated. The choice of approach depends on the screening regime, which is determined by the dimensionless parameter η :

$$\eta = \frac{16Z^2 N_{\text{imp}}^{2/3} R_{\text{H}}^*}{q_{\text{scr}}^2 \epsilon_{\mathbf{k}}}, \quad (2.44)$$

introduced by Ridley [78], who suggested BH to be valid for $\eta < 1$, and CW for $\eta > 1$. $R_{\text{H}}^* = 13.605 m_{\mathbf{k}}^*/m_e \epsilon^2$ eV is the effective Rydberg energy, where $m_{\mathbf{k}}^*$ is the band mass at wavevector \mathbf{k} . The screening wavevector q_{scr}^2 is computed in a medium described by the static dielectric constant ϵ [77] and is different from $q_{\infty,\text{scr}}^2$ in Eq. 2.41 used in the screening of electron-phonon interaction by a factor of $\epsilon_{\infty}/\epsilon$. Based on Ridley's criterion, for densities 10^{17} – 10^{21} cm⁻³ the BH approach should be applicable ($\eta < 1$). The scattering rate for N_{imp} ionized impurities of charge Ze within the BH approach is

given by

$$\begin{aligned} \tau_{\text{imp}}^{-1}(\mathbf{k}) &= \frac{\pi}{2} v_{\mathbf{k}} N_{\text{imp}} \left(\frac{Ze^2}{4\pi\epsilon\epsilon_0\epsilon_k} \right)^2 \\ &\times \left[\ln \left(1 + \frac{8m_{\mathbf{k}}^*\epsilon_k}{\hbar^2 q_{\text{scr}}^2} \right) - \left(1 + \frac{\hbar^2 q_{\text{scr}}^2}{8m_{\mathbf{k}}^*\epsilon_k} \right)^{-1} \right]. \end{aligned} \quad (2.45)$$

2.3.5 Hall mobility and Hall factor

It is common practice in transport experiments to report mobility values based on Hall measurements, where the Lorentz force due to an applied magnetic field acting on the electric-field accelerated carriers [79] is used to extract transport properties. The Hall mobility μ_{H} , reported in Hall measurements, is different from the drift mobility μ (related to the conductivity in Eq. 2.38) by the Hall factor r_{H} [64, 79]:

$$\mu_{\text{H}} = r_{\text{H}} \mu. \quad (2.46)$$

The Hall factor, usually on the order of 1–2, is obtained from the electrical conductivity σ (Eq. 2.38) and the conductivity coefficient σ_{H} as [80, 81]

$$r_{\text{H}} = \frac{\sigma_{\text{H}}}{\sigma^2} ne. \quad (2.47)$$

The conductivity coefficient is calculated using the expression

$$\sigma_{\text{H}} = 2e^3 \int_{\Omega} \frac{d^3k}{(2\pi)^3} \tau^2(\mathbf{k}) \left(-\frac{\partial f_{\mathbf{k}}}{\partial \varepsilon} \right) v_x (v_x M_{yy}^{-1} - v_y M_{xy}^{-1}), \quad (2.48)$$

where, for the case of a hyperbolic band dispersion,

$$M_{ij}^{-1} = \frac{1}{\hbar} \frac{\partial v_j}{\partial k_i} \quad (2.49)$$

$$= [m_{\Gamma}^* (1 + 2\alpha \varepsilon_{\mathbf{k}})]^{-1} (\delta_{ij} - 2\alpha m_{\Gamma}^* v_i v_j). \quad (2.50)$$

For parabolic dispersion, $\alpha = 0$, $M_{yy}^{-1} = (m_{\Gamma}^*)^{-1}$ and $M_{xy}^{-1} = 0$. Due to the dependence of σ_{H} on $\tau^2(\mathbf{k})$, σ on $\tau(\mathbf{k})$ and r_{H} on their ratio, including the k -dependence of $\tau(\mathbf{k})$ is necessary for the calculation of Hall mobility. Neglecting the k dependence results in $r_{\text{H}} = 1$, i.e., the Hall and drift mobilities become identical.

Chapter 3

Implementing field dependence of dielectric constant into Schrödinger-Poisson solver

One of the many interesting and useful phenomena observed in complex oxides is the formation of a high-density 2DEG at an interface between nonpolar and polar complex oxides, as was discussed in Sec. 1.3. Schrödinger-Poisson solvers can be used to model the behavior of the 2DEG. However, this is complicated by the fact that some of the complex oxides, including STO, exhibit a field dependence of their static dielectric constant, which occurs due to the presence of soft phonon modes [25, 26]. The large 2DEG density results in a large band bending, which in turns causes a large electric field. Therefore, it is imperative to account for the field dependence in the static dielectric constant to

model the properties of the 2DEG. Currently available Schrödinger-Poisson solvers do not implement the field dependence of dielectric constant. In this chapter, we incorporate the field dependence into a Schrödinger-Poisson solver, and use the implementation to simulate the intrinsic 2DEG at the $\text{LaAlO}_3/\text{SrTiO}_3$ as well as $\text{GdTiO}_3/\text{SrTiO}_3$ interfaces.

3.1 Introduction

The confinement of carriers in an interfacial potential well [inset of Fig. 3.1] is associated with the presence of a large electric field. The potential profile that confines the carriers is dependent on the dielectric properties of the material. As mentioned in Chapter 1, in many complex oxides, including STO, the dielectric properties depend strongly on the electric field [22, 23, 24], due to the presence of a soft optical phonon mode [26, 27]. Given that the electric field affects the dielectric properties, and that the dielectric properties in turn affect the electric field, modeling of the interface based on a Schrödinger-Poisson (SP) solver should take the field dependence of the dielectric constant into account in a selfconsistent manner. To date, only a few analyses and simulations [27, 29, 30, 31] have accounted for this field dependence at the interface that confines a 2DEG. Taking the field dependence of the dielectric constant into account is not only important in simulations, but is also necessary for the correct interpretation of experimental $C - V$ measurements at large applied voltages [32].

Schrödinger-Poisson simulations can be effective in studying the effect of the field-dependent dielectric constant of STO on the 2DEG confined at the interface of STO/GTO.

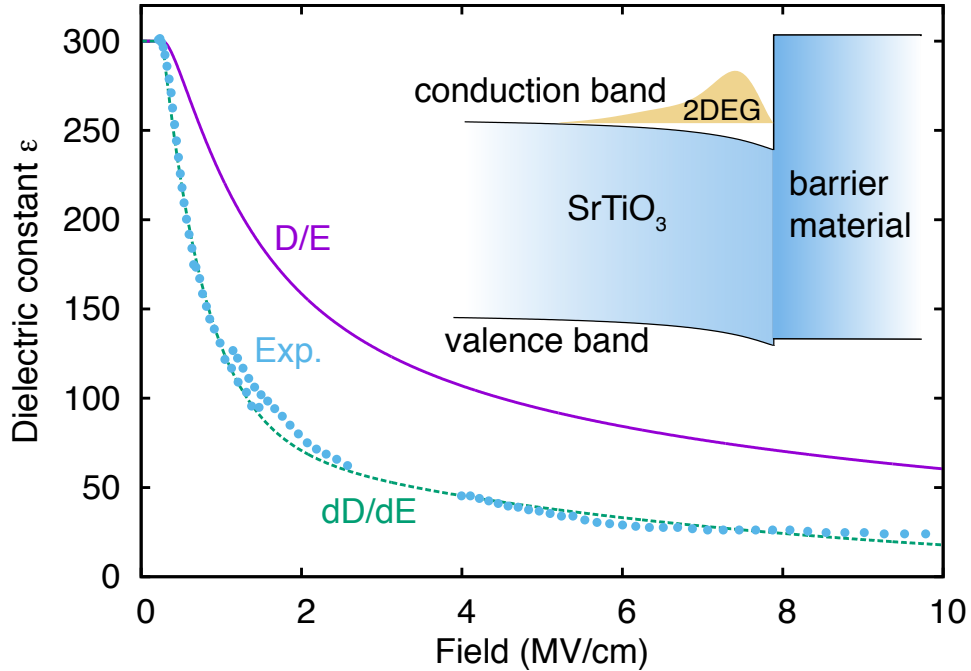


Figure 3.1: Dielectric constant as a function of the electric field. The dashed line is determined by fitting Eq. 3.1 to the experimental measurements of Ref. [24]. These experimental data points are not continuous as they were obtained from 3 different samples. The solid line is determined by integrating over the field, as expressed in Eq. 3.2. The curve fitting, integration and plotting were done by my colleague, Dr. Hartwin Peelaers. The inset shows a schematic band diagram of the confinement of a 2DEG at an interface between STO and a barrier material. The band bending reflects the presence of an electric field.

The basic material parameters, such as band gaps, band offsets and conduction-band effective masses are obtained from first-principles calculations. While we consider the STO/GTO heterojunction with the full 2DEG density of $3.3 \times 10^{14} \text{ cm}^{-2}$ as a prototypical example¹, the physics described here is more general, and the conclusions are applicable to other heterojunctions with a 2DEG confined in STO, as we will explicitly verify by simulations for an STO/LAO interface. Our goal is to produce results that can aid in

¹The band diagram for STO/GTO differs from the one shown in the inset of Fig. 3.1 by the inclusion of a “lower Hubbard band” in the GTO, lying well below the conduction-band minimum of STO (see Ref. [82]). The presence of this band does not affect any of the physics discussed in the present work.

interpreting experiments (e.g., capacitance measurements), and also to provide insight into the physical mechanisms and phenomena that result from the field dependence.

3.2 Implementation details

The dependence of the dielectric constant on electric field is taken from experiment [24] (data points in Fig. 3.1). In principle, this dependence can also be obtained from first-principles calculations, but in practice this requires a large effort that has been executed in only very few instances to date [30], and then only at 0 K. The dielectric constant is actually strongly temperature dependent [22, 23, 24], and since the main interest is in devices that operate at room temperature, it is most appropriate to work with the experimental data [24] that were obtained at room temperature.

Our simulations are based on the *nextnano*³ code [83], modified to implement a field-dependent dielectric constant. The code solves for the electrostatic potential, charge density, and Fermi level (E_F) across the heterojunction. The input parameters include electron effective masses (1.0 m_e , fitted to reproduce the density of states obtained from density functional theory with a hybrid functional [21]) and the static dielectric constant of GTO ($\epsilon = 30$). The static dielectric constant of STO is implemented as a variable that depends on the electric field. Further details of the implementation are described below. The band gaps of GTO and STO are 2.05 eV and 3.27 eV, respectively; the conduction-band offset is 1.47 eV [82]. The heterojunction was simulated with 500 nm of STO on one side interfaced with 500 nm of GTO. No background doping was assumed;

we explicitly checked that uniform doping of the STO, up to levels of $1 \times 10^{18} \text{ cm}^{-3}$ made no difference to the results (change in ϵ smaller than 1 in the region of the highest field). The intrinsic 2DEG of density $3.3 \times 10^{14} \text{ cm}^{-2}$ was simulated by introducing dopants with a concentration of $1.6 \times 10^{22} \text{ cm}^{-3}$ in a 0.2 nm region on the GTO side of the interface.

Obtaining the field dependence of the dielectric constant from experimental data requires careful consideration of its physical meaning. For *linear* media, the dielectric constant is the proportionality factor between the electric displacement D and the electric field E , $D = \epsilon E$. More generally, for *non-linear* media, ϵ depends on the electric field as well, and therefore the previous linear equation should be replaced with a derivative equation: $dD = \epsilon_d(E)dE$, where the subscript in $\epsilon_d(E)$ indicates its derivative nature. My colleague, Dr. Hartwin Peelaers, obtained a functional form for the field-dependent dielectric constant by fitting the results of van der Berg *et al.* [24] to an empirical equation of the following form

$$\epsilon_d(E) = \begin{cases} 300, & E \leq 0.27 \text{ MV/cm} \\ \frac{dD}{dE} = ae^{-bE} + ce^{-fE}, & E > 0.27 \text{ MV/cm}, \end{cases} \quad (3.1)$$

where $a = 358.50$, $b = 1.84 \text{ cm/MV}$, $c = 83.84$, and $f = 0.15 \text{ cm/MV}$ are fitting parameters. At this stage, careful attention should be paid to the form in which the Poisson equation is implemented in the Schrödinger-Poisson solver. In some codes, the Poisson equation is implemented as $E = \int d\mathbf{r}[\rho/\epsilon_d(E)]$, and $\epsilon_d(E)$ can be used directly. However, other codes (including the *nextnano*³ code we use) implement the Poisson

equation as $\nabla \cdot D = \nabla \cdot [\epsilon(E)E] = \rho$, and therefore require a dielectric constant that is obtained by integrating Eq. 3.1 and computing $\epsilon(E) = \frac{1}{E} \int \frac{dD}{dE} dE$:

$$\epsilon(E) = \begin{cases} 300, & E \leq 0.27 \text{ MV/cm} \\ -\frac{1}{E} \left[\frac{a}{b} e^{-bE} + \frac{c}{f} e^{-fE} - 719.307 \right], & E > 0.27 \text{ MV/cm.} \end{cases} \quad (3.2)$$

The experimental data [24] (three separate curves correspond to three different samples), our fit to the data, and the integrated $\epsilon(E)$ are all shown in Fig. 3.1. For electric fields smaller than 0.27 MV/cm, STO behaves as a linear medium; therefore the dielectric constant remains constant at 300 independent of the field, and the dD/dE and D/E curves coincide.

In practice, the *nextnano*³ code assumes linear media when solving the SP equations. To mimic a non-linear medium, we partition the STO region of the device into regions of width 0.1 nm up to 10 nm from the interface, and regions of width 1 nm between 10 nm and 50 nm from the interface. The remainder of the STO region formed one partition. For the first iteration, all the partitions of STO are assigned a dielectric constant of 300. At the end of each iteration, the electric fields in different regions are obtained from the solution of the SP solver. Within each region, the average value of the electric field is then used to calculate the corresponding dielectric constant from Eq. 3.2. The next SP iteration is then performed using the dielectric-constant values assigned to each of the regions, and the electric field is recalculated. We iterate this procedure until the change in the dielectric constant for each region is smaller than 0.01 in consecutive SP iterations.

The converged result is shown in Fig. 3.3. We checked that the partitioning of the STO into regions was fine enough not to affect the results.

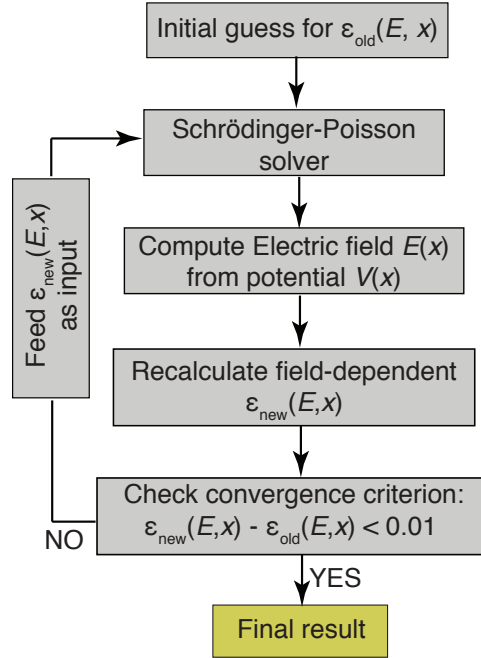


Figure 3.2: Algorithm implemented to account for the field-dependent dielectric permittivity in a Schrödinger-Poisson solver.

3.3 Results and discussion

We find that the electric field reaches a maximum of 20.50 MV/cm at the STO/GTO interface, and rapidly decreases away from the interface. In the region of high electric field a corresponding reduction in the dielectric constant is observed [Fig. 3.3(b)]. Near the interface the dielectric constant in STO is 37, and away from the interface it increases to the low-field value of 300. Our numerical approach required a discretization of the dielectric constant; due to the large electric fields near the interface and the exponential

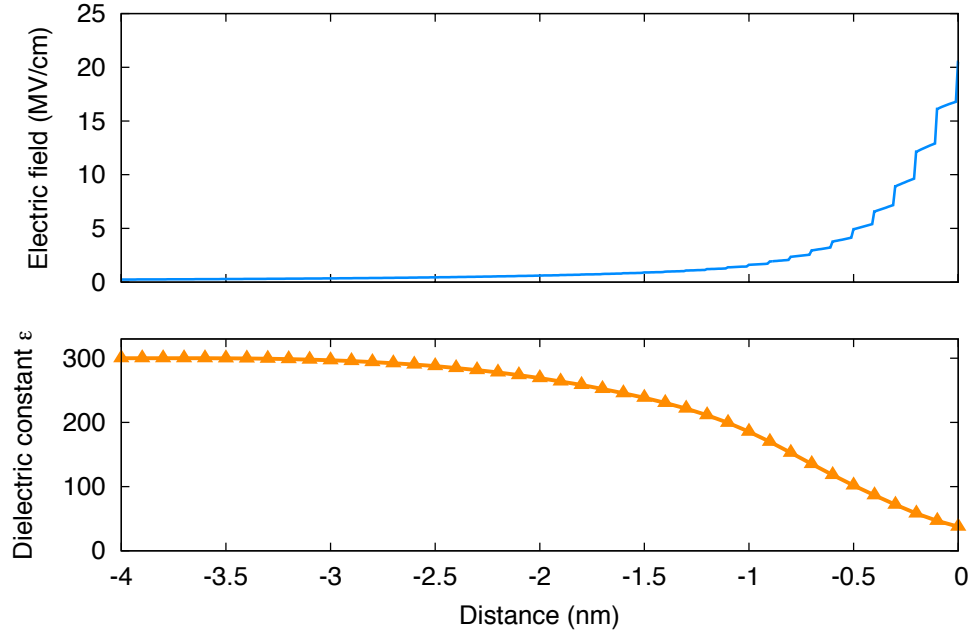


Figure 3.3: (a) Calculated electric field near the STO/GTO heterojunction. The junction is located at 0 nm. (b) Corresponding dielectric constant, as determined from Eq. 3.2 using the calculated average electric field in each region.

dependence of ϵ on the field, adjacent regions within a few \AA of the interface exhibit large differences in dielectric constant values. This results in discontinuities in the electric field curve near the interface (as D is required to be continuous). Regardless, the values for the electric field and the dielectric constant within each region elucidate the real physical mechanism involved.

The proper treatment of the field dependence of the dielectric constant has a distinct effect on the distribution of electrons within the 2DEG. In Fig. 3.4 we compare the electron distribution obtained by taking the field dependence into account with the distribution that is obtained using the traditional assumption of a field-independent dielectric constant (with a value of 300). The field dependence reduces the value of the dielectric constant, and from Poisson's equation a smaller dielectric constant results in a larger

electric field. Therefore, we expect that taking the field dependence of ϵ into account will result in larger electric fields and hence increased band bending as well as stronger confinement of the 2DEG; this is indeed borne out by our simulations, shown in Fig. 3.4. If a constant ϵ is assumed, the 2DEG has a peak density of $1.82 \times 10^{21} \text{ cm}^{-3}$ located 0.62 nm away from the interface, and E_F lies 0.44 eV above the conduction-band minimum (E_C) at the interface. The maximum value of the electric field is 2.17 MV/cm, which leads to a reduction of the dielectric constant (Eq. 3.2). Accounting for this field dependence increases E_F to 0.85 eV above E_C , and causes the peak in the 2DEG density to shift closer to the interface by 0.29 nm compared to the field-independent case. The peak value of the 2DEG density also increases to $2.66 \times 10^{21} \text{ cm}^{-3}$ (see Table 3.1), and its width is distinctly narrowed compared to the constant- ϵ case. Since the screening wavevector in a 2DEG is inversely proportional to the dielectric constant [84], the screening length follows the variation of the dielectric constant [Fig. 3.3(b)]. The increased electron density also could lead to more electron-electron scattering [35]; in addition, the closer proximity of the electrons to the interface may lead to increased interfacial scattering.

For systems other than STO/GTO [12] and γ -Al₂O₃/STO [85], experimentally reported 2DEG densities [6, 7, 86] are smaller than $3.3 \times 10^{14} \text{ cm}^{-2}$; one possible reason for this reduction is the transfer of electrons from the interface to surface states on the polar material [39]. It is therefore of interest to address the variation in dielectric constant and band bending for a range of systems with different 2DEG densities; the results are shown in Table 3.1. We find that 2DEG densities smaller than $1 \times 10^{13} \text{ cm}^{-2}$ leave the dielec-

tric constant unaltered from its low-field value over the entire STO region. In 2DEGs with higher densities, the peak position of the 2DEG shifts towards the interface and its peak value increases. This is accompanied by a larger band bending, and hence a larger electric field that decreases ϵ .

Table 3.1: Field-dependent properties of the 2DEG, namely peak position, peak height, Fermi level relative to conduction-band minimum, minimum value of ϵ and maximum value of the electric field, for different 2DEG densities.

2DEG density (cm^{-2})	peak position (nm)	peak height (10^{20} cm^{-3})	$(E_F - E_C)$ (eV)	min. ϵ	max. el. field (MV/cm)
5.0×10^{13}	1.32	1.38	0.09	162	3.25
1.0×10^{14}	1.01	3.81	0.20	104	6.48
3.3×10^{14}	0.33	26.6	0.85	37	20.51

Very similar results were obtained for the STO/LAO interface, in line with existing estimates based on solving the Poisson equation [31]. This interface differs from the STO/GTO interface by the conduction-band offset being 1.89 eV instead of 1.47 eV. The similarity of the results indicates that the effect of the field dependence is not sensitive to the nature of the wide-band-gap oxide that provides confinement to the 2DEG occurring in STO.

3.4 Conclusion

In conclusion, we have studied the effects of the field dependence of the STO dielectric constant on fields and electron distributions in the 2DEG occurring at complex-oxide interfaces. We used Schrödinger-Poisson simulations that selfconsistently solve for the

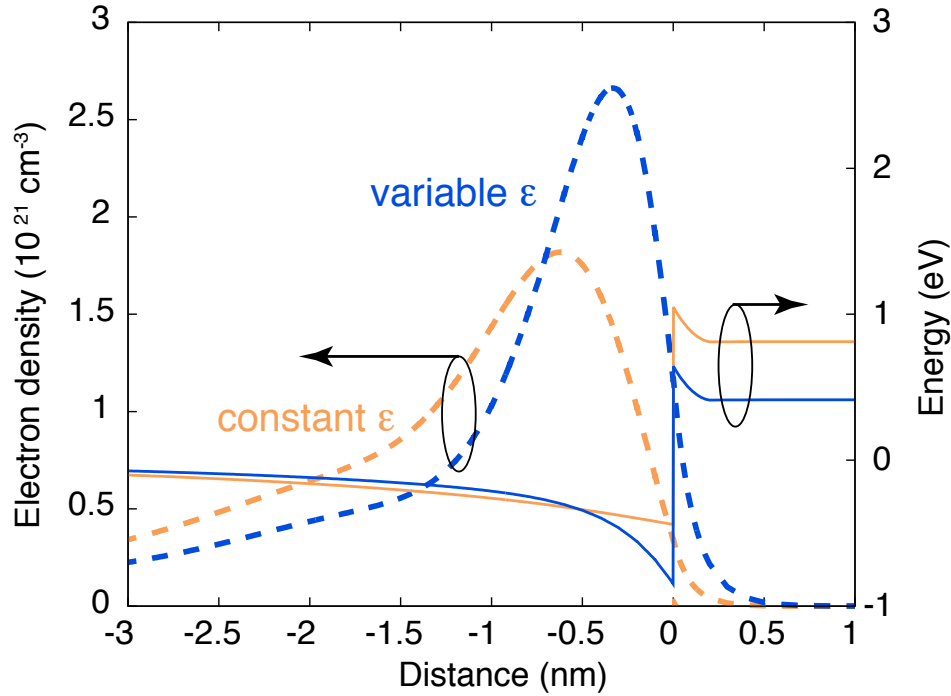


Figure 3.4: Electron distribution at the STO/GTO interface (left axis, dashed lines) assuming either a constant dielectric constant ($\epsilon=300$) or a field-dependent ϵ . The corresponding conduction-band profile is shown in solid lines (right axis).

electric field and the dielectric constant, with parameters obtained from first-principles calculations along with experimental data for the field dependence. The STO/GTO interface was used as a prototypical interface for our study, but our results apply more generally to other STO interfaces containing a 2DEG such as STO/LAO, as they are not sensitive to the barrier material confining the 2DEG. The effect of the field dependence is significant, leading to enhanced confinement and increased density of charge carriers closer to the interface. These insights and qualitative results will aid in understanding and analyzing the distribution of charge carriers.

Chapter 4

First-principles theory of surface charging¹

4.1 Introduction

Observations of a two-dimensional electron gas (2DEG) with high carrier density ($\sim 10^{13} \text{ cm}^{-2}$) (Refs. [6,7,8,9]) at the (001) interface between SrTiO₃ (STO) and LaAlO₃ (LAO) have generated great interest. In spite of a decade of investigations, the mechanisms governing the 2DEG formation and its density are not yet fully understood. The polar catastrophe model [6,14] is still widely used to explain interface doping in this heterostructure, although experimental evidence [13] does not seem to support it. A

¹The content of this chapter was published in the journal *Physical Review B*, Ref. [39]. Copyright (2015) by the American Physical Society.

complete and consistent model that can explain all the experimental findings in the LAO/STO heterostructures is still lacking.

Recent calculations [21,87,88,89,90] as well as experiments [91,92,93,94] have stressed the importance of the LAO surface in determining the density of the 2DEG at this interface. Cen *et al.* [91] demonstrated the reversible process of inducing conductivity at the LAO/STO interface using a conductive tip at the surface of LAO by applying a field. Other groups [92,93,94,95,96,97,98] have observed similar phenomena and find a strong correlation between the environment to which the surface of LAO is exposed and the 2DEG density at the interface. Despite the important role played by the surface, there is a lack of experimental studies to determine the exact nature and structure of the LAO surface in this system. Most groups assume the surface to be AlO₂-terminated by counting the RHEED (Reflection High-Energy Electron Diffraction) intensity oscillations during growth [11,91]. However, the surface termination and its structure may change upon exposure to conditions under which the 2DEG properties are measured.

It has been previously demonstrated that electrons residing in the 2DEG with a density of $3.3 \times 10^{14} \text{ cm}^{-2}$ ($0.5e^-$ per areal unit) are intrinsic to the interface between LAO and STO along the [001] direction [21]. If the LAO layer is sufficiently thin, these electrons can transfer to empty surface states on the LAO surface and deplete the 2DEG density; indeed, the experimentally observed 2DEG densities are much lower than the nominal $3.3 \times 10^{14} \text{ cm}^{-2}$ [7,8,9]. Such a transfer of electrons from the interface also leaves the LAO surface charged. This phenomenon of surface charging is a common occurrence

in many other systems of practical interest as well, but has not been addressed from first principles until very recently [99]. It is our goal in the present study to rigorously address the physics involved with surface charging within a first-principles context, and apply the understanding to model the interactions between the interfacial 2DEG and the surface in LAO/STO heterostructures. We note that Bristowe *et al.* [88] adopted an opposite viewpoint for the mechanism of 2DEG formation: they did not consider the 2DEG to be intrinsic to the LAO/STO interface, but assumed that the carriers appear at the interface in order to screen the field in the LAO. Although in the case of thin LAO films terminated by a surface both viewpoints are equivalent, the arguments in Ref. [88] break down in the case of a superlattice, or LAO capped with another material.

Most theoretical efforts to date have focused on studying the interface properties of the LAO/STO heterostructures [30, 100]. Surface studies for these heterostructures [89, 101] have been limited to a small set of surface structures owing to the high computational cost involved. We overcome this limitation by formulating a model that represents the coupling between the LAO surface and the LAO/STO interface, including the effects of surface charging. This allows us to calculate the properties of the LAO surface separately from those of the interface. We can then use the model to study the heterostructure as a whole. This approach eliminates the need for studying both STO and LAO (i.e., the interface and the surface) within the same calculation, thus greatly lowering the computational demand and allowing us to more thoroughly explore surface reconstructions. Even more importantly, the separation of the surface problem from the interface problem

results in a more general formulation, which will be useful to address similar systems in the future. Bristowe *et al.* [88] have proposed a model to consider O-vacancy defects on the surface, from the viewpoint that the carriers in the 2DEG arise in order to screen the field in LAO. Their model uses a number of parameters taken from different sources, and does not allow for a general comparison between different surface terminations with various defects. In our work, we overcome this limitation by an explicit consideration of the absolute surface energy. There have been other proposed mechanisms for the origin of carriers at the interface, which are based on defects in STO bulk, cation intermixing, and oxygen vacancies near the interface [18, 102, 103]. These issues will not be dealt with in this work.

In order to study the surface of LAO as a separate entity, and to include the effects of charging the surface, calculations that treat charged surfaces of a dielectric are required. The usual theoretical treatment of surface reconstructions assumes that the surfaces always remain neutral. Indeed, the computational treatment of non-neutral surfaces has not been possible in the past, since a non-neutral system clearly leads to divergences in energy, and robust methods for providing charge neutralization in the case of semiconductors or insulators were lacking [104]. Charged surfaces do occur, however, in many situations of practical interest. One example is the surfaces of doped semiconductors, which typically exhibit band bending in the near-surface region. Depletion of carriers leads to fixed charges and the formation of a space-charge region, and the free carriers charge the surface by occupying surface states [105, 106]. The amount of band bending

is determined by Fermi-level pinning at the partially filled surface states. In the case of semiconductor surfaces, the amount of surface charge is typically small relative to the density of atoms on the surface. In contrast, in the LAO/STO system the amount of charge transferred to the surface (0.5 electrons per areal unit cell) is of the order of the surface atomic density. Due to the magnitude of the amount of charge added to the surface, careful treatment of the charged surface is essential to accurately address the energetics.

In this work, we determine the stable surface terminations and reconstructions of LAO films grown on STO substrates. This is accomplished by first calculating surface energies of various surface reconstructions and terminations on the (001) surface of LAO, using first-principles calculations based on hybrid density functional theory, taking into account the effects of charging the surface. Subsequently, the system consisting of a thin LAO film on an STO substrate is analyzed, allowing us to examine the interplay between LAO thickness, density of the 2DEG at the LAO/STO interface, and the stability of surface reconstructions on the LAO surface. We consider Al-adatom, H-adatom and O-vacancy reconstructions, which can be regarded as corresponding to a high density of point defects on the surface. We will also investigate the consequences of modifying the density of such point defects. While we do not explicitly calculate isolated surface defects, but estimate the energetics based on reconstructions with varying coverage, we will use the term “surface defects” to refer to a uniformly spaced 2D array of defects (such as Al-adatoms) with a given concentration. Overall, our interest will be to quantify the

2DEG density remaining at the LAO/STO interface after the transfer to the surface, that would minimize the total energy of the system for a certain thickness of LAO, and result in a stable LAO surface.

The presentation of the work is organized as follows: In Sec. 4.2.1 we describe our first-principles calculations to determine atomic and electronic structure as well as energetics of surfaces. Section 4.2.2 describes the methodology involved in calculating the surface energies of neutral reconstructed as well as unreconstructed LAO surfaces from first principles. The approach developed by Lozovoi et al. [107] to treat charged surface of metals is generalized to the treatment of charged surface of dielectrics, as systematically explained in Sec. 4.2.3. In Sec. 4.3, we calculate and discuss the electronic structure of the bulk and the surface of LAO. In Sec. 4.4 we build on the methodology of Sec. 4.2.3 and the results of Sec. 4.3 to formulate a model for the surface energetics of LAO in LAO/STO heterostructures, i.e., in the presence of an interfacial 2DEG. By applying the model to various surface reconstructions, we can determine the most stable surface termination as well as stable surface reconstructions. Finally, in Sec. 4.5, we discuss the 2DEG density at the LAO/STO interface for surfaces of LAO with varying densities of Al-adatom, H-adatom and O-vacancy surface defects. Based on the results obtained for the 2DEG density, the trends related to the thickness of LAO films are discussed for a variety of environmental conditions to which the surface might be exposed.

4.2 First-principles methodology for charged surfaces

4.2.1 First-principles method

Our first-principles calculations were performed using density functional theory (DFT) with the screened hybrid functional of Heyd, Scuseria and Ernzerhof (HSE) [55,108], and the projector augmented wave method [56,109] as implemented in the Vienna *Ab-initio* Simulation Package (VASP) [58,110]. The use of the HSE hybrid functional with the default mixing parameter α of 25% gives an accurate description of the band gap and lattice parameters of both LAO and STO [82,111].

In order to study surfaces, we used the supercell approach with a symmetric slab geometry based on cubic LAO with a slab thickness of 5.5 unit cells corresponding to 11 layers of LAO with two identical surface terminations along the [001] direction, separated by ~ 15 Å of vacuum [see Fig. 4.1(a)]. Each layer corresponds to a plane of atoms, either an AlO₂-plane or an LaO-plane [See also Sec. 4.3]. Therefore, a supercell having an AlO₂-terminated surface will have 6 layers of AlO₂ and 5 layers of LaO. Our supercells contain only an LAO slab along with vacuum, and do not include STO or any interfaces. We therefore do not explicitly address the electrons in the 2DEG, but focus on the surface properties of LAO, for which the HSE functional provides accurate results [112]. Three layers at the center of the slab were kept fixed to the LAO bulk structure, while atoms within two unit cells (4 layers) of each surface were allowed to relax. Due to the periodic boundary conditions there may be interactions between the periodic images of

the surfaces. We have explicitly verified, by independently varying the slab thickness and vacuum thickness, that our geometry leads to results that are converged to within 0.35 meV/Å². For bulk calculations, integrations over the Brillouin zone used a Monkhorst-Pack [113] k -point mesh of $4 \times 4 \times 4$, while a $4 \times 4 \times 1$ mesh was used for the (1×1) surface calculations, and a $2 \times 2 \times 1$ mesh for the (2×2) surface calculations. The area of a (1×1) unit cell is 14.29 Å².

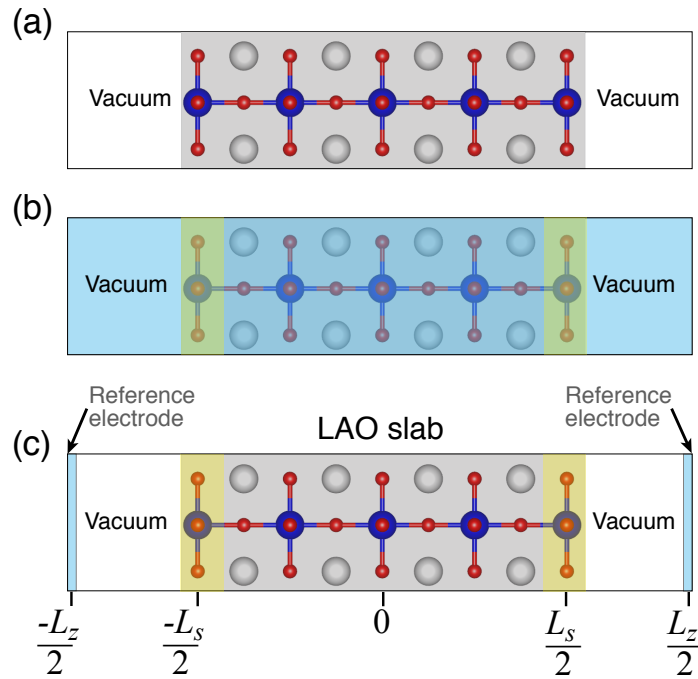


Figure 4.1: Schematic illustration of (a) the supercell used to calculate a symmetric neutral slab with dielectric constant ϵ with vacuum on either side, (b) the process of adding charge (shown in yellow) to the surface of the slab with a uniform compensating background charge (shown in blue) spread throughout the supercell, and (c) an auxiliary system with reference electrodes at the cell edges.

4.2.2 Surface energy of neutral reconstructed LaAlO_3 surfaces

The surface energy can be determined from supercell calculation for a slab with the equation:

$$\begin{aligned} \gamma_{\text{surface}} = \frac{1}{2} [& E_{\text{slab}}(n_{\text{LAO}}) - E_{\text{bulk}}(n_{\text{LAO}}) \\ & - n_{\text{La}} \cdot \mu_{\text{La}} - n_{\text{Al}} \cdot \mu_{\text{Al}} - n_{\text{O}} \cdot \mu_{\text{O}}], \end{aligned} \quad (4.1)$$

where E_{slab} is the total energy of the slab supercell containing two identical surfaces, $E_{\text{bulk}}(n_{\text{LAO}})$ is the total energy of the corresponding number of bulk LAO cells, n_i is the number of excess atoms of species i in the slab supercell, and μ_i is the chemical potential of species i , which is a variable representing experimental conditions.

The stability equation of LAO, expressed in terms of the chemical potentials μ_i of the constituent elements referenced to their elemental phases, is:

$$\mu_{\text{Al}} + \mu_{\text{La}} + 3\mu_{\text{O}} = \Delta H_f(\text{LaAlO}_3), \quad (4.2)$$

where $\Delta H_f(\text{LaAlO}_3)$ is the enthalpy of formation of LAO. The formation of competing phases such as Al_2O_3 in the Al-rich limit, and La_2O_3 in the La-rich limit, imposes additional constraints:

$$\text{Al-rich: } 2\mu_{\text{Al}} + 3\mu_{\text{O}} \leq \Delta H_f(\text{Al}_2\text{O}_3), \quad (4.3a)$$

$$\text{La-rich: } 2\mu_{\text{La}} + 3\mu_{\text{O}} \leq \Delta H_f(\text{La}_2\text{O}_3), \quad (4.3b)$$

where $\Delta H_f(\text{Al}_2\text{O}_3)$ and $\Delta H_f(\text{La}_2\text{O}_3)$ are the enthalpies of formation for Al_2O_3 and La_2O_3 , respectively.

4.2.3 Methodology to treat charged surfaces

The first-principles method to obtain surface energies described above applies to neutral surfaces. Adding charge to a slab supercell creates serious complications, which have stymied calculations for charged 2D systems in the past: since the energy of an infinite, periodic, charged system diverges, the added charge must be compensated so the periodically repeated supercell is overall charge neutral. The issue of charge compensation has been thoroughly studied in the case of point defects in the bulk, where charge compensation is provided by a uniform compensating background charge (CBC), and rigorous prescriptions have been formulated for extrapolating to the dilute limit [57, 114, 115]. Applying a CBC over the entire supercell is, in practice, achieved simply by removing the $\mathbf{G} = 0$ term in the Fourier expansion of the electrostatic potential.

In the case of charged surfaces, two complications arise. Applying a uniform CBC to the entire supercell may create artifacts, since the presence of a uniform charge in the vacuum region is unphysical. The second complication is that, because of the varying dielectric profile the screening of the CBC is different in different regions of the supercell. In the case of point defects on the surface, where the main focus is on removing spurious interactions between defects in neighboring cells in order to determine results

for the dilute limit, specific prescriptions have been formulated to correct the calculated energies [104].

In our present system, however, we are interested not in the dilute limit, but in situations where the concentration of charge on the surface may be on the order of the atomic density. Overall charge neutrality could of course be achieved by calculating the complete system, i.e., including the LAO/STO interface in the supercell [89, 116, 117]; however, as discussed in the introduction, this would require treatment of a system with a very large number of atoms, exceeding what can be addressed with hybrid density functional calculations. More importantly, it is not clear how one would disentangle the properties of the interface and the surface, making it difficult to discuss the physics and also to present the results in a form that can productively be used for further analysis of similar systems (e.g., with different layer thicknesses). Instead, we focus on calculations for a charged LAO slab with a uniform CBC, and correct for spurious effects by adopting a methodology originally developed by Lozovoi *et al.* [107] for charged metal surfaces, which we generalize here for the case of a dielectric slab.

The approach is illustrated schematically in Fig. 4.1. The actual DFT calculations are performed for a charged slab in a compensating background [Fig. 4.1(b)], but we will use post-processing corrections to convert the energies and electrostatic potentials to those of an auxiliary system consisting of the charged slab compensated by grounded metal “reference electrodes” at the supercell boundaries [107]. This allows us to separate the electrostatic effects associated with the addition of surface charge from the changes

in surface energy. The purpose of introducing the “reference electrodes” in the auxiliary system is two-fold: (1) to prevent the divergence of the electrostatic potential due to the charged slab (same role as a compensating charge), and (2) to serve as a consistent reference for the comparison of the energies of surfaces with different charges. The electrodes do not contribute to the energy of the cell as they are infinitely thin, but they determine the value (set to zero) of the electrostatic potential at the boundaries. Relaxation of the atomic positions in a charged supercell could be performed in principle by relaxing the structure based on forces that are appropriately corrected to remove the spurious effect of the CBC. However, such force corrections have not yet been addressed [104, 107]. In the present work we fix the structure to correspond to that of the neutral (relaxed) structure, and neglect any relaxations that may result from charge addition.

The methodology to compute the energy of charged surfaces involves three steps. First, we calculate the total energy and the macroscopic average of the electrostatic potential energy of a slab cell with charged surfaces and a CBC. Second, we correct the macroscopically averaged electrostatic potential energy and the total energy of the slab by removing the contributions from the homogeneous background charge. As the final step, we separate out the surface-energy change due to the addition of charge, by referencing to the neutral surface.

In the following discussions, the symbol V (in units of Volts) will consistently be used to refer to electrostatic *potential*, to be distinguished from the electrostatic *potential*

energy that electrons experience. Since electrons have negative charge (with magnitude e), this potential energy corresponds to $-eV$ (in units of eV).

4.2.3.1 Macroscopic averaging

We first calculate and extract the surface energy of the neutral surface, using the supercell approach described in Sec. 4.2.1. As the surface is perpendicular to the z direction of the supercell, for the quantities of interest such as the charge density and the electrostatic potential energy, it is useful to obtain the *xy planar average* (PA) and consequently, the one-dimensional *macroscopic average* (MA), which is a running average over a period of the lattice [118]. An example for the PA and MA of the electrostatic potential energy (in units of eV) obtained from our first-principles calculation is shown in Fig. 4.2 for a neutral surface terminated by an AlO_2 plane. Note the constant value of the MA potential energy in the vacuum region as well as in the center of the slab region between the two surfaces. This constant value is reached already within two atomic distances from the surface. This rapid convergence is reassuring with regard to the ability of the supercell geometry to capture the results for an isolated surface, avoiding any spurious interactions between the two slab surfaces.

4.2.3.2 Removing the contributions due to the background charge

The electrostatic potential calculated from first principles can be written as a superposition:

$$\tilde{V}(r) = V(r) + V_b(r) \quad (4.4)$$

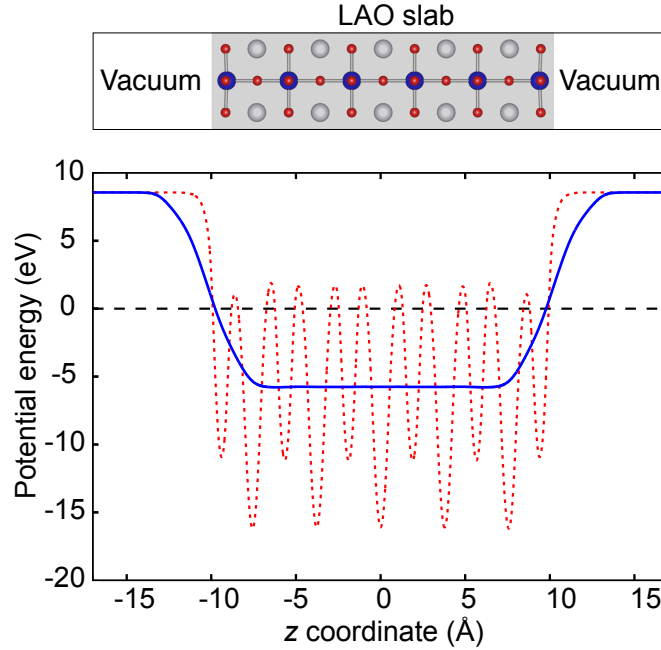


Figure 4.2: Averaged electrostatic potential energy in a supercell containing a slab of LAO with unreconstructed neutral (relaxed) AlO_2 -terminated surfaces. The dotted (red) line corresponds to the planar average of the potential energy in the xy plane; the solid (blue) line is the one-dimensional macroscopic average. The dashed (black) line indicates the average of the electrostatic potential energy taken over the entire supercell, which is arbitrarily set to zero here (a common convention in first-principles calculations). The top panel shows the geometry of the supercell, aligned to the plot of the potential energy.

where $\tilde{V}(r)$ is the electrostatic potential of the slab supercell including the CBC, $V_b(r)$ is the electrostatic potential of the CBC, and $V(r)$ is the quantity we want, namely the electrostatic potential of the charged slab supercell *without* the CBC.

In order to obtain an expression for $V_b(r)$, we make the approximation, as proposed by Komsa and Pasquarello [104], that the electrostatics of the slab supercell can be represented by a *macroscopic* dielectric profile $\varepsilon(z)$ that varies only in the z direction. Within this approximation we can easily solve for the electrostatic potential contribution

from the CBC, $V_b(z)$, using the Poisson equation:

$$\frac{d}{dz} \left(\varepsilon(z) \frac{d}{dz} V_b(z) \right) = -\rho_b = -\frac{q}{\Omega}, \quad (4.5)$$

where q is the total CBC and Ω is the volume of the supercell.

In order to define the boundary conditions in solving for $V_b(z)$ from the Poisson equation in Eq. 4.5, and also to pick a suitable reference potential for comparing systems with different amounts of charge, grounded “reference electrodes” are placed at the cell boundaries. We assume that these reference electrodes are far enough from the slab that the only contribution to the potential at that distance is from $V_b(z)$. Since the reference electrodes are grounded, this gives us the boundary conditions, $V_b(\pm L_z/2) = 0$, to solve the Poisson equation.

To further simplify the analysis, we approximate the dielectric profile to be a piecewise constant function with relative dielectric constant ε in the slab and unity in the vacuum. Since we neglect relaxations, ε is taken to be the “clamped ion” static dielectric constant (electronic part of the static dielectric constant). For LAO, we use $\varepsilon = 4.0$ (Ref. [119]). The approximation of a piecewise constant function requires defining a boundary. We choose the boundary to correspond to the atomic positions of the outermost surface layer.

Solving the Poisson equation gives

$$V_b(z) = \frac{-q}{2\varepsilon_0\Omega} \times \begin{cases} \left(z^2 - \frac{L_z^2}{4}\right), & -L_z/2 < z < -L_s/2 \\ \frac{1}{\varepsilon} \left(z^2 + \frac{L_s^2}{4}(\varepsilon - 1) - \varepsilon \frac{L_z^2}{4}\right), & -L_s/2 < z < L_s/2 \\ \left(z^2 - \frac{L_z^2}{4}\right), & L_s/2 < z < L_z/2. \end{cases} \quad (4.6)$$

Equation 4.6 is a generalization of the results for a metallic slab obtained by Lozovoi *et al.* [107] to the case of a dielectric slab; the equations for a metal slab can be recovered by taking the limit $\varepsilon \rightarrow \infty$.

Using Eq. 4.6 for V_b , we can obtain the corrected electrostatic potential $V(r)$ from the calculated uncorrected potential $\tilde{V}(r)$ using Eq. 4.4. The corrected and uncorrected electrostatic potential energies (which differ by a factor of $-e$ from the electrostatic potential), for the case of $0.25e^-$ added per areal unit cell, are plotted in Fig. 4.3 along with the potential energy due to the CBC, $-eV_b(z)$. In this figure, all the potential energies are shifted by a constant such that their value at $\pm L_z/2$ is set to zero, as required by the placement of the reference electrodes. The discontinuity in the slope of $-eV_b(z)$ at $\pm L_s/2$ is due to our choice of the dielectric profile to be piecewise constant. The corrected potential energy has some key features that illustrate the procedure involved in removing the contribution from the CBC. $-eV_b(z)$ has a smaller curvature within the slab compared to the vacuum region due to the screening present in the slab. Comparing the

profiles of the corrected and uncorrected potential energies within the slab region, we see that the correction removes the parabolic contribution that is present in the uncorrected potential energy due to the presence of the uniform CBC; the corrected potential energy is flat (corresponding to zero electric field) in the interior of the slab. Similarly, the uncorrected potential energy has a curvature in the vacuum region, again due to the presence of the uniform CBC; after correction the potential energy becomes linear in the vacuum region. This linear potential profile is equivalent to the potential drop across a parallel-plate capacitor, with the reference electrode forming one of the plates, and the sheet of excess surface charge forming the other plate. The slope of the potential (in units of $V/\text{\AA}$), which gives the field, is positive in the left vacuum region. This situation corresponds to a sheet of positive charges on the reference electrode, and a sheet of negative charges on the surface, indeed consistent with our addition of $0.25e^-$ per areal unit cell to the surface, compensated by countercharges on the reference electrodes.

It is important to check the sensitivity of the results to the specific details of the approach, namely the shape of the dielectric profile and the placement of the surface plane, $L_s/2$. As will be reported in Sec. 4.4.3, we found that the specific choices made here have only minimal effects on the final surface energies.

For completeness, we should acknowledge that Eq. 4.4, which was our starting point, involves an assumption, namely that we can define the electrostatic potential of the charged slab supercell *without* the CBC by subtracting the contributions due to the CBC $[V_b(r)]$ from the electrostatic potential obtained directly from the first-principles

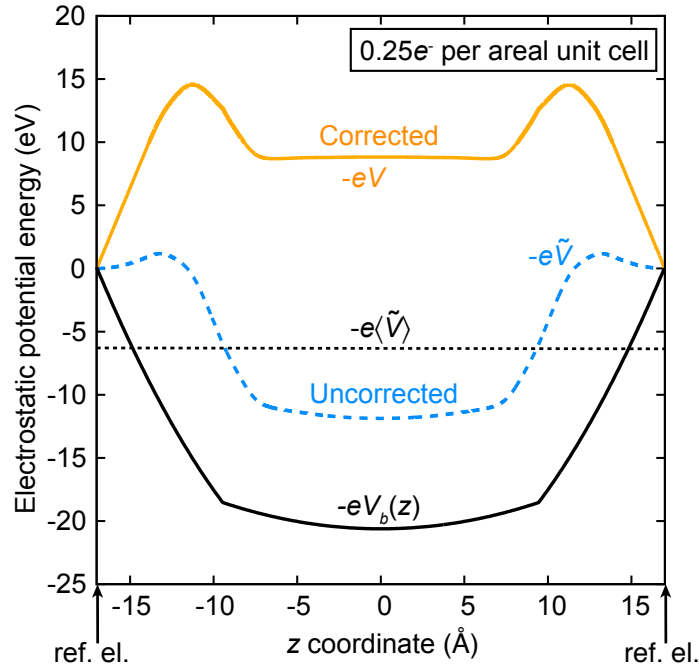


Figure 4.3: Electrostatic potential energies in a supercell containing a slab of LAO with unreconstructed AlO_2 -terminated surfaces, to which a charge of $0.25e^-$ per areal unit cell is added. The calculated uncorrected electrostatic potential energy (labelled $-e\tilde{V}$) shifted to set the value at $\pm L_z/2$ (supercell boundaries) to 0 eV, is shown by the dotted (blue) curve. The electrostatic potential energy corrected by removing contributions due to CBC (labelled $-eV$) is shown by the solid light (orange) curve, and the potential energy due to the CBC is shown as solid black curve. The average value of the uncorrected potential energy, labeled $-e\langle\tilde{V}\rangle$, is shown by the dotted horizontal line. The positions of the reference electrodes are indicated by arrows and labeled “ref. el.”.

calculation $[\tilde{V}(r)]$. In principle, the ground-state charge density obtained from first-principles calculations in the presence of the CBC, which determines the electrostatic potential, will no longer be the “ground state” for the auxiliary system in which the CBC is removed. This unavoidable approximation has been discussed in previous works [120, 121].

Once we have an expression for V_b , we can determine the energy associated with the interaction between the CBC and the slab, and also the self energy of the CBC; removing

these energy contributions from the calculated energy of the supercell (as in Ref. [107]) gives the corrected energy:

$$E_{es} = \tilde{E}_{es} - q\langle\tilde{V}\rangle + \frac{q}{2L_z} \int V_b(z)dz, \quad (4.7)$$

where $\langle\tilde{V}\rangle$ is the averaged electrostatic potential (a non-zero quantity), obtained from the first-principles calculation for the supercell, with the boundary conditions discussed above (see Fig. 4.3). $\langle\tilde{V}\rangle$, and thus the surface energy, depends on the ratio of the thickness of the slab to that of the vacuum region. This dependence is not spurious, but a reflection of the fact that the potential due to a charged surface diverges with distance from the surface. As will be demonstrated in Sec. 4.4.3, the introduction of a reference electrode allows a consistent comparison of surface energies for equally sized cells with different amounts of charge.

For the case of a piecewise constant dielectric profile, we can substitute V_b from Eq. 4.6 into Eq. 4.7 and obtain

$$E_{es} = \tilde{E}_{es} - q\langle\tilde{V}\rangle - \frac{q^2}{24L_z\varepsilon_0\Omega} \left(L_s^3 \left(1 - \frac{1}{\varepsilon}\right) - L_z^3 \right). \quad (4.8)$$

4.2.3.3 Koopmans' theorem for charged surfaces

To analyze the corrected energies, we use “Koopmans’ theorem for charged dielectric surfaces”, which is a generalization of “Koopmans’ theorem for charged metal surfaces” developed by Lozovoi *et al.* [107] For a charged dielectric surface, the theorem states that

the surface energy is given by

$$\gamma(q) = \gamma(0) + \phi\sigma + \frac{1}{\varepsilon_0} \int_0^\sigma t \left[\frac{L_z}{2} - z_c(t) \right] dt, \quad (4.9)$$

where $\gamma(0)$ is the surface energy of the neutral slab; ϕ (a positive quantity in units of volts) is the potential difference between the vacuum level and the lowest unoccupied level (for electron addition) or the highest occupied level (for electron removal), calculated for the neutral dielectric surface; q is the total charge of the CBC (in units of electronic charge); σ is the surface charge density given by $\sigma = q/2A$, where A is the surface area per unit cell; $L_z/2$ is the position of the reference electrode; and z_c is the *centroid* of the excess surface charge given by,

$$z_c(\sigma) = \frac{1}{\sigma} \int_0^{\frac{L_z}{2}} z \delta\rho(\sigma; z) dz. \quad (4.10)$$

Here $\delta\rho(\sigma; z) = \rho(\sigma; z) - \rho_0(z)$, i.e., the excess surface charge is given as the difference between the planar averaged charge density of the charged surface calculation, $\rho(\sigma; z)$, and the planar averaged charge density of the neutral surface, $\rho_0(z)$. When presenting our results for surface energies we will use the explicit definition of z_c (Eq. 4.10), but it is interesting to explore the sensitivity of the result to this value. Reassuringly, we will find in Sec. 4.4.3 that this sensitivity is low; i.e., if z_c is approximated to equal $L_s/2$ (the position of the surface layer in the neutral slab supercell), this results in only a small error in $\gamma(q)$.

The second term in Eq. 4.9 is the energy contribution of adding an electron to the lowest unoccupied state or removing it from the highest occupied state of the neutral slab with the electrodes serving as a reservoir of electrons. The third term is the energy of the electrostatic field in the parallel-plate capacitor formed between the electrode and the charge on the surface.

The term “Koopmans’ theorem” refers to the fact that the ionization energy, in the case of electron removal (or the electron affinity, in the case of electron addition) is given by the highest occupied molecular orbital (or the lowest unoccupied molecular orbital). Indeed, this is expressed by the second term of Eq. 4.9. We also note that, if we approximate z_c by $L_s/2$, all of the elements in Eq. 4.9 can be determined from a calculation for a neutral surface, justifying the name “Koopmans’ theorem for charged dielectric surfaces.” “Koopmans’ theorem for charged metal surfaces” [107] would be recovered by setting ϕ to the difference between the vacuum level and the Fermi level of the metallic surface.

4.3 Electronic structure of the bulk and surface LaAlO_3

4.3.1 Bulk

LAO has a rhombohedral perovskite structure at room temperature and transforms into a cubic phase at ~ 813 K [119]. LAO has been observed to grow coherently in the cubic phase on cubic STO [18, 122]; therefore, we focus on cubic LAO in this study

[Fig. 4.4(a)]. Since STO and LAO have a lattice mismatch of about 3%, LAO thin films grown on STO substrate might be strained. In our analysis, we neglect effects due to strain.

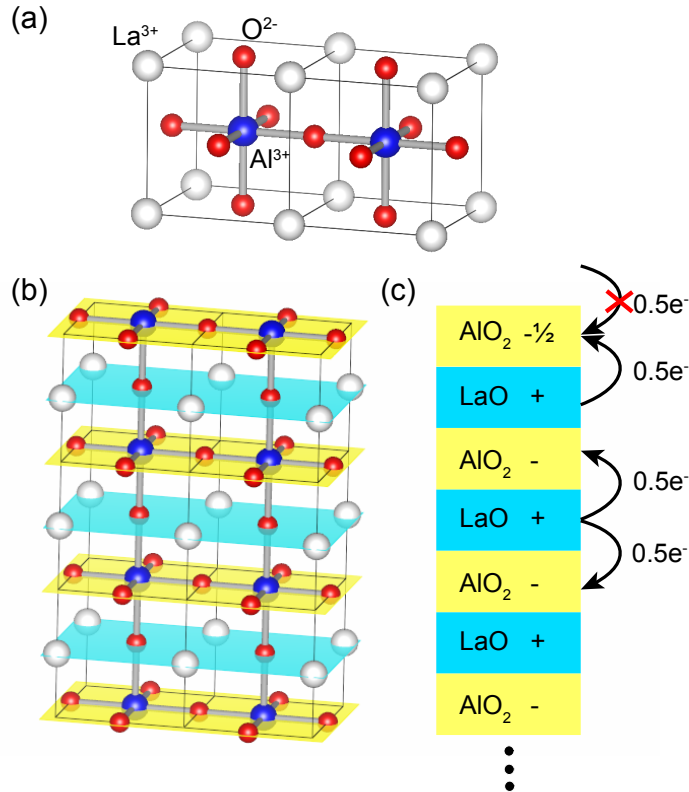


Figure 4.4: (a) Schematic of the structure of cubic LAO, showing two unit cells with the AlO_6 octahedra. (b) Alternating layers of AlO_2 and LaO in a slab, with the surface terminating in an AlO_2 plane. (c) Schematic depicting alternating charged planes and $0.5e^-$ transferred from LaO planes to the neighboring AlO_2 -planes in the bulk. The surface is shown terminated by an AlO_2 plane and lacks $0.5 e^-$.

The electronic structure of LAO bulk calculated from first-principles is shown in Fig. 4.5. The valence-band maximum (VBM) at the R -point is composed mainly of O $2p$ states and the conduction-band minimum (CBM) at the Γ -point is composed mainly of doubly degenerate e_g La $5d$ states. The direct band gap of cubic LAO at the Γ -point

is calculated to be 5.04 eV and the $R \rightarrow \Gamma$ indirect gap is 4.88 eV. Experimental data for the band gap of LAO is available only for the rhombohedral phase. Our calculated band gap for the rhombohedral phase is 5.51 eV, in good agreement with the observed value of 5.6 eV [119].

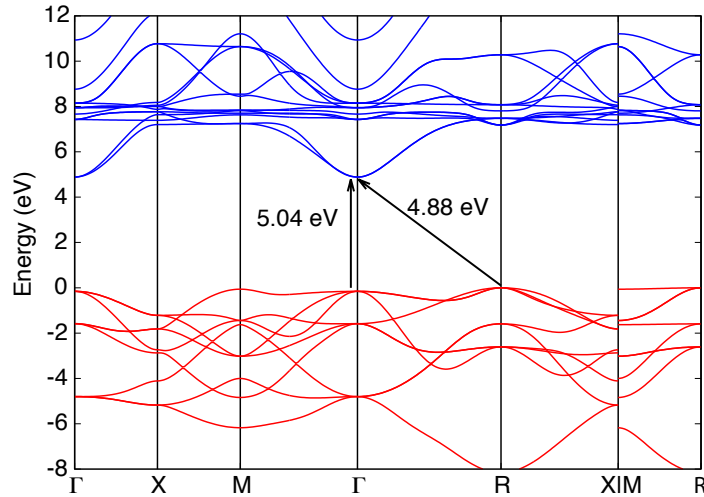


Figure 4.5: Electronic structure of bulk cubic phase LAO. The direct (5.04 eV) and indirect (4.88 eV) band gaps are indicated. The zero of energy was set to the valence-band maximum at the R -point.

4.3.2 Surface

Along the $[001]$ direction, LAO can be viewed as composed of alternating planes of LaO and AlO_2 , as shown in Fig. 4.4(b). In the ionic limit, the La and Al atoms each contribute 3 valence electrons, assuming a +3 charge, while O assumes a -2 charge. Thus, in the bulk an LaO plane ($\text{La}^{+3}\text{O}^{-2}$) has a net charge of +1 per unit cell, whereas an AlO_2 plane ($\text{Al}^{+3}\text{O}_2^{-2}$) has a charge of -1 per unit cell. Within this ionic picture, we can

think of each LaO plane donating $0.5e^-$ per areal unit cell to the AlO_2 plane above and $0.5e^-$ to the AlO_2 plane below, as shown in Fig. 4.4(c).

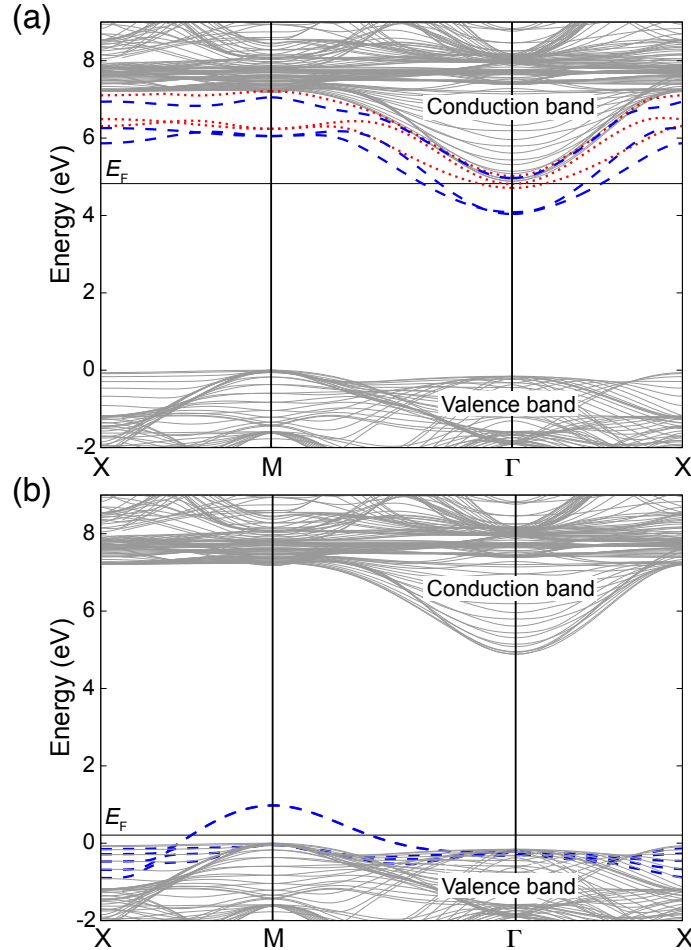


Figure 4.6: Projected band structures for unreconstructed (but relaxed) (1×1) surfaces of LAO: (a) LaO-terminated and (b) AlO_2 -terminated. Solid (gray) curves represent projected bulk states. Dashed (blue) curves indicate spin-up (majority spin) surface states and dotted (red) curves represent spin-down surface states. For the AlO_2 -terminated surface in (b), spin-up and spin-down states are degenerate. The Fermi level E_F is indicated by horizontal solid (black) lines.

At the surface, due to symmetry breaking along the $[001]$ direction, one of the two neighboring planes to an LaO or AlO_2 plane is absent, which leads to a deficit or excess of electrons at the surface. As illustrated in Fig. 4.4(c), the unreconstructed AlO_2 -

terminated surface exhibits a deficit of $0.5 e^-$ (or, equivalently, an excess of 0.5 hole) per areal unit cell due to the lack of an LaO plane above to donate the electrons. Likewise, an unreconstructed LaO-terminated surface has an excess of $0.5e^-$ per unit-cell area due to the absence of an AlO_2 -plane above to accept the electrons.

The electronic structure of the AlO_2 - and LaO-terminated surfaces reflects the physics contained in this simple ionic picture. Figure 4.6 shows the calculated surface band structure of LAO projected onto the bulk valence and conduction bands. For the unreconstructed LaO-terminated surface, the band structure shown in Fig. 4.6(a) reveals surface states of La-5*d* character near the conduction band, partially filled with an excess of $0.5 e^-$ per areal unit, as expected from the ionic picture. On the other hand, for the unreconstructed AlO_2 -termination [Fig. 4.6(b)], surface states of O-2*p* character appear near the valence band, partially filled with 0.5 hole per areal unit.

We see that these surface structures lead to energetically unfavorable situations: occupied electron states occur near the conduction band for the LaO termination, or unoccupied states near the valence band for the AlO_2 termination. Overall these surfaces are expected to be unstable toward atomic reconstructions that fill low-lying states with electrons or remove electrons from high-lying states. We studied the relative stability of atomic reconstructions in detail by calculating their surface energy for both the AlO_2 and LaO terminations for bulk LAO, assuming the surface to be charge neutral. The full set of results and conclusions from the calculations have been reported in Ref. [112]. Here we list the accomplishments and conclusions of the study.

The native atomic reconstructions that were studied are the (2×2) O-vacancy, (3×2) Al-atom, (3×2) La-atom, and (2×1) Al-and-O-atoms reconstructions on the AlO_2 termination, and the (3×2) La-vacancy and (2×2) O-atom reconstructions on the LaO termination. We also studied hydrogenated surfaces: the (2×2) La-vacancy-H-atom reconstruction on the LaO termination, and the (2×1) OH-adsorbate reconstruction on the AlO_2 termination. The key conclusions from the calculations are: (1) among the native reconstructions, the (3×2) La-vacancy reconstruction is the most stable, and (2) the presence of H stabilizes the (2×1) H-atom or the OH-adsorbate reconstructions, whose relative stability depends on the H and O chemical potential. The key insight obtained from the study is that the energy lowering obtained from surface reconstructions involving vacancies or adatoms can be explained with an electron-counting rule [123] that assumes surface states in the upper part of the gap (i.e., with predominantly conduction-band character) should be unoccupied, and states low in the gap (with predominantly valence-band character) should be filled. In the following section, we address situations in which the electrons that fill the low-lying surface states on LAO are provided from another source, namely from the 2DEG at the LAO/STO interface, leading to a charged surface.

4.4 Surface energetics of LAO in STO/LAO heterostructures

Our situation of present interest, namely a thin layer of LAO on top of an STO substrate, provides a means for supplying charge to the surface. As described in Sec. 4.3.2, LAO can be viewed as alternating planes of AlO_2 and LaO , each with a charge of -1 and $+1$ per areal unit cell, respectively. A similar ionic picture for STO yields alternating layers of $(\text{Sr}^{+2}\text{O}^{-2})$ and $(\text{Ti}^{+4}\text{O}_2^{-2})$ with each layer being neutral. At the interface between LAO and STO, if the LAO terminates with an LaO plane and STO terminates with a TiO_2 plane forming a LaO-TiO_2 interface, the $0.5e^-$ per areal unit cell given up by the LaO plane transfers to the TiO_2 layer. Indeed, the TiO_2 layer does not require the excess electrons from the LaO plane for bonding, and the large conduction-band offset at the LAO/STO interface [82] (see Fig. 4.7) ensures that the $0.5e^-$ per areal unit cell end up in the STO conduction band, giving rise to the 2DEG.

This argument is supported by our discussion of unreconstructed surfaces in Sec. 4.3.2, which provides direct insight into the electronic structure of the interface. For instance, the calculated electronic structure for the LaO -terminated surface [Fig. 4.6(a)], reveals the presence of excess electrons in surface states near the conduction band of LAO. If such a layer termination is interfaced with a nonpolar material such as STO, having a conduction band lower than that of LAO, the excess electrons end up occupying the conduction band of STO. Therefore, a 2DEG of density $\sim 3.3 \times 10^{14} \text{ cm}^{-2}$ corresponding

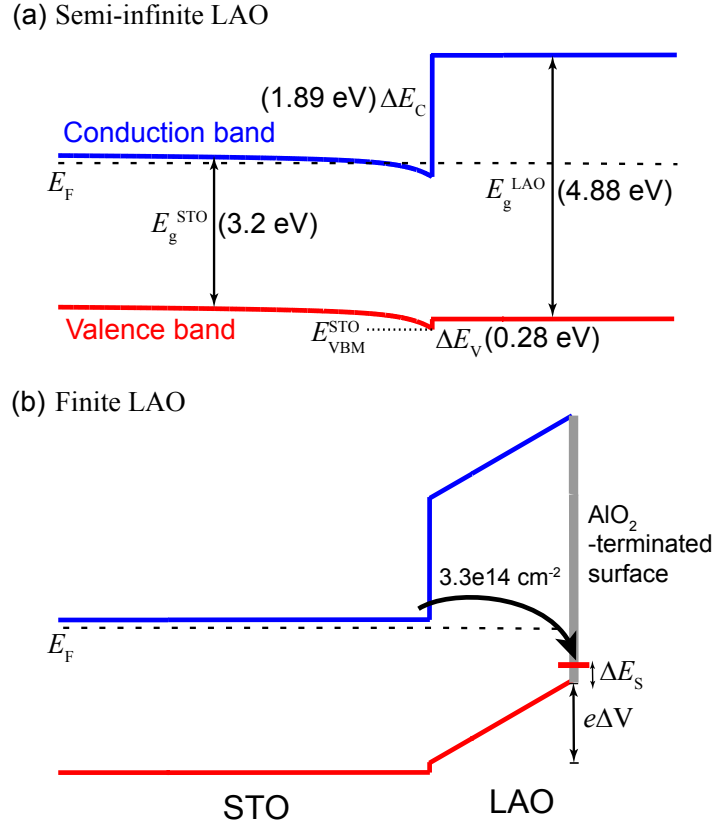


Figure 4.7: Band diagram for the interface between semi-infinite SrTiO₃ and (a) semi-infinite LaAlO₃ showing band offsets and the formation of an intrinsic two-dimensional electron gas (2DEG), and (b) LaAlO₃ with a finite thickness less than the critical thickness, terminated by an AlO₂ plane containing surface states to which electrons from the 2DEG can transfer, leading to an insulating interface. The values for the band offsets are taken from Ref. [82].

to $0.5e^-$ per areal unit cell is intrinsic to the LaO-TiO₂ interface in the LAO/STO system [21].

At the same time, if the actual surface of LAO in the LAO/STO heterostructure that is exposed to the surrounding environment terminates in an unreconstructed AlO₂ plane, the surface would have 0.5 holes per areal unit as in Fig. 4.6(b). These holes would serve as empty surface states that could be filled by electrons from the interfacial 2DEG

transferring to the surface in order to minimize the total energy of the system. We are interested in quantifying the 2DEG density remaining at the interface after the transfer, that would minimize the total energy of the system for a certain thickness of LAO.

4.4.1 Reference structure

For our zero-energy reference structure, we choose an ideal LaO-TiO₂ interface between semi-infinite LAO and semi-infinite STO, which would have an intrinsic 2DEG completely confined near the interface (since the electrons have nowhere else to go), with a density corresponding to $0.5e^-$ per 2D unit cell ($3.3 \times 10^{14} \text{ cm}^{-2}$). Charge neutrality is satisfied because the density of the electrons in the 2DEG exactly equals the density of positive charges (0.5 positive charge per La atom) on the La atoms at the interface that have given up $0.5e^-$. The Fermi level is determined by the charge-neutrality equation, and will lie above the bottom of the STO conduction band in the region where the 2DEG occurs; see the band diagram in Fig. 4.7(a).

4.4.2 Neutral surfaces of LAO

Now we investigate what happens if the STO remains semi-infinite (corresponding to a bulk substrate), but the LAO layer has a finite thickness; i.e., the LAO is terminated by a surface. Let us first consider the (hypothetical) situation in which we do not allow any charge transfer from the interface to the surface. The energy of this system would then simply correspond to the surface energy of the LAO. Using the methodology described

in Sec. 4.2.2, we have calculated the absolute surface energy values for different surface reconstructions and terminations on bulk LAO. A full account is given in Ref. [112]; here we summarize the key results and plot the calculated surface energy values for the unreconstructed as well as reconstructed surfaces for both LaO and AlO₂ terminations in Fig. 4.8.

The surface energy values in Fig. 4.8 depend on the chemical potentials of the constituent atoms, namely μ_{O} , μ_{Al} and μ_{La} , as in Eq. 4.1. These chemical potentials are representative of the chemical environment in which LAO is grown and characterized. We plot the surface energies as a function of μ_{O} , which is the variable that is most commonly controlled in experiments. The stability region of LAO [shaded regions in Fig. 4.8] is defined by these chemical potentials through Eq. 4.2, which forms one constraint. Since there are three variables in total, we have to choose one additional constraint. As discussed in Sec. 4.2.2, we examine the two limits, namely Al-rich conditions [dashed boundary lines in Fig. 4.8], given by Eq. 4.3a, and La-rich conditions [solid boundary lines in Fig. 4.8], given by Eq. 4.3b. Once a limit is chosen, the surface energy becomes dependent on μ_{O} alone.

Figure 4.8 illustrates that the surface energies of unreconstructed surfaces change linearly with μ_{O} , but that the surface energies of the reconstructed surfaces are independent of μ_{O} . The latter occurs because these particular surfaces are stoichiometric with respect to LAO, Al₂O₃, and La₂O₃. For the purposes of this work, we will choose Al-rich condi-

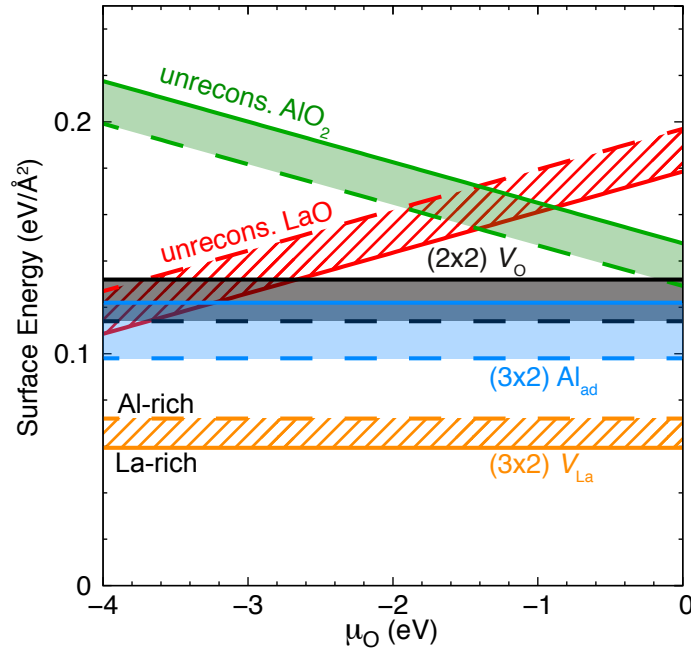


Figure 4.8: Surface energy (in $\text{eV}/\text{\AA}^2$) for (2×2) O-vacancy (V_{O}) (black), (3×2) Al-adatom (Al_{ad}) (blue), and the (3×2) La-vacancy (V_{La}) (orange) reconstructions on the LaAlO_3 surface as a function of μ_{O} . The unreconstructed AlO_2 (green) and LaO (red) terminations are also shown. The regions shaded by diagonal crosshatching indicate the range of surface-energy values for LaO -terminated surfaces, and those shaded by solid colors are for AlO_2 -terminated surfaces, under the conditions within which LaO is stable; the boundaries indicated by dashed lines correspond to Al-rich conditions and those indicated by solid lines correspond to La-rich conditions. Details of stability regions and limiting conditions are discussed in the text.

tions. A more comprehensive treatment, including a discussion of La-rich conditions, is included in Ref. [112].

The reconstructions that are found to be most stable are all consistent with the electron counting rule. For example, let us consider adding an Al adatom to the AlO_2 -terminated surface. The unreconstructed surface has 0.5 holes per areal unit cell [Sec. 4.3.2]. An Al adatom can donate 3 electrons. Therefore, an Al adatom every 6 areal unit cells will result in an insulating state by completely filling all the holes. From the calculations,

we indeed find a (3×2) Al-adatom reconstruction to be the most stable reconstruction on the AlO_2 termination, with the (2×2) O-vacancy slightly higher in energy. On the LaO termination, the (3×2) La-vacancy is the most stable reconstruction. Overall, the LaO termination with the (3×2) La-vacancy has the lowest surface energy, in the absence of impurities.

Our calculations also indicate that the presence of hydrogen alters the stability of the LaO *versus* the AlO_2 termination. Under Al-rich conditions, H binds to an O atom forming a (2×1) H-adatom reconstruction on the AlO_2 -terminated surface, whereas under La-rich conditions a (2×1) OH adsorbate reconstruction forms on the LaO-terminated surface.

4.4.3 Charged surfaces of LAO

In the previous section we considered an LAO layer of finite thickness on top of an STO substrate, and the (hypothetical) situation in which no charge transfer is allowed from the interface to the surface. Not allowing for charge transfer is unphysical, of course. For instance, as we saw in Sec. 4.3.2, the AlO_2 termination has unoccupied surface states in the lower part of the band gap, which lie well below the Fermi level (which is near the CBM of STO at the interface); based on the band alignment between STO and LAO (Fig. 4.7), we thus expect electron transfer from the interface to the surface. On the other hand, the LaO-terminated surface has no such empty states low in the gap [Fig. 4.6(a)], so no electron transfer will occur and the energy of the system with an LaO surface

will remain unchanged. LaO-terminated surfaces would therefore be preferable from the point of view of maintaining a high density of electrons at the interface; however, such surfaces seem more difficult to obtain during thin-film growth [122]. In the remainder of this section we focus on the AlO₂-terminated surface.

In order to study the effect of charging the surface, we consider adding or removing electrons from the unreconstructed (1×1) AlO₂-terminated surface. Our task will be to calculate the surface energy as a function of electrons added or removed; i.e., we wish to perform calculations on LAO slabs with (1×1) AlO₂-terminated surfaces with various amounts of charge added to the cell using the supercell approach to treat charged surfaces as described in Sec. 4.2.3. We perform calculations with the surface charge ranging from −0.5 (addition of 0.5 electrons) to +0.5 (removal of 0.5 electrons, equivalent to addition of 0.5 holes) per 1 × 1 areal unit cell. This surface charge is related to the total CBC, q , as $-q/2A$, where A is the area of a unit cell and the factor of $\frac{1}{2}$ accounts for having two identical surfaces in the supercell. Figure 4.9 shows results for the total energy for different amounts of charge added to the supercell. The uncorrected surface energy (in meV/Å²) is obtained directly from the first-principles calculation using Eq. 4.1, referenced to the corresponding neutral surface.

As discussed in Sec. 4.2.3, the total energy (and hence the surface energy) obtained from a charged supercell calculation must be corrected for the spurious interaction due to the compensating background charge. We obtain the corrected surface energy by following the steps explained in Sec. 4.2.3 leading to Eq. 4.8. The corrected energy

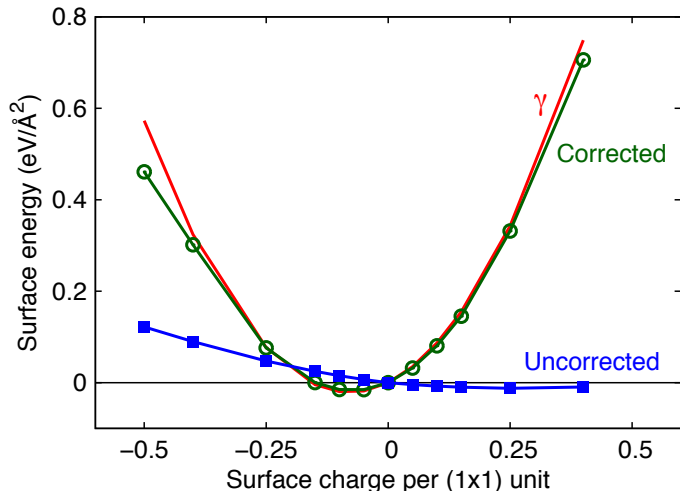


Figure 4.9: Surface energy change (in $\text{eV}/\text{\AA}^2$) with respect to the neutral surface as a function of surface charge (in units of the magnitude of electronic charge) per (1×1) unit. Negative charge indicates added electrons and positive charge corresponds to electrons removed (or holes added). Solid squares (blue) are results without correction and open circles (green) represent corrected values. The solid (red) line shows the results of Eq. 4.9, based on Koopmans’ theorem generalized for charged surfaces.

corresponds to an auxiliary system where charge compensation is provided by reference electrodes placed at the edges of the supercell, and is also plotted in Fig. 4.9.

In order to analyze and disentangle the various energy contributions, we turn to the generalized “Koopmans’ theorem for charged dielectric surfaces” discussed in Sec. 4.2.3.3. According to the theorem, the energy of a charged surface of a dielectric upon the addition/removal of charge can be obtained solely from quantities related to the neutral surface, and is given by Eq. 4.9. We plot $\gamma(q)$ along with our uncorrected and corrected surface energies obtained from explicit charged-cell calculations in Fig. 4.9.

To ensure that the approximations made in Sec. 4.2.3 are reasonable, we assess the sensitivity of the corrected surface energy values to the parameters being approximated. We performed these assessments for the case of $0.5 e^-$ per areal unit cell added, which

can be considered a “worst case.” We explored different spatial profiles for the dielectric, such as the error-function profile suggested by Komsa and Pasquarello [104], but found that introducing a smearing of 1 Å results in a change of less than 15 meV/Å² in the corrected surface energy (which is small compared to the magnitude of this energy, see Fig. 4.9). A 0.5 Å change in the position of the surface plane, $L_s/2$, also changed the results by less than 15 meV/Å². With regard to Eq. 4.9, we examined the case where z_c is assumed to be independent of the charge added. Taking $z_c = L_s/2$ resulted in an error of only 20 meV/Å² in the surface energy $\gamma(q)$.

The approximate expression for $\gamma(q)$ (Eq. 4.9) is remarkably very close to the results from our full first-principles calculations. We can therefore conclude that all of the changes in the surface energy due to charge addition are *extrinsic*, by which we mean that they result purely from the transfer of electrons between a reservoir of electrons (represented by the electrodes) and the surface. This *extrinsic* energy change can be separated into (1) the energy gained or lost due to the transfer of electrons between the reservoir at the vacuum level and the highest occupied/lowest unoccupied level on the surface (second term in Eq. 4.9), and (2) an electrostatic contribution, which is equal to the energy required to charge a parallel-plate capacitor of separation equal to the vacuum thickness (third term in Eq. 4.9).

Any deviation between the full, corrected result and the result based on Koopmans’ theorem must be attributed to *intrinsic* contributions, i.e., due to changes in the electronic structure of the surface upon charge addition. Our results indicate that these

contributions are quite small, amounting to changes in the surface energy by less than 10 meV/Å² for amounts of added charge up to a magnitude of about $0.4e^-$ per areal unit cell. This is small compared to the absolute value of the neutral AlO₂-terminated surface energy, which is about 130 meV/Å² (under Al-rich conditions at $\mu_O = 0$ eV; see Fig. 4.8). Larger deviations in the surface energy occur for charge addition exceeding $0.4e^-$ per areal unit cell. We attribute this to electrons spilling out into the vacuum, which occurs due to the lowering of the potential in vacuum for such large CBC densities. This is actually an artifact of our first-principles calculations due to the presence of CBC in the vacuum region, and does *not* indicate that Koopmans' theorem (Eq. 4.9) is less accurate.

4.4.4 Energetics of LAO/STO with surface charging

We can now apply the general formalism for the surface-energy correction to the case of a thin layer of LAO on STO. We start from our zero-energy reference structure [Sec. 4.4.1], which is the interface between semi-infinite LAO and semi-infinite STO, at which an intrinsic 2DEG with a density of $0.5e^-$ per 2D unit cell area (3.3×10^{14} cm⁻²) is present [Fig. 4.7(a)].

When the thickness of LAO is finite, an energy cost needs to be paid associated with the creation of a surface. In the case of a neutral AlO₂-terminated surface, and given our definition of the reference structure, this cost is simply equal to the surface energy for an unreconstructed AlO₂-terminated surface, $\gamma_{\text{AlO}_2}(\mu_O)$, which is shown in Fig. 4.8. But it is clear from Fig. 4.7 that the energy can be lowered by transferring electrons

from the 2DEG to unoccupied surface states on the surface, which in the case of the AlO₂-terminated surface occur in the lower part of the band gap. This energy gain can be obtained from the approach discussed for LAO slabs in Sec. 4.4.3: the surface-energy change is given by the energy related to the transfer of electrons from the electrode to the LAO surface. Within that formalism, the electrode acts as a reservoir for electrons, and its potential was set to zero. In a realistic LAO-STO system, which we are discussing now, the intrinsic 2DEG at the interface acts as the electron reservoir.

As charge is transferred between the 2DEG and the surface, a field builds up across the LAO layer, as shown in Fig. 4.7(b). This is the same type of field that was present in the vacuum, within the methodology for an isolated LAO slab discussed in Sec. 4.4.3. This field contributes to the parallel-plate capacitor energy accounted for by the third term in Eq. 4.9. If we assume z_c to be constant (as discussed at the end of Sec. 4.2.3.3), then $(L_z/2 - z_c)$ is equivalent to the thickness d of the LAO layer. Equation 4.9 can then be rewritten for the specific case of LAO/STO, where the field is present across the LAO film, as

$$\begin{aligned} \gamma_{\text{AlO}_2}^{\text{LAO/STO}}(\mu_{\text{O}}) &= \gamma_{\text{AlO}_2}(\mu_{\text{O}}) - \\ &\frac{\sigma_t}{e} [(E_{\text{F}} - E_{\text{VBM}}^{\text{STO}}) - \Delta E_v - \Delta E_s] + \frac{1}{2} \frac{\sigma_t^2 d}{\varepsilon} \\ &= \gamma_{\text{AlO}_2}(\mu_{\text{O}}) - \sigma_t \Delta V + \frac{1}{2} \frac{\sigma_t^2 d}{\varepsilon} \end{aligned} \quad (4.11)$$

where $\gamma_{\text{AlO}_2}(\mu_{\text{O}})$ is the surface energy of the neutral AlO₂-terminated surface [which depends on μ_{O} , see Sec. 4.2.2], σ_t is the charge density transferred from the interface to the

surface, d is the LAO film thickness, and E_F , $E_{\text{VBM}}^{\text{STO}}$, ΔE_v , and ΔE_s are defined in Fig. 4.7. In the third line, we have combined these terms as $\Delta V = [(E_F - E_{\text{VBM}}^{\text{STO}}) - \Delta E_v - \Delta E_s] / e$, which is the potential change when an electron is transferred from the 2DEG to the surface states, analogous to the quantity ϕ in Eq. 4.9.

Comparing this expression to that developed by Bristowe *et al.* (Eq. 16 in Ref. [88]), we see that we have a very similar expression, but with opposite signs on the terms. The difference in the signs is due to the choice of the zero-energy reference structure, which in Ref. [88] is taken to be the LAO/STO structure with an insulating interface and a field in LAO. The energy that they derive is for electron-hole pairs being created and separated by the field to form the 2DEG and charge the surface. We, on the other hand, take the 2DEG as intrinsic to the interface between semi-infinite LAO and semi-infinite STO, which is our zero-energy reference structure [Sec. 4.4.1]. We feel our choice more accurately reflects the physics, and clearly identifies the origin of the electrons in the 2DEG.

Equation 4.11 shows that the surface energy depends on d and σ_t . Since there is an equal density of electrons in the interfacial 2DEG and excess holes on the AlO_2 -terminated surface, there will be full transfer of electrons from the interface to the surface if the thicknesses d is small enough. The upper limit on this “small enough” thickness will be set by the situation where the surface states are raised high enough in energy to coincide with the Fermi level. This raising of the surface states occurs because of the presence of an electric field in the LAO layer. The field arises from the electron transfer, which

leaves both the interface and the surface with a net charge, and can be calculated from Gauss' law: $E = \sigma_t / \varepsilon \varepsilon_0$. For the case $\sigma_t / e = 3.3 \times 10^{14} \text{ cm}^{-2}$, using $\varepsilon = 25$ (Ref. [124]), this leads to a field $E = 2.4 \times 10^7 \text{ V/cm}$. The critical thickness is reached when the potential difference over the LAO layer, given by $E \cdot d$, becomes equal to ΔV (calculated to be 3.1 V), the difference between the Fermi level at the LAO/STO interface for the case of semi-infinite LAO (including band bending in STO due to the 2DEG), and the surface-state level E_s on the LAO surface; at that point the surface states are raised to the level of the Fermi level. This determines the maximum potential difference, because for larger values of d the electric field will be reduced by the transfer of electrons from the surface back to the interface. For a field $E = 2.4 \times 10^7 \text{ V/cm}$ and with $\Delta V = 3.1 \text{ V}$, the critical thickness is 1.3 nm (~ 3.5 unit cells), in agreement with the experimental value of 4 unit cells.

In general, for any given thickness d , the total charge transferred to the surface depends on ΔV as discussed above. Defining σ_{int} to be the intrinsic 2DEG density corresponding to $0.5e^-$ per areal unit, we can write σ_t as a function of d :

$$\sigma_t = \begin{cases} \frac{\Delta V \varepsilon}{d}, & \Delta V \leq \frac{\sigma_{\text{int}} d}{\varepsilon} \\ \sigma_{\text{int}}, & \Delta V \geq \frac{\sigma_{\text{int}} d}{\varepsilon} \end{cases} \quad (4.12)$$

In Eq. 4.12, as the thickness of LAO becomes large ($d \rightarrow \infty$), the density of 2DEG electrons transferred to the surface becomes small ($\sigma_t \rightarrow 0$) with a $1/d$ dependence

because the cost of transferring electrons to the surface becomes forbiddingly large. As a result, the 2DEG is restored back to the interface for very thick LAO.

4.5 Surface stability and its effect on 2DEG density

4.5.1 Unreconstructed AlO_2 -termination

The discussion in Sec. 4.4.4 shows that, for small thicknesses of LAO, the system with an unreconstructed but charged AlO_2 -terminated surface can significantly reduce its energy with respect to the neutral surface. In the present section we will address that energy lowering quantitatively, and also investigate whether the energy of the charged unreconstructed surface would become lower than the energy of reconstructed surfaces. The (corrected) surface energy for a 2-unit-cell thick LAO layer with an AlO_2 -terminated surface is plotted in Fig. 4.10; the energy gained by charging the surface lowers the surface energy by $85 \text{ meV}/\text{\AA}^2$. We see that under O-rich conditions ($\mu_{\text{O}} \geq -1 \text{ eV}$) this charged surface is lower in energy than all of the reconstructed surfaces considered.

4.5.2 Energetics due to surface defects and reconstructions

In Sec. 4.4, we considered the unreconstructed AlO_2 -terminated surface, and showed that charging the surface can significantly lower its energy, for small thicknesses of LAO films. The resulting energies need to be compared with those of the reconstructed surfaces; as discussed in Sec. 4.4.2, reconstructions on neutral surfaces can also significantly

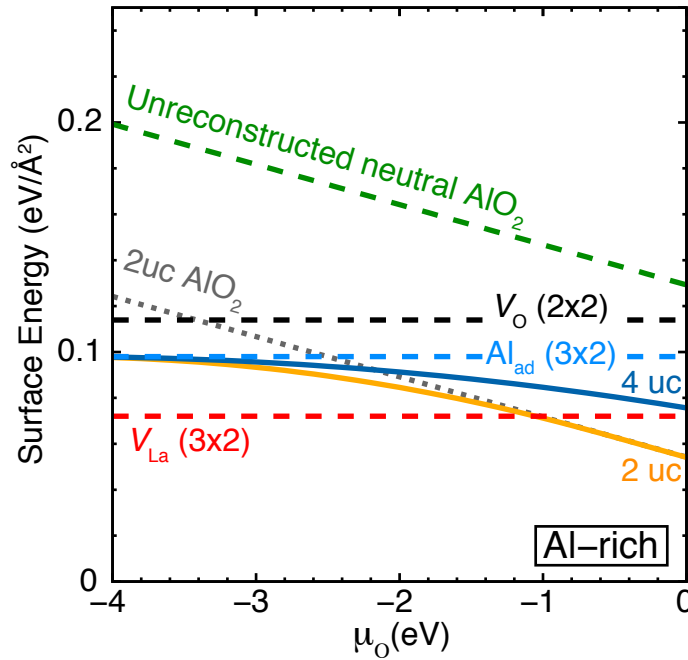


Figure 4.10: Surface energy (in $\text{eV}/\text{\AA}^2$) for AlO_2 -terminated thin films of LAO as a function of μ_{O} under Al-rich conditions (see Eq. 4.3a). Results for an LaO-terminated surface with a (3×2) La-vacancy reconstruction are included for comparison. The dotted (gray) line labeled “2uc AlO_2 ” is the corrected surface energy after electron transfer to the unreconstructed AlO_2 -terminated surface for a 2-unit-cell LAO film. Solid lines refer to the minimized surface energy under a combination of electron transfer and an Al-adatom surface density of $C_{\text{Al}_{\text{ad}}}$ at each μ_{O} corresponding to a 2-unit-cell LAO film [light (orange) line] and a 4-unit-cell film [dark (blue) line]. The dashed lines refer to surface energies of (3×2) La-vacancy [$V_{\text{La}}(3 \times 2)$] (red), (2×2) O-vacancy [$V_{\text{O}}(2 \times 2)$] (black), and (3×2) Al-adatom [$\text{Al}_{\text{ad}}(3 \times 2)$] (blue) reconstructions, and the unreconstructed (but relaxed) AlO_2 -terminated surface (green).

reduce the surface energy [112]. For the AlO_2 -terminated surface, the energetically favorable reconstructions are the ones that fill the holes in surface states in the lower part of the band gap. For instance, Al adatoms act as donors, supplying 3 electrons per adatom; electron counting then indicates that a reconstruction consisting of one Al adatom in a 3×2 unit cell will exactly fill all the holes on the AlO_2 -terminated surface.

The result for a fully reconstructed $\text{Al}_{\text{ad}} 3 \times 2$ surface is included in Fig. 4.10. We observe that for μ_O values above -2.4 eV the energy of the charged surface (in the 2-uc case) is lower than that of the reconstructed $\text{Al}_{\text{ad}} 3 \times 2$ surface. However, in order to obtain a complete picture, we need to allow for the possibility that the filling of low-energy unoccupied surface states could result from a mixture of electron transfer and atomic reconstructions. Each Al adatom can compensate three holes on the surface. Energy is gained by filling the low-lying surface states, but there is a cost associated with the formation of the adatom “defects”. (We use the term “surface defects” here not to imply that we performed explicit calculations of surface point defects, but to refer to a uniformly spaced 2D array of a specific defect with a given concentration on the surface.) The process of forming a surface defect competes with the transfer of electrons from the 2DEG at the interface, which also has a cost, reflected in the third term of Eq. 4.11 (essentially the energy of a capacitor).

Let us assume we have donor defects of type i with a surface defect density C_i , which each contribute q_i electrons to the AlO_2 -terminated surface states. The sheet charge density of electrons transferred from the 2DEG to the surface, σ'_t , is now reduced because a fraction of the surface holes are compensated by the donor defects, leading to a modified version of Eq. 4.11:

$$\begin{aligned} \gamma_{\text{AlO}_2}^{\text{LAO/STO}}(\mu_O) = & \gamma_{\text{AlO}_2}(\mu_O) - \sigma'_t \Delta V + \frac{1}{2} \frac{(\sigma'_t)^2 d}{\epsilon} \\ & + \sum_i \frac{C_i}{C_{\text{max}}} \Delta \gamma_i. \end{aligned} \quad (4.13)$$

σ'_t is given by

$$\sigma'_t = \begin{cases} \frac{\Delta V \varepsilon}{d}, & \Delta V \leq \frac{(\sigma_{\text{int}} - \sum_i C_i q_i) d}{\varepsilon} \\ \sigma_{\text{int}} - \sum_i C_i q_i, & \Delta V \geq \frac{(\sigma_{\text{int}} - \sum_i C_i q_i) d}{\varepsilon} \end{cases} \quad (4.14)$$

C_{max} is the defect density on the surface that would correspond to a completely reconstructed surface (i.e., completely filling the hole states) formed by the defect species; for instance, for Al adatom defects this corresponds to one Al adatom every six surface unit cells. $\Delta\gamma_i$ is the energy difference per areal unit between the completely reconstructed surface and the unreconstructed surface. Since energy is gained by forming the defect, $\Delta\gamma_i$ is a negative quantity. In our model, we approximate the surface energy in the presence of defects by a linear interpolation between the unreconstructed surface and the completely reconstructed surface formed by the defect. This allows us to obtain $\Delta\gamma_i$ from the calculated surface energies for a fully reconstructed surface (denoted γ_i) compared to that of the unreconstructed surface:

$$\Delta\gamma_i = [\gamma_i(\mu_O) - \gamma_{\text{AlO}_2}(\mu_O)]. \quad (4.15)$$

Given a specific defect, and a thickness of LAO, our task will be to find the density of surface defects, and the 2DEG density remaining at the surface, that minimizes the energy of the system given by $\gamma_{\text{AlO}_2}^{\text{LAO/STO}}(\mu_O)$ in Eq. 4.13. The constraint we impose for this minimization is the requirement that there are no empty states present on the surface

in the lower part of band gap; i.e., all the holes on the surface are completely filled either by electrons transferred from the 2DEG or by electrons donated by surface defects.

4.5.3 Effect of surface defects and reconstructions on the 2DEG density

We now investigate the effect of surface reconstructions and defects on thin LAO films and the 2DEG density at the interface. As discussed earlier, the formation of these defects cause a reduction in the available surface states because of their donor nature. Due to this, there will now be fewer electrons, σ'_t transferring to the surface from the interface, in comparison to the case where there are no such surface defects, for a given thickness d . The effect of these surface defects will be to alter the 2DEG density at the interface from the intrinsic density value, σ_{int} . Therefore, the resulting 2DEG density at the interface is given by $(\sigma_{\text{int}} - \sigma'_t)$. For a specific surface defect, our task will be to determine σ'_t , for a given thickness d , which minimizes the energy of the LAO/STO system (compared to our zero-energy reference system) given in Eq. 4.13. As a consequence, we also determine the density of surface defects, C_i that also simultaneously minimizes the energy in Eq. 4.13 for a given d .

Oxygen vacancies as surface defects have been extensively discussed in the literature (Ref. [88] and references therein). Our own calculations indicate, however, that Al adatoms (Al_{ad}) in a 3×2 configuration are more stable for all experimental growth conditions than O-vacancies (V_{O}) in a 2×2 configuration [112] [Fig. 4.8]. In addition, it may be

necessary to consider adsorption of impurities. In particular, hydrogen is present in most growth and annealing environments. We therefore also consider the effect of H adatoms on the 2DEG density. Indeed, from our previous calculations [112] we found that H adatoms (H_{ad}) serve as donors on the AlO_2 -termination by completely filling the holes on the surface and forming a (2×1) surface reconstruction. In the following analysis, we focus on these specific surface defects, namely Al_{ad} , V_{O} and H_{ad} , and study their effect on the surface energies of the AlO_2 -terminated surface and the resulting 2DEG densities at the interface.

The number of electrons donated by a specific defect is obtained from the charge state of the defect. An Al_{ad} donates $3e^-$. Therefore, for any given surface density of Al_{ad} , $C_{\text{Al}_{\text{ad}}}$, the sheet density of empty states on the surface, which can take up electrons, can be determined. In practice, to determine $C_{\text{Al}_{\text{ad}}}$ that minimizes the energy of the LAO/STO structure, we calculate the energy in Eq. 4.13 at different values for $C_{\text{Al}_{\text{ad}}}$, for a given thickness and fixed chemical potentials (for example $\mu_{\text{O}} = 0$ eV) with the constraint that the holes in surface states are completely filled either by electrons donated by surface defects or by electrons transferred from the 2DEG or a combination of both. The minimum of the surface energies computed determines $C_{\text{Al}_{\text{ad}}}$, as well as the resulting 2DEG density at the interface ($\sigma_{\text{int}} - \sigma'_t$), for a given d and chemical potential. The minimized values for the surface energy in the presence of Al-adatom defects for 2- and 4-unit-cell thick LAO are plotted as a function μ_{O} in Fig. 4.10. We see that for these thicknesses, it is more favorable to transfer electrons to the surface under O-rich

conditions. As we move towards O-poor conditions, $C_{\text{Al}_{\text{ad}}}$ increases, tending towards the value corresponding to the (3×2) reconstruction under extremely O-poor conditions.

The resulting 2DEG density is plotted as a function of thickness d for two oxygen chemical-potential values, $\mu_{\text{O}} = 0$ eV (O-rich conditions) [Fig. 4.11(a)] and $\mu_{\text{O}} = -2$ eV (O-poor conditions) [Fig. 4.11(b)]. Due to the constraint imposed on the surface to be insulating, as holes in LAO surface states are energetically unfavorable, the density of Al adatoms on the surface, $C_{\text{Al}_{\text{ad}}}$, exhibits the same trend with thickness as does the 2DEG density at the interface. A treatment for V_{O} leads to similar trends in the 2DEG density with thickness, as plotted in Fig. 4.11. Each V_{O} donates $2e^-$. For both Al_{ad} and V_{O} the critical thickness and the 2DEG density strongly depend on the oxygen chemical potential μ_{O} , with O-rich conditions favoring a higher 2DEG density.

Results for H_{ad} , which donates $1e^-$, are also included in Fig. 4.11. Since the energy of surfaces with H_{ad} depends on the hydrogen chemical potential μ_{H} , in addition to its dependence on oxygen chemical potential μ_{O} , we present results for two cases: $\mu_{\text{H}} = -1$ eV (H-rich), and $\mu_{\text{H}} = -2$ eV (H-poor). The critical thickness and the 2DEG density are strongly altered by the hydrogen chemical potential, with H-rich conditions giving a higher 2DEG density. We note, however, that the 2DEG density for H_{ad} is independent of μ_{O} . This is because the AlO_2 -terminated surface with H adatoms has the same stoichiometry as an unreconstructed AlO_2 -terminated surface, which leads to an identical dependence on μ_{O} for $\gamma_{\text{H}_{\text{ad}}}(\mu_{\text{O}})$ and $\gamma_{\text{AlO}_2}(\mu_{\text{O}})$. Therefore, the energy gain in Eq. 4.15 becomes independent of μ_{O} . The 2DEG density in the absence of surface

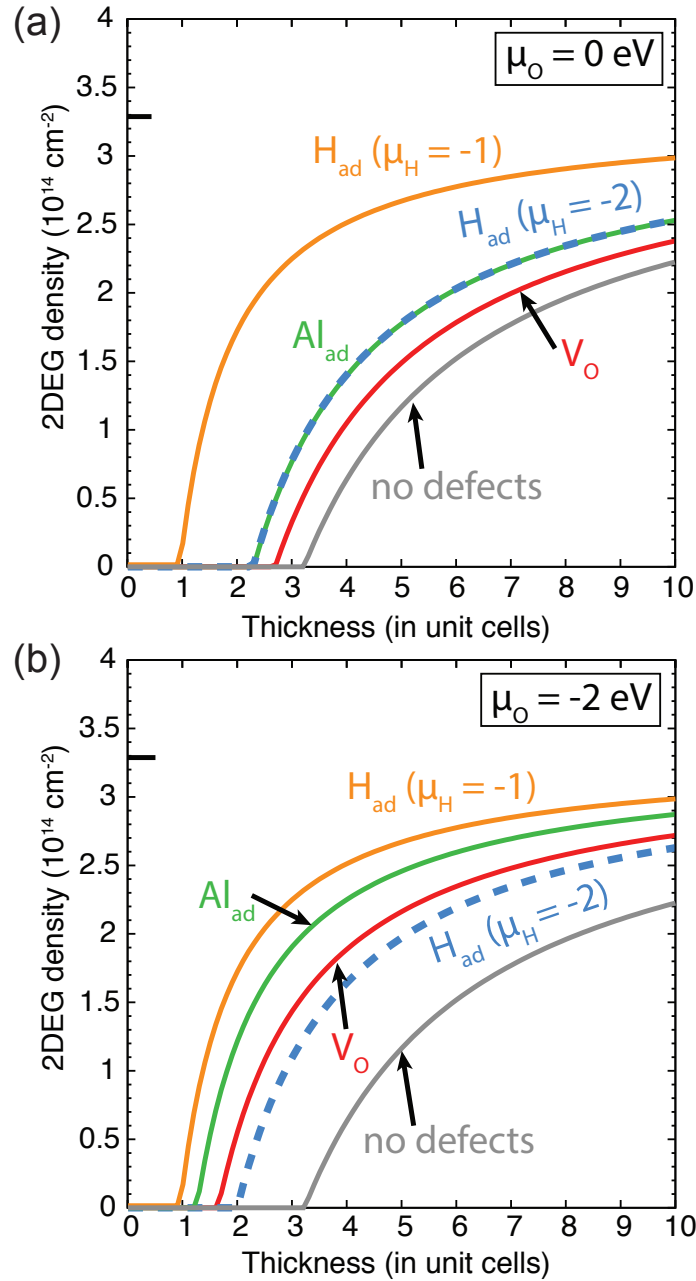


Figure 4.11: 2DEG density (in units of 10^{14} cm^{-2}) under Al-rich conditions as a function of LAO thickness for different surface defects, namely, Al-atom (Al_{ad}) (green), O-vacancy (V_O) (red), and H-atom (H_{ad}) for $\mu_H = -1 \text{ eV}$ (solid orange) and for $\mu_H = -2 \text{ eV}$ (dotted blue) at (a) $\mu_O = 0 \text{ eV}$, and (b) $\mu_O = -2 \text{ eV}$. For comparison, the 2DEG density in the absence of surface defects is plotted in gray (labeled “no defects”). The maximum 2DEG density corresponding to $3.3 \times 10^{14} \text{ cm}^{-2}$ is indicated by the black horizontal bar.

defects is also plotted in Fig. 4.11 for comparison. It can be seen that the presence of surface defects increases the 2DEG density and alters the critical thickness required to form the 2DEG. These trends are consistent with experimental observations by Xie *et al.* [94, 96, 97] They observed that increasing the exposure of the surface to adsorbates modulates the 2DEG density, and for certain cases even switches the interface from an insulating to a conductive state. This is due to the strong influence of the exposure conditions on the adsorbate density on LAO.

Our calculated values for the 2DEG densities and for the critical thickness are in qualitative agreement with the majority of experimental reports [9, 92, 93, 94, 95, 96, 97, 98, 125]; however, quantitative agreement is still lacking. One reason for the discrepancies might be the sensitivity of the results to the value of the dielectric constant. We used $\varepsilon = 25$ (Ref. [124]), but ε is known to be dependent on strain and electric field, as noted by Chen *et al.* [102] Values ranging from 21 to 46 have been used in the literature [87, 88, 102], recognizing that the critical thickness and the 2DEG density are sensitive to ε . We also note that there is a lack of agreement between different experimental methods of measuring the 2DEG density; specifically, transport and optical measurements give different results [10]. The experimentally reported 2DEG densities obtained for different samples vary by an order of magnitude. Our aim in the present work was to comprehensively address the effects of the LAO surface on the 2DEG density. We are confident that the trends obtained from our analysis are correct and informative. However, the actual 2DEG density probed by experiments can be affected by a number of other mechanisms,

such as carrier localization, defect-related trapping centers, and stoichiometry. These effects are beyond the scope of the present work, but could be readily incorporated into the general model we have developed. Specifically, our model can be extended to various surface processes that might occur on the LAO surface, and can be used to explore heterostructures other than LAO/STO.

4.6 Conclusions

In this chapter, we have developed and outlined a general methodology for addressing the commonly occurring problem in surface science where there is an exchange of charge between the surface and a source/sink of charge within the system. This includes semiconductor surfaces, where exchange of charge between an interface or dopants/defects near the surface (reservoir) and surface states gives rise to band bending. Instead of performing first-principles calculations on the complete system (including the surface as well as the reservoir), which is often computationally prohibitive, our approach allows us to treat the surface in isolation and simultaneously take the charge exchange into account by way of charged surface calculations, thereby greatly reducing the computational cost involved. In order to assess the surface energetics for such charged surfaces we developed a methodology for charged dielectric surfaces.

Equipped with this methodology, we have addressed LAO/STO heterostructures and established a consistent model that describes the 2DEG formation as well as charge transfer and interactions between the 2DEG and the LAO surface. Quantitative results

were obtained using first-principles calculations based on hybrid density functional theory. A 2DEG of density $3.3 \times 10^{14} \text{ cm}^{-2}$ is intrinsic to the LaO-TiO₂-type interface. However, in the presence of an LAO surface, the electrons from the 2DEG may transfer to surface states leaving the interface insulating or with a smaller 2DEG density. In particular, an AlO₂-terminated surface exhibits empty states near the valence band that can be filled by the 2DEG electrons. Indeed, we find that filling these surface states stabilizes the AlO₂-termination significantly, and provides an explanation for the observed insulating behavior of samples below a certain critical thickness [7, 8, 9].

We also allowed for the presence of defects on the surface. Using first-principles values for surface energies, we then obtained the 2DEG density as a function of thickness of the LAO layer. We find that the critical thickness required to form the 2DEG is sensitive to the oxygen chemical potential (as well as the hydrogen chemical potential, in case of hydrogen being present in the environment), and that increasing the surface defect density reduces the critical thickness.

Chapter 5

Surface study of a Mott insulator:

GdTiO₃

5.1 Introduction

GdTiO₃ (GTO) is a $3d^1$ ferromagnetic Mott insulator, whose band gap is a result of strong intra-atomic electron-electron interaction that splits one of the Ti $3d$ orbitals into a completely occupied spin-up channel known as the lower Hubbard band (LHB), and an unoccupied spin-down channel known as the upper Hubbard band (UHB) [82, 126]. It is a distorted perovskite with an orthorhombic crystal structure ($Pnmb$ space group) [see Fig. 5.1]. The Ti atoms in GTO have a 3+ charge. In the ionic picture, it can be viewed as alternating planes of $(\text{Ti}^{3+}\text{O}_2^{-2})_2$ layers with a net charge of -2 per 1×1 areal unit (a 1×1 areal unit of GTO has 2 formula units of TiO_2) and $(\text{Gd}^{+3}\text{O}^{-2})_2$ layers with

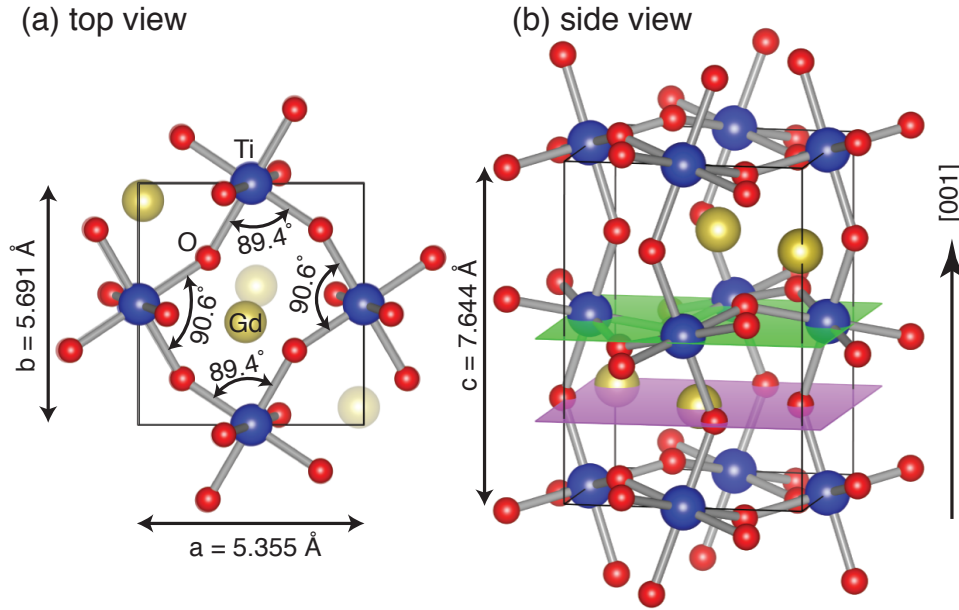


Figure 5.1: (a) Top view of the (001) plane of the 20-atom distorted perovskite structure of GdTiO_3 indicating the lattice parameters and O-Ti-O bond angles, and (b) side view depicting its polar nature with alternating TiO_2 and GdO planes along the [001] direction.

a net charge of $+2$ per 1×1 areal unit (i.e., per 1×1 unit that has 2 formula units of GdO) along the [001] direction as shown in Fig. 5.1(b). Owing to charge neutrality and its polar nature along [001], the symmetry of such stacking in its bulk form leads to each of the GdO (*donor-like*) planes donating $1e^-$ per 1×1 areal unit, corresponding to an electron density of $3.3 \times 10^{14} \text{ cm}^{-2}$, to the two neighboring TiO_2 (*acceptor-like*) planes on either side.

However, this symmetry gets broken at a nonpolar/polar heterointerface or at a surface, which creates an imbalance in the number of *donor-like* and *acceptor-like* planes. This is the mechanism behind the formation of a high-density two-dimensional electron gas (2DEG) on the order of 10^{14} cm^{-2} in the $\text{GTO}/\text{SrTiO}_3(\text{STO})$ and $\text{LaAlO}_3(\text{LAO})/\text{STO}$

interface systems, where STO is the nonpolar material perpendicular to the interface [12, 21]. Here the interface terminates in a GdO plane that donates $3.3 \times 10^{14} \text{ cm}^{-2}$ electrons to the conduction band of STO; the conduction-band offset serves to confine the electrons within STO. Similarly, at the TiO_2 surface termination one of the neighboring GdO planes is missing, and hence results in a lack of an equal density ($3.3 \times 10^{14} \text{ cm}^{-2}$) of electrons (or equivalently, presence of holes).

According to the Tasker concept [127], such surfaces with a perpendicular dipole moment are classified as Type III, and are predicted to be unstable due to a diverging electrostatic field, commonly referred to as the “polar catastrophe”. Based on this concept, the polar surfaces are expected to undergo significant atomic relaxations and changes in surface stoichiometry to overcome the instability.

Here, we discuss our study on the stability of (001) polar terminations in GTO, namely GdO and TiO_2 terminations, based on their absolute surface energies and electronic structures calculated using first-principles methods. We indeed find a lack (excess) of $1e^-$ per 1×1 areal unit cell for the TiO_2 (GdO) termination, consistent with the ionic picture. However, contrary to Tasker’s argument, we find the polar TiO_2 termination to be quite stable with a remarkably low absolute surface energy of $71 \text{ meV}/\text{\AA}^2$ under Ti-rich conditions. We also explore the effect of H adatoms on the surface energetics of the TiO_2 termination. An important goal of our investigations is to address the extent of electron transfer from the high-density 2DEG at the GTO/STO heterointerface to the

surface in the case of thin GTO films, and to compare the behavior of this system with that of the LAO/STO system.

5.2 Computational methodology

Our calculations of the bulk and surface properties rely on density functional theory utilizing the HSE06 hybrid functional [55] with the default mixing parameter of 25%, and screening parameter of 0.2 \AA^{-1} . This functional has been empirically shown to yield accurate band structures for most oxides [52, 53, 55, 82], and has recently been able to reproduce the band gap of GTO accurately [128, 129]. The calculations were performed using the Vienna *ab initio* Simulation Package (VASP) [58] with projector augmented waves [56], and a plane-wave cutoff of 500 eV. The polar (001) surfaces are studied using a slab geometry with two identical surfaces separated by vacuum. Based on convergence tests for the slab thickness and vacuum thickness, we determined a slab with 13 layers (thickness $\sim 23 \text{ \AA}$) separated by $\sim 23 \text{ \AA}$ of vacuum to be sufficiently large. In the surface calculations, we relax the first 4 layers (2 TiO₂ and 2 GdO layers) closest to each of the surfaces, and keep the remaining 5 bulk-like layers fixed. The relaxations were performed until forces on all the atoms relaxed (near-surface atoms) were less than 0.05 eV/\AA . For Brillouin zone (BZ) integrations, we use a Monkhorst-Pack mesh of $4 \times 4 \times 2$ for the bulk calculations, and $4 \times 4 \times 1$ for the surfaces. All these choices were made to ensure that the calculated surface energies were converged to within 1 meV/\AA^2 .

The calculation of surface energies follows the same methodology applied to the neutral surfaces of LAO in Sec. 4.2.2. The absolute surface energy for a given surface structure is computed based on the total energy of the slab supercell $E_{\text{slab}}(n_{\text{GTO}})$, and the total energy of the bulk supercell having the same number of GTO unit cells $E_{\text{bulk}}(n_{\text{GTO}})$ as:

$$\gamma_{\text{surface}} = \frac{1}{2} [E_{\text{slab}}(n_{\text{GTO}}) - E_{\text{bulk}}(n_{\text{GTO}}) - n_{\text{Gd}}\mu_{\text{Gd}} - n_{\text{Ti}}\mu_{\text{Ti}} - n_{\text{O}}\mu_{\text{O}}], \quad (5.1)$$

where n_i accounts for the number of excess atoms of species i present in the surface supercell compared to the bulk, and μ_i is the chemical potential that represents experimental growth conditions for species i . The chemical potentials μ_i are related to each other via the phase stability equation for GTO, namely

$$\mu_{\text{Gd}} + \mu_{\text{Ti}} + 3\mu_{\text{O}} = \Delta H_f(\text{GdTiO}_3), \quad (5.2)$$

where $\Delta H_f(\text{GdTiO}_3)$ is the enthalpy of formation of GTO. The range of values that μ_i can take is limited by the formation of other competing phases, namely, TiO₂ (rutile), Gd₂Ti₂O₇, Gd₂O₃, Gd metal, Ti metal and the O₂ molecule. These constraints are represented by the following inequality equation for each competing phase:

$$p \cdot \mu_{\text{Gd}} + q \cdot \mu_{\text{Ti}} + r \cdot \mu_{\text{O}} \leq \Delta H_f(\text{Gd}_p\text{Ti}_q\text{O}_r), \quad (5.3)$$

where (p, q, r) is the number of (Gd, Ti, O) atoms present in the competing phase with an enthalpy of formation $\Delta H_f(\text{Gd}_p\text{Ti}_q\text{O}_r)$. For example, the chemical potentials μ_{Ti} and μ_{O} are limited by the formation of the TiO_2 phase ($p = 0, q = 1, r = 2$) as: $\mu_{\text{Ti}} + 2\mu_{\text{O}} \leq \Delta H_f(\text{TiO}_2)$. The calculated values for the enthalpy of formation for the competing phases $\Delta H_f(\text{Gd}_p\text{Ti}_q\text{O}_r)$ are tabulated in Table 5.1 along with $\Delta H_f(\text{GdTiO}_3)$.

Table 5.1: Enthalpy of formation (ΔH_f), in units of eV/(formula unit), for GdTiO₃ and its competing phases.

Material	Enthalpy of formation ΔH_f	
	Calculated	Experimental
GdTiO ₃	-17.20	
Gd ₂ O ₃	-18.68	-18.85 [Ref. [130]]
TiO ₂	-9.16	-9.74 [Ref. [131]]
Gd ₂ Ti ₂ O ₇	-38.02	-39.62 [Ref. [132]]

The combination of Eqs. 5.2 and 5.3 determines the entire range of allowed values for μ_{Gd} , μ_{Ti} , and μ_{O} within which GTO can form. This range can be represented by the phase stability diagram in Fig. 5.2, plotted as a function of μ_{Ti} and μ_{O} , where μ_{Gd} can be obtained from Eq. 5.2. From the diagram (Fig. 5.2), for a given μ_{O} , the boundary between GTO and TiO_2 represents the most Ti-rich conditions for GTO, while the boundary between GTO and Gd_2O_3 represents the most Gd-rich conditions. We also see that μ_{O} is restricted as $-5.24 \text{ eV} < \mu_{\text{O}} < -3.62 \text{ eV}$ for Gd-rich, and $-4.58 \text{ eV} < \mu_{\text{O}} < -3.62 \text{ eV}$ for Ti-rich conditions, due to the formation of $\text{Gd}_2\text{Ti}_2\text{O}_7$ and Ti metal ($\mu_{\text{Ti}} > 0 \text{ eV}$). These restrictions on μ_{O} determine the O-poor (most negative μ_{O}) and O-rich (least negative μ_{O}) limits under Gd-rich or Ti-rich conditions. We will

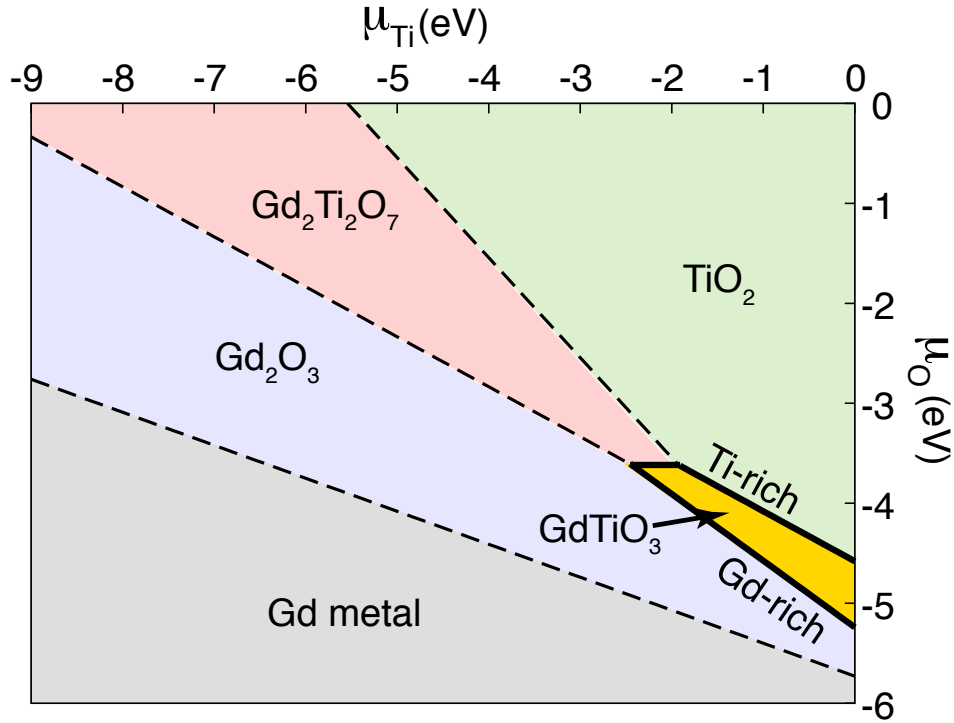


Figure 5.2: Stability region of GdTiO_3 (yellow region enclosed by solid lines) along with its competing phases, namely $\text{Gd}_2\text{Ti}_2\text{O}_7$, Gd_2O_3 , and TiO_2 as a function of μ_{Ti} and μ_{O} . The phase boundary with Gd_2O_3 is indicated as Gd-rich, while the boundary with TiO_2 is indicated as Ti-rich.

discuss the calculated surface energies in the Ti-rich as well as the Gd-rich conditions, while varying μ_{O} between O-poor and O-rich limits. From the temperature and partial O_2 pressure, μ_{O} can be directly related to the experimental conditions during growth or annealing.

5.3 Bulk properties

The calculated lattice parameters for the 20-atom orthorhombic unit cell of GTO are: $a = 5.355 \text{ \AA}$, $b = 5.731 \text{ \AA}$ and $c = 7.644 \text{ \AA}$ (indicated in Fig. 5.1), in good agreement with

experimental values [133] (5.393 Å, 5.691 Å and 7.664 Å). In order to explain structural relaxations, we will use the O-Ti-O bond angles between atoms lying along the (001) plane as an indicator of distortions. It is important to note that we are *not* referring to angles between atomic positions *projected* on a plane, but refer to the angle taking into account the atomic positions in 3 dimensions. Figure 5.1(a) shows the O-Ti-O bond angles in the bulk, which are slightly off 90.0° , namely 89.4° and 90.6° , and sum up to give 360° . However, since all the O-Ti-O angles do not lie exactly on a single plane, the sum of angles is not geometrically constrained to the value for a quadrilateral, 360° . The electronic structure consists of the completely filled LHB, containing $4e^-$ ($1e^-$ per Ti atom), separated from the UHB by 2.06 eV, which is the fundamental band gap. The dispersion (or bandwidth) of the LHB spans less than 0.7 eV. The occupied O-2*p* bands occur at 2.56 eV below the bottom of the LHB.

5.4 Surface band structure

The atomic structure of the relaxed TiO_2 surface shows deviations of its in-plane O-Ti-O bond angles from the bulk value: the unoccupied Ti (94.0° , and 81.9°) favors a smaller angle than the occupied Ti (97.9° , and 86.2°) as shown in Fig. 5.3(a); the sum of the angles, however, does not deviate from 360° . The electronic band structure for the surfaces can be obtained by projecting the 3-dimensional (3D) bulk band structure onto the 2D BZ along with the 2D band structure for the slab supercell as shown in Fig. 5.4. States appearing in the gap are most likely surface states, although the rigorous method

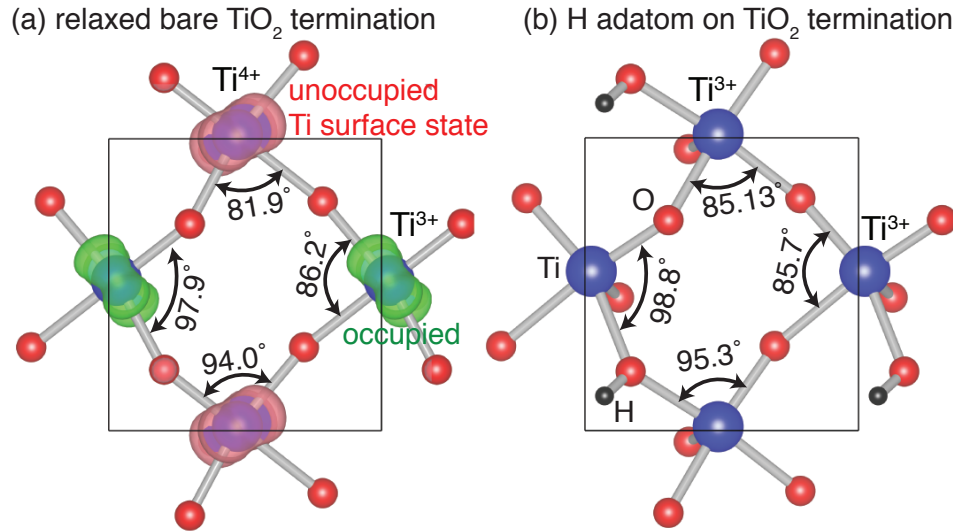


Figure 5.3: Surface atomic structure indicating the in-plane O-Ti-O bond angles of the (a) bare (but relaxed) TiO_2 termination, and (b) H-adatom reconstruction of the TiO_2 termination. The charge densities of the highest occupied (in green) and lowest unoccupied (in red) surface states of the bare termination are also shown in (a). Charge on the Ti atoms are also indicated.

of identifying surface states is to see if their charge density is localized on the surface. For all of the discussions below, we have explicitly checked if the charge density of the surface states is truly localized on the surface layers.

The TiO_2 termination shows unoccupied surface states (holes) within the band gap > 1.3 eV above the LHB [see Fig. 5.4(a)], which means the lowest excitation energy is about 1.3 eV. From electron counting, we find that the LHB lacks $2e^-$, i.e., $1e^-$ per 1×1 areal unit is missing compared to bulk GTO such that one Ti atom has +4 charge and the other Ti atom has 3+ charge [see Fig. 5.3(a)]. This is consistent with our ionic picture of the polar discontinuity, where we expect a lack of $1e^-$ per 1×1 areal unit (which contains 2 formula units of TiO_2). The occupied states appearing within 0.3 eV above the LHB are surface states localized on $3d$ orbitals of the other surface Ti atom; they are states

of the LHB perturbed by the surface termination. The charge density corresponding to these states confirms this picture: the highest occupied state is localized on one of the surface Ti atoms, while the lowest unoccupied state occurs on the other Ti atom [see Fig. 5.3(a)]. The absolute position of the top of the LHB, i.e., with respect to the vacuum level, was calculated to be -3.94 eV, which is quite high compared to the positions of the valence-band maximum of other complex oxides [41, 82], which lie at 6.5–7.5 eV below vacuum level. From this information, we can say that the *unoccupied* surface states occur at > -2.9 eV on an absolute scale. Since their energetic position is high on an absolute scale, occupying these states with electrons will be energetically unfavorable.

GdO termination, on the other hand, has *occupied* states between 1 eV and 2 eV relative to the top of the LHB (see Fig. 5.4), corresponding to an excess of $1e^-$ per 1×1 surface unit, which is also consistent with our ionic picture. These occupied states are found to be of Gd *5d* orbital character, which are more dispersive than the Ti *3d* orbitals. For the GdO termination, the calculated position of the topmost LHB state is 5.29 eV below vacuum. This leads to a difference of 2.36 eV in ionization energies between the two polar terminations, with the GdO termination having a larger ionization energy than the TiO₂ termination. The position of the highest occupied state for the GdO termination, i.e., the Fermi level E_F , occurs at 3.22 eV below vacuum level. Compared to the TiO₂ termination, the occupied states for GdO termination occur at lower energies on the absolute scale, which would lead us to *naively* expect that the GdO termination is more stable based on the electronic structure, since occupied states at higher energies

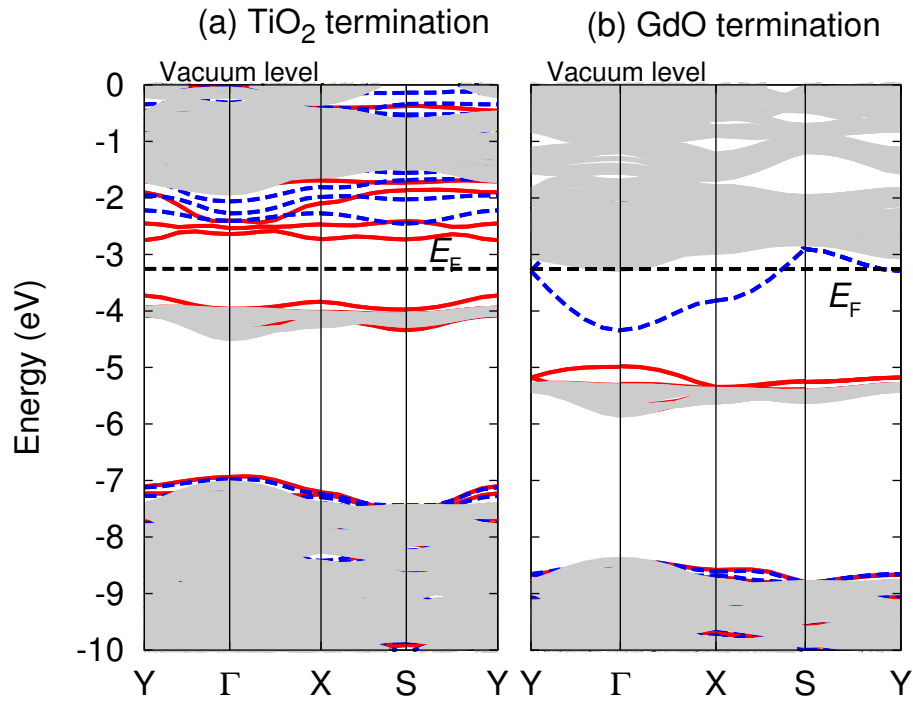


Figure 5.4: Surface band structure of (a) TiO_2 -terminated, and (b) GdO -terminated GTO projected onto the 2D (001) Brillouin zone. The gray regions are bulk states projected onto the 2D surface BZ. The solid (red) lines are the spin-up (majority spin) channel of the surface supercell, while dashed (blue) lines represent the spin-down (minority spin) channel. The Fermi levels (E_F), determined based on the occupation of states in the slab supercell calculations, are also indicated. The vacuum level for each of the terminations is set to 0 eV.

are energetically unfavorable. However, in order to definitely and quantitatively address the relative stability of the terminations, we must compute and compare their absolute surface energies using Eq. 5.1, which also includes the structural energy cost/gain as well as the chemical potential of different species.

5.5 Results and discussion of surface energies

5.5.1 Native surface terminations

Under Ti-rich conditions, the absolute surface energy of the TiO₂ termination is calculated to be 71 meV/Å² for all μ_{O} [Fig. 5.5(b)]. Under the same conditions, GdO termination has a surface energy of 125 meV/Å², which is 54 meV/Å² higher, i.e., *less* stable, than the TiO₂ termination. The surface energies being independent of μ_{O} under Ti-rich conditions is a consequence of the surface stoichiometry, which cancels out the variable μ_{O} due to the limiting phase being TiO₂. Gd-rich conditions, on the other hand, introduce a μ_{O} -dependence in the surface energies due to the limiting phase being Gd₂O₃. From Fig. 5.5(a), under Gd-rich conditions, we find that the TiO₂ termination still has a lower surface energy (and hence is more stable) than the GdO termination for $\mu_{\text{O}} > -4.26$ eV, while lower oxygen chemical potentials ($\mu_{\text{O}} < -4.26$ eV) favor the GdO termination. Contrary to our *naive* expectation based on the electronic structure, this result indicates a higher stability of the TiO₂ termination over GdO termination, for

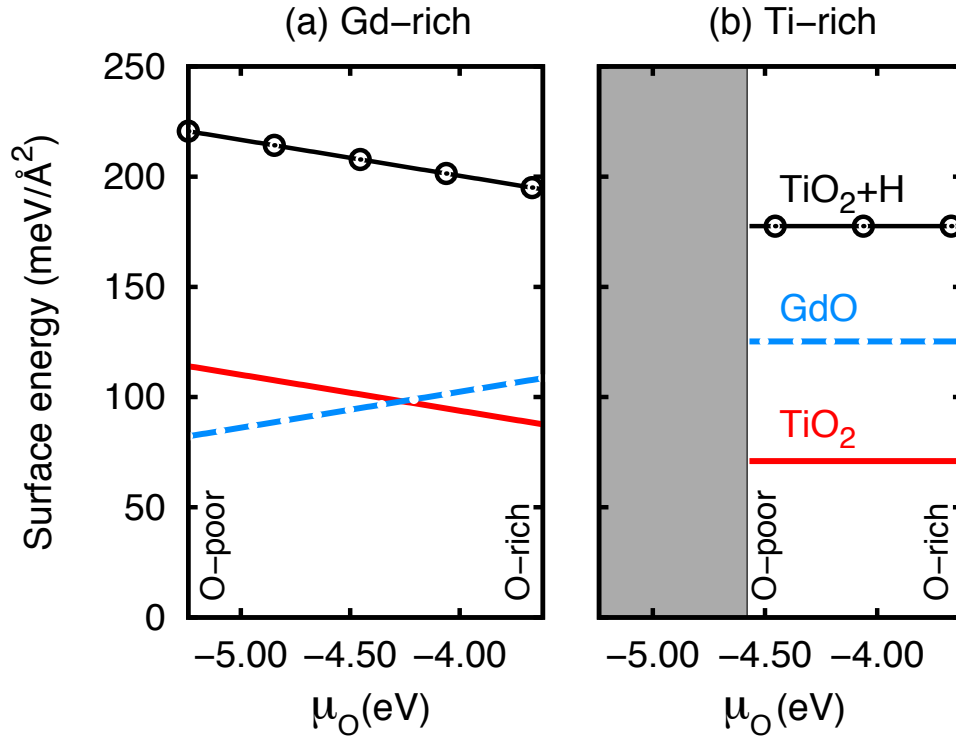


Figure 5.5: Surface energy ($\text{meV}/\text{\AA}^2$) of TiO_2 -termination (solid red), GdO -termination (dashed blue) and (1×1) H-adatom reconstruction on TiO_2 -termination (open circles) calculated under (a) Gd-rich and (b) Ti-rich conditions is plotted as a function of μ_{O} . Under Gd-rich conditions, the formation of competing phases of GTO restricts μ_{O} to the range $-5.24 \text{ eV} < \mu_{\text{O}} < -3.62 \text{ eV}$, while under Ti-rich conditions the restricted range, $-4.58 \text{ eV} < \mu_{\text{O}} < -3.62 \text{ eV}$, is smaller. The gray box in panel (b) indicates the μ_{O} values for which GTO is unstable under the constraint imposed by Ti-rich conditions. See text in Sec. 5.2 and Fig. 5.2 for a more detailed explanation.

many combinations of chemical potentials. This conclusion suggests strong contributions from the structural relaxation energy.

As discussed earlier in Sec. 5.4, upon examination of the surface electronic structure, there are unoccupied states corresponding to a lack of $1e^-$ per 1×1 areal unit on the TiO_2 surface. Therefore, it is reasonable to expect that additional electrons from donor adatoms or other electron sources would fill these unoccupied states, and make the TiO_2 surface more stable by lowering its surface energy. We will address the effect of two

such sources: (1) the H-adatom reconstruction and (2) electron transfer from the 2DEG resulting due to polar discontinuity at the GTO/STO interface. The GdO termination, on the other hand, has occupied surface states close to the minimum of the UHB, which is an unfavorable energetic situation. In principle, two mechanisms could lower its surface energy: (1) native atomic reconstructions involving Gd vacancies similar to La-vacancy reconstructions on LaO termination in LaAlO₃ as discussed in Sec. 4.4.2 and Ref. [112], or (2) via electron transfer *from* the surface *to* the 2DEG at the GTO/STO interface. Since our main goal here is to address the issue of charge transfer *from* the 2DEG to unoccupied surface states in the GTO/STO system, we will restrict our present study to the TiO₂ surface.

5.5.2 H-adatom reconstruction on TiO₂ termination

Hydrogen, owing to its small size and ubiquity, has been known to passivate surface states in many materials [123, 134, 135], especially in oxides [136, 137] due to its ability to form strong H-O bonds. Hydrogen is also very reactive, and forms many stable hydrides. Therefore, H serves as a perfect prototype impurity to study adatom reconstructions on the TiO₂ termination, and to test its stability. Based on the electron counting rule [123], a single donor per 1×1 unit would be required to passivate the TiO₂ surface; for this reason, we focus our study on the 1×1 H-adatom reconstruction.

The calculation of the atomic structure shows that the H adatom relaxes to a position near an O atom on the surface forming a strong H-O bond [see Fig. 5.3(b)] with a

bond distance of 0.958 Å. We verified that this configuration results in the lowest-energy structure compared to the other configuration where H bonds to a Ti atom. This indicates a stronger H-O bond than the H-Ti bond. The H adatom donates electrons to the unoccupied Ti surface states of the bare TiO₂ termination [see Fig. 5.3(a)], which was verified from the occupancy of its electronic structure, leaving both the surface Ti atoms occupied. As was calculated for the bare surface, occupying the Ti atom increased its O-Ti-O bond angles to 95.3° and 85.1° (compared to 94.0° and 81.9° for the unoccupied Ti). The addition of H causes the sum of the angles to be 364.9°, instead of 360°.

The surface energy of the H-adatom reconstruction was calculated using Eq. 5.1 with the addition of taking the H chemical potential (μ_{H} , referenced to the H₂ molecule) into account. Its surface energy has the same μ_{O} dependence as the bare TiO₂ termination, and differs only by a μ_{H} -dependent term, which is treated as an independent variable in our analysis. Under H-rich conditions, corresponding to $\mu_{\text{H}} = 0$, we find that the H adatom on the TiO₂ termination *increases* the surface energy by 107 meV/Å² compared to the bare TiO₂ [see Fig. 5.5]. This result shows that H is *unlikely* to bind to the TiO₂-terminated surface, and that an unreconstructed (but relaxed) polar surface lacking 1e⁻ per 1 × 1 areal unit (based on electron counting) is much more stable than an adatom reconstruction that fills the unoccupied Ti states.

Considering that H has been known to stabilize the surface of many materials [123, 135, 136, 137], this result is indeed highly unexpected. However, the situation is different for the TiO₂-terminated surface compared to other semiconductors. Hydrogen forms a very

strong O-H bond, and we therefore expect H to bond with a surface oxygen atom. Indeed, on many oxide semiconductor surfaces that have partially occupied surface states with oxygen character (i.e., O dangling bonds), H binds to the oxygen atoms and stabilizes the surface. On the TiO_2 -terminated GTO surface, however, the unoccupied surface states are localized on the Ti atoms having a +4 charge, rather than on O atoms, and occur at much higher energy than the completely filled O $2p$ states. In forming the O-H bond, the excess electron donated by H has to occupy these high-lying Ti states, which costs energy. This is the energy cost that makes the H-atom reconstructed surface energetically unfavorable. Therefore, this is not a case of passivation of surface states as in the context of traditional semiconductor surfaces, where H would bond to an O atom with a partially occupied dangling bond. This realization reconciles the unexpected behavior of H on the TiO_2 -terminated surface of GTO.

5.5.3 Implications for polar surfaces of Mott insulators

Mott insulators with a $3d^1$ configuration are stabilized by the strong electron-electron interactions that localize the excess $3d$ electron on the cation [126, 138]. In the case of GTO and other titanate Mott insulators [139], such as YTiO_3 and SmTiO_3 , the electron is localized on the Ti atom, which assumes a +3 charge in the bulk. However, on the TiO_2 -terminated GTO surface, there is a deficit of $1e^-$ per 1×1 areal unit cell (with two Ti atoms), which leads to one Ti^{+4} atom and one Ti^{+3} atom. From our discussion above, it is clear that transferring electrons donated by H adatoms to the Ti^{+4} atoms on

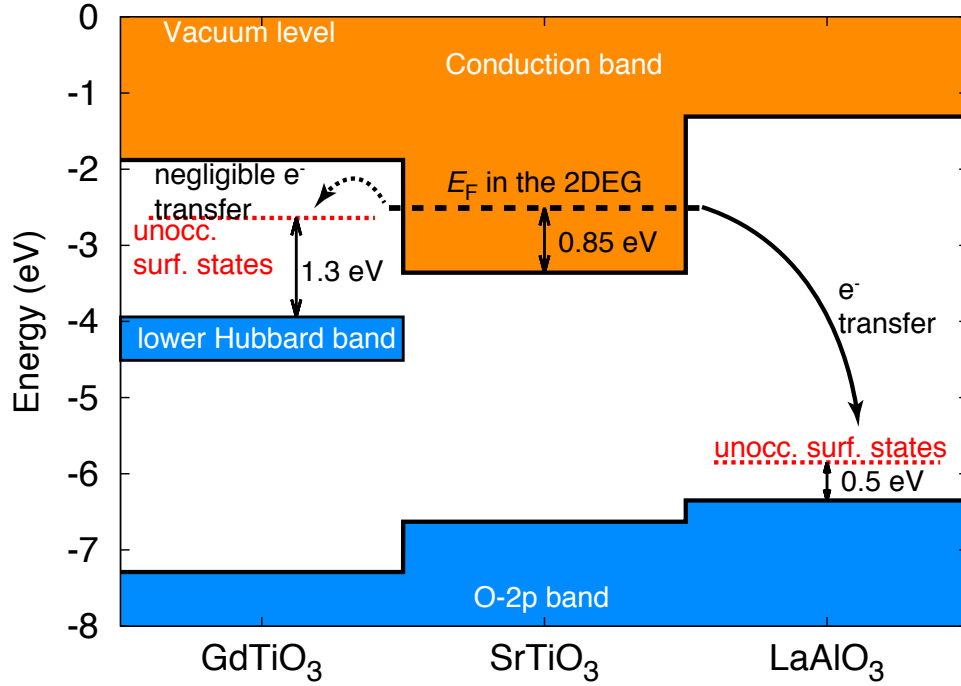


Figure 5.6: Band lineup between GTO, LAO and STO from Ref. [82] is shown referenced to the vacuum level calculated for the TiO_2 -terminated GTO surface. Dotted red lines show unoccupied surface state levels for the TiO_2 -terminated GTO and AlO_2 -terminated LAO surfaces [see Figs. 5.4(a) and 4.6(b)]. The Fermi level E_F in STO (dashed black line) was calculated using SP simulations assuming a 2DEG density of $3.3 \times 10^{14} \text{ cm}^{-2}$ (see Table 3.1). Electron transfer occurs from the 2DEG to low-lying LAO surface states, but the transfer to high-lying GTO surface states is far less favorable.

the TiO_2 surface is energetically unfavorable. We expect this conclusion to be applicable more generally to polar surfaces of other Mott insulators due to their similar electronic structure [126, 138, 139, 140, 141].

5.6 Impact on 2DEG at STO/GTO interface

Similar to the LAO/STO interface discussed in Chapter 4, the polar discontinuity at the GTO/STO interface also results in a 2DEG of density $3.3 \times 10^{14} \text{ cm}^{-2}$, corresponding

to $1e^-$ per 1×1 areal unit of GTO [12], which is exactly equal to the density of missing electrons at the TiO₂ surface termination of GTO. The large conduction-band offset of STO with GTO confines these excess electrons on the STO side of the interface [82, 141]. In Chapter 4, we performed a detailed first-principles analysis on the LAO/STO system [21, 39], and showed that unoccupied states residing on the surface of LAO films serve as a sink for the 2DEG electrons. In the case of LAO/STO, the thickness of LAO films as well as the surface conditions have been observed to strongly affect the properties of the 2DEG [7, 97]. However, no such effects have been reported for the GTO/STO system. Our goal is to shed light on the distinguishing character of the GTO surface that prevents the electron transfer from the 2DEG to the surface in the GTO/STO system.

In the case of LAO/STO, the energy gain by electron transfer from the 2DEG to the unoccupied surface states depended on two factors: (1) the spatial proximity of the 2DEG to the LAO surface containing holes, and (2) the energetic lineup of the 2DEG states (i.e., Fermi level E_F in the 2DEG) and the unoccupied states as indicated in Fig. 5.6; see the discussion in Sec. 4.4. For thin LAO films, the situation favored electron transfer to the surface, and led to a significant gain in energy. The Fermi level E_F position indicated in Fig. 5.6 was computed using SP simulations assuming a 2DEG density of $3.3 \times 10^{14} \text{ cm}^{-2}$ (see Sec. 3.3, Table 3.1, and Ref. [40]).

In the GTO/STO system, on the other hand, the band alignment [82, 141] shows the empty surface state level for the TiO₂ termination to occur only slightly below the E_F in the 2DEG (see Fig. 5.6). Therefore, the energy gain due to transfer from the

2DEG to the surface states, which is always balanced by an electrostatic energy *cost* (third term in Eq. 4.9), is small. This situation results in the transfer of only a small concentration of electrons, and the 2DEG density remains close to the full density. In the LAO/STO system, even though there is an electrostatic energy cost involved, the energy gain (difference between E_F and surface state level) is large enough to overcome the cost below the critical thickness. This explains why the GTO/STO system exhibits the full 2DEG density independent of the GTO thickness, while the LAO/STO system has a critical thickness for 2DEG formation due to transferring some electrons to the surface for energy gain.

5.7 Conclusion

Our study of the polar surface terminations in GTO has revealed the surprisingly stable nature of its TiO_2 polar surface with unoccupied surface states derived from the LHB. H adatom is known to form strong bonds with surface O atoms in semiconductors with unoccupied surface states. However, in the case of the TiO_2 surface of GTO, the O-H bond does not lead to a lowering of the surface energy, but in fact *increases* it. We reconcile this unexpected behavior of H on the GTO surface based on the argument that the unoccupied surface states occur on Ti, instead of an O atom as in many semiconductors. The small ionization energy of the LHB, and the high absolute position of the unoccupied surface states are understood to be responsible for the high surface stability of the TiO_2 termination, since mechanisms that occupy these high-lying surface states

would be energetically unfavorable. The understanding of surface stability gained from studying the behavior of GTO surfaces is expected to be more general, and applicable to other d -band Mott insulators that have similar electronic structure. Finally, based on the electronic structure of the TiO_2 surface, we explained why the GTO/STO interface system retains the full 2DEG density that results from the polar discontinuity, whereas the LAO/STO system shows a lower 2DEG density.

Chapter 6

First-principles analysis of electron transport in complex oxides

6.1 Introduction

Recent demonstrations [36, 37, 38] of electron mobilities as high as $320 \text{ cm}^2\text{V}^{-1}\text{s}^{-1}$ at room temperature (RT) have sparked interest in the transparent cubic perovskite oxide BaSnO_3 (BSO) for electronic applications. The ease of achieving high levels of *n*-type doping [36, 142] ($5 \times 10^{20} \text{ cm}^{-3}$) with conductivities on the order of 10^6 S m^{-1} makes it attractive as a transparent conducting oxide (TCO). Moreover, it has the highest RT mobility among TCOs [143]. Its RT mobility is more than an order of magnitude higher than that of perovskite oxides [33] with conduction bands derived from *d* orbitals, of which SrTiO_3 (STO) [34, 35, 144, 145] is a prototypical example.

Efforts to further improve mobility in BSO through growth of high-quality bulk as well as thin films have been undertaken by many groups [38, 146, 147, 148]. However, the characteristics of BSO that impart such a high mobility, and the fundamental limits on this mobility, are still poorly understood. The small effective mass has been suggested as the primary cause for the high mobility [36, 149]. Here we will show that the mass is not the only reason, and that BSO has a significantly lower scattering rate than, for instance, STO.

In this work, we explore the underlying mechanisms responsible for the high RT mobility by calculating the transport properties using Boltzmann transport theory and first-principles calculations. We use the relaxation time approximation, but unlike the majority of the electron transport studies that assume a constant relaxation time [150, 151, 152, 153], we take the \mathbf{k} dependence of the relaxation time into account. The value of τ is often approximated by taking the value at Γ [152] or by treating it as a fitting parameter in the analysis of experimental results. A few groups have performed first-principles studies on other materials systems [65, 81, 154, 155, 156] that explicitly take the \mathbf{k} dependence of τ into account; however, the most common assumption in the literature is to take τ as a constant [150, 151, 152, 153], i.e., to approximate $\tau_n(\mathbf{k})$ to be independent of \mathbf{k} . Here, we explicitly take the \mathbf{k} dependence of τ into account; this allows us to check the validity of the constant- τ approximation, as well as calculate the Hall mobility. As recognized in other material systems [65, 66, 79], we will see that there is a significant \mathbf{k} dependence in the relaxation time. This has important consequences when analyzing

the dependence of mobility on carrier concentration and temperature, and also allows us to calculate Hall mobility (μ_{H}), which differs from the drift mobility (μ), for comparing against experimental reports. We also address technical issues related to numerically computing the scattering rates, as well as the importance of adequate sampling of the band structure in order to obtain converged results.

BSO has a 5-atom unit cell that leads to a total of 15 phonon modes, three of which are polar longitudinal optical (LO) modes [157]. In polar crystals, LO phonons tend to dominate scattering at RT compared to other phonons due to their strong long-range coulomb interaction. In addition, we need to assess ionized impurity scattering, since large concentrations of dopants are intentionally introduced in order to achieve carrier densities as high as $10^{19} - 10^{21} \text{ cm}^{-3}$.

The presentation of the work is organized as follows: In Sec. 6.2, we discuss our first-principles results for the atomic and electronic structure of BSO. Using the methodology based on Boltzmann transport equation described in Section 2.3, we describe our computational implementation for calculating transport properties accounting for LO-phonon and ionized impurity scattering in Sec. 6.3. Section 6.4 contains the calculated results and a discussion of scattering mechanisms. Section 6.5.1 addresses the results of the calculations of Hall factor and Hall mobility, and discusses of an explicit comparison to experimental transport measurements on bulk and thin films. In Sec. 6.5.2, we address why the mobility in BSO is larger than that of other perovskite oxides, with the goal of

guiding the search for other high-mobility materials. In Section 6.5.3, finally, we suggest avenues for enhancing the RT mobility of BSO.

6.2 Atomic and Electronic structure

Our first-principles analysis is based on density functional theory (DFT) calculations. An accurate description of the electronic structure is essential to obtain reliable results for transport properties; we therefore use the HSE06 hybrid functional [55], which has been shown to yield accurate band structures for solids [52,53,82]. The calculations were performed using the Vienna *Ab initio* Simulation Package (VASP) [58] with projector augmented waves [56,109]. Sn *d* states were treated as part of the core; we verified this did not affect the calculated structure and affected the band gap by less than 0.1 eV. We used a plane-wave basis with 500 eV cutoff, and the default mixing parameter of 25% and screening parameter of 0.2 \AA^{-1} for HSE06. An $8 \times 8 \times 8$ *k*-point grid with the Monkhorst-Pack mesh was used for Brillouin-zone integrations.

BSO has a cubic structure with the space group $\text{Pm}\bar{3}\text{m}$, and has 5 atoms (one Ba, one Sn and 3 O) in its unit cell. The calculated lattice parameter is 4.13 \AA , in good agreement with the experimental value [38,158] of 4.12 \AA . Our calculated band structure is shown in Fig. 6.1. The conduction band (CB) is derived from Sn *5s* orbitals and is highly dispersive. There is also a significant nonparabolicity in the dispersion away from Γ , which will be quantified in Sec. 6.3. The valence band (VB) is derived from O *2p* orbitals, and has much lower dispersion than the CB.

We find an indirect band gap ($R \rightarrow \Gamma$) of 2.40 eV, in agreement with a previous HSE06 calculation [142]. Our calculated direct band gap of 2.88 eV at Γ is in reasonable agreement with the reported experimental direct gap of 3.1 eV from optical absorption measurements by Mizoguchi *et al.* [149] and Kim *et al.* [38], but disagrees with the value of 3.5 eV reported by Chambers *et al.* [159] and Li *et al.* [160]. Experimentally determined indirect gaps [38, 159] vary between 2.95–3.1 eV and are again larger than our calculated value. Further work will be needed to resolve the nature and magnitude of the gaps. We emphasize that our transport calculations do not rely on the value of the band gap, as we will see in the next section.

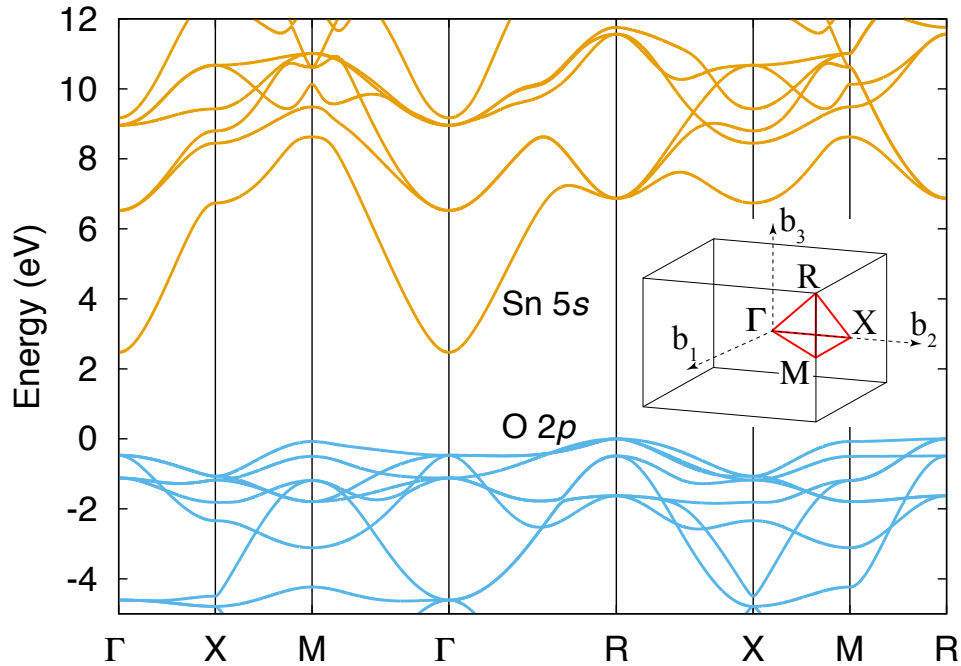


Figure 6.1: Band structure of BSO calculated from first principles using the HSE06 hybrid functional. The inset indicates the high symmetry points in the Brillouin zone. The indirect gap $R \rightarrow \Gamma$ is 2.40 eV, and the direct gap at Γ is 2.88 eV.

6.3 Computational implementation of transport calculation

The LO-phonon scattering rates are computed based on Eq. 2.39. BaSnO₃ has a single nondegenerate CB and therefore only intraband scattering occurs ($m = n = 1$). We use the experimental values determined by Stanislavchuk *et al.* [157] for the three polar LO (154, 421 and 723 cm⁻¹); or 18, 51 and 88 meV) and the corresponding three doubly-degenerate TO (135, 245 and 628 cm⁻¹; or 17, 30 and 78 meV) mode frequencies, for the high-frequency dielectric constant ($\epsilon_\infty=4.3$), and the static dielectric constant ($\epsilon=20$).

For ionized impurity scattering, the scattering rate is computed using Eq. 2.45. BaSnO₃ is often doped with substitutional La (La_{Ba}⁺¹) which is a single donor having a +1 charge state [38]. Therefore, in our study, we simulate this situation by assuming ionized dopants to have +1 electronic charge, and their concentrations were chosen to be equal to the electron concentration, $N_{\text{imp}} = n$ (i.e., we assume full ionization, and no charge compensation). For $Z > 1$, we would need fewer impurities to give rise to a given electron concentration n (since $n = ZN_{\text{imp}}$, assuming complete ionization), but because the scattering rate is proportional to $N_{\text{imp}}Z^2$ (Eq. 2.45), the rate effectively increases linearly with Z . Singly charged impurities are therefore optimal in terms of mobility. For instance, doping with a double donor would reduce the impurity-related part of the mobility by a factor of 2 compared to a single donor.

The computation of mobility via Eq. 2.38 involves evaluating a three-dimensional (3-D) integral over the BZ. The three quantities required for evaluating this integral are $v_{n,x}$, $\partial f_{\mathbf{k}}/\partial \varepsilon_{\mathbf{k}}$ and $\tau_n(\mathbf{k})$. The first two quantities $v_{n,x}$, and $\partial f_{\mathbf{k}}/\partial \varepsilon_{\mathbf{k}}$ converge reasonably well for finer grids, although working with such fine grids using hybrid functionals results in a prohibitively large computational cost unless an interpolation technique such as Wannier interpolation [161] is used. However, the main bottleneck in computing the LO-phonon scattering process lies in obtaining $\tau_n(\mathbf{k})$ (Eq. 2.39), which involves a 3-D integral over the phonon wavevector \mathbf{q} with its integrand containing a δ function. This integral can in principle be numerically evaluated from the full first-principles band structure. In practice, however, any numerical technique employed will require a fine grid and the use of smearing to implement the energy-conserving δ function present in Eq. 2.39. This leads to inaccuracies in the results because of its sensitivity to the choice of the smearing parameter [65, 81]. In addition, quantifying the error in the mobility is difficult without the knowledge of the exact result.

We circumvent these problems here by using an analytic expression for the CB dispersion. This allows us to solve for one of the components of \mathbf{q} using the condition for energy conservation *exactly*, thus reducing the integral to 2-D by getting rid of the δ function. This has the added advantage of decreasing the computational complexity as well as producing the exact result that can be used to validate the choice of the smearing parameter in the numerical approach [65, 81]. Of course, this approach is contingent on the analytic expression being able to accurately reproduce the first-principles band

structure, at least in the vicinity of the Fermi level, i.e., in the regions of the BZ where the factor $\partial f_{\mathbf{k}}/\partial \varepsilon_{\mathbf{k}}$ is non negligible. The resulting integral can then be evaluated using any numerical integration technique. Here we use the trapezoidal rule on a uniform grid separated by $\Delta k = 5 \times 10^{-3} \text{ \AA}^{-1}$ along each dimension.

We plot the CB dispersion in Fig. 6.2. It is clear that for energies larger than 0.3 eV nonparabolicity is significant. Since the Fermi level may lie well above this energy for commonly used doping levels (also indicated in Fig. 6.2) using a parabolic dispersion relation would be inaccurate. Instead, we use the hyperbolic dispersion relation derived from **k.p** theory [162]:

$$\hbar^2 k^2 / 2m_{\Gamma}^* = \varepsilon_{\mathbf{k}}(1 + \alpha \varepsilon_{\mathbf{k}}). \quad (6.1)$$

Fitting our first-principles band structure of the CB to the hyperbolic dispersion relation yields an effective mass near Γ , $m_{\Gamma}^* = 0.20 m_e$, which we find to be isotropic. However, the nonparabolicity parameter α was found to be slightly anisotropic as evident from inspecting the E -vs.- k relation along the three high-symmetry directions in the BZ up to $k = 0.4 \text{ \AA}^{-1}$ (along $\Gamma \rightarrow X$, $\Gamma \rightarrow M$, and $\Gamma \rightarrow R$; see Table 6.1). Since the deviation in α due to the anisotropy is small ($\pm 0.03 \text{ eV}^{-1}$), to avoid complications in our transport analysis, we use an isotropic α value of 0.25 eV^{-1} determined by averaging α along the high-symmetry directions. We find that the averaged α value yields an accuracy of better than $\pm 0.05 \text{ eV}$ for energies up to 1.5 eV ($k \sim 0.32 \text{ \AA}^{-1}$) above the CB minimum (see Fig. 6.2). For reference, the Fermi level ε_F corresponding to an electron concentration

of 10^{21} cm^{-3} is at 1.34 eV; our fit will therefore be entirely adequate for all achievable doping densities.

Table 6.1: The effective mass near Γ , m_{Γ}^* and the nonparabolicity parameter α for the hyperbolic fit (Eq. 6.1) along three high-symmetry directions.

Direction	$m_{\Gamma}^* (m_e)$	$\alpha (eV^{-1})$
$\Gamma \rightarrow X$	0.20	0.208
$\Gamma \rightarrow M$	0.20	0.253
$\Gamma \rightarrow R$	0.20	0.285

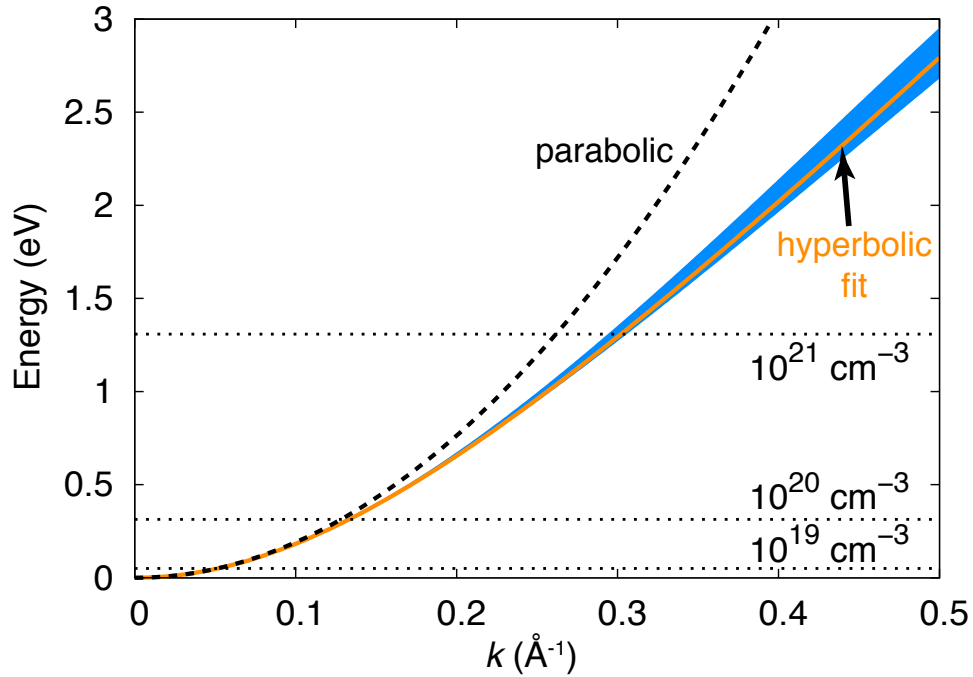


Figure 6.2: Dispersion of the lowest CB around Γ , showing the slight anisotropy evident from the difference in dispersion along the high-symmetry directions (Γ -X, Γ -M, and Γ -R) (shaded in blue). The fitted hyperbolic dispersion (solid orange line) and parabolic dispersion (dashed black line) are shown. Fermi levels for different electron densities are also indicated.

For the hyperbolic dispersion, the band velocity is given by

$$v_{\mathbf{k}} = \frac{1}{\hbar} \frac{\partial \varepsilon_{\mathbf{k}}}{\partial \mathbf{k}} = \frac{\hbar \mathbf{k}}{m_{\Gamma}^*} (1 + 2\alpha \varepsilon_{\mathbf{k}})^{-1} \quad (6.2)$$

and the band mass accounting for nonparabolicity is given by

$$m_{\mathbf{k}}^* = m_{\Gamma}^* (1 + 2\alpha \varepsilon_{\mathbf{k}})^3. \quad (6.3)$$

Our value for m_{Γ}^* is in agreement with other HSE06 calculations [142, 163] except for one study [164], in which the use of incorrect units for k led to an overestimation of the mass ($0.46 m_e$) by a factor of $(2\pi/a)^2$, where $a = 4.13$ is the lattice parameter in Å. The value reported based on the hybrid functional PBE0 [142, 147] is $0.22 m_e$, and values based on LDA and GGA functionals [38, 165] range between 0.05 and $0.40 m_e$. To our knowledge, values for the nonparabolicity parameter have not been reported.

To date, three studies have reported a wide range of experimental effective masses for the CB in BSO [38, 166, 167]. Kim *et al.* [38] estimated the mass to be $0.60 m_e$ based on the Burstein-Moss shift at $n = 2.3 \times 10^{20} \text{ cm}^{-3}$. Seo *et al.* [166] used the plasma frequency that fitted the observed Drude conductivity at an electron density of $8.9 \times 10^{19} \text{ cm}^{-3}$ to arrive at $0.35 m_e$. Both these reports significantly overestimate m_{Γ}^* compared to the calculated value of $0.20 m_e$. However, the effective mass value of $\sim 0.20 m_e$ determined from reflectivity measurements by Allen *et al.* [167] is in good agreement with our calculation.

6.4 Results

Using the implementation described in the previous section, we now proceed to calculate the scattering rates and mobilities due to LO-phonon and ionized impurity scattering. We first discuss the results obtained for the individual scattering processes separately. Then, in Sec. 6.4.3, we discuss the overall mobility combining the effect of both processes via Matthiessen's rule.

6.4.1 LO-phonon scattering

The LO-phonon scattering rates are obtained using Eq. 2.39 by summing the contributions from the three polar LO modes. The \mathbf{k} dependence of the calculated scattering rate is plotted in Fig. 6.3 for two values of the electron density, 10^{19} and 10^{20} cm^{-3} . Our hyperbolic dispersion fit is valid over the plotted range (up to 0.4 \AA^{-1}), and since isotropic dispersion is a good approximation, the rate plotted is representative of all directions in the BZ. We can explain the overall features in Fig. 6.3 in terms of some basic mechanisms. As k increases, the band curvature decreases (see Fig. 6.2), and the radius of the energy surface at $\varepsilon_{\mathbf{k}+\mathbf{q}}$ increases. Both these characteristics cause the phonon wavevector \mathbf{q} to be *larger* in order to satisfy the energy conservation, $\varepsilon_{\mathbf{k}+\mathbf{q}} = \varepsilon_{\mathbf{k}} \pm \hbar\omega_{\text{LO}}$ due to the following two reasons: (1) a smaller band curvature leads to a larger $\mathbf{k} + \mathbf{q}$ for a given $\varepsilon_{\mathbf{k}+\mathbf{q}}$, and (2) a larger radius of the energy surface $\varepsilon_{\mathbf{k}+\mathbf{q}}$ leads to an increase in the magnitude of q for the *majority* of q vectors satisfying energy conservation. The \mathbf{k} dependence of the scattering rate can therefore be related to the q dependence in Eq. 2.40. We thus

expect that near $k=0$, for q values small compared to $q_{\infty,scr}$, the rate will be proportional to $q^2/q_{\infty,scr}^4$, while for larger k values, if q becomes larger than $q_{\infty,scr}$, the rate should decrease as $1/q^2$. The behavior in Fig. 6.3 is more complicated, however, due to the following reasons. In Fig. 6.3(a), for 10^{19} cm^{-3} , the decrease at large k can be observed beyond $k = 0.15 \text{ \AA}^{-1}$, but the initial rise near $k=0$ is overshadowed by the presence of a “dip” in the curve near the Fermi level; the origin of this feature will be explained below. Figure 6.3(b), for 10^{20} cm^{-3} , does show the expected rise in the scattering rate for small k values, but a decrease at large k values is not evident. This is due to the large value of $q_{\infty,scr}$ in this case, which requires a much larger q , and hence a larger k , to observe the $1/q^2$ behavior.

The dip in the scattering rate around the Fermi level is a consequence of the energy dependence of the factor in square brackets in Eq. 2.39 that determines the probability of scattering due to emission or absorption of a phonon. For a given phonon mode ν and Fermi level ε_F , $n_{\mathbf{q}\nu}$ is a constant (since phonon energy is independent of \mathbf{q} in the Fröhlich model), and therefore the \mathbf{k} dependence of this factor is due only to the electronic occupation functions $f_{\mathbf{k}+\mathbf{q}}$ multiplied by their respective δ function for phonon absorption and emission. With this information, this factor can be expressed solely in terms of the magnitude of the energy separation between the initial scattering state and the Fermi level, $|\varepsilon_{\mathbf{k}} - \varepsilon_F|$. For initial states located exactly at the Fermi level ($\varepsilon_{\mathbf{k}} = \varepsilon_F$), this factor reaches a minimum at which the combined scattering probability due to emission and absorption is lowest, causing the dip in the scattering rate centered at the Fermi level.

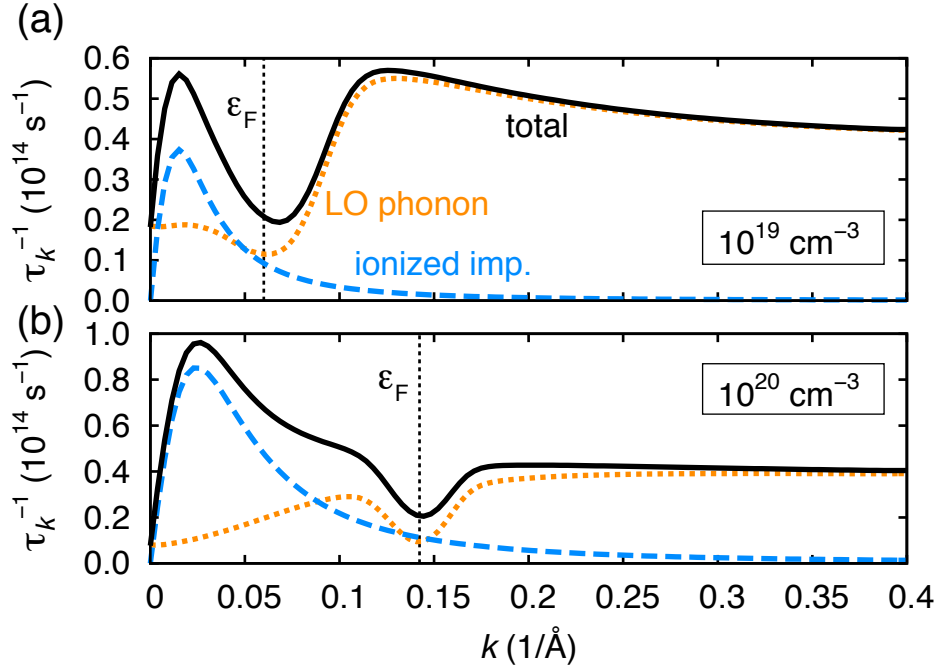


Figure 6.3: (Color online) Calculated scattering rates [10^{14} s^{-1}] versus electron wavevector k (\AA^{-1}) for LO-phonon scattering (orange dotted lines), ionized impurity scattering (blue dashed lines) and the total rate obtained via Matthiessen's rule (black solid lines) at RT (300 K) for electron densities (a) 10^{19} cm^{-3} and (b) 10^{20} cm^{-3} . Values are plotted along $\Gamma \rightarrow X$ but are representative of all directions in the BZ due to the almost isotropic band structure. Note the different vertical scales in panels (a) and (b). The Fermi level ε_F is indicated by vertical dashed lines.

For initial states located below the Fermi level ($\varepsilon_{\mathbf{k}} < \varepsilon_F$), the absorption term, which is proportional to the occupation of the final state dominates [see first term in Eq. 2.39]. The opposite is true for $\varepsilon_{\mathbf{k}} > \varepsilon_F$: the emission term becomes dominant when the final states are unoccupied due to the $(1-f_{\mathbf{k}+\mathbf{q}})$ term, which occurs for initial states occurring above ε_F . As the doping is varied, the center of the dip in $\tau^{-1}(\mathbf{k})$ moves along with the Fermi level, as is evident by comparing the \mathbf{k} dependence of the rates for two different densities in Figs. 6.3(a) and (b).

Finally, we discuss the absolute value of the scattering rate at Γ . This depends on the electron density because of (1) screening, with the rate being proportional to $q^2/q_{\infty,scr}^4$ for small wavevectors, and (2) the dip that moves along with the Fermi level, as discussed above. For $n=10^{19}$ cm $^{-3}$ [Fig. 6.3(a)] the rate at Γ is depressed partly due to the dip near ε_F , and partly due to screening. At electron densities 10^{20} cm $^{-3}$ [Fig. 6.3(b)] and above, the Fermi level is pushed sufficiently high to ensure that the dip does not influence the value at $k=0$, and screening becomes the main effect near Γ ; higher doping leads to more screening and hence decreases the rate (see Eq. 2.40).

The calculated mobility values μ_{LO} based on the k -dependent LO-phonon scattering rates at RT (300 K) are listed in Table 6.2 for various doping levels. Figure 6.3 shows that the scattering rate in the vicinity of the Fermi level (which is what matters for mobility) can be different from the scattering rate at Γ . Therefore, using a scattering rate calculated at Γ in a constant- τ approximation could lead to inaccurate mobilities as well as incorrect trends with electron density (or ε_F). For example, at RT for $n = 10^{20}$ cm $^{-3}$, the mobility calculated using a k -independent scattering rate with the value evaluated at Γ ($\tau_{\Gamma}^{-1} = 0.080 \times 10^{14}$ s $^{-1}$) is 943 cm 2 V $^{-1}$ s $^{-1}$. This value overestimates the actual mobility (calculated taking the \mathbf{k} dependence into account), 594 cm 2 V $^{-1}$ s $^{-1}$. Based on the factor $\partial f_{\mathbf{k}}/\partial \varepsilon_{\mathbf{k}}$ in Eq. 2.38, which renders the mobility sensitive only to rates in the vicinity of ε_F , one would expect a constant τ evaluated at ε_F (τ_{k_F}) to yield more accurate values. However, we find that using $\tau_{k_F}^{-1} (= 0.095 \times 10^{14}$ s $^{-1}$) yields 792 cm 2 V $^{-1}$ s $^{-1}$, which still significantly overestimates the actual mobility by about 33% (200 cm 2 V $^{-1}$ s $^{-1}$). On

the other hand, for $n = 10^{19} \text{ cm}^{-3}$, we find a different trend: using τ_{Γ}^{-1} ($= 0.186 \times 10^{14} \text{ s}^{-1}$) gives a reasonable mobility of $455 \text{ cm}^2\text{V}^{-1}\text{s}^{-1}$ compared to the actual mobility of $487 \text{ cm}^2\text{V}^{-1}\text{s}^{-1}$, whereas using $\tau_{k_{\text{F}}}^{-1}$ ($= 0.116 \times 10^{14} \text{ s}^{-1}$) yields $733 \text{ cm}^2\text{V}^{-1}\text{s}^{-1}$, which is a severe overestimation by about 50% ($246 \text{ cm}^2\text{V}^{-1}\text{s}^{-1}$).

Table 6.2: Calculated drift mobility values (in $\text{cm}^2\text{V}^{-1}\text{s}^{-1}$) at RT (300 K) taking into account scattering due to LO phonons (μ_{LO}), ionized dopants (μ_{imp}), and their total (μ_{tot}) for different electron densities n (cm^{-3}). The corresponding Fermi level ε_{F} (eV) (referenced to the conduction-band minimum, CBM), Fermi wavevector k_{F} (\AA^{-1}), and the screening wavevectors $q_{\infty, \text{scr}}$ (\AA^{-1}) (Eq. 2.41) and q_{scr} (\AA^{-1}) are also given.

n	$\varepsilon_{\text{F}} - \varepsilon_{\text{CBM}}$	k_{F}	$q_{\infty, \text{scr}}$	q_{scr}	μ_{LO}	μ_{imp}	μ_{tot}
10^{17}	-0.079	0.036	0.013	0.006	321	29850	307
10^{18}	-0.017	0.036	0.038	0.018	389	5195	318
10^{19}	0.074	0.063	0.083	0.039	487	1445	329
10^{20}	0.354	0.142	0.137	0.063	594	666	305
10^{21}	1.343	0.307	0.240	0.111	530	290	183

We note that for nondegenerate doping, where the Fermi level lies in the band gap, the reasoning based on $\partial f_{\mathbf{k}}/\partial \varepsilon_{\mathbf{k}}$ leads us to expect that using τ_{Γ} should give reasonably accurate mobility values. Indeed, for $n=10^{17} \text{ cm}^{-3}$, using $\tau_{\Gamma}^{-1} = 0.263 \times 10^{14} \text{ s}^{-1}$ gives a mobility of $334 \text{ cm}^2\text{V}^{-1}\text{s}^{-1}$, in good agreement with the \mathbf{k} -dependent τ calculation value $321 \text{ cm}^2\text{V}^{-1} \text{ s}^{-1}$. However, for $n=10^{18} \text{ cm}^{-3}$, $\tau_{\Gamma}^{-1} = 0.178 \times 10^{14} \text{ s}^{-1}$ results in $487 \text{ cm}^2\text{V}^{-1}\text{s}^{-1}$, a serious overestimate compared to the actual value of $389 \text{ cm}^2\text{V}^{-1}\text{s}^{-1}$ obtained using the full \mathbf{k} dependence of τ . This example demonstrates that using the rate at Γ is a good approximation only for low doping concentrations, corresponding to Fermi levels well below the CBM, where only carriers very close to Γ contribute to transport.

For higher doping levels there is no justification for using a constant- τ value determined either at the Γ or near ε_F .

Figure 6.4 shows the temperature dependence of the mobility based on LO-phonon scattering: the mobility decreases by more than two orders of magnitude going from 50 K to 300 K. This strong dependence results from the phonon occupation factor $n_{q\nu}$ entering into the LO-phonon scattering rate (Eq. 2.39). This behavior as a function of temperature is similar for all electron concentrations. Figure 6.4 also shows the contributions to the mobility due to the individual LO phonon modes. As expected, at low temperatures (0–100 K), only the lowest frequency mode (LO₁) is occupied and contributes to limiting the mobility. Starting at 100 K the LO₂ mode (51 meV) gets populated. The highest energy (88 meV) LO₃ mode starts contributing to scattering at temperatures above 250 K.

LO-phonon contributions to mobility are often fitted [34, 35, 168] to an expression that is inversely proportional to the BE distribution as derived by Low and Pines [169] for a single LO mode. For materials with multiple LO modes, such as the perovskite oxides, the fits are performed by adding the reciprocal mobilities due to each mode with some assumption or knowledge about which modes dominate in the temperature range of interest [34, 168]. To assess the validity of such a procedure, we fitted our calculated mobilities due to the individual LO phonon modes to a BE-distribution-like term, as well

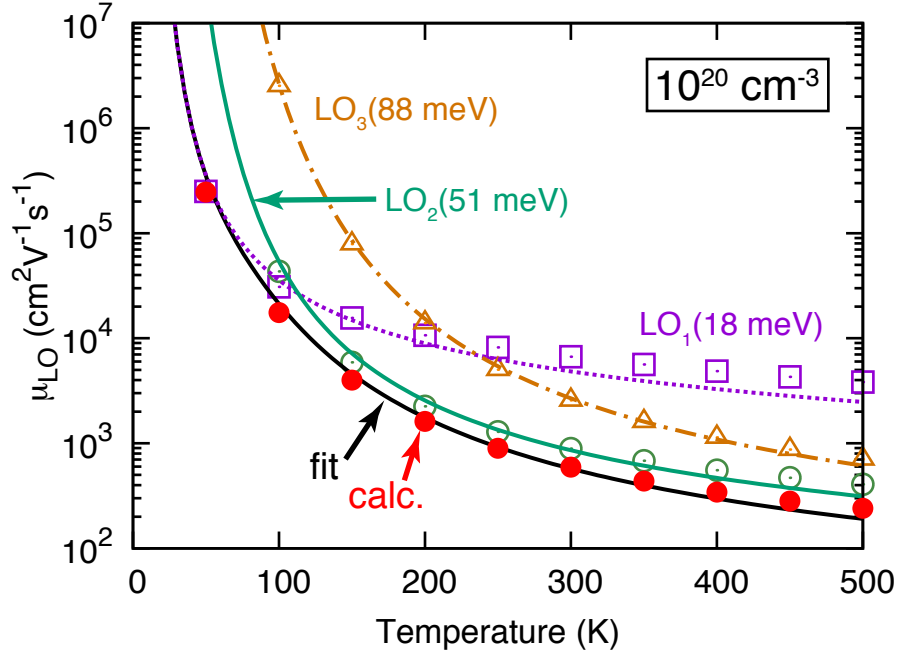


Figure 6.4: (Color online) Calculated mobility *versus* temperature for LO-phonon scattering (μ_{LO}) (solid red circles) for $n=10^{20} \text{ cm}^{-3}$. The calculated mobility due to scattering from the individual phonon modes is shown: μ_{LO1} (purple open squares), μ_{LO2} (green open circles), and μ_{LO3} (orange triangles) with energies 18, 51 and 88 meV, respectively. The lines are analytic fits for the mobilities based on the BE distribution (see text): μ_{LO} (black solid line), μ_{LO1} (purple dotted lines), μ_{LO2} (green dashed line), and μ_{LO3} (orange dash-dot line).

as their combined mobility by summing their reciprocals:

$$\mu_{\text{LO}}^{-1} = \mu_{\text{LO1}}^{-1} + \mu_{\text{LO2}}^{-1} + \mu_{\text{LO3}}^{-1} = \sum_{\nu} \frac{c_{\nu}}{\exp\left(\frac{\hbar\omega_{\nu}}{k_{\text{B}}T}\right) - 1}, \quad (6.4)$$

where c_{ν} is the fitting coefficient corresponding to the phonon mode ν with energy $\hbar\omega_{\nu}$. The fits for the individual modes (see Fig. 6.4) perform very well when $k_{\text{B}}T \ll \hbar\omega_{\text{LO}}$, consistent with the fact that the expression was derived in the low-temperature limit by Low and Pines [169]. At higher temperatures, the fits tend to slightly underestimate the mobility.

6.4.2 Ionized impurity scattering

We now proceed to calculate ionized impurity scattering, based on Eq. 2.45. The \mathbf{k} dependence of the scattering rate is shown in Fig. 6.3, we observe that the behavior is linear in k near Γ , and decreases as k^{-3} beyond the peak. The resulting mobility values calculated at RT are included in Table 6.2 for doping densities 10^{17} – 10^{21} cm^{-3} . Fig. 6.5 shows the temperature dependence of the drift mobility for various doping densities. For doping densities below 10^{19} cm^{-3} , the mobility depends strongly on temperature, while for higher doping densities the mobility is temperature independent. Inspection of Eq. 2.38 shows that the temperature dependence arises from $\partial f_{\mathbf{k}}/\partial \varepsilon_{\mathbf{k}}$ centered around the Fermi level ε_{F} with a temperature-dependent width. The screening wavevector q_{scr} appearing in Eq. 2.45 is also dependent on $\partial f_{\mathbf{k}}/\partial \varepsilon_{\mathbf{k}}$ (see Eq. 2.41). Therefore, any temperature dependence in the mobility should come primarily from $\partial f_{\mathbf{k}}/\partial \varepsilon_{\mathbf{k}}$ and ε_{F} .

As the temperature decreases two changes occur: (1) the width of $\partial f_{\mathbf{k}}/\partial \varepsilon_{\mathbf{k}}$ narrows and approaches a δ function at 0 K, and (2) the Fermi level ε_{F} itself increases. Both these dependences affect the mobilities when the scattering rate varies rapidly with energy (or k) around the Fermi level. This is indeed the case for the ionized impurity scattering rate close to Γ , i.e., for ε_{F} near or below the CBM. Test calculations for 10^{18} and 10^{19} cm^{-3} in which the width of the Fermi derivative $\partial f_{\mathbf{k}}/\partial \varepsilon_{\mathbf{k}}$ as well as ε_{F} itself were fixed to their values at 300 K confirmed this reasoning; the resulting mobilities showed no temperature dependence. At doping densities above 10^{19} cm^{-3} the variation of the rate around the Fermi level is slow, resulting in a very weak temperature dependence of the mobilities.

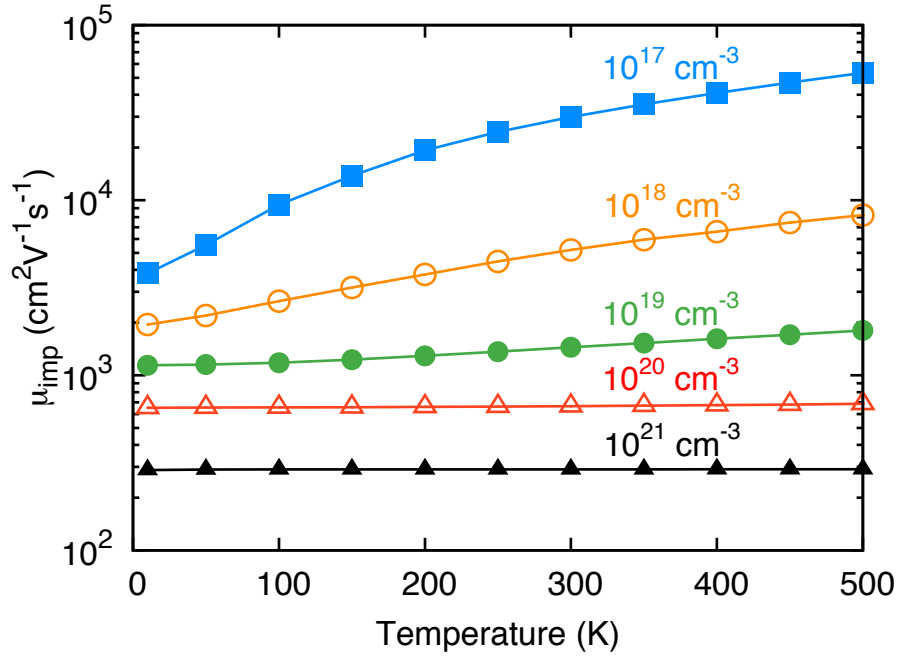


Figure 6.5: Calculated drift mobility *versus* temperature in the case of ionized impurity scattering (μ_{imp}) for five different electron densities: 10^{17} (blue squares), 10^{18} (orange open circles), 10^{19} (green solid circles), 10^{20} (red open triangles), and 10^{21} (black closed triangles) cm^{-3} .

6.4.3 Total drift mobility

We now combine the effect of LO-phonon and ionized impurity scattering via Matthiessen's rule, $\tau_{\text{tot}}^{-1} = \tau_{\text{LO}}^{-1} + \tau_{\text{imp}}^{-1}$. The temperature dependence of the total drift mobility [see Fig. 6.6] shows the typical behavior [170]: ionized impurity scattering dominates at low temperatures, and as the temperature increases LO-phonon scattering reduces the mobility. At RT and for doping densities less than 10^{18} cm^{-3} , the total mobility (see Table 6.2) is limited mainly by LO-phonon scattering. At higher doping levels impurity scattering plays an increasingly important role. This highlights the importance of efforts to reduce ionized impurity scattering, as discussed in Sec. 6.5.3.

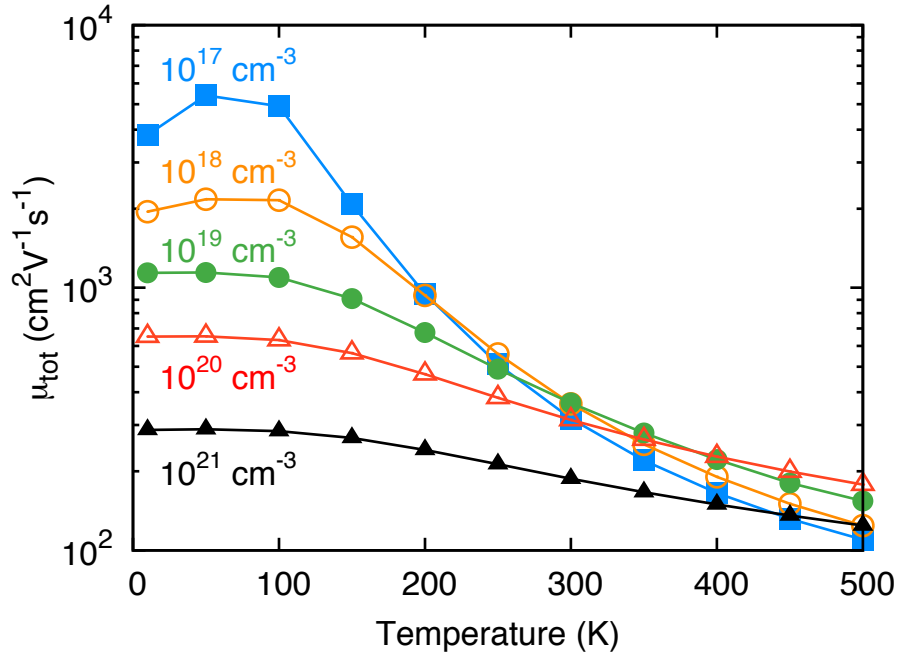


Figure 6.6: Calculated drift mobility *versus* temperature due to a combination of LO-phonon and ionized impurity scattering (μ_{tot}) for five different electron densities: 10^{17} (blue squares), 10^{18} (orange open circles), 10^{19} (green solid circles), 10^{20} (red open triangles), and 10^{21} (black closed triangles) cm^{-3} .

6.4.4 Mobility *vs.* electron density

The trends in the RT mobility-*vs.*-density (μ -*vs.*- n) as well as the dominant scattering mechanism at a given doping level can be visualized more clearly from Fig. 6.7. First, we discuss the trends for the two scattering mechanisms individually. Ionized impurities are seen to reduce the mobility with doping as n^m (linear on the log-log plot), where the exponent m is different for the two identifiable density regimes: (1) nondegenerate doping: $n < 10^{18} \text{ cm}^{-3}$, when the Fermi level lies in the band gap, where the mobility decreases as $\sim n^{-0.75}$, and (2) degenerate doping: $n > 5 \times 10^{18} \text{ cm}^{-3}$, when the Fermi level is above the CBM, where the mobility decreases more slowly as $\sim n^{-0.33}$. As discussed in

Sec. 6.3, we have set $n = N_{\text{imp}}$ for an ionized donor of +1 charge. In the nondegenerate doping regime, screening is weak (q_{scr} is small) and the factor outside the square brackets in Eq. 2.45 dominates and yields a N_{imp}^{-1} dependence, close to but not quite equal to the $N_{\text{imp}}^{-0.75}$ behavior extracted from the full results in Fig. 6.7. In the degenerate doping regime, screening is significant (large value of q_{scr}), and the factor within square brackets in Eq. 2.45 becomes important. An expansion of Eq. 2.45 for large q_{scr} shows that the mobility should decrease as $N_{\text{imp}}^{-1} q_{0,\text{scr}}^4 \propto n^{-1/3}$, in agreement with the behavior in Fig. 6.7(a). Here we have used $q_{\text{scr}} \sim n^{1/6}$ from Thomas-Fermi theory for degenerate doping.

For LO-phonon scattering, we find that screening plays a significant role for densities 10^{18} cm^{-3} and higher, as seen by comparing mobilities with and without screening in Fig. 6.7(b). To elucidate the role played by the band structure and the Fermi level, we focus on the *unscreened* case. Based on the physics, three distinct regions can be identified in the μ -vs.- n curve: (1) for low densities $\leq 10^{18} \text{ cm}^{-3}$, the mobility is fairly constant, at $\sim 300 \text{ cm}^2\text{V}^{-1}\text{s}^{-1}$; (2) for densities in the range 10^{18} – 10^{19} cm^{-3} , the mobility decreases slightly to $\sim 200 \text{ cm}^2\text{V}^{-1}\text{s}^{-1}$; and (3) for doping densities $> 10^{19} \text{ cm}^{-3}$, the mobility increases with electron density from ~ 200 to $\sim 300 \text{ cm}^2\text{V}^{-1}\text{s}^{-1}$. The effect of screening is to increase the mobility with increasing density.

In Region 1 the Fermi level lies below $\varepsilon_{\text{CBM}} + \hbar\omega_{\text{LO1}}$, where $\hbar\omega_{\text{LO1}} = 18 \text{ meV}$ is the lowest LO-phonon energy among the three LO modes. This makes emission of LO phonon almost impossible, since most of the carriers are at the CBM and do not have

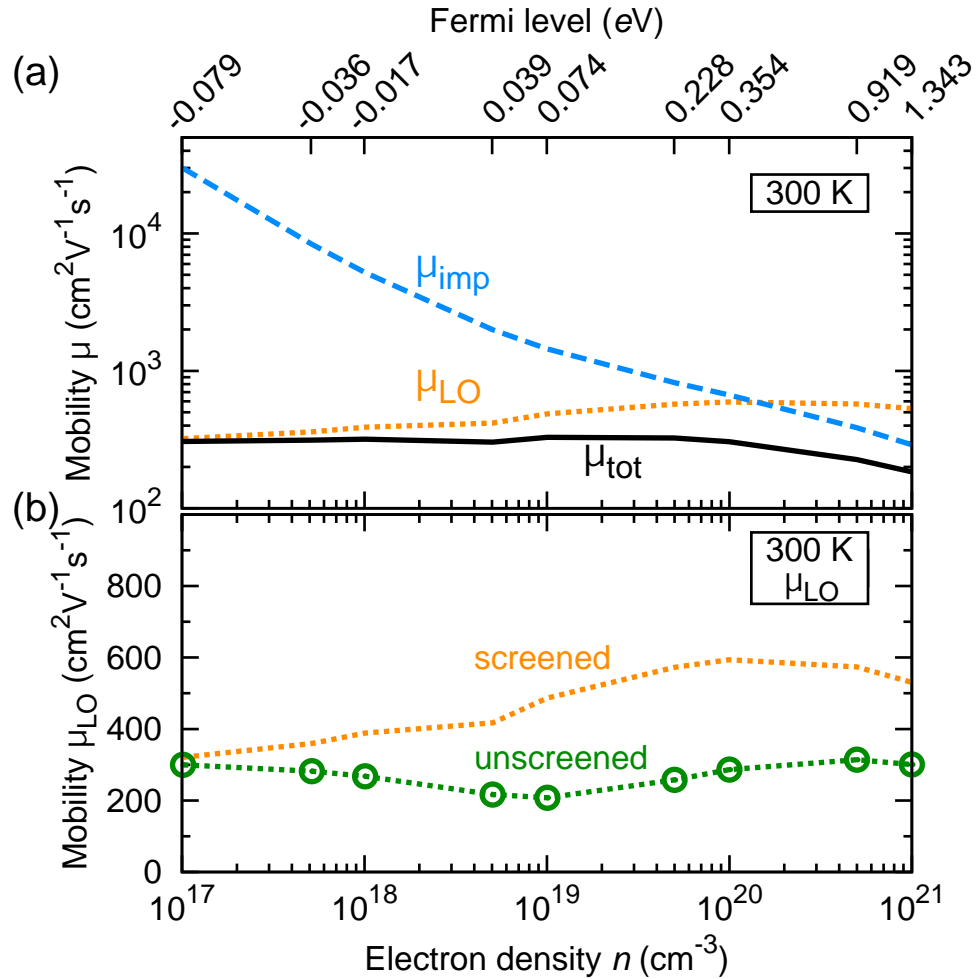


Figure 6.7: (a) Calculated drift mobility *versus* electron density (cm^{-3}) at 300 K (RT) for LO-phonon scattering, μ_{LO} (orange dotted line), and ionized impurity scattering, μ_{imp} (blue dashed line), as well as the total drift mobility, μ_{tot} (black solid line). (b) Comparison of the screened (orange dotted line) and unscreened (green open circles on dotted line) values for μ_{LO} *versus* electron density.

any states below to relax to after emission. Phonon absorption remains as the only LO-phonon scattering process, and determines the mobility. As the Fermi level moves above $\varepsilon_{\text{CBM}} + \hbar\omega_{\text{LO1}}$ with doping, we enter Region 2, where LO-phonon emission becomes possible and reduces the mobility. Raising the Fermi level further (Region 3) results in an *increase* in mobility, which can be attributed to a decrease in band curvature and a

larger energy surface as discussed in Sec. 6.4.1. In the presence of screening, for densities greater than 10^{18} cm^{-3} , it is the screening wavevector $q_{\infty, \text{scr}}$ that mainly determines the mobility by enhancing it.

Overall, however, the *total* mobility is seen to decrease with increasing electron density [Fig. 6.7(a)] due to the strong contribution from ionized impurity scattering. On comparing μ_{LO} and μ_{imp} , it is clear that ionized dopants affect the RT mobility already at densities $n > 10^{18} \text{ cm}^{-3}$, and are the dominant source of scattering for $n > 10^{20} \text{ cm}^{-3}$. For $n > 10^{18} \text{ cm}^{-3}$, dopants in combination with LO-phonon scattering limit the total mobility to less than $330 \text{ cm}^2\text{V}^{-1}\text{s}^{-1}$. Below $n = 10^{18} \text{ cm}^{-3}$, the limit is determined by LO-phonon scattering, but the lack of screening results in a lower mobility of $\sim 300 \text{ cm}^2\text{V}^{-1}\text{s}^{-1}$. Of course, reducing the doping would also reduce the conductivity; it is therefore important to consider doping techniques that can mitigate impurity scattering without sacrificing the carrier concentration and conductivity. We will discuss two such techniques in Sec. 6.5.3.

6.5 Discussion

6.5.1 Comparison with experimental measurements

Our discussions thus far have focused on the drift mobility. However, all of the transport measurements on BSO [36, 37, 147, 148, 164], with the exception of one report of transistor-based measurements [146] on thin films, have been based on Hall mea-

surements. To allow for a direct quantitative comparison with experiments we need to compute the Hall mobility, which is related to the drift mobility μ via the Hall factor r_H as given in Eq. 2.46.

Due to its dependence on $\tau(\mathbf{k})$, the Hall factor r_H calculated using Eq. 2.47 depends on the scattering process, and shows a strong dependence on carrier concentration (see Fig. 6.8) as well as temperature. With increasing carrier concentration, as the Fermi level approaches the CBM and moves above into the CB, r_H decreases and saturates to a constant value of ~ 1.09 for LO-phonon scattering, and ~ 1.03 for ionized impurity scattering.

We now explicitly compare the temperature dependence of our calculated Hall mobility μ_H with experiment. We focus on the highest mobility values reported to date, from experiments on bulk single crystals [37] as well as thin films [148].

6.5.1.1 Bulk crystals

In Fig. 6.9(a) we show experimental values for bulk single crystals measured by Kim *et al.* [37] Their 300 K value at $8 \times 10^{19} \text{ cm}^{-3}$ doping, $320 \text{ cm}^2\text{V}^{-1}\text{s}^{-1}$, is the highest RT mobility reported to date. When comparing with experimental measurements it is important to recognize that scattering mechanisms in addition to the LO-phonon and ionized impurity scattering may be present, for instance due to the presence of point defects such as compensating centers and neutral impurities, as well as extended defects such as dislocations or grain boundaries. At large carrier densities ($> 5 \times 10^{19} \text{ cm}^{-3}$), we

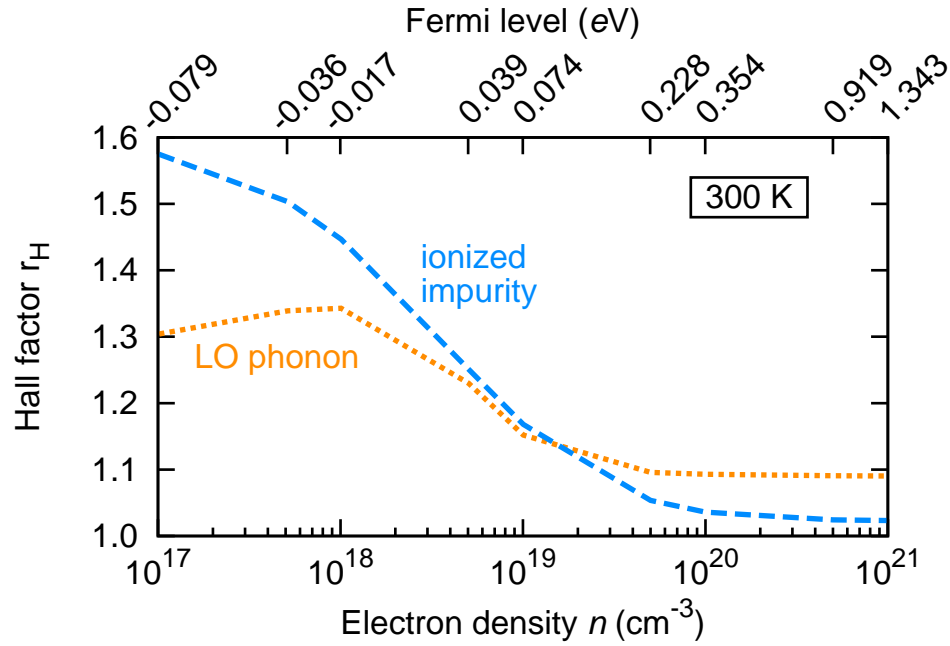


Figure 6.8: (Color online) Calculated Hall factor r_H versus carrier concentration for ionized impurity (blue dashed line) and LO-phonon scattering (orange dotted line).

find ionized impurity scattering to be temperature independent (see Fig. 6.5); and neutral impurity scattering is also temperature independent [171]. Therefore, we take these additional mechanisms into account via a *temperature-independent* mobility contribution μ_{add} chosen to reproduce the experimental *low-temperature* mobility value.

Taking these additional contributions into account, the calculated Hall mobilities for $8 \times 10^{19} \text{ cm}^{-3}$ and $1.2 \times 10^{20} \text{ cm}^{-3}$ doped samples agree very well with experiment. For $8 \times 10^{19} \text{ cm}^{-3}$ doping, $\mu_{\text{add}} = 4500 \text{ cm}^2\text{V}^{-1}\text{s}^{-1}$ indicating weak scattering due to other mechanisms. However, for $1.2 \times 10^{20} \text{ cm}^{-3}$, the μ_{add} required for the fit was $1000 \text{ cm}^2\text{V}^{-1}\text{s}^{-1}$. This suggests a significant presence of extended defects, neutral impurities or ionized defects. Wang *et al.* have observed Ruddlesden-Popper type {001} stacking faults in BSO that could explain some of the additional scattering [172]. However,

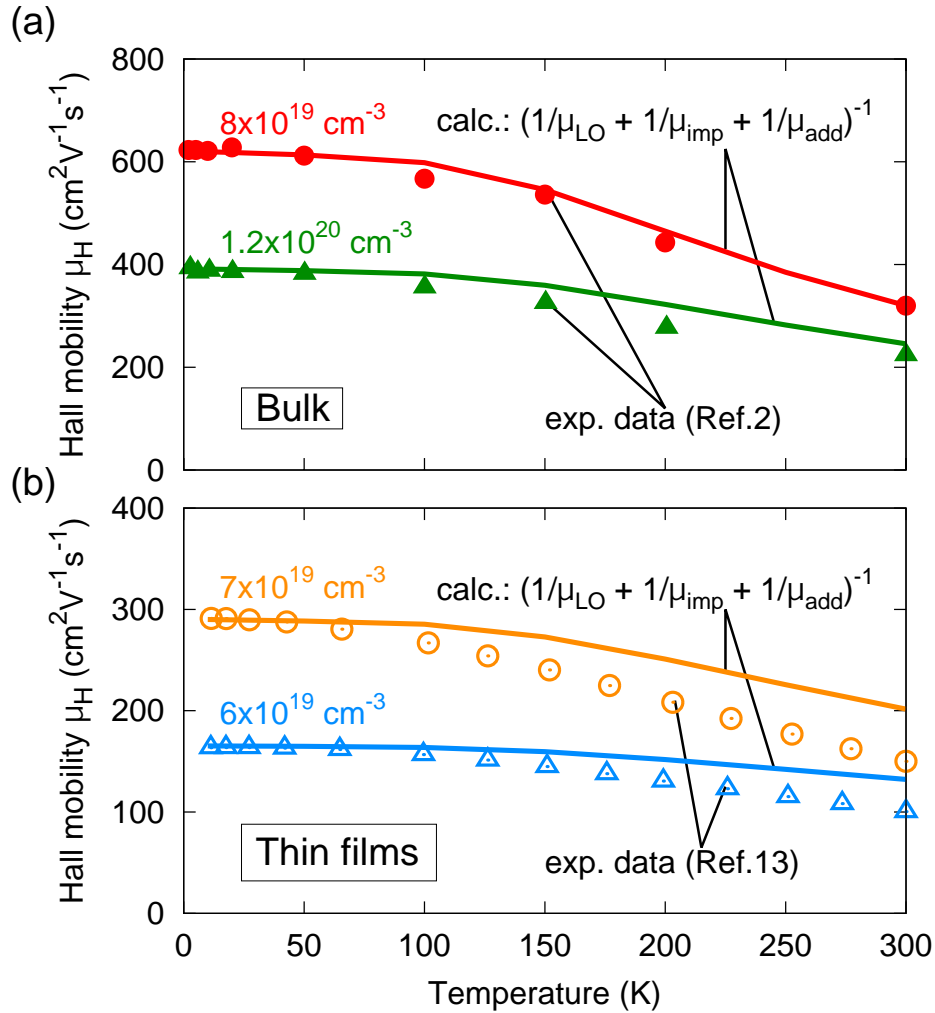


Figure 6.9: (Color online) Solid lines: calculated Hall mobility *versus* temperature due to ionized impurity and LO-phonon scattering, with addition of a temperature-independent scattering contribution: $(1/\mu_{\text{imp}} + 1/\mu_{\text{LO}} + 1/\mu_{\text{add}})^{-1}$, for different experimental doping densities. Symbols indicate the corresponding experimental Hall measurements (a) on bulk crystals from Ref. [37], for $8 \times 10^{19} \text{ cm}^{-3}$ (solid red circles) and $1.2 \times 10^{20} \text{ cm}^{-3}$ (solid green triangles) doping, and (b) on thin films from Ref. [148], for $6 \times 10^{19} \text{ cm}^{-3}$ (open orange circles) and $7 \times 10^{19} \text{ cm}^{-3}$ (open blue triangles) doping. For bulk crystals (a), μ_{add} is $4500 \text{ cm}^2\text{V}^{-1}\text{s}^{-1}$ for $8 \times 10^{19} \text{ cm}^{-3}$, and $1000 \text{ cm}^2\text{V}^{-1}\text{s}^{-1}$ for $1.2 \times 10^{20} \text{ cm}^{-3}$, and for thin films (b), μ_{add} is $210 \text{ cm}^2\text{V}^{-1}\text{s}^{-1}$ for $6 \times 10^{19} \text{ cm}^{-3}$, and $475 \text{ cm}^2\text{V}^{-1}\text{s}^{-1}$ for $7 \times 10^{19} \text{ cm}^{-3}$.

more likely mechanisms, at such large dopant concentrations, include the formation of charge-compensating centers or carrier traps, or of neutral centers due to a decrease in

the fraction of ionized dopants or because the dopant solubility limit is approached. In Ref. [37], Kim *et al.* suggested that ionized impurity scattering was the dominant scattering mechanism in these samples, and neglected LO-phonon scattering in their analysis. In contrast, as evident from our analysis related to Fig. 6.7(a) as well as Fig. 6.9(a), LO-phonon scattering that causes a temperature dependence plays an equally important role in limiting the RT mobility for $\sim 10^{20} \text{ cm}^{-3}$ doping.

6.5.1.2 Thin films

BSO thin films [36,37,38,147,148] exhibit a wide range in measured mobilities, which may reflect variations in growth technique and quality of the films. The highest mobility reported is $150 \text{ cm}^2\text{V}^{-1}\text{s}^{-1}$ in thin films grown using molecular beam epitaxy [148]. In Fig. 6.9(b) we show an analysis similar to that used for bulk samples in Sec. 6.5.1.1 to compare our calculated Hall mobility with the experimental values of Ref. [148]. Our analysis of the temperature dependence in thin films suggests strong additional scattering mechanisms to be present compared to bulk. These additional scatterers could be related to dislocations or grain boundaries due to lattice mismatch with the substrate, as noted in the experimental reports [37, 38, 148]. The temperature-independent contributions necessary to match the low-temperature mobility are $\mu_{\text{add}}=210 \text{ cm}^2\text{V}^{-1}\text{s}^{-1}$ for $6 \times 10^{19} \text{ cm}^{-3}$, and $\mu_{\text{add}}=475 \text{ cm}^2\text{V}^{-1}\text{s}^{-1}$ for $7 \times 10^{19} \text{ cm}^{-3}$. We note that there seem to be additional *temperature-dependent* scattering mechanisms that reduce the mobilities more strongly with temperature than taken into account in our analysis.

One complication in thin films is its finite thickness (30–64 nm) in Ref. [148], which is smaller than or comparable to the average mean free path for electron-phonon scattering (calculated to be $v_{k_F}\langle\tau\rangle = 53$ nm). This suggests that some of the carriers that have a momentum component perpendicular to the boundary will be limited by surface (or substrate-interface) scattering rather than LO phonon scattering [64]. Therefore, in the calculation of mobility in thin films, inclusion of this effect will result in a reduction in mobility, and should be taken into account. In fact, as reported in Ref. [148], increasing the film thickness from 30 nm to 64 nm increases the RT mobility from 100 to 124 $\text{cm}^2\text{V}^{-1}\text{s}^{-1}$. Another finite-size effect is the close proximity to the substrate that could cause additional scattering from substrate phonons.

6.5.2 Comparison to other perovskite oxides

It is striking that the LO-phonon-limited mobility in BSO is about two orders of magnitude higher than in STO [34, 144] and other perovskite oxides with CBs made up of d states [173]. We now show that this result provides some profound insights in the relative impact of various material properties on electron mobility. The higher mobility of BSO has often been attributed to the lower effective mass of the CB. This argument is based on the Drude model, where the mobility is given by $\mu = e\tau/m_{\Gamma}^*$, and assumes the scattering rate to be the same for both BSO and STO. Here we point out that the scattering rates are actually significantly different in the two materials, and have a larger impact on the mobility than the effective masses.

Our calculated scattering rate in BSO, $\sim 10^{13} \text{ s}^{-1}$, is an order of magnitude smaller than the scattering rate in STO, $\sim 10^{14} \text{ s}^{-1}$, calculated in Ref. [144]. We now examine the origins of this difference. First, we direct our attention to the strength of electron-phonon coupling. To quantify this strength, we calculated the value of the q -independent factor in the electron-phonon coupling matrix element $|g_{\mathbf{q}\nu}|^2$ (Eq. 2.40) for the second LO mode (LO_2), which we found to be the dominant scattering mode near RT (see Sec. 6.4.1 and Fig. 6.4). Using the LO and TO frequencies from Ref. [174], this coupling factor in STO is computed to be $2.08 \times 10^{-20} \text{ J}^2\text{m}^{-2}$. This value is quite similar to the value computed for BSO, $1.77 \times 10^{-20} \text{ J}^2\text{m}^{-2}$, and hence electron-phonon coupling strength cannot explain the difference in the scattering rate of BSO relative to STO.

The only other differences between BSO and STO that can explain the reduced scattering rate are the CB degeneracy and density of states (DOS). In STO (and most other perovskite oxides) the CB is derived from d orbitals of t_{2g} character and hence is three-fold degenerate near Γ (possibly split by spin-orbit coupling, which is relatively weak in STO). In contrast, BSO has a singly-degenerate CB composed of Sn s orbitals. This implies that in STO, each electronic state can scatter into two more bands via interband processes compared to BSO. In addition, the lower CB dispersion in STO leads to an increase in the DOS. Both these factors lead to an increase in the density of accessible final states in STO, which significantly raises the scattering rate. We conclude that the higher mobility of BSO is not just due to a smaller effective mass, as previously empha-

sized [36,149]. but more importantly to a significant reduction in the DOS that reduces the scattering rate.

This insight provides valuable guidance for selecting perovskite oxides for high-mobility applications. The requirement of a small DOS does not necessarily mean that materials with CB derived from d orbitals cannot exhibit high mobilities. Any phenomena, such as spin-orbit coupling or biaxial strain, that remove the CB degeneracy by separating one or more bands away from the lowest CB by an amount exceeding the dominant LO phonon energy will reduce the scattering rate, and can enhance the mobility in perovskite oxides [144].

6.5.3 Enhancing mobility in BaSnO_3

From our discussion in Sec. 6.4.4, it is clear that ionized impurity scattering significantly limits the mobility in BSO, particularly at higher doping densities. If high conductivity is required in bulk crystals or thick films, the presence of ionized impurities cannot be avoided since dopants are required for introducing electrons into the CB. The problem of ionized impurity scattering has been recognized as the dominant mechanism limiting mobility at high doping in other TCOs as well [143]. In thin films, however, techniques are available to avoid or mitigate ionized impurity scattering.

One approach is to separate the ionized dopants from carriers in the channel; this has been the basis of several semiconductor heterostructure designs [170]. A commonly used technique is modulation doping, where the dopants are introduced not in the channel,

but in the barrier material [170] Carriers from the dopants transfer into the channel forming a two-dimensional electron gas (2DEG), and are less prone to dopant scattering due to their spatial separation from the dopants. BSO could benefit from such a doping technique provided appropriate barrier materials are identified. In Chapter [41].

Perovskite oxides, including BSO, can also be doped by another technique, namely polar-discontinuity doping [6, 12, 21, 82]. This approach takes advantage of the polar discontinuity that exists, for particular interface orientations, between a nonpolar material (BSO, STO) and a polar perovskite oxide such as LaAlO_3 , GdTiO_3 , LaInO_3 , or KTaO_3 . This polar discontinuity leads to the formation of an intrinsic 2DEG with a theoretical maximum density of $1/2$ electron per interface atom ($\sim 10^{14} \text{ cm}^{-2}$) in the nonpolar oxide, provided that the conduction-band offset is sufficiently high to confine the carriers. Since the doping is intrinsic to the interface, carriers appear in the channel without the need for extrinsic doping. The host atoms in the interfacial layer effectively act as donors, but since they are arranged in a periodic lattice they do not give rise to scattering. This eliminates ionized impurity scattering, and thus in principle offers mobilities close to the phonon-scattering-limited value.

STO has been the material of choice to explore polar-discontinuity doping [6, 12] as well as other functional properties [175] in perovskite oxides, but it suffers from a low RT mobility of $\sim 10 \text{ cm}^2\text{V}^{-1}\text{s}^{-1}$ [34, 144]. BSO, which has an intrinsic RT mobility in the range of $300\text{--}600 \text{ cm}^2\text{V}^{-1}\text{s}^{-1}$ [Table 6.2] thus presents an interesting high-mobility alternative to STO. However, the low DOS of BSO makes confining the 2DEG within the

channel challenging; a careful design of the heterostructure barriers with a large enough CB offset is necessary. These issues related to confinement and DOS will be quantitatively addressed in the next chapter, Chapter 7, using Schrödinger-Poisson simulations. The results for the simulations have also been reported in Ref. [41], along with the design guidelines for BSO heterostructures based on modulation doping and polar-discontinuity doping.

6.6 Conclusion

In summary, we have used first-principles analysis along with a careful numerical procedure to calculate the mobility of BSO from Boltzmann transport theory within the relaxation time approximation, accounting for LO-phonon scattering as well as ionized impurity scattering. We find that the surprisingly large mobility of BSO stems not only from the small effective mass (as had been previously suggested), but is also due to a significant reduction in the LO-phonon scattering rate compared to other perovskite oxides. The reduction in the rate is shown to be due to a decrease in the number of states that the electrons can scatter into because of the low DOS in BSO. Ionized impurity scattering was found to be a significant scattering mechanism, even at RT, limiting the mobilities to less than $330 \text{ cm}^2\text{V}^{-1}\text{s}^{-1}$ for dopant densities above 10^{19} cm^{-3} . Ionized impurity scattering can be avoided by using modulation doping or polar-discontinuity doping, which may enable achieving LO-phonon-limited mobility values, which are calculated to exceed $500 \text{ cm}^2\text{V}^{-1}\text{s}^{-1}$ for electron concentrations $> 1 \times 10^{19} \text{ cm}^{-3}$.

Chapter 7

Evaluating BaSnO_3 as a channel material

The high-density 2DEG in SrTiO_3 at an interface with a polar material is very attractive for electronic applications. However, in order to realize a practical device, the carrier mobility at room temperature (RT) is an important property of channel material to be considered. In Chapter 6, we computed the electron mobility in BaSnO_3 (BSO) to be an order of magnitude higher than in SrTiO_3 . We understood that this large improvement in electron mobility in BSO is due to its low density of states (DOS). BSO is also nonpolar along [001], similar to STO, and can form a high-density 2DEG at an interface with a polar-[001] material, such as LaAlO_3 . However, the low DOS in BSO raises the question of whether the high-density 2DEG formed at the interface would be confined within BSO.

In this chapter, we will study the aspect of 2DEG confinement in BSO with perovskite oxide barrier materials using Schrödinger-Poisson (SP) simulations.

7.1 Introduction

BaSnO₃ (BSO) is a cubic perovskite that has been recognized as a transparent conducting oxide (TCO) [176]. It has gained attention owing to the recent experimental demonstrations [177, 178] of room-temperature mobilities ($320 \text{ cm}^2\text{V}^{-1}\text{s}^{-1}$) higher than most TCOs [143]. This room-temperature mobility is also the highest ever observed for a perovskite oxide, and about two orders of magnitude larger than that of the widely used SrTiO₃ (STO) [34]. Recently, bulk single crystals of BSO have been grown using the solution-based PbO-flux method [179]. High-quality thin films of BSO grown using molecular beam epitaxy (MBE) have also been shown to exhibit high mobilities ($\sim 150 \text{ cm}^2\text{V}^{-1}\text{s}^{-1}$) [148]. The properties that make BSO a good TCO also render it suitable as a channel material that can provide high current density and low power dissipation in transistors.

To date, introducing carriers into BSO has relied on La substitutional doping (1–7%) for both bulk and thin films [146, 148, 177, 180]. Such high levels of doping have been shown to cause large impurity scattering and limit the mobility [180]. As we have shown in Chapter 6, the phonon-scattering-limited mobility can be much higher than currently achieved in bulk and thin films [39]. Therefore, identifying alternative methods

of introducing carriers into BSO that minimize impurity scattering could greatly enhance mobility and provide pathways to more efficient transistors.

Here, we will study two methods of introducing carriers into BSO that can minimize impurity scattering: the traditional modulation doping; and doping due to the polar discontinuity at a nonpolar/polar heterojunction. In modulation doping [170], dopants are introduced in a barrier material whose conduction band (CB) lies higher than that of BSO. Electrons from the dopants transfer into BSO forming a two-dimensional electron gas (2DEG) at the interface; this 2DEG is separated from the dopants and therefore less prone to impurity scattering. Various dopant profiles are possible; here we focus on delta doping, where the dopants are introduced as a sheet in the barrier material at a distance d away from the interface (see Fig. 7.1(a)). STO seems like a good candidate for a barrier material: good-quality substrates are available, growth techniques are well established, and high doping can be achieved [12, 89]. What needs to be verified is that the conduction-band offset (CBO) between STO and BSO is adequate to confine the 2DEG.

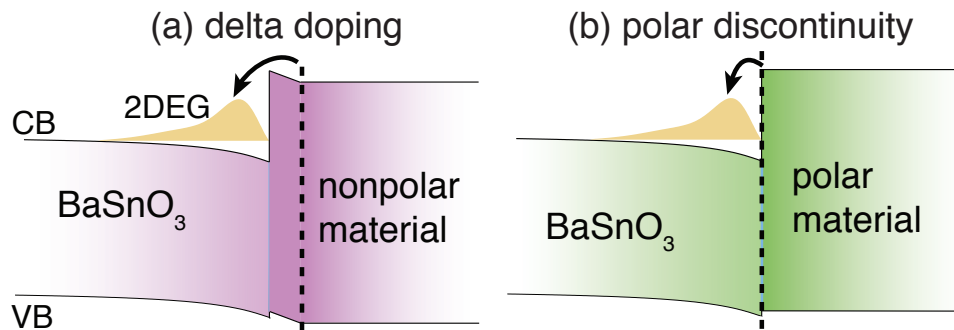


Figure 7.1: Schematic band diagrams depicting (a) delta doping at a nonpolar interface, and (b) polar discontinuity doping at a polar interface.

Unlike modulation doping, polar discontinuity doping does not require dopant introduction but relies on the polar discontinuity at a nonpolar/polar interface [12, 21][see Fig. 7.1(b)]. BSO is nonpolar along [001] consisting of alternating neutral planes of Ba⁺²O⁻² and Sn⁺⁴O₂⁻² (inset of Fig. 7.2). For the polar material, LaInO₃ (LIO) is a good candidate: this polar perovskite is almost lattice matched to BSO with good band offsets [146] and consists of alternating planes of La⁺³O⁻² (net charge of +1 per areal unit cell) and In⁺³O₂⁻² (-1 per areal unit cell). Each LaO plane donates 0.5e⁻ to each of the neighboring InO₂ planes. At a SnO₂-LaO interface between BSO and LIO, 0.5e⁻ per areal unit cell from the LaO plane will transfer to the nonpolar BSO, acting as the intrinsic source of electrons for a high-density 2DEG (2.9×10¹⁴ cm⁻²; calculated assuming in-plane lattice constant of BSO) [see Fig. 7.1]. Another candidate for polar discontinuity doping is KTaO₃ (KTO), which contains alternating planes of K⁺¹O⁻² (charge -1) and Ta⁻⁵O₂⁻² (charge +1).

Whichever the doping method, confining high-density 2DEGs requires a sufficiently large CBO between BSO and the barrier material. This requirement is particularly severe in the case of BSO because of the small density of states (DOS) of its CB, which consists of Sn *s* states and has a small effective mass. The goal of the present work is to quantitatively address the confinement of the 2DEG at BSO interfaces, and discuss strategies for designing and doping the heterostructures. First-principles calculations are performed to obtain the band structure of BSO and its band alignment with STO, LIO

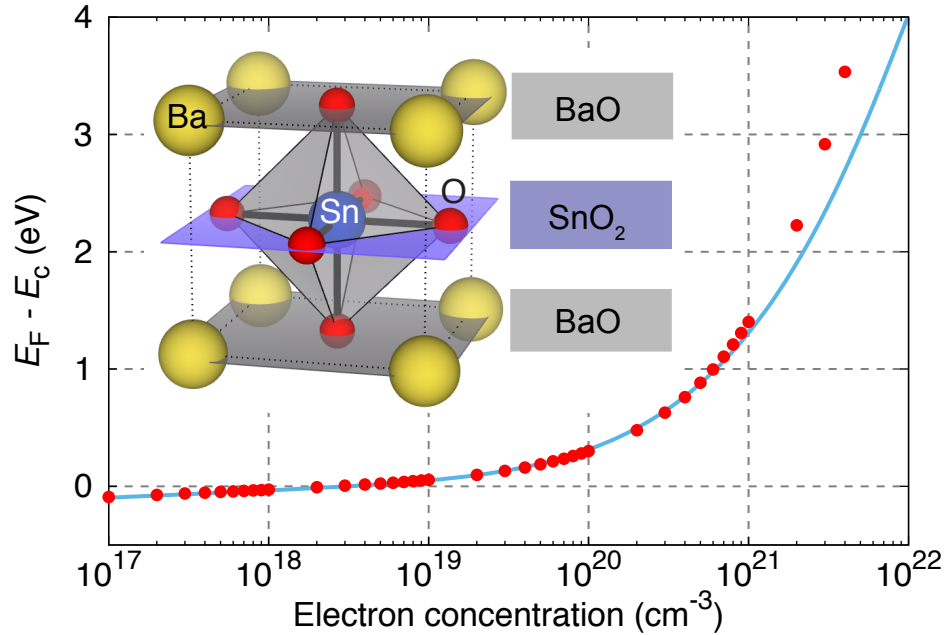


Figure 7.2: Fermi level relative to the CBM ($E_F - E_C$) as a function of electron density in BSO at 300 K based on the first-principles HSE06 band structure (solid blue line) and compared to values obtained from SP simulations (solid red circles) using a parabolic effective mass $m_{\text{fit}} = 0.26 m_e$ that produces the best fit for electron densities upto 10^{21} cm^{-3} . The inset shows the atomic structure of BSO, with alternating planes of BaO and SnO₂ along [001].

and KTO. The calculated parameters serve as input to the SP simulations that quantify the confined 2DEG density.

7.2 First-principles method

The first-principles calculations are based on density functional theory using the HSE06 hybrid functional [108] with the default mixing parameter of 25%. Use of HSE06 not only yields the correct band structure, but also provides accurate positions for the valence and conduction bands on an absolute energy scale [53]. The calculations were

done using the Vienna *Ab initio* Simulation Package (VASP) [58]. For Brillouin-zone integrations, an $8 \times 8 \times 8$ k -point grid was used with the Monkhorst-Pack method for bulk calculations, while a $4 \times 4 \times 1$ grid was used for the interface and surface supercells used to calculate band offsets and vacuum-level alignment. The band alignments reported here are the ‘natural’ band alignments between materials at their equilibrium volume calculated following the methodology described in Ref. [82]. Determination of the Fermi level (E_F) in BSO for a given carrier concentration requires a very fine sampling of the Brillouin zone, which is difficult to achieve with the computationally demanding hybrid-functional approach. E_F is therefore computed from the band structure interpolated on a $100 \times 100 \times 100$ k -point mesh constructed using the maximally-localized Wannier functions [181].

7.3 Band structure and band offsets for BaSnO₃

The calculated lattice parameters are listed in Table 7.1 and are in good agreement with experiment [158,182,183]. BSO, STO, and LAO are cubic; LIO has an orthorhombic structure (GdFeO₃-type with 20 atoms per unit cell). The pseudo-cubic lattice parameter (i.e., the lattice parameter of a cubic structure that would yield the same volume per formula unit as the orthorhombic structure) of LIO is 4.12 Å, indicating a very good lattice match to BSO.

BSO was calculated to have an indirect band gap ($R \rightarrow \Gamma$) of 2.40 eV, in agreement with a previous HSE06 calculation [142]. The direct or indirect nature of the experimental

Table 7.1: Structural and electronic properties of perovskites calculated from first principles (unless otherwise noted). The band offsets reported were calculated by my colleague, Dr. Lars Bjaalie.

Property	BaSnO ₃	SrTiO ₃	KTaO ₃	LaInO ₃
Lattice parameters (Å)	4.13	3.90	3.99	$a = 5.71$ $b = 5.95$ $c = 8.24$
Band gap E_g (eV)	2.40	3.27	3.40	4.33
CBO to BaSnO ₃ (eV)	–	1.14	1.29	2.06
parabolic mass m_{fit} (m_e)	0.26	1.0	1.0	1.0
dielectric const. ϵ (exp.)	20 (Ref. [179])	300 (Ref. [28])	200 (Ref. [184])	39 (Ref. [146])

band gap is still a subject of debate [149,178], with values ranging from 3 to 4 eV. Optical absorption [149] indicates a gap of 3.1 eV, in reasonable agreement with our calculated direct band gap of 2.88 eV at Γ . The lowest conduction band has Sn $5s$ character and is highly dispersive with significant nonparabolicity away from Γ . Fitting the band structure to the hyperbolic dispersion relation $\hbar^2 k^2 / 2m_{\Gamma}^* = E(1 + \alpha E)$ yields an effective mass near Γ , $m_{\Gamma}^* = 0.20 m_e$ and a nonparabolicity parameter $\alpha = 0.21 \text{ eV}^{-1}$. The effective mass away from Γ increases and is dependent on the k -point. A similar hyperbolic fit was performed for STO in Ref. [111] with parameters $m_{\Gamma}^* = 0.39 m_e$ and $\alpha = 0.40 \text{ eV}^{-1}$ for the two degenerate t_{2g} bands, and $m_{\Gamma}^* = 6.1 m_e$ and $\alpha = 2.61 \text{ eV}^{-1}$ for the heavier band along $\Gamma \rightarrow X$.

The band alignments between BSO and the candidate barrier materials was calculated by my colleague, Dr. Lars Bjaalie, using the methodology outlined in Ref. [82], and are reported in Table 7.1 and in Fig. 7.3. The largest CBO offset occurs for LIO, with a value of 2.06 eV. Based on tunneling measurements, Kim *et al.* [146] reported a CBO of

1.6 eV. Their underestimation for the CBO could be related to the effective-mass value assumed in their model. The valence-band offset for the BSO/STO interface were measured by Chambers *et al.* [159], using X-ray photoelectron spectroscopy technique, to be 0.25 eV, which is in excellent agreement with our value of 0.27 eV. The vacuum-level alignment for BSO was calculated for a SnO₂-terminated slab. The electron affinity of 4.20 eV (Fig. 7.3) is remarkably large compared to many complex oxides [82], and explains the ease of doping BSO *n*-type.

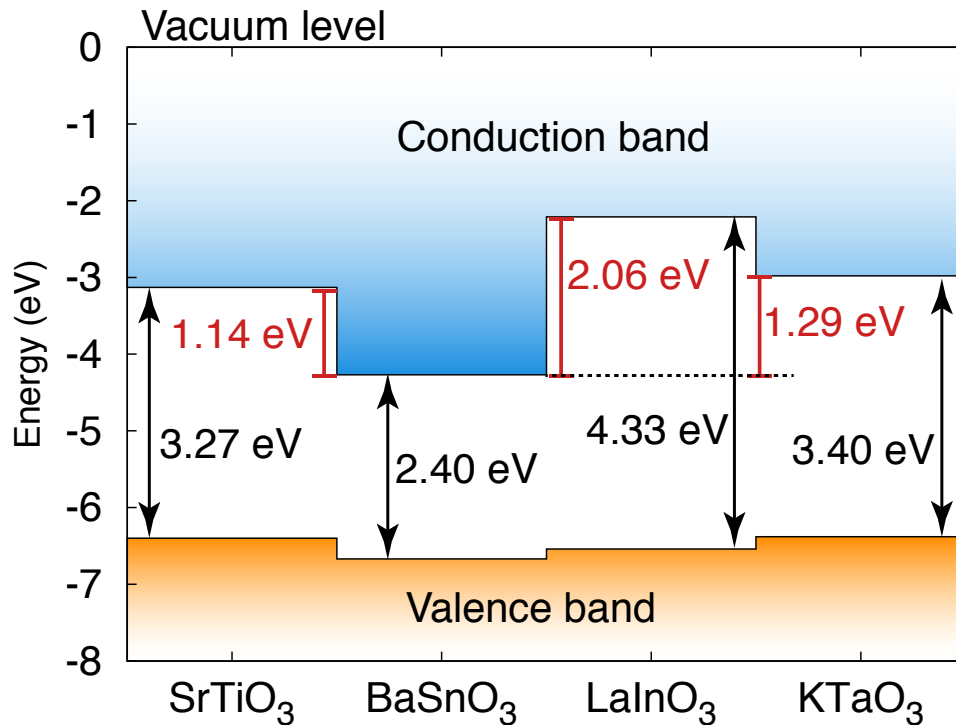


Figure 7.3: Natural band alignment between BSO, STO, LIO, and KTO calculated from first principles. The band alignment calculations were performed by my colleague, Dr. Lars Bjaalie. The BSO band structure was referenced to the vacuum level based on a calculation for an SnO₂-terminated surface.

7.4 Schrödinger-Poisson

Our SP simulations, which are performed within the effective-mass model, are not able to account for nonparabolicity. We therefore introduce a parabolic approximation with an effective-mass value $m_{\text{fit}} = 0.26 m_e$ chosen to accurately reproduce the dependence of E_F on the electron density up to densities of 10^{21} cm^{-3} (see Fig. 7.2); this covers the range relevant for our 2DEG simulations. A similar parabolic fit to reproduce the DOS was performed for STO as well (Table 7.1), and we assumed the same m_{fit} value applied to KTO and LIO, which have CB character similar to STO. Although the small effective mass of BSO is favorable to achieve high mobilities, the resulting low DOS causes E_F to rise rapidly with electron concentration, as shown in Fig. 7.2. This presents an obstacle for achieving adequate carrier confinement in BSO heterostructures, and therefore a careful design of barrier materials with the knowledge of their band offsets is necessary.

We now turn to 1D SP simulations of BSO/STO, BSO/KTO and BSO/LIO heterostructures to study delta doping and polar discontinuity doping in these structures. The simulations, performed within the effective-mass model, use the *nextnano*³ code [185], with the input parameters listed in Table 7.1. The simulated structures consisted of 500 nm of BSO interfaced with 500 nm of barrier material. Delta doping was simulated with dopants placed within a 2 Å region in the barrier at a spacing distance d from the interface; we study $d=2$ nm and 10 nm. Polar-discontinuity doping is simulated by placing dopants within a 2 Å region in the barrier *exactly* at the interface. Varying the doping width to 4 Å changed our calculated 2DEG density by less than 3%, and does

not affect our conclusions. A uniform background doping of 10^{17} cm^{-3} was assumed in BSO to account for unintentional defects or impurities that may be present; this has no discernible effect on our reported 2DEG densities. We assume complete ionization of the dopants.

7.5 Results and Discussion of SP simulations

From our SP simulations shown in Fig. 7.4 we find that in the delta-doped ($d = 2$ nm) BSO/STO heterostructures, which have a CBO of 1.14 eV (Fig. 7.3), the maximum electron density that can be confined in BSO without spillover is $\sim 8 \times 10^{13} \text{ cm}^{-2}$. At this density, the peak of the 2DEG profile occurs at 4 Å from the interface with a value of $5 \times 10^{20} \text{ cm}^{-3}$. The limit on the 2DEG density for a given CBO is due to $E_F - E_c$ approaching the CBO value. For the calculated peak density $5 \times 10^{20} \text{ cm}^{-3}$, the E_F position in bulk would be about 0.9 eV (Fig. 7.2), which is close to the CBO of 1.14 eV. Beyond this density the CBO is not sufficient to prevent the spread of electrons into the barrier material. In addition to the actual spillover of electrons (which reduced the achievable 2DEG density), inadequate confinement leads to penetration of the wavefunctions of the confined electrons into the barrier layer, which is detrimental to the transport properties of the 2DEG. Compared to $d = 2$ nm case, $d = 10$ nm involves a larger electrostatic energy cost to separate the electrons from the dopants, and therefore results in smaller 2DEG densities. Having an abrupt dopant profile closer to the interface thus improves the 2DEG density [89].

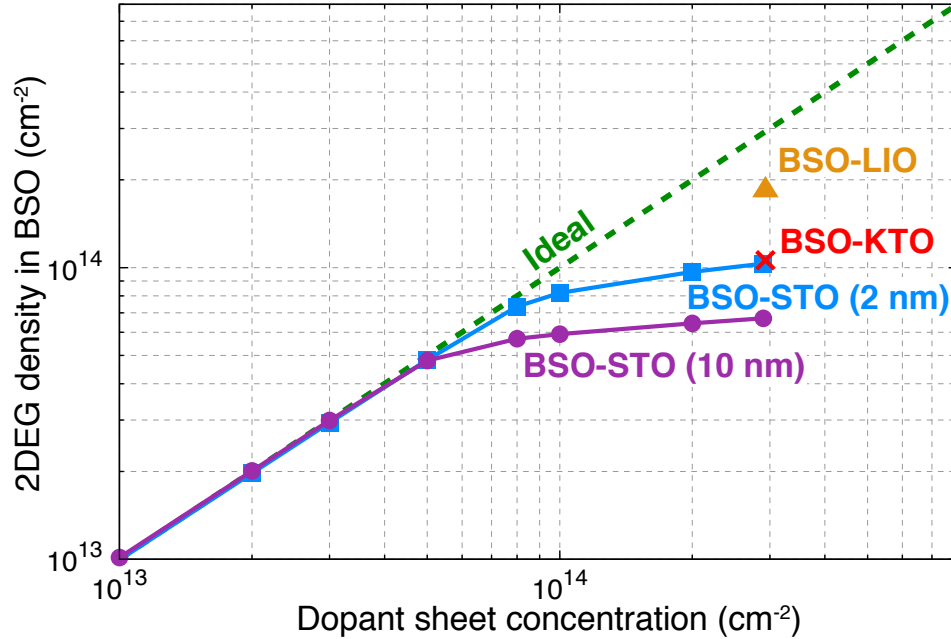


Figure 7.4: Computed 2DEG density confined in BSO as a function of dopant sheet concentration based on SP simulations for delta-doped BSO/STO interfaces with $d=2$ nm (blue solid squares) or 10 nm (purple solid circles). Values for polar-discontinuity-doped BSO/LIO (orange triangle) and BSO/KTO (red cross) interfaces are also shown. The ideal situation, where all the electrons introduced are confined in BSO, is shown as a dashed green line.

At the BSO/KTO and BSO/LIO interfaces, polar discontinuity doping in principle provides an electron density of $2.9 \times 10^{14} \text{ cm}^{-2}$, but a significant fraction of these electrons cannot be confined in the BSO. Spillover occurs even in the case of LIO, which provides the largest CBO (2.06 eV) among the barrier materials studied here.

Higher 2DEG densities could be achieved by using a barrier material (or alloy) that offers a larger CBO to BSO, as illustrated in Fig. 7.5. The results indicate that a CBO of 3.2 eV is necessary to confine a 2DEG of $2.9 \times 10^{14} \text{ cm}^{-2}$. Alloys of STO with SrZrO₃ (SZO) and SrHfO₃ (SHO) have already been used in modulation-doped heterostructures [186]. The CBO of SrZrO₃ with BSO is 2.88 eV, and that of SrHfO₃ is

3.27 eV; both much larger than the CBO of STO [82]. SZO (SHO) has a pseudo-cubic lattice parameter of 4.10 (4.07) Å (Ref. [82]). Alloys of STO with SZO or SHO may therefore provide suitable confinement and also mitigate the lattice mismatch with BSO. For any barrier, with the knowledge of CBO determined experimentally or theoretically, results in Fig. 7.5 can readily be used to estimate the confined 2DEG density.

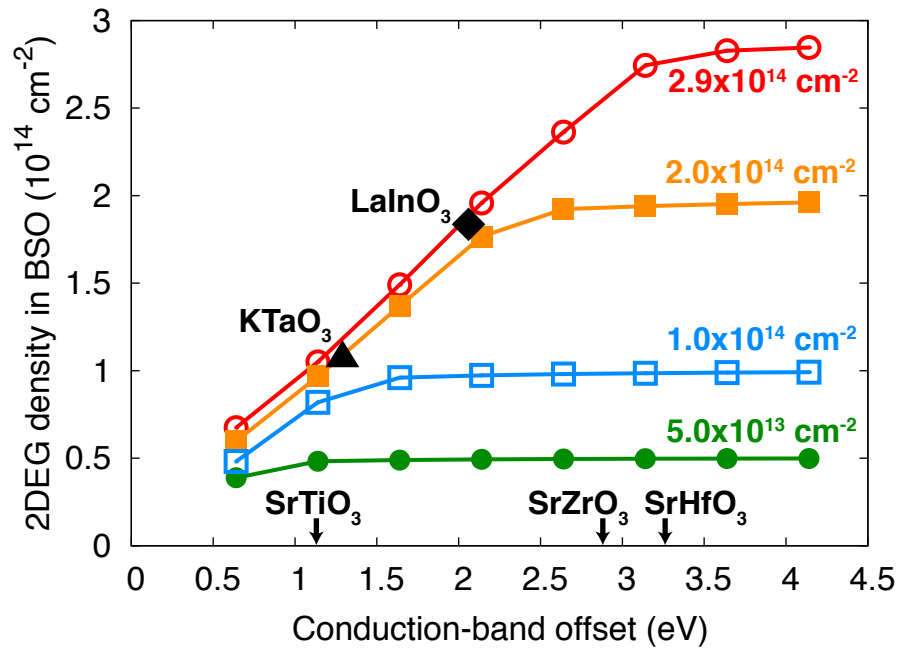


Figure 7.5: 2DEG density confined in BSO as a function of CBO for various sheet dopant concentrations placed at $d=2$ nm in the barrier. The results for the polar BSO/KTO (solid triangle) and BSO/LIO (solid diamond) interfaces are also shown. CBO values for STO, SHO and SZO are indicated by arrows.

7.6 Conclusions

In summary, we used a combination of first-principles calculations and SP simulations to quantify the effects of the low DOS in BSO and the ensuing challenges involved in

confining a high 2DEG density. For the case of polar discontinuity doping, we find that the CBOs of KTO and LIO are insufficient to confine the entire 2DEG density. Modulation-doped nonpolar structures offer more flexibility in device design, with Fig. 7.5 providing a guide for the magnitude of the CBO needed to confine a given carrier density. We propose alloys of STO with SZO or SHO as suitable barrier materials providing good lattice matching and adequate confinement of the 2DEG

Chapter 8

Summary and future prospects

8.1 Overall summary

We began this dissertation with the goal of building a fundamental understanding of the electronic properties of complex oxides in order to facilitate, and aid their wide-scale adoption into future electronic applications and devices. To build such an understanding, we used a combination of first-principles approaches based on DFT to calculate their fundamental properties, and SP simulations to model their behavior at larger length scales. The following issues relating to the high-density 2DEG formed at certain heterointerfaces as well as transport in complex oxides were addressed:

1. In Chapter 3, we used SP simulations to study the effect that the field dependence of the dielectric constant in STO has on the spatial distribution of the 2DEG. Incorporation of the field dependence in an SP solver was accomplished by developing

- a wrapper script that selfconsistently solved for the electric field and the spatial variation of the dielectric permittivity. Inclusion of the field dependence leads to a significant increase in confinement of the 2DEG, which has important implications for the interpretation of experimental measurements related to the 2DEG.
2. In Chapter 4, we addressed the general phenomenon of surface charging using first-principles approaches, and developed a general and rigorous methodology to calculate the energetics of a charged surface. We applied this methodology to the LAO/STO heterostructures to explain the interactions between the LAO surface and the 2DEG at the interface involving electron transfer into LAO surface states. We were able to calculate the 2DEG density that remains at the interface as a function of LAO thickness, accounting for the formation of surface defects.
 3. Applying the methodology for surface charging developed in Chapter 4 to the GTO/STO heterostructures, we find that the transfer of electrons from the 2DEG into GTO surface states seems much less likely compared to the transfer occurring in the LAO/STO system. This difference can be attributed to the fact that the unoccupied GTO surface states lie much closer to the Fermi level of the 2DEG, while unoccupied LAO surface states lie at much lower energies, which favors electron transfer.
 4. In Chapter 6, we built a fundamental understanding of the LO-phonon scattering mechanism in complex oxides by using accurate computational techniques that were

- developed as part of the study. We find that the large DOS (i.e., the number of states a carrier can scatter into) in STO is responsible for its low RT carrier mobility relative to BSO, which has much higher mobility. Based on this insight, we predict that complex oxides having a single conduction band should have a higher mobility compared to complex oxides with multiple conduction bands. This also provides us with a general recipe for identifying or designing high-mobility complex oxides.
5. Finally, in Chapter 7, we performed a quantitative assessment of the confinement of carriers in the 2DEG within BSO. The simulations suggest that the band offsets of BSO with the polar materials, LIO and KTO, are insufficient to confine the full 2DEG density of $3.3 \times 10^{14} \text{ cm}^{-2}$. The results of the simulations should serve as a guide to engineering barriers for BSO-based heterostructures.

Overall, in this dissertation, we have addressed the following aspects of complex oxides: 2DEG properties, surface properties, and carrier mobility. To carry out these studies, we developed three theoretical tools that are general and applicable to other material systems: (1) implementation of the field dependence of dielectric permittivity into an SP solver, (2) a general and rigorous methodology for calculating properties of charged surfaces within DFT, and (3) an accurate computational code to calculate carrier mobility and other transport properties.

In addition to the work explicitly presented in this dissertation, we have carried out two other investigations that have been published in two journal articles:

1. We studied the absolute energetics of reconstructions on neutral LAO surfaces. Some of the results obtained from this work were utilized in Chapter 4. The complete results of the investigation have been published in the journal, *Physical Review B* (Phys. Rev. B 90, 235436 (2015); Ref. [112]).
2. We also studied the impact of hole-trapping defects in III-nitrides using SP simulations to shed light on the microscopic mechanism that causes anomalous dispersion effects in the current-voltage curve, and to explain the lack of a 2D hole gas expected to form due to the polarization mismatch. The results of the investigation have been published in the journal, *IEEE Electron Device Letters* (*IEEE Electron Device Lett.* 37, 154 (2016); Ref. [187]).

8.2 Prospects for future research in complex oxides

Here we address some areas in which the work described in this dissertation can be extended. Additionally, we mention some challenges in complex oxides that can be the subject of future research.

8.2.1 Extensions of the present work

8.2.1.1 Field-dependent dielectric permittivity

In Chapter 3, we modeled the high-density 2DEG at the interface by fully accounting for the field dependence of the dielectric permittivity in STO. The modeling involved

implementing the field dependence into an SP solver, *nextnano*³ with the help of a wrapper script written using the Python programming language. This works very well for our intended purpose. However, for the implementation to be useful to many others, it would be preferable to incorporate the field dependence directly into an SP solver as a single package, instead of having a separate wrapper script. There many other materials, including ferroelectrics, with a field-dependent dielectric permittivity. In principle, the approach demonstrated in this dissertation for STO can be extended to model these materials as well. The outcome of these efforts will enable a more general adoption of SP simulations for materials with a field-dependent dielectric response.

8.2.1.2 Forces in charged surface calculations

In developing the methodology for calculating charged surface energetics in Chapter 4, we took the atomic structure from a calculation for the neutral system. I.e., any additional relaxations resulting from charging of the surface were disregarded. In principle, atomic relaxations can be performed but require a correction for the spurious forces acting on atoms due to interactions with the neutralizing background charges. Here, we briefly outline the methodology that would enable implementation of the force corrections. According to the force theorem [188], the force acting on a nucleus or ion I is given by

$$\mathbf{F}_I = -\frac{\partial E}{\partial \mathbf{R}_I} \quad (8.1)$$

From Eq. 2.13, it is clear that only two terms of the total energy, namely V_{ext} and E_{II} , depend explicitly on the ionic position \mathbf{R}_I . Therefore, from Eq. 2.13, the force on the ion I can be written as

$$\mathbf{F}_I = -\frac{\partial E}{\partial \mathbf{R}_I} = -\int d\mathbf{r} \frac{\partial V_{\text{ext}}(\mathbf{r})}{\partial \mathbf{R}_I} n(\mathbf{r}) - \frac{\partial E_{II}}{\partial \mathbf{R}_I}. \quad (8.2)$$

Unlike the ions that can move in space, the neutralizing background charges are spatially fixed, and therefore the “force” acting on these charges due to the ions or the charge density $n(\mathbf{r})$ need not be corrected. Therefore, the force correction can be accomplished just by removing the force acting on the ions due to the background charge, which is part of the term: $\partial E_{II}/\partial \mathbf{R}_I$.

The force on an ion of charge Q_I due to a uniform background charge of density q/Ω can be obtained from the potential $V_b(\mathbf{r})$ due to the background charge using the relation:

$$\mathbf{F}_I = -Q_I \nabla V_b(\mathbf{r}) \big|_{\mathbf{r}=\mathbf{R}_I}. \quad (8.3)$$

In Chapter 4, we obtained an expression for the macroscopically- x - y -averaged potential $V_b(z)$, which is given by Eq. 4.6. Utilizing Eq. 4.6 in Eq. 8.3 gives the z -component of the spurious force that needs to be corrected due to the background charges acting on ion I .

A major challenge involving the practical implementation of a force correction scheme is to ensure convergence of the corrected forces. The relaxation of the atomic positions

will be performed outside of the DFT code and will be based on the corrected forces that mimic the effect of removing the background charges. The forces calculated internally within the DFT code will account for the background charges, but will use an atomic structure that is not consistent with those forces. Therefore, the specific details of the force correction need to be derived in a rigorous manner, and its practical implementation requires careful consideration.

8.2.1.3 Building on the model for LAO/STO

In Chapter 4, we focused on the surface charging aspect of the LAO/STO heterostructures to describe the transfer of electrons from the 2DEG to the surface. Having established a rigorous model, one can in principle consider additional effects, such as interface stoichiometry, defect-related traps, and carrier localization, and examine their impact on the 2DEG formation.

8.2.1.4 Mobility in thin films of BSO

In Chapter 6, we were able to calculate and explain the temperature dependence of the mobility observed in single crystals of BSO. However, for thin films the comparison between our calculations and experiment indicated that additional mechanisms are at play. It would be worthwhile to explain the physical mechanism that causes the additional temperature dependence in thin films. Such an explanation may point to improvements that could lead to enhanced mobility.

8.2.1.5 Exploring high-mobility complex oxides

Based on the conclusions of our work on transport in complex oxides, we found several pathways that can enhance their electron mobility. A fruitful approach is to identify materials with a low DOS. Among the materials similar to the tin perovskite BSO, germanate perovskites are potential candidates. These materials, with a chemical composition $(\text{Sr}, \text{Ba}, \text{Ca})\text{GeO}_3$, have a nondegenerate conduction band and hence a low DOS. Computing their mobility from first principles will help inform experimentalists to explore this materials space.

8.2.2 General challenges for use of complex oxides in electronic applications

In addition to the aspects of complex oxides addressed in this dissertation—namely, surface charging, confinement of the 2DEG, field-dependent dielectric permittivity, and carrier mobility—there exist other fundamental challenges that need to be considered and addressed at the theoretical as well as experimental levels. Overcoming these challenges could help in the adoption of complex oxides for use in reliable and wide-scale electronic applications. Here, we present two of these challenges.

8.2.2.1 Lack of good conducting *p*-type oxides

Modern circuits based on metal-oxide-semiconductor field-effect transistors (MOS-FETs) rely on using complementary devices, namely *p*-type, and *n*-type devices, to

greatly reduce the power consumption. p -type devices conduct current via holes (unoccupied states near the VBM), and n -type devices conduct via electrons. This is the basis of CMOS technology, which stands for “Complementary Metal-Oxide-Semiconductor”, where the oxide serves as an insulating barrier and the semiconductor serves as the conducting channel [63,189]. Most oxides, in general, can be readily doped n -type. However, achieving p -type conductivity has been very challenging for two major reasons [190,191]: (1) the valence band of oxides is composed of O $2p$ orbitals that are quite localized in nature, and tend to form hole polarons (localized holes accompanied by lattice distortions), and (2) for Fermi levels near the valence band, a necessity for p doping, the formation of donor defects becomes highly likely and tends to compensate any acceptors that might be present. These challenges are fundamental to the nature of oxides. The reason for the compensation of acceptors could be mainly attributed to the valence band, constituted of O $2p$ orbitals, being very low in energy relative to the vacuum level. The presence of holes at such low energies creates an energetically unfavorable situation, which would favor any mechanism that can lead to energy gain. One of the energy-gain mechanisms is compensation by donors, which would lead these low-lying states being occupied. Another mechanism is via the formation of localized hole polarons that raises the position of the unoccupied states to higher energies. Due to these fundamental reasons, finding good p -type complex oxides seems extremely difficult. Some computational efforts using high-throughput discovery are currently being pursued [192]. An alternative approach

would be to design novel devices and circuits that eliminate the need for p -type doped materials while providing the same or better level of functionalities.

8.2.2.2 Electrostatics of modulating large 2DEG densities

One of the most interesting phenomena in complex oxides, from an electronic device perspective, is the extremely dense 2DEG that occurs at a polar/nonpolar heterointerface. However attractive they may seem for devices, to realize an FET, one needs to be able to modulate the large 2DEG density that is on the order of 10^{14} cm^{-2} , which is unprecedented in semiconductors. The modulated charge Q in an FET is related to the applied voltage V through the gate-barrier capacitance C as $Q = CV$. This gate-barrier capacitance is determined by the dielectric constant ϵ of the barrier material and its thickness d as $C = \epsilon\epsilon_0/d$. In a typical MOSFET, using SiO_2 as the barrier material, the modulated charge density is on the order of 10^{12} cm^{-2} . Modulating a charge of 10^{14} cm^{-2} with the same barrier thickness and dielectric constant requires an applied voltage V larger by two orders of magnitude. This increases the electric field in the barrier correspondingly by two orders of magnitude, which can lead to dielectric breakdown. Therefore, modulating such a large 2DEG density poses a difficult challenge: finding the appropriate gate-barrier materials with large dielectric constant. This challenge needs to be overcome to reap the benefits associated with the high-density 2DEG at complex oxide heterostructures. Recently, progress has been made on this front by Rajan *et al.* [193]

using STO as the gate dielectric, which has a large dielectric constant of $\epsilon = 300$ as well as large breakdown voltage.

Appendix A

Reading list

The purpose of this Appendix is to provide a collection of books, some key review articles, and seminal papers that are related to DFT, transport theory, semiconductor theory, device physics, and electron-phonon scattering. The collection could be useful as a starting point for graduate students and others who are interested in these topics.

A.1 Books and review articles

Quantum mechanics

1. H. Kroemer, “Quantum Mechanics for Engineers: Material Science and Applied Physics,” *Pearson* (1994).
2. G. Giuliani and G. Vignale, “Quantum Theory of the Electron Liquid,” *Cambridge University Press* (2005).

Solid state physics and Semiconductors

3. P. Y. Yu and M. Cardona, “Fundamentals of Semiconductors,” *Springer Berlin Heidelberg*, Berlin, Heidelberg (2010).
4. M. S. Dresselhaus, “Lecture notes on Solid State Physics I–IV” (2001).
5. K. Seeger, “Semiconductor Physics” (Springer Berlin Heidelberg, Berlin, Heidelberg, 2004).
6. U. Mishra and J. Singh, “Semiconductor Device Physics” (2008).
7. M. S. Dresselhaus, “Lecture notes on Solid State Physics I–IV” (2001).

Density Functional Theory

8. W. Kohn, *Rev. Mod. Phys.* **71**, 1253 (1999).
9. K. Burke, “The ABC of DFT” <http://dft.uci.edu/doc/g1.pdf>.
10. A. Zangwill, “The education of Walter Kohn and the creation of density functional theory,” *Arch. Hist. Exact Sci.* **68**,775 (2014).
11. R. M. Martin, “Electronic Structure: Basic Theory and Practical Methods,” *Cambridge University Press* (2004).
12. E. Engel and R. M. Dreizler, “Density Functional Theory- An Advanced Course”, *Springer* (1996).

13. M. A. L. Marques, N. T. Maitra, F. M. S. Nogueira, E. K. U. Gross, and A. Rubio, “Fundamentals of Time-Dependent Density Functional Theory,” *Springer Berlin Heidelberg*, Berlin, Heidelberg (2012).
14. M. C. Payne, M. P. Teter, D. C. Allan, T. A. Arias, and J. D. Joannopoulos, “Iterative minimization techniques for ab initio total -energy calculations: molecular dynamics and conjugate gradients,” *Rev. Mod. Phys.* **64**, (1992).
15. R. O. Jones and O. Gunnarsson, “The density functional formalism, its applications and prospects,” *Rev. Mod. Phys.* **61**, 689 (1989).
16. R. O. Jones, “Density functional theory: Its origins, rise to prominence, and future,” *Rev. Mod. Phys.*, **87**, 897 (2015).
17. C. Freysoldt, B. Grabowski, T. Hickel, J. Neugebauer, G. Kresse, A. Janotti, and C. G. Van de Walle, “First-principles calculations for point defects in solids,” *Rev. Mod. Phys.* **86**, 253 (2014).

Transport

18. J. M. Ziman, “Electrons and Phonons: The Theory of Transport Phenomena in Solids”, OUP Oxford (1960).

A.2 Original articles

1. P. Hohenberg and W. Kohn, “Inhomogeneous Electron Gas”, *Phys. Rev.* **136**, B864 (1964).
2. W. Kohn and L. J. Sham, “Self-Consistent Equations Including Exchange and Correlation Effects”, *Phys. Rev.* **140**, A1133 (1965).
3. J. P. Perdew, K. Burke, M. Ernzerhof, “Generalized Gradient Approximation Made Simple”, *Phys. Rev. Lett.* **77**, 3865 (1996).
4. G. Kresse, “Efficient iterative schemes for ab initio total-energy calculations using a plane-wave basis set”, *Phys. Rev. B* **54**, 11169 (1996).
5. G. Kresse, “From ultrasoft pseudopotentials to the projector augmented-wave method”, *Phys. Rev. B* **59**, 1758 (1999).
6. G. Kresse and J. Furthmüller, “Efficiency of ab-initio total energy calculations for metals and semiconductors using a plane-wave basis set”, *Comput. Mater. Sci.* **6**, 15 (1996).
7. P. E. Blöchl, “Projector augmented-wave method”, *Phys. Rev. B* **50**, 17953 (1994).
8. G. Makov and M. C. Payne, “Periodic boundary conditions in ab initio calculations”, *Phys. Rev. B* **51**, 4014 (1995).

-
9. X. Gonze and C. Lee, “Dynamical matrices, Born effective charges, dielectric permittivity tensors, and interatomic force constants from density-functional perturbation theory”, *Phys. Rev. B* **55**, 10355 (1997).
 10. N. Marzari, A. A. Mostofi, J. R. Yates, I. Souza, and D. Vanderbilt, “Maximally localized Wannier functions: Theory and applications”, *Rev. Mod. Phys.* **84**, 1419 (2012).
 11. C. G. Van de Walle and R. M. Martin, “Theoretical study of band offsets at semiconductor interfaces”, *Phys. Rev. B* **35**, 8154 (1987).
 12. C. G. Van de Walle, “Band lineups and deformation potentials in the model-solid theory”, *Phys. Rev. B* **39**, 1871 (1989).

Appendix B

Extended Fröhlich model

Here we derive the expression in SI units for the electron-LO-phonon coupling matrix element based on the Fröhlich coupling modified by inclusion of multiple LO modes.

We start with the expression—derived by Toyozawa (see the derivation leading up to Eq. 3.27 in Ref. [68])—for the electron-phonon coupling potential, $V_{q\nu}$, relating it to the derivative of the frequency-dependent dielectric constant, $\epsilon(\omega)$:

$$V_{q\nu} = \frac{1}{\sqrt{V_{\text{cell}}}} \frac{e}{q} \left(\frac{\hbar}{\epsilon_0 \frac{\partial \epsilon(\omega)}{\partial \omega} |_{\omega_{L,\nu}}} \right)^{1/2}, \quad (\text{B.1})$$

where the frequency-dependent dielectric constant (for n LO and TO modes) is given by the generalized Lyddane-Sachs-Teller relation [68, 69, 194, 195]:

$$\epsilon(\omega) = \epsilon_\infty \prod_{j=1}^n \frac{\omega^2 - \omega_{L,j}^2}{\omega^2 - \omega_{T,j}^2}. \quad (\text{B.2})$$

The Fröhlich coupling constant, α_j , is defined to be

$$V_{q\nu} = \frac{\hbar\omega_{L,\nu}}{q} \frac{e}{q} \left(\frac{\alpha_\nu}{\epsilon_0 V_{\text{cell}}} \right)^{1/2} \left(\frac{\hbar}{2m^*\omega_{L,\nu}} \right)^{1/4}. \quad (\text{B.3})$$

For the n -mode case, the derivative of the dielectric constant with respect to frequency is

$$\frac{\partial\epsilon(\omega)}{\partial\omega}\Big|_{\omega=\omega_{L,\nu}} = \epsilon_\infty 2\omega_{L,\nu} \frac{\prod_{j \neq \nu} \omega_{L,\nu}^2 - \omega_{L,j}^2}{\prod_{j=1}^n \omega_{L,\nu}^2 - \omega_{T,j}^2} \quad (\text{B.4})$$

$$= \epsilon_\infty \frac{2}{\omega_{L,\nu}} \frac{\prod_{j \neq \nu} \left(1 - \frac{\omega_{T,j}^2}{\omega_{L,\nu}^2}\right)}{\prod_{j=1}^n \left(1 - \frac{\omega_{T,j}^2}{\omega_{L,\nu}^2}\right)}. \quad (\text{B.5})$$

Using Eq. B.5 in Eq. B.1, we obtain

$$V_{q\nu} = \frac{1}{q} \left(\frac{e^2 \hbar \omega_{L,\nu}}{2V_{\text{cell}} \epsilon_0 \epsilon_\infty} \right)^{1/2} \left(\left| \frac{\prod_{j=1}^n \left(1 - \frac{\omega_{T,j}^2}{\omega_{L,\nu}^2}\right)}{\prod_{j \neq \nu} \left(1 - \frac{\omega_{T,j}^2}{\omega_{L,\nu}^2}\right)} \right| \right)^{1/2}. \quad (\text{B.6})$$

For a single LO mode, this reduces to the well-known Fröhlich model:

$$V_{q\nu} = \frac{1}{q} \left(\frac{e^2 \hbar \omega_{L,\nu}}{2V_{\text{cell}} \epsilon_0 \epsilon_\infty} \right)^{1/2} \left(1 - \frac{\epsilon_\infty}{\epsilon(0)} \right)^{1/2}. \quad (\text{B.7})$$

Appendix C

Hyperbolic dispersion

The hyperbolic dispersion relation derived from **k.p** theory [162] is given by

$$\frac{\hbar^2 k^2}{2m_\Gamma^*} = \varepsilon_{\mathbf{k}}(1 + \alpha\varepsilon_{\mathbf{k}}), \quad (\text{C.1})$$

where m_Γ^* is the effective mass around Γ (CBM), and α (in units of eV^{-1}) captures the degree of nonparabolicity.

Rearranging Eq. C.1 in a quadratic form, we get

$$\alpha\varepsilon^2 + \varepsilon - \frac{\hbar^2 k^2}{2m_\Gamma^*} = 0. \quad (\text{C.2})$$

The two roots of this equation are

$$\varepsilon = -\frac{1}{2\alpha} \pm \frac{1}{2\alpha} \sqrt{1 + 4\alpha \frac{\hbar^2 k^2}{2m_\Gamma^*}}. \quad (\text{C.3})$$

The solution with the positive term describes the dispersion of a conduction band with a positive curvature, while the solution with the negative term represents the dispersion of a valence band, which has a negative curvature. The “zero” occurs at the CBM, and the band gap separating the valence and conduction bands is $1/\alpha$.

The velocity vector for the conduction band is given by

$$\mathbf{v}_{nk} = \left(\frac{\hbar \mathbf{k}}{m_{\Gamma}^*} \right) \left[1 + \frac{2\alpha \hbar^2 k^2}{m_{\Gamma}^*} \right]^{-1/2} \quad (\text{C.4})$$

$$= \left(\frac{\hbar \mathbf{k}}{m_{\Gamma}^*} \right) (1 + 2\alpha \varepsilon_{n,\mathbf{k}})^{-1} \quad (\text{C.5})$$

and the band mass accounting for nonparabolicity is given by

$$m^* = m_{\Gamma}^* (1 + 2\alpha \varepsilon_{n,\mathbf{k}})^3. \quad (\text{C.6})$$

The density of states (DOS) is given by

$$D(\varepsilon_{n,k}) = \frac{1}{V_{\text{cell}}} \sum_k \delta(\varepsilon - \varepsilon_{n,k}) \quad (\text{C.7})$$

$$= \sum_k \delta(k - k_0) \frac{1}{\left| \frac{\partial \varepsilon_k}{\partial k} \right|_{k_0}} \quad (\text{C.8})$$

$$= 2 \frac{1}{8\pi^3} \frac{1}{\left| \frac{\partial \varepsilon_k}{\partial k} \right|_{k_0}} \int dk^3 \delta(k - k_0) \quad (\text{C.9})$$

$$= 2 \frac{1}{8\pi^3} 4\pi k^2 \frac{1}{|\hbar v_k|_{k_0}} \quad (\text{C.10})$$

$$= \frac{1}{\pi^2} |\mathbf{k}| \left(\frac{m_{\Gamma}^*}{\hbar^2} \right) (1 + 2\alpha \varepsilon_{n,\mathbf{k}}). \quad (\text{C.11})$$

Expressing Eq. C.11 entirely in terms of ε yields

$$D(\varepsilon_{n,k}) = \frac{1}{\pi^2} \sqrt{2\varepsilon_{n,k} (1 + \alpha\varepsilon_{n,k})} \left(\frac{m_{\Gamma}^*}{\hbar^2} \right)^{3/2} (1 + 2\alpha \varepsilon_{n,k}). \quad (\text{C.12})$$

From the DOS, the electron density as a function of Fermi level ε_{F} at $T = 0$ K can be obtained by integrating Eq. C.12,

$$n(\varepsilon_{\text{F}})|_{T=0} = \frac{1}{3\pi^2} (2\varepsilon_{\text{F}}(\alpha\varepsilon_{\text{F}} + 1))^{3/2} \left(\frac{m_{\Gamma}^*}{\hbar^2} \right)^{3/2}. \quad (\text{C.13})$$

For $T \neq 0$, the Fermi-Dirac distribution is to be multiplied with the DOS, and integrated.

Bibliography

- [1] L. Edgar, “Method and apparatus for controlling electric currents,” US Patent 1,745,175 (1930).
- [2] W. Shockley, “The theory of p - n junctions in semiconductors and p - n junction transistors,” *Bell System Technical Journal* **28**, 435 (1949).
- [3] J. Kilby, “Plug-in circuit units,” US Patent 2,892,130 (1959).
- [4] T. Ishihara, *Perovskite Oxide for Solid Oxide Fuel Cells*. Fuel Cells and Hydrogen Energy. Springer US, Boston, MA, 2009.
- [5] J. G. Bednorz and K. A. Müller, “Possible high- T_c superconductivity in the Ba-La-Cu-O system,” *Zeitschrift für Phys. B Condens. Matter* **64**, 189 (1986).
- [6] A. Ohtomo and H. Y. Hwang, “A high-mobility electron gas at the LaAlO₃/SrTiO₃ heterointerface.,” *Nature* **427**, 423 (2004).
- [7] S. Thiel, G. Hammerl, A. Schmehl, C. W. Schneider, and J. Mannhart, “Tunable quasi-two-dimensional electron gases in oxide heterostructures.,” *Science* **313**, 1942 (2006).
- [8] A. Brinkman, M. Huijben, M. van Zalk, J. Huijben, U. Zeitler, J. C. Maan, W. G. van der Wiel, G. Rijnders, D. H. A. Blank, and H. Hilgenkamp, “Magnetic effects at the interface between non-magnetic oxides.,” *Nature Mater.* **6**, 493 (2007).
- [9] S. Gariglio, N. Reyren, A. D. Caviglia, and J.-M. Triscone, “Superconductivity at the LaAlO₃/SrTiO₃ interface.,” *J. Phys. Condens. Matter* **21**, 164213 (2009).
- [10] G. Berner, S. Glawion, J. Walde, F. Pfaff, H. Hollmark, L.-C. Duda, S. Paetel, C. Richter, J. Mannhart, M. Sing, and R. Claessen, “LaAlO₃/SrTiO₃ oxide heterostructures studied by resonant inelastic x-ray scattering,” *Phys. Rev. B* **82**, 241405 (2010).
- [11] T. C. Asmara, A. Annadi, I. Santoso, P. K. Gogoi, A. Kotlov, H. M. Omer, M. Motapothula, M. B. H. Breese, M. Rübhausen, T. Venkatesan, Ariando, and A. Rusydi, “Mechanisms of charge transfer and redistribution in LaAlO₃/SrTiO₃ revealed by high-energy optical conductivity.,” *Nat. Commun.* **5**, 3663 (2014).

- [12] P. Moetakef, T. A. Cain, D. G. Ouellette, J. Y. Zhang, D. O. Klenov, A. Janotti, C. G. Van de Walle, S. Rajan, S. J. Allen, and S. Stemmer, “Electrostatic carrier doping of $\text{GdTiO}_3/\text{SrTiO}_3$ interfaces,” *Appl. Phys. Lett.* **99**, 232116 (2011).
- [13] Y. Segal, J. H. Ngai, J. W. Reiner, F. J. Walker, and C. H. Ahn, “X-ray photoemission studies of the metal-insulator transition in $\text{LaAlO}_3/\text{SrTiO}_3$ structures grown by molecular beam epitaxy,” *Phys. Rev. B* **80**, 241107 (2009).
- [14] N. Nakagawa, H. Y. Hwang, and D. A. Muller, “Why some interfaces cannot be sharp,” *Nature Mater.* **5**, 204 (2006).
- [15] C. W. Schneider, M. Esposito, I. Marozau, K. Conder, M. Doebeli, Y. Hu, M. Mallepell, A. Wokaun, and T. Lippert, “The origin of oxygen in oxide thin films: Role of the substrate,” *Appl. Phys. Lett.* **97**, 192107 (2010).
- [16] J. N. Eckstein, “Oxide interfaces: Watch out for the lack of oxygen,” *Nat. Mater.* **6**, 473 (2007).
- [17] M. Basletic, J.-L. Maurice, C. Carrétéro, G. Herranz, O. Copie, M. Bibes, É. Jacquet, K. Bouzouane, S. Fusil, and A. Barthélémy, “Mapping the spatial distribution of charge carriers in $\text{LaAlO}_3/\text{SrTiO}_3$ heterostructures,” *Nat. Mater.* **7**, 621–625 (2008).
- [18] S. Chambers, M. Engelhard, V. Shutthanandan, Z. Zhu, T. Droubay, L. Qiao, P. Sushko, T. Feng, H. Lee, T. Gustafsson, E. Garfunkel, A. Shah, J.-M. Zuo, and Q. Ramasse, “Instability, intermixing and electronic structure at the epitaxial $\text{LaAlO}_3/\text{SrTiO}_3(001)$ heterojunction,” *Surf. Sci. Rep.* **65**, 317 (2010).
- [19] W. Wunderlich, H. Ohta, and K. Koumoto, “Enhanced effective mass in doped SrTiO_3 and related perovskites,” *Physica B Condens. Matter* **404**, 2202 (2009).
- [20] V. Vonk, J. Huijben, D. Kukuruznyak, A. Stierle, H. Hilgenkamp, A. Brinkman, and S. Harkema, “Polar-discontinuity-retaining *A*-site intermixing and vacancies at $\text{SrTiO}_3/\text{LaAlO}_3$ interfaces,” *Phys. Rev. B* **85**, 045401 (2012).
- [21] A. Janotti, L. Bjaalie, L. Gordon, and C. G. Van de Walle, “Controlling the density of the two-dimensional electron gas at the $\text{SrTiO}_3/\text{LaAlO}_3$ interface,” *Phys. Rev. B* **86**, 241108 (2012).
- [22] H.-M. Christen, J. Mannhart, E. J. Williams, and C. Gerber, “Dielectric properties of sputtered SrTiO_3 films,” *Phys. Rev. B* **49**, 12095 (1994).
- [23] J. Hemberger, P. Lunkenheimer, R. Viana, R. Böhmer, and A. Loidl, “Electric-field-dependent dielectric constant and nonlinear susceptibility in SrTiO_3 ,” *Phys. Rev. B* **52**, 13159 (1995).

- [24] R. A. van der Berg, P. W. M. Blom, J. F. M. Cillessen, and R. M. Wolf, “Field dependent permittivity in metal-semiconducting SrTiO₃ Schottky diodes,” *Appl. Phys. Lett.* **697**, 697 (1995).
- [25] W. Cochran, “Crystal stability and the theory of ferroelectricity,” *Adv. Phys.* **9**, 387 (1960).
- [26] R. A. Cowley, “Lattice Dynamics and Phase Transitions of Strontium Titanate,” *Phys. Rev. A* **134**, 981 (1964).
- [27] G. Khalsa and A. MacDonald, “Theory of the SrTiO₃ surface state two-dimensional electron gas,” *Phys. Rev. B* **86**, 125121 (2012).
- [28] K. A. Müller and H. Burkard, “SrTiO₃: An intrinsic quantum paraelectric below 4 K,” *Phys. Rev. B* **19**, 3593 (1979).
- [29] K. V. Reich, M. Schecter, and B. I. Shklovskii, “Accumulation, inversion, and depletion layers in SrTiO₃,” *Phys. Rev. B* **91**, 115303 (2015).
- [30] M. Stengel, “First-Principles Modeling of Electrostatically Doped Perovskite Systems,” *Phys. Rev. Lett.* **106**, 136803 (2011).
- [31] O. Copie, V. Garcia, C. Bödefeld, C. Carrétéro, M. Bibes, G. Herranz, E. Jacquet, J.-L. Maurice, B. Vinter, S. Fusil, K. Bouzehouane, H. Jaffrès, and A. Barthélémy, “Towards Two-Dimensional Metallic Behavior at LaAlO₃/SrTiO₃ Interfaces,” *Phys. Rev. Lett.* **102**, 216804 (2009).
- [32] D. Kahng and S. H. Wemple, “Measurement of nonlinear polarization of KTaO₃ using schottky diodes,” *J. Appl. Phys.* **36**, 2925 (1965).
- [33] S. H. Wemple, M. Didomenico, and A. Jayaraman, “Electron scattering in perovskite-oxide ferroelectric semiconductors,” *Phys. Rev.* **180**, 547 (1969).
- [34] A. Verma, A. P. Kajdos, T. A. Cain, S. Stemmer, and D. Jena, “Intrinsic Mobility Limiting Mechanisms in Lanthanum-Doped Strontium Titanate,” *Phys. Rev. Lett.* **112**, 216601 (2014).
- [35] E. Mikheev, B. Himmetoglu, A. P. Kajdos, P. Moetakef, T. A. Cain, C. G. Van de Walle, and S. Stemmer, “Limitations to the room temperature mobility of two- and three-dimensional electron liquids in SrTiO₃,” *Appl. Phys. Lett.* **106**, 062102 (2015).
- [36] H. J. Kim, U. Kim, H. M. Kim, T. H. Kim, H. S. Mun, B.-G. Jeon, K. T. Hong, W.-J. Lee, C. Ju, K. H. Kim, and K. Char, “High Mobility in a Stable Transparent Perovskite Oxide,” *Appl. Phys. Express* **5**, 061102 (2012).

- [37] H. J. Kim, U. Kim, T. H. Kim, J. Kim, H. M. Kim, B.-G. Jeon, W.-J. Lee, H. S. Mun, K. T. Hong, J. Yu, K. Char, and K. H. Kim, “Physical properties of transparent perovskite oxides $(\text{Ba},\text{La})\text{SnO}_3$ with high electrical mobility at room temperature,” *Phys. Rev. B* **86**, 165205 (2012).
- [38] H. J. Kim, J. Kim, T. H. Kim, W.-J. Lee, B.-G. Jeon, J.-Y. Park, W. S. Choi, D. W. Jeong, S. H. Lee, J. Yu, T. W. Noh, and K. H. Kim, “Indications of strong neutral impurity scattering in $\text{Ba}(\text{Sn},\text{Sb})\text{O}_3$ single crystals,” *Phys. Rev. B* **88**, 125204 (2013).
- [39] K. Krishnaswamy, C. E. Dreyer, A. Janotti, and C. G. Van de Walle, “First-principles study of surface charging in $\text{LaAlO}_3/\text{SrTiO}_3$ heterostructures,” *Phys. Rev. B* **92**, 085420 (2015).
- [40] H. Peelaers, K. Krishnaswamy, L. Gordon, D. Steiauf, A. Sarwe, A. Janotti, and C. G. Van de Walle, “Impact of electric-field dependent dielectric constants on two-dimensional electron gases in complex oxides,” *Appl. Phys. Lett.* **107**, 183505 (2015).
- [41] K. Krishnaswamy, L. Bjaalie, B. Himmetoglu, A. Janotti, L. Gordon, and C. G. Van de Walle, “ BaSnO_3 as a channel material in perovskite oxide heterostructures,” *Appl. Phys. Lett.* **108**, 083501 (2016).
- [42] L. H. Thomas, “The calculation of atomic fields,” *Mathematical Proceedings of the Cambridge Philosophical Society* **23**, 542 (1927).
- [43] E. Fermi, “Eine statistische methode zur bestimmung einiger eigenschaften des atoms und ihre anwendung auf die theorie des periodischen systems der elemente,” *Zeitschrift für Physik* **48**, 73–79 (1928).
- [44] E. Fermi, “Statistical method to determine some properties of atoms,” *Rend. Accad. Naz. Lincei* **6**, 602 (1927).
- [45] P. Hohenberg and W. Kohn, “Inhomogeneous Electron Gas,” *Phys. Rev.* **136**, B864 (1964).
- [46] A. Zangwill, “The education of Walter Kohn and the creation of density functional theory,” *Arch. Hist. Exact Sci.* **68**, 775 (2014).
- [47] W. Kohn and L. J. Sham, “Self-consistent equations including exchange and correlation effects,” *Phys. Rev.* **140**, A1133 (1965).
- [48] D. M. Ceperley and B. J. Alder, “Ground State of the Electron Gas by a Stochastic Method,” *Phys. Rev. Lett.* **45**, 566 (1980).
- [49] J. P. Perdew and A. Zunger, “Self-interaction correction to density-functional approximations for many-electron systems,” *Phys. Rev. B* **23**, 5048 (1981).

- [50] J. P. Perdew and Y. Wang, “Accurate and simple analytic representation of the electron-gas correlation energy,” *Phys. Rev. B* **45**, 13244 (1992).
- [51] J. P. Perdew, M. Ernzerhof, and K. Burke, “Rationale for mixing exact exchange with density functional approximations,” *J. Chem. Phys.* **105**, 9982 (1996).
- [52] J. Paier, M. Marsman, K. Hummer, G. Kresse, I. C. Gerber, and J. G. Angyan, “Screened hybrid density functionals applied to solids,” *J. Chem. Phys.* **124**, 154709 (2006).
- [53] A. Grüneis, G. Kresse, Y. Hinuma, and F. Oba, “Ionization Potentials of Solids: The Importance of Vertex Corrections,” *Phys. Rev. Lett.* **112**, 096401 (2014).
- [54] C. Franchini, “Hybrid functionals applied to perovskites,” *J. Phys. Condens. Matter* **26**, 253202 (2014).
- [55] J. Heyd, G. E. Scuseria, and M. Ernzerhof, “Hybrid functionals based on a screened Coulomb potential,” *J. Chem. Phys.* **118**, 8207 (2003).
- [56] P. E. Blöchl, “Projector augmented-wave method,” *Phys. Rev. B* **50**, 17953 (1994).
- [57] C. Freysoldt, B. Grabowski, T. Hickel, J. Neugebauer, G. Kresse, A. Janotti, and C. G. Van de Walle, “First-principles calculations for point defects in solids,” *Rev. Mod. Phys.* **86**, 253 (2014).
- [58] G. Kresse and J. Furthmüller, “Efficiency of ab-initio total energy calculations for metals and semiconductors using a plane-wave basis set,” *Comp. Mater. Sci.* **6**, 15 (1996).
- [59] P. Giannozzi, S. Baroni, N. Bonini, M. Calandra, R. Car, C. Cavazzoni, D. Ceresoli, G. L. Chiarotti, M. Cococcioni, I. Dabo, A. Dal Corso, S. de Gironcoli, S. Fabris, G. Fratesi, R. Gebauer, U. Gerstmann, C. Gougoussis, A. Kokalj, M. Lazzeri, L. Martin-Samos, N. Marzari, F. Mauri, R. Mazzarello, S. Paolini, A. Pasquarello, L. Paulatto, C. Sbraccia, S. Scandolo, G. Sclauzero, A. P. Seitsonen, A. Smogunov, P. Umari, and R. M. Wentzcovitch, “QUANTUM ESPRESSO: a modular and open-source software project for quantum simulations of materials,” *J. Phys. Condens. Matter* **21**, 395502 (2009).
- [60] X. Gonze, B. Amadon, P.-M. Anglade, J.-M. Beuken, F. Bottin, P. Boulanger, F. Bruneval, D. Caliste, R. Caracas, M. Ct., T. Deutsch, L. Genovese, P. Ghosez, M. Giantomassi, S. Goedecker, D. Hamann, P. Hermet, F. Jollet, G. Jomard, S. Leroux, M. Mancini, S. Mazevet, M. Oliveira, G. Onida, Y. Pouillon, T. Rangel, G.-M. Rignanese, D. Sangalli, R. Shaltaf, M. Torrent, M. Verstraete, G. Zerah, and J. Zwanziger, “Abinit: First-principles approach to material and nanosystem properties,” *Comput. Phys. Commun.* **180**, 2582 (2009).

- [61] J. M. Soler, E. Artacho, J. D. Gale, A. García, J. Junquera, P. Ordejón, and D. Sánchez-Portal, “The siesta method for ab initio order- n materials simulation,” *J. Phys. Condens. Matter* **14**, 2745 (2002).
- [62] D. Marx and J. Hutter, *Ab Initio Molecular Dynamics*. Cambridge University Press, 2009. <http://www.cambridge.org/gb/knowledge/isbn/item2327682/>.
- [63] U. Mishra and J. Singh, *Semiconductor Device Physics*. 2008.
- [64] J. M. Ziman, *Electrons and Phonons: The Theory of Transport Phenomena in Solids*. International series of monographs on physics. OUP Oxford, 1960.
- [65] W. Li, “Electrical transport limited by electron-phonon coupling from Boltzmann transport equation: An ab initio study of Si, Al, and MoS₂,” *Phys. Rev. B* **92**, 075405 (2015).
- [66] J. Zhou, B. Liao, and G. Chen, “First-principles calculations of thermal, electrical, and thermoelectric transport properties of semiconductors,” *Semicond. Sci. Technol.* **31**, 043001 (2016).
- [67] F. Giustino, “Electron-phonon interactions from first principles,”.
- [68] Y. Toyozawa, *Polarons in ionic crystals and polar semiconductors*. NATO Advanced Study Institutes Series. North-Holland Pub. Co., 1972.
- [69] J. T. Devreese, S. N. Klimin, J. L. M. van Mechelen, and D. van der Marel, “Many-body large polaron optical conductivity in SrTi_{1-x}Nb_xO₃,” *Phys. Rev. B* **81**, 125119 (2010).
- [70] H. Fröhlich, “Electrons in lattice fields,” *Adv. Phys.* **3**, 325 (1954).
- [71] H. Ehrenreich, “Screening effects in polar semiconductors,” *J. Phys. Chem. Solids* **8**, 130 (1959).
- [72] M. E. Kim, A. Das, and S. D. Senturia, “Electron scattering interaction with coupled plasmon-polar-phonon modes in degenerate semiconductors,” *Phys. Rev. B* **18**, 6890 (1978).
- [73] N. W. Ashcroft and N. D. Mermin, *Solid state physics*. Science: Physics. Saunders College, 1976.
- [74] S. Doniach, “Lattice Screening in Polar Semiconductors,” *Proc. Phys. Soc.* **73**, 849 (1959).
- [75] B. B. Varga, “Coupling of plasmons to polar phonons in degenerate semiconductors,” *Phys. Rev.* **137**, 1896 (1965).

- [76] A. Mooradian and G. B. Wright, “Observation of the Interaction of Plasmons with Longitudinal Optical Phonons in GaAs,” *Phys. Rev. Lett.* **16**, 999 (1966).
- [77] D. Chattopadhyay and H. J. Queisser, “Electron scattering by ionized impurities in semiconductors,” *Rev. Mod. Phys.* **53**, 745 (1981).
- [78] B. K. Ridley, “Reconciliation of the Conwell-Weisskopf and Brooks-Herring formulae for charged-impurity scattering in semiconductors: Third-body interference,” *J. Phys. C* **10**, 1589 (1977).
- [79] K. Seeger, *Semiconductor Physics*. Advanced Texts in Physics. Springer Berlin Heidelberg, Berlin, Heidelberg, 2004.
- [80] Y. Fu, K. B. Joelsson, K. J. Grahm, W.-X. Ni, G. V. Hansson, and M. Willander, “Hall factor in strained p -type doped $\text{Si}_{1-x}\text{Ge}_x$ alloy,” *Phys. Rev. B* **54**, 11317 (1996).
- [81] J. R. Yates, X. Wang, D. Vanderbilt, and I. Souza, “Spectral and Fermi surface properties from Wannier interpolation,” *Phys. Rev. B* **75**, 195121 (2007).
- [82] L. Bjaalie, B. Himmetoglu, L. Weston, A. Janotti, and C. G. Van de Walle, “Oxide interfaces for novel electronic applications,” *New J. Phys.* **16**, 025005 (2014).
- [83] S. Birner, S. Hackenbuchner, M. Sabathil, G. Zandler, J. A. Majewski, T. Andlauer, T. Zibold, R. Morschl, A. Trellakis, and P. Vogl, “Modeling of semiconductor nanostructures with nextnano³,” *Acta Phys. Pol. A* **110**, 111 (2006). <http://www.nextnano.de/>.
- [84] T. Ando, A. B. Fowler, and F. Stern, “Electronic properties of two-dimensional systems,” *Rev. Mod. Phys.* **54**, 437 (1982).
- [85] Y. Z. Chen, N. Bovet, F. Trier, D. V. Christensen, F. M. Qu, N. H. Andersen, T. Kasama, W. Zhang, R. Giraud, J. Dufouleur, T. S. Jespersen, J. R. Sun, A. Smith, J. Nygård, L. Lu, B. Büchner, B. G. Shen, S. Linderoth, and N. Pryds, “A high-mobility two-dimensional electron gas at the spinel/perovskite interface of $\gamma\text{-Al}_2\text{O}_3/\text{SrTiO}_3$,” *Nat. Commun.* **4**, 1371 (2013).
- [86] C. Cen, S. Thiel, J. Mannhart, and J. Levy, “Oxide nanoelectronics on demand.,” *Science* **323**, 1026 (2009).
- [87] N. C. Bristowe, P. B. Littlewood, and E. Artacho, “Surface defects and conduction in polar oxide heterostructures,” *Phys. Rev. B* **83**, 205405 (2011).
- [88] N. C. Bristowe, P. Ghosez, P. B. Littlewood, and E. Artacho, “The origin of two-dimensional electron gases at oxide interfaces: insights from theory,” *J. Phys. Condens. Matter* **26**, 143201 (2014).

- [89] W.-J. Son, E. Cho, J. Lee, and S. Han, “Hydrogen adsorption and carrier generation in LaAlO₃-SrTiO₃ heterointerfaces: a first-principles study,” *J. Phys. Condens. Matter* **22**, 315501 (2010).
- [90] R. Arras, V. G. Ruiz, W. E. Pickett, and R. Pentcheva, “Tuning the two-dimensional electron gas at the LaAlO₃/SrTiO₃(001) interface by metallic contacts,” *Phys. Rev. B* **85**, 125404 (2012).
- [91] C. Cen, S. Thiel, G. Hammerl, C. W. Schneider, K. E. Andersen, C. S. Hellberg, J. Mannhart, and J. Levy, “Nanoscale control of an interfacial metal-insulator transition at room temperature.,” *Nature Mater.* **7**, 298 (2008).
- [92] F. Bi, D. F. Bogorin, C. Cen, C. W. Bark, J.-W. Park, C.-B. Eom, and J. Levy, “Water-cycle mechanism for writing and erasing nanostructures at the LaAlO₃/SrTiO₃ interface,” *Appl. Phys. Lett.* **97**, 173110 (2010).
- [93] Y. Xie, C. Bell, T. Yajima, Y. Hikita, and H. Y. Hwang, “Charge Writing at the LaAlO₃/SrTiO₃ surface.,” *Nano Lett.* **10**, 2588 (2010).
- [94] Y. Xie, Y. Hikita, C. Bell, and H. Y. Hwang, “Control of electronic conduction at an oxide heterointerface using surface polar adsorbates.,” *Nat. Commun.* **2**, 494 (2011).
- [95] A. Kumar, T. Arruda, Y. Kim, and I. Ivanov, “Probing Surface and Bulk Electrochemical Processes on the LaAlO₃-SrTiO₃ Interface,” *ACS Nano* **6**, 3841 (2012).
- [96] Y.-W. Xie and H. Y. Hwang, “Tuning the electrons at the LaAlO₃ /SrTiO₃ interface: From growth to beyond growth,” *Chin. Phys. B* **22**, 127301 (2013).
- [97] Y. Xie, C. Bell, Y. Hikita, S. Harashima, and H. Y. Hwang, “Enhancing electron mobility at the LaAlO₃/SrTiO₃ interface by surface control.,” *Adv. Mater.* **25**, 4735 (2013).
- [98] C. Bark, P. Sharma, Y. Wang, and S. Baek, “Switchable induced polarization in LaAlO₃/SrTiO₃ heterostructures,” *Nano Lett.* **12**, 1765 (2012).
- [99] O. Sinai, O. T. Hofmann, P. Rinke, M. Scheffler, G. Heimel, and L. Kronik, “Multiscale approach to the electronic structure of doped semiconductor surfaces,” *Phys. Rev. B* **91**, 075311 (2015).
- [100] F. Cossu, U. Schwingenschlögl, and V. Eyert, “Metal-insulator transition at the LaAlO₃/SrTiO₃ interface revisited: A hybrid functional study,” *Phys. Rev. B* **88**, 045119 (2013).

- [101] A. Sorokine, D. Bocharov, S. Piskunov, and V. Kashcheyevs, “Electronic charge redistribution in $\text{LaAlO}_3(001)$ thin films deposited at $\text{SrTiO}_3(001)$ substrate: First-principles analysis and the role of stoichiometry,” *Phys. Rev. B* **86**, 155410 (2012).
- [102] H. Chen, A. M. Kolpak, and S. Ismail-Beigi, “Electronic and magnetic properties of $\text{SrTiO}_3/\text{LaAlO}_3$ interfaces from first principles,” *Adv. Mater.* **22**, 2881 (2010).
- [103] L. Yu and A. Zunger, “A polarity-induced defect mechanism for conductivity and magnetism at polar-nonpolar oxide interfaces,” *Nat. Commun.* **5**, 5118 (2014).
- [104] H.-P. Komsa and A. Pasquarello, “Finite-Size Supercell Correction for Charged Defects at Surfaces and Interfaces,” *Phys. Rev. Lett.* **110**, 095505 (2013).
- [105] W. Mönch, *Semiconductor Surfaces and Interfaces*. Springer Science & Business Media, New York, NY, USA, 2001.
- [106] N. A. Richter, S. Siculo, S. V. Levchenko, J. Sauer, and M. Scheffler, “Concentration of Vacancies at Metal-Oxide Surfaces: Case Study of $\text{MgO}(100)$,” *Phys. Rev. Lett.* **111**, 045502 (2013).
- [107] A. Y. Lozovoi, A. Alavi, J. Kohanoff, and R. M. Lynden-Bell, “Ab initio simulation of charged slabs at constant chemical potential,” *J. Chem. Phys.* **115**, 1661 (2001).
- [108] J. Heyd, G. E. Scuseria, and M. Ernzerhof, “Erratum: Hybrid functionals based on a screened Coulomb potential [*J. Chem. Phys.* 118, 8207 (2003)],” *J. Chem. Phys.* **124**, 219906 (2006).
- [109] G. Kresse and D. Joubert, “From ultrasoft pseudopotentials to the projector augmented-wave method,” *Phys. Rev. B* **59**, 1758 (1999).
- [110] G. Kresse and J. Hafner, “Ab initio molecular dynamics for liquid metals,” *Phys. Rev. B* **47**, 558 (1993).
- [111] A. Janotti, D. Steiauf, and C. G. Van de Walle, “Strain effects on the electronic structure of SrTiO_3 : Toward high electron mobilities,” *Phys. Rev. B* **84**, 201304 (2011).
- [112] K. Krishnaswamy, C. E. Dreyer, A. Janotti, and C. G. Van de Walle, “Structure and energetics of $\text{LaAlO}_3(001)$ surfaces,” *Phys. Rev. B* **90**, 235436 (2014).
- [113] H. Monkhorst and J. Pack, “Special points for Brillouin-zone integrations,” *Phys. Rev. B* **13**, 5188 (1976).

- [114] C. Freysoldt, J. Neugebauer, and C. G. Van de Walle, “Fully Ab Initio Finite-Size Corrections for Charged-Defect Supercell Calculations,” *Phys. Rev. Lett.* **102**, 016402 (2009).
- [115] C. Freysoldt, J. Neugebauer, and C. G. Van de Walle, “Electrostatic interactions between charged defects in supercells,” *Phys. Status Solidi B* **248**, 1067 (2011).
- [116] J. Lee and A. A. Demkov, “Charge origin and localization at the n -type SrTiO₃/LaAlO₃ interface,” *Phys. Rev. B* **78**, 193104 (2008).
- [117] Y. Li and J. Yu, “Modulation of electron carrier density at the n -type LaAlO₃/SrTiO₃ interface by water adsorption,” *J. Phys. Condens. Matter* **25**, 265004 (2013).
- [118] A. Baldereschi, S. Baroni, and R. Resta, “Band Offsets in Lattice-Matched Heterojunctions: A Model and First-Principles Calculations for GaAs/AlAs,” *Phys. Rev. Lett.* **61**, 734 (1988).
- [119] S.-G. Lim, S. Kriventsov, T. N. Jackson, J. H. Haeni, D. G. Schlom, A. M. Balbashov, R. Uecker, P. Reiche, J. L. Freeouf, and G. Lucovsky, “Dielectric functions and optical bandgaps of high-K dielectrics for metal-oxide-semiconductor field-effect transistors by far ultraviolet spectroscopic ellipsometry,” *J. Appl. Phys.* **91**, 4500 (2002).
- [120] M. Leslie and N. Gillan, “The energy and elastic dipole tensor of defects in ionic crystals calculated by the supercell method,” *J. Phys. C* **18**, 973 (1985).
- [121] G. Makov and M. C. Payne, “Periodic boundary conditions in ab initio calculations,” *Phys. Rev. B* **51**, 4014 (1995).
- [122] M. Huijben, G. Rijnders, D. H. A. Blank, S. Bals, S. Van Aert, J. Verbeeck, G. Van Tendeloo, A. Brinkman, and H. Hilgenkamp, “Electronically coupled complementary interfaces between perovskite band insulators,” *Nature Mater.* **5**, 556 (2006).
- [123] G. Srivastava, “The electron counting rule and passivation of compound semiconductor surfaces,” *Appl. Surf. Sci.* **252**, 7600 (2006).
- [124] X.-b. Lu, Z.-g. Liu, Y.-p. Wang, Y. Yang, X.-p. Wang, H.-w. Zhou, and B.-y. Nguyen, “Structure and dielectric properties of amorphous LaAlO₃ and LaAlO_xN_y films as alternative gate dielectric materials,” *J. Appl. Phys.* **94**, 1229 (2003).
- [125] Y. Yamada, H. K. Sato, Y. Hikita, H. Y. Hwang, and Y. Kanemitsu, “Spatial density profile of electrons near the LaAlO₃/SrTiO₃ heterointerface revealed by time-resolved photoluminescence spectroscopy,” *Appl. Phys. Lett.* **104**, 151907 (2014).

- [126] N. F. Mott, “Metal-insulator transition,” *Rev. Mod. Phys.* **40**, 677 (1968).
- [127] P. W. Tasker, “The stability of ionic crystal surfaces,” *J. Phys. C* **12**, 4977 (1979).
- [128] L. Bjaalie, D. G. Ouellette, P. Moetakef, T. A. Cain, A. Janotti, B. Himmetoglu, S. J. Allen, S. Stemmer, and C. G. Van de Walle, “Small hole polarons in rare-earth titanates,” *Appl. Phys. Lett.* **106**, 232103 (2015).
- [129] L. Bjaalie, A. Janotti, K. Krishnaswamy, and C. G. Van de Walle, “Point defects, impurities, and small hole polarons in GdTiO_3 ,” *Phys. Rev. B* **93**, 115316 (2016).
- [130] R. J. M. Konings, O. Beneš, A. Kovács, D. Manara, D. Sedmidubský, L. Gorokhov, V. S. Iorish, V. Yungman, E. Shenyavskaya, and E. Osina, “The Thermodynamic Properties of the f-Elements and their Compounds. Part 2. The Lanthanide and Actinide Oxides,” *J. Phys. Chem. Ref. Data* **43**, 013101 (2014).
- [131] M. Chase, “NIST-JANAF Thermochemical Tables, 4th Edition,” (1998).
- [132] K. Helean, S. Ushakov, C. Brown, A. Navrotsky, J. Lian, R. Ewing, J. Farmer, and L. Boatner, “Formation enthalpies of rare earth titanate pyrochlores,” *J. Solid State Chem.* **177**, 1858 (2004).
- [133] D. A. MacLean, H.-N. Ng, and J. Greedan, “Crystal structures and crystal chemistry of the $RE\text{TiO}_3$ perovskites: $RE = \text{La, Nd, Sm, Gd, Y}$,” *J. Solid State Chem.* **30**, 35 (1979).
- [134] C. G. Van de Walle and J. Neugebauer, “First-principles calculations for defects and impurities: Applications to III-nitrides,” *J. Appl. Phys.* **95**, 3851 (2004).
- [135] C. G. Van de Walle and J. Neugebauer, “Hydrogen in semiconductors,” *Annu. Rev. Mater. Res.* **36**, 179 (2006).
- [136] V. K. Lazarov, R. Plass, H.-C. Poon, D. K. Saldin, M. Weinert, S. A. Chambers, and M. Gajdardziska-Josifovska, “Structure of the hydrogen-stabilized $\text{MgO}(111)-(1\times 1)$ polar surface: Integrated experimental and theoretical studies,” *Phys. Rev. B* **71**, 115434 (2005).
- [137] B. Meyer, “First-principles study of the polar O-terminated ZnO surface in thermodynamic equilibrium with oxygen and hydrogen,” *Phys. Rev. B* **69**, 045416 (2003).
- [138] J. B. Goodenough, “The two components of the crystallographic transition in VO_2 ,” *J. Solid State Chem.* **3**, 490 (1971).
- [139] B. Himmetoglu, A. Janotti, L. Bjaalie, and C. G. Van de Walle, “Interband and polaronic excitations in YTiO_3 from first principles,” *Phys. Rev. B* **90**, 161102 (2014).

- [140] G. Catalan, R. M. Bowman, and J. M. Gregg, “Metal-insulator transitions in NdNiO₃ thin films,” *Phys. Rev. B* **62**, 7892 (2000).
- [141] A. Janotti, L. Bjaalie, B. Himmetoglu, and C. G. Van de Walle, “Band alignment at band-insulator/Mott-insulator interfaces,” *Phys. Status Solidi RRL* **8**, 577 (2014).
- [142] D. O. Scanlon, “Defect engineering of BaSnO₃ for high-performance transparent conducting oxide applications,” *Phys. Rev. B* **87**, 161201 (2013).
- [143] K. Ellmer, “Past achievements and future challenges in the development of optically transparent electrodes,” *Nat. Photonics* **6**, 808 (2012).
- [144] B. Himmetoglu, A. Janotti, H. Peelaers, A. Alkauskas, and C. G. Van de Walle, “First-principles study of the mobility of SrTiO₃,” *Phys. Rev. B* **90**, 241204 (2014).
- [145] X. Lin, B. Fauque, and K. Behnia, “Scalable T^2 resistivity in a small single-component Fermi surface,” *Science* **349**, 945 (2015).
- [146] U. Kim, C. Park, T. Ha, Y. M. Kim, N. Kim, C. Ju, J. Park, J. Yu, J. H. Kim, and K. Char, “All-perovskite transparent high mobility field effect using epitaxial BaSnO₃ and LaInO₃,” *APL Mater.* **3**, 036101 (2015).
- [147] Z. Lebens-Higgins, D. O. Scanlon, H. Paik, S. Sallis, Y. Nie, M. Uchida, N. F. Quackenbush, M. J. Wahila, G. E. Sterbinsky, D. A. Arena, J. C. Woicik, D. G. Schlom, and L. F. J. Piper, “Direct Observation of Electrostatically Driven Band Gap Renormalization in a Degenerate Perovskite Transparent Conducting Oxide,” *Phys. Rev. Lett.* **116**, 027602 (2016).
- [148] S. Raghavan, T. Schumann, H. Kim, J. Y. Zhang, T. A. Cain, and S. Stemmer, “High-mobility BaSnO₃ grown by oxide molecular beam epitaxy,” *APL Mater.* **4**, 016106 (2016).
- [149] H. Mizoguchi, H. W. Eng, and P. M. Woodward, “Probing the Electronic Structures of Ternary Perovskite and Pyrochlore Oxides Containing Sn⁴⁺ or Sb⁵⁺,” *Inorg. Chem.* **43**, 1667 (2004).
- [150] J. Sun and D. J. Singh, “Thermoelectric properties of n -type SrTiO₃,” *APL Mater.* **4**, 104803 (2016).
- [151] G. Pizzi, D. Volja, B. Kozinsky, M. Fornari, and N. Marzari, “BoltzWann: A code for the evaluation of thermoelectric and electronic transport properties with a maximally-localized Wannier functions basis,” *Comput. Phys. Commun.* **185**, 422 (2014).

- [152] G. K. Madsen and D. J. Singh, “BoltzTraP. A code for calculating band-structure dependent quantities,” *Comput. Phys. Commun.* **175**, 67 (2006).
- [153] A. Slassi, “New potential dopants for BaSnO₃-based transparent conducting oxides,” *Opt. Quantum Electron.* **48**, 350 (2016).
- [154] K. Ghosh and U. Singiseti, “Ab initio calculation of electron-phonon coupling in monoclinic β -Ga₂O₃ crystal,” *Appl. Phys. Lett.* **109**, 072102 (2016).
- [155] K. Kaasbjerg, K. S. Thygesen, and K. W. Jacobsen, “Phonon-limited mobility in *n*-type single-layer MoS₂ from first principles,” *Phys. Rev. B* **85**, 115317 (2012).
- [156] X. Li, J. T. Mullen, Z. Jin, K. M. Borysenko, M. Buongiorno Nardelli, and K. W. Kim, “Intrinsic electrical transport properties of monolayer silicene and MoS₂ from first principles,” *Phys. Rev. B* **87**, 115418 (2013).
- [157] T. N. Stanislavchuk, A. A. Sirenko, A. P. Litvinchuk, X. Luo, and S.-W. Cheong, “Electronic band structure and optical phonons of BaSnO₃ and Ba_{0.97}La_{0.03}SnO₃ single crystals: Theory and experiment,” *J. Appl. Phys.* **112**, 044108 (2012).
- [158] Y. Hinatsu, “Electron Paramagnetic Resonance Spectra of Pr⁴⁺ in BaCeO₃, BaZrO₃, BaSnO₃, and Their Solid Solutions,” *J. Solid State Chem.* **122**, 384 (1996).
- [159] S. A. Chambers, T. C. Kaspar, A. Prakash, G. Haugstad, and B. Jalan, “Band alignment at epitaxial BaSnO₃/SrTiO₃(001) and BaSnO₃/LaAlO₃(001) heterojunctions,” *Appl. Phys. Lett.* **108**, 152104 (2016).
- [160] B. Li, Q. Liu, Y. Zhang, Z. Liu, and L. Geng, “Highly conductive Nb doped BaSnO₃ thin films on MgO substrates by pulsed laser deposition,” *J. Alloys Compd.* **680**, 343 (2016).
- [161] N. Marzari, A. A. Mostofi, J. R. Yates, I. Souza, and D. Vanderbilt, “Maximally localized Wannier functions: Theory and applications,” *Rev. Mod. Phys.* **84**, 1419 (2012).
- [162] M. S. Dresselhaus, G. Dresselhaus, and A. Jorio, *Group Theory: Application to the Physics of Condensed Matter*. Springer-Verlag Berlin Heidelberg, 2008.
- [163] H.-R. Liu, J.-H. Yang, H. J. Xiang, X. G. Gong, and S.-H. Wei, “Origin of the superior conductivity of perovskite Ba(Sr)SnO₃,” *Appl. Phys. Lett.* **102**, 112109 (2013).
- [164] B. G. Kim, J. Jo, and S. Cheong, “Hybrid functional calculation of electronic and phonon structure of BaSnO₃,” *J. Solid State Chem.* **197**, 134 (2013).

- [165] E. Moreira, J. M. Henriques, D. L. Azevedo, E. W. S. Caetano, V. N. Freire, and E. L. Albuquerque, “Structural and electronic properties of $\text{Sr}_x\text{Ba}_{1-x}\text{SnO}_3$ from first principles calculations,” *J. Solid State Chem.* **187**, 186 (2012).
- [166] D. Seo, K. Yu, Y. Jun Chang, E. Sohn, K. Hoon Kim, and E. J. Choi, “Infrared-optical spectroscopy of transparent conducting perovskite (La,Ba) SnO_3 thin films,” *Appl. Phys. Lett.* **104**, 022102 (2014).
- [167] S. James Allen, S. Raghavan, T. Schumann, K.-m. Law, and S. Stemmer, “Conduction band edge effective mass of La-doped BaSnO_3 ,” *Appl. Phys. Lett.* **108**, 252107 (2016).
- [168] H. P. R. Frederikse and W. R. Hosler, “Hall Mobility in SrTiO_3 ,” *Phys. Rev.* **161**, 822 (1967).
- [169] F. E. Low and D. Pines, “Mobility of Slow Electrons in Polar Crystals,” *Phys. Rev.* **98**, 414 (1955).
- [170] P. Y. Yu and M. Cardona, *Fundamentals of Semiconductors*. Graduate Texts in Physics. Springer Berlin Heidelberg, Berlin, Heidelberg, 2010.
- [171] C. Erginsoy, “Neutral Impurity Scattering in Semiconductors,” *Phys. Rev.* **79**, 1013 (1950).
- [172] W. Y. Wang, Y. L. Tang, Y. L. Zhu, J. Suriyaprakash, Y. B. Xu, Y. Liu, B. Gao, S.-W. Cheong, and X. L. Ma, “Atomic mapping of Ruddlesden-Popper faults in transparent conducting BaSnO_3 -based thin films,” *Sci. Rep.* **5**, 16097 (2015).
- [173] A. Sakai, T. Kanno, S. Yotsuhashi, H. Adachi, and Y. Tokura, “Thermoelectric Properties of Electron-Doped KTaO_3 ,” *Jpn. J. Appl. Phys.* **48**, 097002 (2009).
- [174] J. L. Servoin, Y. Luspain, and F. Gervais, “Infrared dispersion in SrTiO_3 at high temperature,” *Phys. Rev. B* **22**, 5501 (1980).
- [175] S. Ismail-Beigi, F. J. Walker, S.-W. Cheong, K. M. Rabe, and C. H. Ahn, “Alkaline earth stannates: The next silicon?,” *APL Mater.* **3**, 062510 (2015).
- [176] S. M. Xing, C. Shan, K. Jiang, J. J. Zhu, Y. W. Li, Z. G. Hu, and J. H. Chu, “Optoelectronic properties and interband transition of La-doped BaSnO_3 transparent conducting films determined by variable temperature spectral transmittance,” *J. Appl. Phys.* **117**, 103107 (2015).
- [177] H. J. Kim, U. Kim, H. M. Kim, T. H. Kim, H. S. Mun, B. G. Jeon, K. T. Hong, W. J. Lee, C. Ju, K. H. Kimy, and K. Char, “High mobility in a stable transparent perovskite oxide,” *Appl. Phys. Express* **5**, 61102 (2012).

- [178] X. Luo, Y. S. Oh, A. Sirenko, P. Gao, T. A. Tyson, K. Char, and S.-W. Cheong, “High carrier mobility in transparent $\text{Ba}_{1-x}\text{La}_x\text{SnO}_3$ crystals with a wide band gap,” *Appl. Phys. Lett.* **100**, 172112 (2012).
- [179] T. N. Stanislavchuk, A. A. Sirenko, A. P. Litvinchuk, X. Luo, and S.-W. Cheong, “Electronic band structure and optical phonons of BaSnO_3 and $\text{Ba}_{0.97}\text{La}_{0.03}\text{SnO}_3$ single crystals: Theory and experiment,” *J. Appl. Phys.* **112**, 044108 (2012).
- [180] U. Kim, C. Park, T. Ha, R. Kim, H. S. Mun, H. M. Kim, H. J. Kim, T. H. Kim, N. Kim, J. Yu, K. H. Kim, J. H. Kim, and K. Char, “Dopant-site-dependent scattering by dislocations in epitaxial films of perovskite semiconductor BaSnO_3 ,” *APL Mater.* **2**, 056107 (2014).
- [181] A. A. Mostofi, J. R. Yates, Y.-S. Lee, I. Souza, D. Vanderbilt, and N. Marzari, “wannier90: A tool for obtaining maximally-localised wannier functions,” *Comput. Phys. Commun.* **178**, 685 (2008).
- [182] G. E. Jellison, I. Paulauskas, L. A. Boatner, and D. J. Singh, “Optical functions of KTaO_3 as determined by spectroscopic ellipsometry and comparison with band structure calculations,” *Phys. Rev. B* **74**, 1 (2006).
- [183] K. Sood, K. Singh, and O. Pandey, “Co-existence of cubic and orthorhombic phases in Ba-doped LaInO_3 and their effect on conductivity,” *Phys. B Condens. Matter* **456**, 250 (2015).
- [184] C. Ang, A. Bhalla, and L. Cross, “Dielectric behavior of paraelectric KTaO_3 , CaTiO_3 , and $(\text{Ln}_{1/2}\text{Na}_{1/2})\text{TiO}_3$ under a dc electric field,” *Phys. Rev. B* **64**, 3 (2001).
- [185] A. Trellakis, T. Zibold, T. Andlauer, S. Birner, R. K. Smith, R. Morschl, and P. Vogl, “The 3D nanometer device project nextnano: Concepts, methods and result.,” *J. Comput. Electron.* **5**, 285 (2006).
- [186] A. P. Kajdos, D. G. Ouellette, T. A. Cain, and S. Stemmer, “Two-dimensional electron gas in a modulation-doped $\text{SrTiO}_3/\text{Sr}(\text{Ti}, \text{Zr})\text{O}_3$ heterostructure,” *Appl. Phys. Lett.* **103**, 082120 (2013).
- [187] J. L. Lyons, K. Krishnaswamy, L. Gordon, A. Janotti, and C. G. Van de Walle, “Identification of Microscopic Hole-Trapping Mechanisms in Nitride Semiconductors,” *IEEE Electron Device Lett.* **37**, 154 (2016).
- [188] R. M. Martin, *Electronic Structure: Basic Theory and Practical Methods*. Cambridge University Press, 2004.
- [189] Y. Taur and T. Ning, *Fundamentals of Modern VLSI Devices*. Cambridge University Press, 1998.

- [190] S.-H. Wei, “Overcoming the doping bottleneck in semiconductors,” *Comput. Mater. Sci.* **30**, 337 (2004).
- [191] W. Walukiewicz, “Intrinsic limitations to the doping of wide-gap semiconductors,” *Physica B Condens. Matter* **302–303**, 123 (2001).
- [192] N. Sarmadian, R. Saniz, B. Partoens, and D. Lamoen, “Easily doped p-type, low hole effective mass, transparent oxides,” *Scientific Reports* **6**, 20446 (2016).
supplementary:
<http://www.nature.com/articles/srep20446#supplementary-information>.
- [193] M. Boucherit, O. F. Shoron, T. A. Cain, C. A. Jackson, S. Stemmer, and S. Rajan, “Extreme charge density SrTiO₃/GdTiO₃ heterostructure field effect transistors,” *Appl. Phys. Lett.* **102**, 242909 (2013).
- [194] R. H. Lyddane, R. G. Sachs, and E. Teller, “On the Polar Vibrations of Alkali Halides,” *Phys. Rev.* **59**, 673 (1941).
- [195] A. J. Sievers and J. B. Page, “Generalized Lyddane-Sachs-Teller relation and disordered solids,” *Phys. Rev. B* **41**, 3455 (1990).